Danielle Cristina Teles Ferreira

# Tracking the thiobases photophysics: time-resolved spectroscopy studies of the relaxation pathways

Thesis presented to the Post-Graduation Program in Physics from the Instituto de Ciências Exatas of the Universidade Federal de Minas Gerais as a partial requirement for obtaining the title of Doctor of Science.

Supervisor: Ana Maria de Paula

Belo Horizonte

2020

Dados Internacionais de Catalogação na Publicação (CIP)

F383t Ferreira, Danielle Cristina Teles.
Tracking the thiobases photophysics: time-resolved spectroscopy studies of the relaxation pathways / Danielle Cristina Teles Ferreira. – 2020.
149f., enc. : il.

Orientadora: Ana Maria de Paula.
Tese (doutorado) – Universidade Federal de Minas Gerais, Departamento de Física.
Bibliografia: f. 99-114.

1. Espectroscopia, teses. 2. Óptica. 3. Dinâmica molecular.
I. Título. II. Paula, Ana Maria de. III. Universidade Federal de Minas Gerais, Departamento de Física.

CDU – 543.42 (043)

Ficha catalográfica elaborada por Romário Martins – CRB6 3595
Biblioteca Professor Manoel Lopes de Siqueira – Departamento de Física - UFMG

**Universidade Federal de Minas Gerais**
**Instituto de Ciências Exatas**
**Programa de Pós-Graduação em Física**
Caixa Postal 702
30.123-970 Belo Horizonte - MG - Brasil

Telefone (xx) (31) 3409 5637
(xx) (31) 3409 5633
Fax (xx) (31) 3409 5688
(xx) (31) 3409 5600
e-mail pgfisica@fisica.ufmg.br

A presente tese, intitulada **"Tracking the thiobases photophysics: time-resolved spectroscopy studies of the relaxation pathways"** de autoria de **Danielle Cristina Teles Ferreira** submetida à Comissão Examinadora, abaixo-assinada, foi aprovada para obtenção do grau de **DOUTORA EM CIÊNCIAS**, em dezessete de abril de 2020.

Belo Horizonte, 17 de Abril de 2020.

Profa. Ana Maria de Paula
Orientadora da estudante
Departamento de Física/UFMG

Prof. Leandro Malard Moreira
Departamento de Física/UFMG

Prof. Sebastião José Nascimento de Pádua
Departamento de Física/UFMG

Prof. Maurício da Silva Baptista
Instituto de Química/USP

Prof. Cleber Renato Mendonça
Instituto de Física/USP São Carlos

# Acknowledgements

Initially, I thank God for His infinite goodness and for all the things in nature whose mechanism have always intrigued me and aroused my curiosity. Also I am extremely grateful to several people without whom this work would not be possible. First, to Prof. Ana Maria de Paula, my supervisor, for knowing how to guide my PhD studies with patience, dedication, enthusiasm and for granting me the oportunity of the sandwich PhD scolarship in Italy. To Prof. Gerald for including me in the very productive discussions of his group about DNA and nitrogenous bases. To the qualifying committee: Prof. Simone Silva Alexandre, Prof. Sebastião José Nascimento de Pádua, Prof. Pedro Licínio de Miranda Barbosa for the suggestions and advice that I took during my PhD. To Prof. Giulio Cerullo and my supervisor abroad, Cristian Manzoni, from the Politecnico di Milano, Department of Physics, for the scientific discussions and for opening the doors of their group in Italy to me, which allowed me a unique and invaluable experience of personal and academic growth. To the laboratory colleagues in Italy for the exchange of knowledge and welcome. Especially Lucia and Rocío for providing my training for the operation of the experimental setups in the first months. To Prof. Marco Garavelli, Irene Conti and Artur Nenov from Università Degli Studi di Bologna, Department of Industrial Chemistry, for the high-level calculations and data discussions that made it possible to interpret the experimental results that I obtained. Also to Ivo HM van Stokkum (from Vrije Universiteit Amsterdam) for data analysis discussions. To Prof. Tiago Antônio da Silva Brandão from the Chemistry Department at UFMG for making it possible for me to access the UV chemistry laboratory and for the tips on how to improve results in photoluminescence experiments. To Prof. Cristiano Fantini and Rafael Nunes Gontijo for making the Raman measurements feasible. To Prof. Lívia for the synthesis of gold nanoparticles that I used in preliminary tests linked to Thiobases and Daniele Cristina Ferreira for the help in the preliminary measures of EPR. To all friends and colleagues of the Physics Department for sharing several moments of productive discussions about science. To colleagues in the Biophotonics group for the continuous exchange of knowledge. To Prof. Elmo Salomão who was my teaching internship tutor in the Sala de demonstrações and to the entire team of the Sala de demonstrações (which I am proud to have been part of) where I got involved in several wonderful physics teaching and science communication projects. To my English teacher, Andreia de Castro, for the lessons and availability during the writing of the articles and the thesis. To the secretaries, the librarians and the cleaning ladies in the Physics Department for their promptness and cordiality. To my parents Conceição Aparecida Teles Ferreira e Geraldo José Ferreira for fomenting my curiosity for science and for their unconditional love. To my husband Reinaldo José Marra Nogueira for all the love and companionship that since my

choice of the undergraduate course in Physics he has always been by my side encouraging and supporting me sweetly. To my dear brothers Danilo Tadeu Teles Ferreira and Daniel Lucas Teles Ferreira for affection and friendship especially during that period. To all my family and friends who always cheer and celebrate every little achievement of mine. I am extremely grateful for UFMG and the funding agencies: Fapemig, CAPES, CNPq for the financial support and for making research feasible in our country. I am specially grateful for the sandwich scholarship from CAPES at the program CSF-PVE-S (process 88887.127441/2016-00). I tried my best through the PhD to make the very most of all the opportunities. I hope that all the knowledge accumulated until here can be converted in some way into benefits for the Brazilian people who are the ones who paid for my academic education and who are the ones that most need to have quality services as a return.

# Abstract

Nucleobases with sulfur oxygen substitution, named thiobases, are important for a range of biotechnological applications. They show distinguished properties as compared to the canonical nucleobases as fast intersystem crossing, redshift absorbance and the high triplet quantum yield rate enabled by the thio-substitution. These properties facilitates their applications in photodynamic therapy, chemotherapy for the treatment of skin cancers and superficial tumors, photosensitive prototypes for pharmacology application, as well as giving the thiopyrimidines great utility as photolabels. Recent experimental and theoretical studies have shown that the degree and position of the sulfur atom substitution, the environment and the sugar presence have important effects on the magnitude of the intersystem crossing timescale. Here, we use sub-20 fs broadband transient transmission spectroscopy, supported by Raman and photoluminescence experiments, combined with Quantum Mechanics/Molecular Mechanics calculations that enabled to rationalize the thiobases deactivation decay pathway. A common behavior about the relaxation decay path was observed for all the studied thiobases: the triplet manifold population happens either directly through an intersystem crossing process between the bright and the triplet states, or through an intermediate dark state. A global analysis of the transient transmission data confirms this scenario and reveals the time constants involved in these processes. In particular, concerning the thiouracils, we observed that the 2,4-dithiouracil decay processes are qualitatively reproduced by the 2-thiouracil and 4-thiouracil processes depending only on the excitation wavelength. In addiction, for the thiothymidines, the intersystem crossing time constants presented in the literature, obtained from experiments with more than 200 fs time resolution, are reproduced very well by our data. Also, we found for all thiobases a fast time constant, not yet observed, related to the excited bright singlet state lifetime. Furthermore, in the 4-thiouracil and 4-thiothymidine 2D transient transmission map we can also clearly observe coherent oscillations impulsively excited by the short pulses that have not yet been seen in ultrafast transient spectroscopy experiments for these molecules. Therefore, this work represents great advances in the understanding of the thiobases photophysics.

**Keywords**: Thiobases, Intersystem Crossing, Short Pulses, Transient Transmission Spectroscopy, Photoluminescence , Raman, Relaxation Pathways.

# Resumo

A substituição de oxigênio por enxofre em nucleobases leva às chamadas tiobases, que são importantes para várias aplicações em biotecnologia. As tiobases se distinguem das bases canônicas pelo cruzamento intersistemas rápido, o deslocamento para o vermelho dos picos no espectro de absorção e a alta taxa de população do estado tripleto. Tais características facilitam suas aplicações em terapia fotodinâmica, quimioterapia para o tratamento de câncer de pele e tumores superficiais, protótipos fotossensíveis para aplicação farmacológica, bem como viabiliza a aplicação das tiopirimidinas como fotomarcadores. Estudos experimentais e teóricos recentes mostraram que o grau e a posição da substituição do átomo de oxigênio pelo átomo de enxofre, o ambiente e a presença do grupo funcional de açúcar têm efeitos importantes na ordem de grandeza da escala de tempo da transição intersistemas. Neste trabalho, utilizamos espectroscopia de transmissão transiente com pulsos de banda larga e duração inferior a 20 fs, suportada por experimentos de Raman e fotoluminescência, e ainda combinada com cálculos de mecânica quântica e mecânica molecular, que permitiram racionalizar o caminho de decaimento da desativação das tiobases. Um comportamento comum sobre o caminho de decaimento foi observado em todas as tiobases estudadas: os estados tripletos são populados ou diretamente através de um processo de cruzamento intersistemas proveniente do estado oticamente excitado, ou através de um estado escuro intermediário. Uma análise global dos dados de dinâmica espectral confirma esse cenário e revela as constantes de tempo envolvidas nesses processos. Em particular, para as tiouracilas, observamos que os processos de decaimento da 2,4-ditiouracil são reproduzidos qualitativamente pelos processos de decaimento da 2-tiouracil e da 4-tiouracil, dependendo apenas do comprimento de onda da excitação. Além disso, para as tiotimidinas, as constantes de tempo de cruzamento entre sistemas observadas nos trabalhos da literatura com resolução temporal superior a 200 fs são reproduzidas muito bem por nossos resultados. E ainda, para todas tiobases obtemos os tempos de vida relacionados ao estado de singleto excitado. Além disso, no mapa 2D da transmissão transiente para a 4-tiouracil e a 4-tiotimidina podemos observar claramente a excitação coerente de modos vibracionais ultrarrápidos, impulsivamente excitados pelos pulsos curtos, até agora ainda não observados em experimentos de espectroscopia transiente ultrarrápida para essas moléculas. Portanto, este trabalho representa avanços importantes na compreensão da fotofísica das tiobases.

**Palavras-chave**: Tiobases, Cruzamento Intersistemas, Pulsos Curtos, Espectroscopia de Transmissão Transiente, Fotoluminescência, Raman, Vias de Relaxação

# List of Figures


Figure 1 – Pyrimidines and purines canonical bases. . . . . 25
Figure 2 – Bonding and antibonding molecular orbitals formation. . . . . 29
Figure 3 – Energy level diagrams: absorption and emission spectra. . . . . 31
Figure 4 – Broadband collimated light to focus in a cuvette. . . . . 32
Figure 5 – PES representation of the decay relaxation processes. . . . . 38
Figure 6 – Pulse compression approach: prism pair and CMs. . . . . 44
Figure 7 – SHG and SFG processes. . . . . 47
Figure 8 – OPA process. . . . . 48
Figure 9 – Energy levels on the pump-probe signals. . . . . 52
Figure 10 – Experimental setup: pump at 330 nm and probe in the visible. . . . . 54
Figure 11 – Experimental setup: pump at 330 nm and probe in the UV. . . . . 55
Figure 12 – NOPA spectrum. . . . . 57
Figure 13 – Pump pulses obtained by: (a) SFG (b) SHG. . . . . 59
Figure 14 – Probe pulses. . . . . 60
Figure 15 – Sample jet setup. . . . . 61
Figure 16 – 2DSI setup and 2D-map. . . . . 63
Figure 17 – UV pulse (a) at time domain; (b) at frequency domain. . . . . 64
Figure 18 – (a) The thiouracils LA. (b) The thiothymidines LA. . . . . 68
Figure 19 – (a) The 2TC LA. (b) The 6TG LA. . . . . 68
Figure 20 – Thiouracils PL. . . . . 70
Figure 21 – 2TT, 4TT, and 6TG PL. . . . . 72
Figure 22 – Raman measurements. . . . . 73
Figure 23 – Thiouracils absorption data fit with Gaussian curves. . . . . 76
Figure 24 – Thiouracils TTS 2D maps. . . . . 77
Figure 25 – Thiouracils TTS dynamics at selected wavelengths. . . . . 78
Figure 26 – Thiouracils TTS spectra at selected wavelengths in the visible range. . 79
Figure 27 – Thiouracils TTS spectra at selected wavelengths in the UV range. . . . 80
Figure 28 – Thiouracils EAS. . . . . 81
Figure 29 – Proposed relaxation mechanism for 4TU and the transient transmission spectra plotted as a 3D map. . . . . 82
Figure 30 – Sketch illustrating the 2TU relaxation mechanisms. . . . . 82
Figure 31 – Proposed relaxation mechanism for the 24TU after excitation with 20 fs pulses centered at 330 nm. . . . . 84
Figure 32 – Proposed relaxation mechanism for the 24TU after excitation with 20 fs pulses centered at 270 nm. . . . . 84
Figure 33 – 2TT TTS spectra at selected time delay and 2D map. . . . . 86

Figure 34 – 4TT and 2TT TTS UV 2D map. . . . . 86
Figure 35 – 2TT TTS dynamics at selected probe wavelengths and EAS. . . . . 86
Figure 36 – 4TT TTS 2D map and spectra probed in the visible range. . . . . 88
Figure 37 – 4TT TTS dynamics at selected probe wavelengths and the EAS. . . . . 88
Figure 38 – 2TT and 4TT energy relaxation pathway. . . . . 88
Figure 39 – Oscillatory pattern obtained from the TTS residue matrix map. . . . . 89
Figure 40 – Osculations FT. . . . . 90
Figure 41 – 4TT oscillations. . . . . 90
Figure 42 – 2TC TTS 2D map and spectra. . . . . 92
Figure 43 – 2TC TTS dynamics at selected probe wavelengths and EAS. . . . . 92
Figure 44 – TTS 2D map for the 2TC probing on the UV range. . . . . 92
Figure 45 – 2TC general relaxation mechanism scheme comparison. . . . . 93
Figure 46 – 6TG TTS 2D map and spectra. . . . . 95
Figure 47 – 6TG TTS dynamics and EAS. . . . . 95
Figure 48 – 6TG mechanism. . . . . 96
Figure 49 – Experimental setup to generate the 270 nm pump pulses and the visible probe pulses. . . . . 122
Figure 50 – Experimental setup to generate the 270 nm pump pulses and the UV probe pulses. . . . . 123
Figure 51 – 2DES results. . . . . 127
Figure 52 – TTS 2D map obtained with 100-fs pulses. . . . . 130

# List of Tables

Table 1 – Samples details. . . . . 67
Table 2 – Thiobases time constants extracted from the pump and probe results with the sub-20 fs broadband pulses. . . . . 98

# List of abbreviations and acronyms

| | |
|---|---|
| DNA | Deoxyribonucleic Acid |
| UV | Ultraviolet |
| RNA | Ribonucleic Acid |
| 2TU | 2-Thiouracil |
| 4TU | 4-Thiouracil |
| 24TU | 2,4-Dithiouracil |
| 2TT | 2-Thiothymidine |
| 4TT | 4-Thiothymidine |
| 6TG | 6-Thioguanine |
| 2TC | 2-Thiocytosine |
| SOC | Spin Orbit Coupling |
| TTS | Transient Transmission Spectroscopy |
| PES | Potential Energy Surface |
| CI | Conical Intersection |
| VC | Vibrational Cooling |
| IC | Internal Conversion |
| ISC | Intersystem Crossing |
| TAS | Transient transmission Spectroscopy |
| PS | Photoelectron Spectroscopy |
| FT | Fourier Transform |
| GD | Group Delay |
| GDD | Group Delay Dispersion |
| GD | Third Order Dispersion |

| | |
|---|---|
| OPA | Parametric Optical Amplification |
| IR | Infrared |
| SFG | Sum Frequency Generation |
| DFG | Difference Frequency Generation |
| SHG | Second Harmonic Generation |
| SF | Self Focusing |
| SPM | Self Phase Modulation |
| CM | Chirped Mirrors |
| IR | Infrared |
| BS | Beam-Spliter |
| M | Mirror |
| DCM | Double-Chirp Mirrors |
| TWINS | Translating-Wedge-Based Identical Pulses eNcoding System |
| 2DSE | Two-dimensional electronic spectroscopy |
| 2DSI | Two-Dimensional spectral Shearing Interferometry (2DSI) |
| SPIDER | Spectral Phase Interferometry for Direct Electric-field Reconstruction |
| $\beta$-BBO | Beta Barium Borate |
| EAS | Evolution Associated Spectra |
| PBS | Phosphate-Buffered Saline |
| LA | Linear Absorption |
| PL | Photoluminescence |
| 2DSE | Two-dimensional electronic spectroscopy in the UV range |
| TT | Thiothymidines |
| TU | Thiouracils |

# Contents


**1 INTRODUCTION . . . . . 21**

**2 THEORETICAL REFERENCE: FUNDAMENTALS OF PHOTOCHEMISTRY . . . . . 25**

**2.1 Molecules . . . . . 26**

**2.2 Absorption and emission processes . . . . . 30**

**2.3 Lambert-Beer law . . . . . 32**

**2.4 Selection rules that govern the transition between two energy levels by dipole approximation . . . . . 34**

**2.5 The state lifetimes . . . . . 35**

**2.6 Photophysical processes in electronically excited molecules . . . . . 36**

**3 NONLINEAR OPTICS . . . . . 41**

**3.1 Ultrashort pulses . . . . . 41**

3.1.1 Pulse compression . . . . . 44

**3.2 Ultrafast parametric amplifiers and the basics of nonlinear optics . . 45**

3.2.1 Second-order nonlinear optical effects for monochromatic waves . . . . . 45

3.2.2 Parametric amplification over a broadband frequency range . . . . . 49

**3.3 White light generation . . . . . 50**

**4 TECHNICAL APPROACHES . . . . . 51**

**4.1 Ultrafast Transient Transmission Spectroscopy . . . . . 51**

**4.2 TTS experimental setup with SFG: broadband pulses centered at 330 nm with sub-20 fs time duration . . . . . 53**

4.2.1 Pump Line . . . . . 56

4.2.1.1 NOPA . . . . . 56

4.2.1.2 SFG . . . . . 57

4.2.2 Probe line . . . . . 59

4.2.2.1 Probe beam in the visible range . . . . . 59

4.2.2.2 Probe beam in the UV range . . . . . 60

4.2.3 Using liquid sample in a jet flow configuration . . . . . 60

**4.3 Detection scheme . . . . . 61**

**4.4 Sub-20-fs pulse characterization 2DSI . . . . . 62**

**4.5 Global Analysis and data processing . . . . . 64**

**4.6 Linear Absorption . . . . . 65**

**4.7 Steady-state Photoluminescence . . . . . 65**

**4.8 Raman . . . 65**

**5 SAMPLES CHARACTERIZATION . . . 67**
**5.1 Samples details . . . 67**
**5.2 Linear Absorption: results and discussion . . . 68**
**5.3 PL results . . . 70**
**5.4 Raman results . . . 72**

**6 SUB-20 FS TRANSIENT TRANSMISSION SPECTROSCOPY: RESULTS AND DISCUSSIONS . . . 75**
**6.1 Thiouracils . . . 75**
6.1.1 Overview . . . 75
6.1.2 TU Results . . . 75
**6.2 Thiothymidines . . . 85**
6.2.1 Overview . . . 85
6.2.2 TT Results . . . 85
**6.3 Coherent Oscillation . . . 89**
**6.4 2-Thiocytosine . . . 91**
6.4.1 Overview . . . 91
6.4.2 2TC Results . . . 91
**6.5 6-Thioguanine . . . 94**
6.5.1 Overview . . . 94
6.5.2 6TG Results . . . 94

**7 CONCLUSIONS AND OUTLOOK . . . 97**
**7.1 Concluding remarks . . . 97**
**7.2 Open questions and outlook . . . 99**

**BIBLIOGRAPHY . . . 101**

**APPENDIX 117**

**APPENDIX A – TECHNICAL DETAILS . . . 119**
**A.1 Number of absorbed photons in the jet experiments . . . 119**
**A.2 Magic angle in the TTS . . . 120**
**A.3 Experimental setup SHG: 270 nm centered broadband pulses with sub-20 fs duration . . . 122**

**APPENDIX B – TWO-DIMENSIONAL SPECTROSCOPY IN THE UV RANGE RESULTS . . . 125**

APPENDIX C – TRANSIENT TRANSMISSION SPECTROSCOPY WITH LONG PULSES RESULTS . . . . . 129

ANNEX 131

ANNEX A – THESIS-RELATED ARTICLES PUBLISHED DURING THE PH.D . . . . . 133

# 1 Introduction

One of the key challenges in the field of biomolecule spectroscopy is to decipher the energy relaxation processes followed by molecules to return to the ground state after photoexcitation. The DNA and RNA bases strongly absorb in the UV [1]. When DNA is excited by UV light source, for example by solar radiation, dangerous photoproducts can be generated that can disrupt the cellular processing of DNA. DNA damaged by light is usually repaired by enzymes, but repairs have a high energy cost [2]. The imbalance between the damage generation and the reparation system can launch genetic mutations in the body that result, for example, in skin cancer [3]. However, the presence of harmful products generated by the UV absorption process is remarkably low, because DNA dissipates the absorbed energy very efficiently and quickly, mainly through non-radiative decay processes that enable the stability of all genetic material [4, 5]. The photoprotection property of DNA, and nucleic acids, in general, is required for the permanence and replication of life on Earth, which leads invariably to the maintenance and propagation of genetic heredity information [6, 7].

In 1950, George Hitchings and Gertrude Elion discovered the potential for the use of merely sulfur-substituted nucleobases with a sulfur atom in place of the oxygen atom in the treatment of numerous diseases [8–11]. Such sulfur substituted bases are known as thiobases. These researchers were honored with the Nobel Prize in 1988 in the category of Physiology or Medicine. Since 1950, there has been a great effort to unravel the energy deactivation pathways of thiobases [12, 13]. The exchange of oxygen atom by sulfur atom in the nucleobases causes noticeable changes in the photophysics of these molecules [14–28]: there is a redshift in the canonical nucleobases absorption spectrum to the 280-400 nm range and it confers the loss of photostability when excited by UV light. The loss of the photostability happens because unlike the canonical bases, which repopulate the ground state quickly after UV light excitation, thiobases after photoexcitation have a very long-lived state (in the order of microseconds) called a triplet state with a high quantum yield[1] [30]. This is the reason why the high rate of singlet oxygen formation is possible in the thiobases, which enables their pharmacological use and their other numerous applications. For example, they have been used to enhance the polymerase chain reaction for DNA/RNA replication and as chromophores for investigating specific interactions between nucleic acids and proteins. Also, due to the high transfer efficiency to the triplet states, several applications have been demonstrated as chemotherapeutic agents for the treatment of some types of skin cancer [31–39]. In addition to their practical applications,

[1] Quantum yield is the ratio of the number of molecules species decomposed or formed by the number of photons absorbed [29].

they provide an excellent model system for understanding how a single atom substitution can modify energy relaxation processes relative to canonical DNA/RNA nucleobases.

In spite of that, their photophysics and photoinduced dynamics still pose unresolved questions. One of the open questions that have been widely discussed in the literature is the efficient process of triplet state formation by an intersystem crossing (ISC) process that occurs shortly after the excited singlet state. In the literature is discussed two possible triplet state population pathways: one is mediated by a dark state and the other one is a direct transition from the bright singlet state to the triplet state [20, 40–48]. In this work we perform a comprehensive experimental analysis for this class of compounds by ultrafast time resolved spectroscopy techniques to solve this puzzle and try to get more information about the thionated nucleobases intriguing photophysical properties. In particular, we present the description of the photophysical mechanisms leading to the population of the triplet state and their timescales in solvated thiopyrimidines (2-thiouracil, 4-thiouracil, 2,4-dithiouracil, 2-thiothymidine, 4-thiothymidine, and 2-thiocytosine) and the thiopurine 6-thioguanine.

We have started the studies with broadband transient transmission spectroscopy (TTS), featuring unprecedented sub-20-fs temporal resolution in the ultraviolet (prior experimental results had about 200 fs resolution [11,47–50]). In this technique, the temporal resolution is obtained indirectly, since there are no such fast detectors. For this, the laser beam is divided into two: a more intense pump beam, which excites the sample and another weaker, called a test beam (or probe beam) which interacts with the excited state. The pump beam start the transition, while the probe beam verifies the decay as a function of time. By scanning the time interval between these two pulses, it is possible to study the dynamics of the various excited states in the sample.

As a result, we observed two kinds of signals from TTS: a negative signal with related to an excited state absorption (present in all samples studied in this thesis) and a positive signal which is related to the stimulated emission or the ground state bleaching. The stimulated emission is present in the 4-thiouracil, 4-thiothymidine and the 2,4-dithiouracil and it is confirmed by steady-state fluorescence. We also observed that the dynamics are modulated by an oscillatory pattern (present in the 4-thiouracil and 4-thiothymidine) which are related to the vibrational modes confirmed by the Raman spectroscopy, and by the simulations from our theoretical collaborators.

All measurements with temporal resolution were performed by me over a year at the Politecnico di Milano (period referring to the sandwich doctorate). During this period in Milan I was under the supervision of Dr Cristian Manzoni, from Prof. Giulio Cerulo group. We also had collaboration with Prof. Marco Garavelli, Irene Conti and Artur Nenov from Università degli Studi di Bologna (Italy) who provided molecular dynamics simulations to support some of our experimental results.

These results brought relevant insights into the relaxation pathways of these bases on an ultrafast time scale [51–53], that will be extensively discussed in this thesis. This thesis is organized as the following: in Chapter 2 and 3 I will present the literature review about molecules and nonlinear optics, respectively; in Chapter 4 I will describe the experimental techniques used; in Chapter 5 I will present the sample characterization results and in the Chapter 6 there is the discussion of the ultrafast results obtained; in the Chapter 7 I will present the conclusions and outlook; in the Appendix A, I present some technical details related to the pump probe measurements; in the Appendix B there is the 2D spectroscopy data description for the 4-thiouracil; in the Appendix C there is the time resolved experimental results with long pulses; and in the Annex A is included the papers related to this thesis that were published during the PhD.

# 2 Theoretical reference: fundamentals of photochemistry

Nucleic acids are composed of nucleotides which in turn are composed of a nitrogenous base, a pentose and one or more phosphates. Nitrogenous bases are classified as purines or pyrimidines. The purine bases of both DNA and RNA are guanine and adenine. The pyrimidine bases are thymine, cytosine and uracil [7].The purine and pyrimidine functional groups are nitrogen rings, carbonyl groups, and exocyclic amino groups, see Figure 1. Hydrogen bonds involving amino or carbonyl groups are the most important forms between two (or more) complementary nucleic acid chains.

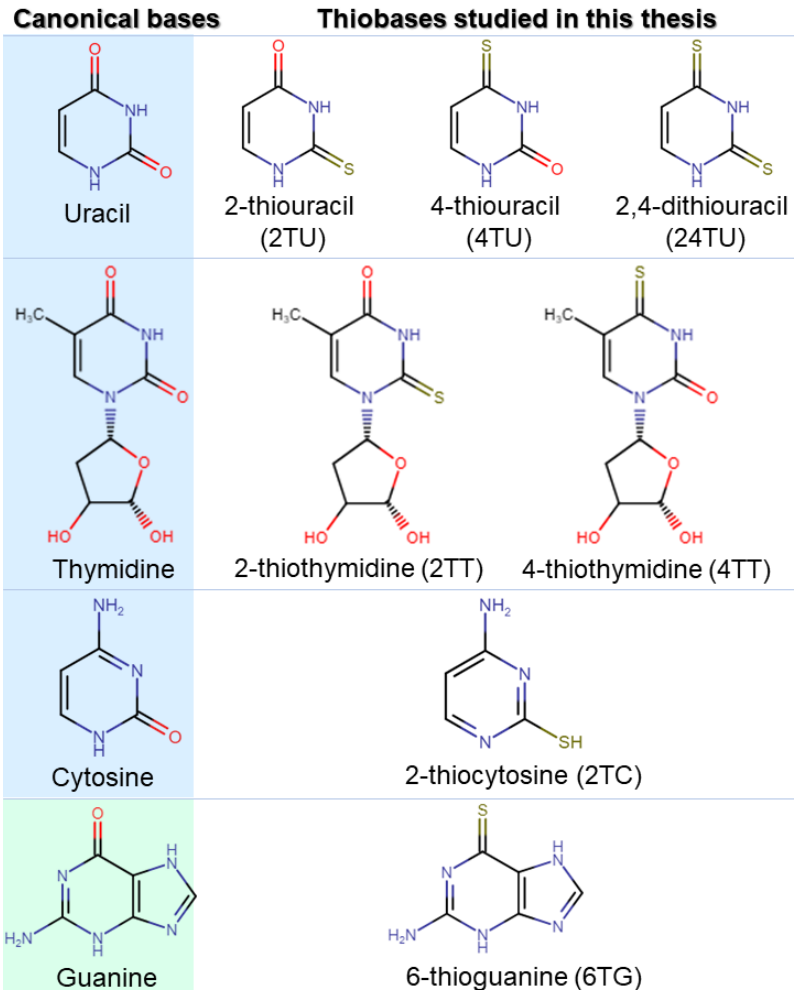



Figure 1 – Pyrimidines and purines canonical bases in blue and green background respectively. The respective sulfur-substitute derivatives bases studied at this thesis is in the white background. The chemical drawings are made using the software *Chemistry 4-D Draw.*

The thiobases are bases derived from the nucleotides. In these molecules, one or more exocyclic oxygen atoms are replaced by sulfur atom. The Figure 1 shows all the thiobases studied in this thesis compared to its respective original canonical base. One of the most important differences between the thiobases and the nucleobases is the changes in their absorption spectra. However, how do the molecules interact with the light? This is what we discuss in the next subsections through a bibliographic review of their photochemistry based on references [54–58]

## 2.1 Molecules

The formation of molecules occurs through the connection and interaction of a set of atoms. So, initially, we will do a brief review of the atomic phenomena that are relevant for the understanding of molecular properties.

The probability density of finding the electron in an atom region is described by the electron wave function $\Psi(\vec{r},t)$. In the hydrogen atom, for example, the wave function is the solution of a second-order partial differential equation that involves kinetic energy and potential energy $V(\vec{r},t)$ terms. This equation is known as the Schrodinger equation [58]:

$$i\hbar\frac{\partial\Psi(\vec{r},t)}{\partial t} = -\frac{\hbar^2}{2m}\nabla^2\Psi(\vec{r},t) + V(\vec{r},t)\Psi(\vec{r},t). \tag{2.1}$$

As the potential that the electron is subjected in the hydrogen atom is from Colombian origin, it is independent of time, so it is feasible to use the method of separation of variables to separate the temporal part from the spatial part at Schrodinger equation, thus obtaining the stationary states as solution. The spatial part equation becomes:

$$E\Psi(\vec{r}) = -\frac{\hbar^2}{2m}\nabla^2\Psi(\vec{r}) + V(\vec{r})\Psi(\vec{r}). \tag{2.2}$$

With a correct choice of coordinate system considering the spherical Coulomb potential symmetry we can find a set of solutions which are eigenfunctions: $\Psi_1, \Psi_2, ...$ that are characterized respectively by the energies $E_1, E_2, ...$

$$\Psi(\vec{r},t) = \sum_{n=1}^{\infty} c_n\Psi_n(\vec{r})e^{-iE_nt/\hbar}. \tag{2.3}$$

Therefore, electrons can only assume discrete energy values. The first of them is denoted by the letter 'n' and is known as the main quantum number which is related to the energies that each state can assume. The 'n' values are the non-zero and positive integers: $n = 1, 2, 3 \ldots$. The electron movement around the nucleus (that is described by spherical harmonics functions) is associated with the azimuth quantum number denoted by the letter 'l'. This quantum number is related to the geometry of the atomic orbital, which is the volume of space in which there is a probability of finding the electron

calculated from the wave function. The azimuth quantum number can assume values $l = 0, 1, 2, 3, \ldots, n-1$[1]. Therefore, it is defined according to the main quantum number value[2]. The quantum number of the magnetic moment is represented by the letter 'm' defines the orientation of the orbital in space. It assumes values of $m = 0, \pm 1, \pm, 2 \ldots \pm l$. There is also a fourth quantum number denoted by 's' known as the intrinsic angular momentum or spin quantum number that is -1/2 or +1/2[3]. This number must be adopted in compliance with the Pauli Exclusion Principle, which says that two electrons can not have all the same quantum numbers ($n, l, m$, and $s$). If $n, l$, and $m$ are equal for both of them, then s must be different. Therefore, the electron wave function that take in account the spin is given by:

$$\Phi = \Psi_{n,l,m}\sigma_S, \tag{2.4}$$

where $\Psi_{n,l,m}$ denotes the spatial part and $\sigma_S$ expresses the dependence on the spin.

Since the interaction between intrinsic and extrinsic angular momentum can occur, another quantum number labeled as 'j' is designated, which is the quantum number of the total angular momentum: $j = l + s$.

There are four possible combinations for a pair of s=1/2 particles: $|\downarrow\downarrow\rangle$, $|\uparrow\uparrow\rangle$, $\frac{1}{\sqrt{2}}(|\downarrow\uparrow\rangle + |\uparrow\downarrow\rangle)$, and $\frac{1}{\sqrt{2}}(|\downarrow\uparrow\rangle - |\uparrow\downarrow\rangle)$. The first three carry a total spin momentum 1 and the last one carries a total spin momentum 0. The set of the first three is called the triplet states and the last one is an orthogonal state to the triplet called the singlet state. The multiplicity of the singlet is 1 and of the triplet 3 (see the footnote[4]).

There may be an interaction between spin angular moment and orbital angular moment generating a total angular moment: $J = j_1 + j_2 \ldots$ where $j_1 = l_1 + s_1 \ldots$, $j_2 = l_2 + s_2 \ldots$ This type of interaction is known as spin-orbit interaction. It is detectable by the division of degenerate energy states into $2S + 1$ states.

The electronic transitions between the energy levels by photon absorption in an atom happen under some selection rules. That for electric dipole transitions are (i) there is no restriction for the changes in the quantum number $n$: $\Delta n =$ any value. (ii) the change in the total spin must be zero $\Delta S = 0$, (iii) the change in the total azimuth quantum number must be $\Delta L = 0, \pm 1$ and (iv) the change in the total angular momenta must be $\Delta J = 0, \pm 1$ [54, 58].

---

1 These values are commonly represented by the letters $s, p, d, f$... which correspond to the values 0,1,2,3... respectively.

2 It means that when $n = 1, l = 0$; when $n = 2, l = 0, 1$; when $n = 3, l = 0, 1, 2$ and so on.

3 When s = -1/2 we say that the electron has spin down and when $s = +1/2$ we say the electron has spin up.

4 The multiplicity is calculated by 2S + 1 where S is the total spin of the system: $S = S_1 + S_2$.

Molecules are formed by atoms associations. In the molecules, there is more than one nucleus that moves in relation to each other. As the nuclei mass is much larger than the electrons mass, the movement of the electrons and the nucleus can be treated separately thanks to the Born-Oppenheimer approximation [57]. The nuclei can vibrate and rotate around the molecular axis. The vibration and rotation energies are quantized and their transition energies are in the infrared and microwave spectral range, respectively. Transitions between electronic levels are from the UV to visible range [59].

The wave function that describes a molecular system is obtained by the linear combination of the molecular orbitals of its constituting atoms:

$$\Psi_{MO} = \sum_{n} c_\nu \Phi_\nu, \tag{2.5}$$

where $c_\nu$ is the coefficient of the $\nu$ th atom whose orbital is described by the $\phi_\nu$ function. The component of the angular momentum in the direction of the bond is designated by $\lambda$ [54]. The role of the magnetic number $m$ is now played by $\lambda$ that can assume the following values 0 $\pm$1, $\pm$2, $\pm$3... and they can be represented by the Greek letters $\sigma$, $\pi$ .... In the molecular context, the total angular momentum in the direction of the bond axis ($\Lambda$) is given by the sum of all $i$ possible values of $\lambda$:

$$\Lambda = \sum_{i} \lambda_i. \tag{2.6}$$

The total spin angular momentum (S) is given by the sum of all $i$ possible values of $s$:

$$S = \sum_{i} s_i. \tag{2.7}$$

The sum of the angular momenta ($\Omega$) is given by:

$$\Omega = \Lambda + S. \tag{2.8}$$

The molecular orbitals are identified by their symmetry properties that come from their constituent atoms symmetry properties. Each orbital has its properties. For example, sigma-type molecular orbitals are symmetric with respect to reflection on a plane passing through the molecular axis. The $\sigma^*$ is the antibond orbital equivalent to sigma (see Figure 2). They are assembled by the superposition of the atomic $s$ or $p$ orbitals or by the hybridization of $sp, sp^2, sp^3$ orbitals along the direction of the bond [54]. These orbitals form strong bonds by two antiparallel spin electrons.

Orbitals of the $\pi$ type are antisymmetric concerning reflection operation from a plane that passes through a plane of the molecule and besides, there is a node in the perpendicular plane to the bond. These orbitals are formed by the superposition of $p_x$, $p_y$ and $p_z$ orbitals or by the hybridization of orbitals of similar symmetry. The electrons that

form the bonds of these orbitals have antiparallel spins. They are found in double and triple bonds. These orbitals can be delocalized over a set of atoms. $\pi$ bonds are less strong than $\sigma$ bonds.

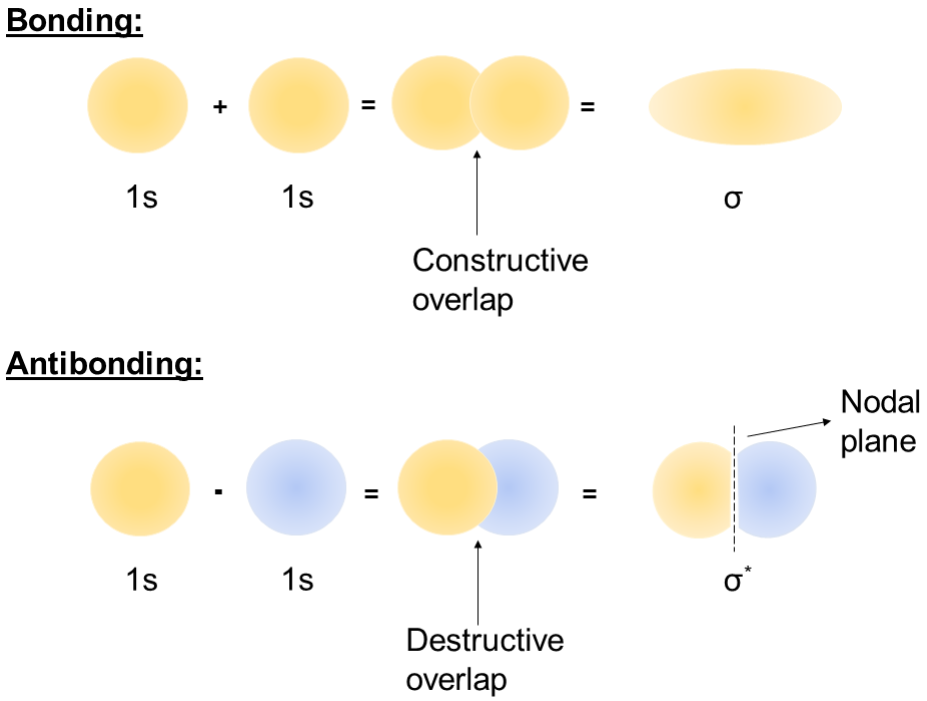



Figure 2 – Two 1s orbitals combine to form a bonding and an antibonding molecular orbitals. Figure inspired at the reference [54].

In turn, $n$ orbitals are almost purely atomic orbitals that have not taken part in the molecular orbitals construction and are thus called nonbounding or just $n$ orbitals. The electrons that occupy these orbitals are called nonbinding or lone pair electrons. The same concept of singlet and triplet states defined for atoms is valid for molecules. The multiplicity of the singlet is 1 and the triplet multiplicity is 3.

When the electronic structure is unknown or is not relevant to a given application, a common method of naming them is due to their multiplicity, so we can call them as: singlet or triplet. In this thesis we will use this nomenclature. Thus, the lowest energy fundamental state that is a singlet state will be denoted by $S_0$ and the excited singlet states will be denoted by $S_1$, $S_2$ ... and the triplets by $T_1$, $T_2$ .... Another possible notation that we will use involves the initial and final states of the electrons. Thus, a state called $\pi\pi^*$ means that the electron left the $\pi$ orbital and goes to the antibond orbital $\pi^*$ or, for example, a state called $\sigma\pi^*$ means that the electron left the orbital $\sigma$ and go to the antibound orbital $\pi^*$ and so on. It is observed that the transition from one orbital $n$ to another orbital such as the $\pi$ orbital has a low probability of happening [54].

## 2.2 Absorption and emission processes

We will now present some of the mechanisms of absorption and emission of photons in photochemical processes. When an electromagnetic wave interacts with an atom or molecule, it can promote electrons from a lower energy level to higher energy levels, in case the incident wave frequency is resonant with some atomic or molecular transition, by a photon absorption. Furthermore, this electromagnetic wave has the potential to disturb the electron cloud around this atom or molecule by creating a dipole oscillation due to the interaction between the charges and the electric field. The dipole is generated in the same direction as the incident electric field vector. The dipole moment can be written as:

$$\vec{\mu} = e\vec{r}, \tag{2.9}$$

where $e$ is electric charge and $\vec{r}$ is the vector distance between the center of mass of the charges involved. In the condition of resonance, we call the transition as electric dipole transition.

Once a photon is absorbed the molecule can decay through emission processes. Figure 3 represents a potential energy diagram for a molecule where the curves correspond to the electronic states and the horizontal lines are the vibrational levels. For simplicity, rotational levels were not represented. Note that changes in vibrational levels can be detected in the emission and absorption spectra.

The emission processes occur in a short time scale in comparison to the nucleus motion time. Therefore, the final populated state is usually an excited vibrational state of the ground electronic state [60]. Fluorescence emission is usually shifted to longer wavelengths than the absorption, and, usually, there is no overlap between transition $\nu = 0 \leftrightarrow \nu = 0$ [61]. The energy losses between the excitation and emission processes could be due to thermal and solvent effects, excited-state reactions, and/or energy transfer [62]. The energy difference between the maximum of the absorption and emission is known as the Stokes shift (see the bottom panel of Figure 3).

To obtain the absorption or emission rate, Einstein's coefficients are used. Considering a two-level system, of energies $E_m$ and $E_n$ where $E_m > E_n$ and the absorbed frequency is given by:

$$\nu_{mn} = \frac{E_m - E_n}{\hbar}. \tag{2.10}$$

The absorption rate (that is the probability per unit of time of an electron in this system to absorb radiation of frequency $\nu_{nm}$) is proportional to the density (unit of energy divided by volume) $\rho(\nu_{nm})$ of the incident radiation and to the number of particles $N_n$ in the state $n$, that is:

$$\text{Absorption rate} = B_{nm} N_n \rho(\nu_{nm}), \tag{2.11}$$

where $B_{nm}$ is the absorption coefficient.

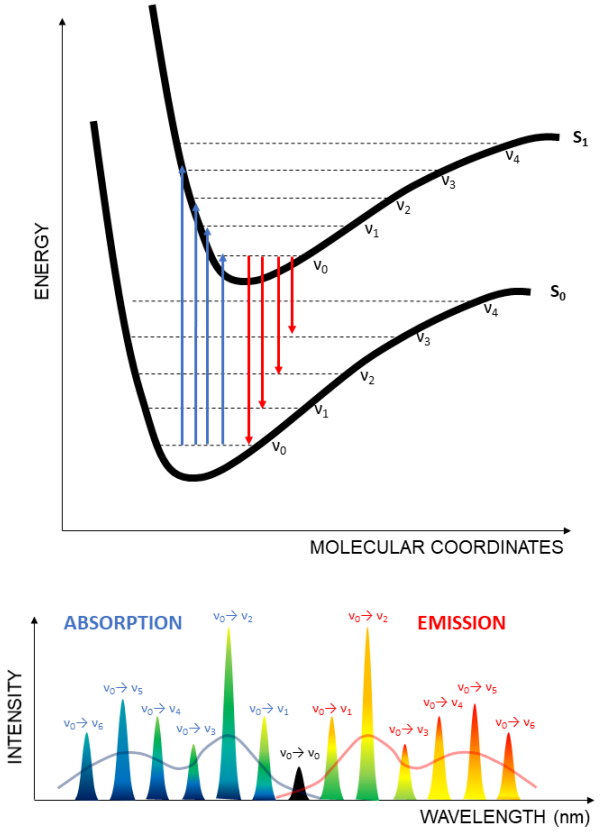



Figure 3 – Energy level diagrams with absorption and emission transitions indicated by the blue and red lines, respectively. The lower panel shows the absorption (in blue) and emission spectra (in red). The emission spectra is red shifted compared to the absorption spectra due to the energy loss to vibrational transitions. Figure inspired by references [60–63]

Similarly, the emission rate is given by:

$$\text{Emission rate} = B_{mn} N_m \rho(\nu_{mn}) + A_{mn} N_m, \tag{2.12}$$

where $B_{mn}$ is the Einstein coefficient due to the stimulated emission which is a phenomenon that occurs when a specific frequency photon interacts with an excited electron causing its decay to a lower energy level. $A_{mn}$ is the Einstein coefficient due to spontaneous emission, which is a decay process that occurs without the influence of a photon inducing the process.

In equilibrium, the rate of emission and absorption tends to match, which brings us to the following relationships using the concept of the energy density for a black body[5]:

$$B_{mn} = B_{mn}, \tag{2.13}$$

$$A_{mn} = \frac{8\pi h\nu^3}{c^3} B_{mn}, \tag{2.14}$$

[5] The energy density obtained by Plank of a black body as a function of temperature is given by: $\rho(\nu_{mn}) = \frac{8\pi h\nu^3}{c^3}\left(\frac{1}{e^{h\nu/k_B T}-1}\right)$

$$\frac{N_n}{N_m} = e^{h\nu/k_B T}, \tag{2.15}$$

where $m > n$.

Using the above equations and the time-dependent perturbation theory it is possible to estimate the probability of stimulated emission when the system goes from one steady-state to another under the influence of an oscillating electric dipole. Thus, the time-dependent perturbation theory gives us the rate at which an electron changes from a stationary state to another under the influence of an electromagnetic field that induces an electric dipole due to molecule electron oscillations. When calculating this rate by the perturbation theory, we can link it to Einstein's coefficients, thus finding, for example, the probability of stimulated emission (details about this calculations can be found in the reference [54]).

## 2.3 Lambert-Beer law

The absorption intensity is given by the Lambert-Beer law [54]. It is a very important empirical law that links the absorbance (A $(\nu)$)[6] concept with the sample concentration, the optical path, and the molar absorption coefficient, denoted, respectively, as $C$, $l$, and $\epsilon(\nu)$.

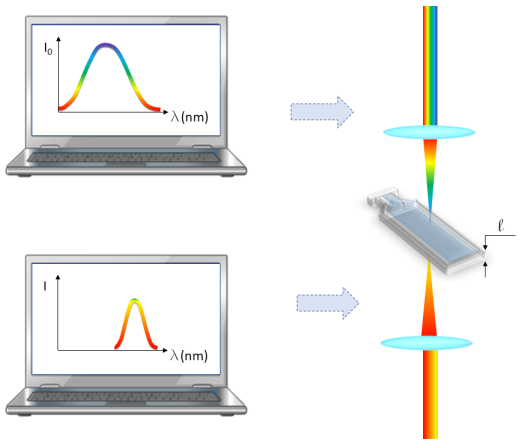



Figure 4 – The broadband light is focused in a cuvette with optical path $l$ and the transmitted light is collected by a lens with known absorption spectrum information.

The $\epsilon(\nu)$ depends on the molecular absorbers and environment features and the incident radiation frequencies. Moreover, it is proportional to the difference of the number of molecules in the ground state and the number of molecules in the excited state. When a beam passes through an absorbing homogeneous and isotropic sample, it decreases the

[6] The absorbance is also known as optical density (OD) and it is the nomenclature that we use in the Results chapter.

transmitted intensity $I$ by $dI$ which is proportional to the absorption probability by Mol for the light frequency $\nu$, $\alpha_\nu$, concentration, $C$, intensity, $I$, and the thickness, $dl$ of the absorbing material (see Figure 4), which is :

$$\frac{dI}{I} = \alpha_\nu C dl. \tag{2.16}$$

Considering that at $l = 0$ the $I = I_0$, by an integration over the thickness of the sample gives:

$$ln\left(\frac{I}{I_0}\right) = \alpha_\nu C l \tag{2.17}$$

$$\epsilon_\nu = \alpha_\nu / 2.303 \tag{2.18}$$

$$\epsilon_\nu = \frac{1}{Cl} log(I/I_0). \tag{2.19}$$

For a range of frequencies:

$$A = \int \epsilon d\nu = \frac{1}{Cl} \int log(I/I_0) d\nu, \tag{2.20}$$

where $A$ is the absorbance (adimensional), $C$ (unit of Mol per liter M/L) is the concentration, $d$ is the sample thickness (unit of a centimeter) and $\epsilon$ is the molar absorption coefficient (unit of a liter per Mol per centimeter L/M cm).

Therefore, it is easy to see that the intensity of the light transmitted over the sample decreases exponentially as the thickness of the absorbent medium and the sample concentration increases arithmetically. It is known as the Lambert-Beer law and we used this law to calculate the sample concentrations as shown in Chapter 5 and detailed in Appendix A. It is not valid to the very intense radiation incidence and neither very long-lived states.

The absorption probability, for a transition from an electronic level to another one, is proportional to the probability of absorption between the two energy states. This value can be calculated using the concept of total transition momentum. The total transition momentum from a fundamental state $\Psi_0$ to the first excited state $\Psi_1$ is given by:

$$M_{01} = \int \psi_0 \widehat{\mu} \psi_1 d\tau, \tag{2.21}$$

where $\widehat{\mu}$ is the dipole momentum operator. If we assume that electrons optically excited to energy levels greater than the fundamental are attracted by a parabolic potential, the wave functions that are solutions of the harmonic oscillator can be used to calculate the momentum of the total transition. Substituting these wave functions in 2.21, we can evaluate the strength of an electronic transition also known as the oscillator strength expressed by the letter $f$. It is defined as the ratio of the probability of experimental transition $M_{mn}$ to the probability of transition in the ideal case of a harmonic oscillator $M_{01}$

2.21. The oscillator strength can be described in terms of the total transition momentum as follows:

$$f = \frac{|M_{nm}|^2}{|M_{01}|^2}, \tag{2.22}$$

$f = 1$ refers to the case when the transition is 100% allowed.

## 2.4 Selection rules that govern the transition between two energy levels by dipole approximation

Considering the dipole approximation, the absorption of photons by the interaction between light and matter is only possible if there is a electric dipole momentum created by such interaction. Thus:

$$|M_{nm}| = \left| \int_{-\infty}^{\infty} \Psi_n \widehat{\mu}_{nm} \Psi_m d\tau \right|^2 \neq 0 \tag{2.23}$$

This inequality can be evaluated by taking into account the symmetry arguments of the two states $\Psi_n$ and $\Psi_m$ within their integration interval. States coming from prohibited transitions ($|M_{nm}| = 0$) are called dark states, while states coming from allowed transitions ($|M_{nm}| \neq 0$) are called bright states. In thiobases, the dark states come from the $n \rightarrow \pi^*$ transitions and the bright states come from the $\pi \rightarrow \pi^*$ transitions.

In the same way that atoms are subjected to selection rules when interacting with light, molecules also have a set of restrictions regarding transitions from one state to another. In general, transitions are allowed for intramolecular states by observing the conservation of the intrinsic angular momentum ($\Delta S = 0$) and changes in the component of the orbital angular momentum in the direction of the molecular axis ($\Delta\lambda = 0, \pm 1$).

Thanks to the Born-Oppenheimer approximation, the total electron wave function can be factored as follows:

$$\Psi = \Phi\chi S, \tag{2.24}$$

where $\Phi, \chi$, and $S$ are the orbital, vibrational and spin functions respectively, we obtain the transition dipole momentum in module:

$$|M_{nm}| = \int_{-\infty}^{\infty} \Psi_n e\vec{r}\Psi_m d\tau = \int_{-\infty}^{\infty} \Phi_n\chi_n S_n e\vec{r}\Phi_m\chi_m S_m d\tau_e d\tau_\nu d\tau_S \tag{2.25}$$

$$|M_{nm}| = \int \Phi_n e\vec{r}\Phi_m d\tau_e \int \chi_n\chi_m d\tau_\nu \int S_n S_m d\tau_S, \tag{2.26}$$

where $d\tau_e, d\tau_\nu$, and $d\tau_S$ are the volume differences in the space of electronic, vibrational and spin configurations assuming that one is independent of the other.

The first integral refers to the electronic transition momentum previously discussed. The second integral refers to the requirement of the superimposition of the vibrational

molecular eigenfunctions. The third integral refers to the conservation of the spin which is the strictest rule since the two different spin eigenfunctions are orthogonal, thus it is non-zero only when both are equals. Therefore, only transitions between states of the same multiplicity of spin are allowed: singlet-singlet or triplet-triplet. The singlet-triplet transition is forbidden unless a perturbation causes the spin-orbit coupling (SOC), thus enabling the singlet-triplet transition. This perturbation can be due to the nuclear magnetic field. Therefore, it is a function of the atomic mass (effect of heavy atoms). The Hamiltonian that causes the perturbation and generates a mixture between these two states is given by:

$$H_{SO} = k\xi(L \cdot S), \tag{2.27}$$

where $\epsilon$ is a function that depends on the electric field due to the nucleus, $k$ is a constant of the molecule and $L \cdot S$ is the scalar product between the orbital and spin angular momentum, respectively. The wave function obtained from the spin-orbit coupling, $\Psi_{so}$, is a linear combination between the wave function of a pure triplet state and the wave function of a pure singlet state:

$$\Psi_{SO} = \Psi_T + \lambda\Psi_S, \tag{2.28}$$

where $\lambda$, in this case, is the degree of mixing between the triplet and singlet wave functions $\Psi_T$ and $\Psi_S$, respectively. So, under the effect of the spin orbit coupling the dipole momentum for the transition from the fundamental state to an excited state will be given by:

$$|M| = \int \Psi_{SO}\hat{\mu}\Psi_0 d\tau \tag{2.29}$$

$$|M| = \int (\Psi_T + \lambda\Psi_S)\,\hat{\mu}\Psi_0 d\tau \tag{2.30}$$

$$|M| = \underbrace{\int \Psi_T\hat{\mu}\Psi_0 d\tau}_{Forbidden} + \underbrace{\lambda\int \Psi_S\hat{\mu}\Psi_0 d\tau}_{Allowed}, \tag{2.31}$$

this makes the transition dipole momentum not null.

The difference between the thiobases and the canonical bases, structurally speaking, is just the exchange of the oxygen atom in the canonical bases for the sulfur atom in thiobases. The atomic mass of sulfur is twice the atomic mass of oxygen. This greatly increases the effects of the spin-orbit coupling for these sulfur-substituted bases [10–12]. Such a change opens up the possibility for the electrons to relax from the excited state to different spin multiplicity states, which does not occur on canonical bases [4].

## 2.5 The state lifetimes

An obvious question that arises when electrons are excited from one state to another, is how long the electron will remain in the excited state until it decays to lower energy states. The amount of time that the electron stays in the excited state before following

its decay pathways is called the state lifetime. The main experimental tool that we use to decipher the thiobases relaxation pathways is time resolved Transient Transmission Spectroscopy (TTS) that allows to obtain the excited state lifetime.

In a system with a large number of particles the decay rate is given by:

$$I(t) = I_0 e^{-kt}, \tag{2.32}$$

where $I_0$ and $I(t)$ are the intensities of the radiation emitted at time $t$ before and after the electron excitation. $k$ is the decay rate that is given by:

$$k = \frac{1}{\tau}, \tag{2.33}$$

where $\tau$ is the state lifetime.

Therefore, the lifetime of a state is defined as the time needed for the emission intensity to fall to $1/e$ of the initial value.

## 2.6 Photophysical processes in electronically excited molecules

An excited molecule returns to the fundamental state unless it is involved in chemical reaction. The decay pathway to the ground state is not always the obvious direct emission from the excited state to the ground state. It depends on: the intrinsic energy level, properties of the molecules, the interaction of the molecule with the solvent or the interaction with neighboring molecules[7], external perturbations, excitation region, and the lifetime of the excited states among of things.

The energy relaxation processes can be classified as unimolecular or bimolecular. The unimolecular decay process involves only the studied molecule and its internal processes and the bimolecular relaxation pathway involves also the interaction between other close molecules in the environment. Here, we will pay attention only to the unimolecular process.

In an unimolecular process, the relaxation decay pathway to the ground state can be by a nonradiative process or by a radiative process. Among many other factors, the decay pathway by radiative or nonradiative is completely dependent on the molecule Potential Energy Surface (PES). There are some regions where the energies of two states in the PES become degenerated. These regions appear due to molecular geometry distortions. Examples of distortions in canonical nucleobases are the pyramidalization in $C2$ for purines and the deformation of the $C5 = C6$ bond in pyrimidines, mostly forming Conical Intersections (CIs) between the $\pi\pi^*$ and $n\pi^*$ states or directly with the ground state [64,65].

[7] The interaction with the solvent enables the molecule to reach points that would not be possible without this interaction. Because of this, it is not possible to compare excited state lifetimes obtained by a technique that the molecules are in the gas phase with other techniques that the molecule is in a solution, as well as compare the lifetimes for the molecule in different solutions.

The CI is the doorway to other states without photon state coupling. It can be more or less accessible due to the PES barriers absence or presence, respectively. In the CI point, the energy of both states are degenerated and they are isoenergetic (see the Figure 5)

The possible radiative relaxation processes are fluorescence or phosphorescence emissions. In both processes, the excited state is coupling by electric dipole momentum with the ground state, it makes these transitions possible, as was described before. For the fluorescence emission, there is no change in the state spin multiplicity. Nevertheless, there is a state spin multiplicity change in the phosphorescence. In fluorescence, the transition happens from a bright excited singlet state, while in the phosphorescence it happens from a bright triplet state which is a metastable state. The time constants related to the fluorescence are usually in the range of tens of picoseconds up to nanoseconds, while in phosphorescence they are in the range of nanoseconds up to hundreds of seconds. The phosphorescence lifetimes are usually much longer than the fluorescence ones due to the spin-exchange. The low intensity fluorescence in some molecules can be due to bright excited states ultrafast lifetimes, in the way that it occurs in the canonical nucleobases [4], or even in the energy transfer to the dark states or to the triplet manifold, as in the way that it occurs in the thiobases [66].

The nonradiative conversions are the most common processes in biomolecules, that can act as a lifetime reducer for the excited states. The excess of vibrational energy is lost to the environment as thermal energy in these processes. In this way, the molecule can move around in the vibrational levels since the environment acts as a heat reservoir. The relaxation processes to low vibrational levels within the same state, by transfer of excess vibrational energy to the solvent, is known as vibrational cooling (VC). If the molecule reaches a CI point in the PES, there are two possible unimolecular nonradiative transitions: Internal Conversion (IC) or Intersystem Crossing (ISC), as shown Figure 5.

The ISC happens from a singlet to a triplet state and also in the other way around. The ISC is facilitated due to SOC as discussed in the subsection 2.4. The triplet state must be populated indirectly by a nonradiative process as ISC since it is not accessible by excitation from the ground state due to the fact that the $S_0 \rightarrow T_x$ transition is forbidden by selection rules. Up to now, the observed time constant range related to ISC is about tens of picoseconds to microseconds in biomolecules. However, in this thesis, we will show in the Results Chapter, 6, that in the thiobases there is an ultrafast ISC in a range of few hundreds of femtoseconds. We demonstrate that the exchange of an oxygen atom by a sulfur atom facilitated the ISC process due to an increase of the molecular SOC.

The diagram in Figure 5 represents a PES with all the processes described above. The dashed lines represent the nonradiative processes and the continuum line the radiative ones.

The IC occurs when the molecule passes through a CI to another electronic state

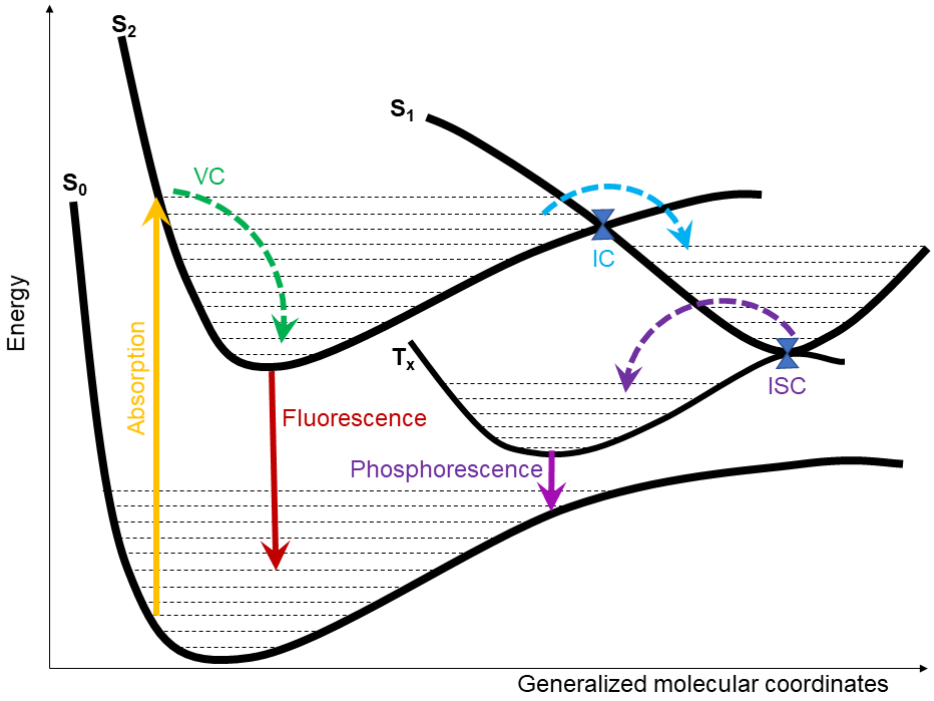



Figure 5 – PES representation with the possible radiative (continuous line) and nonradiative (dashed lines) processes. The hourglass symbols are CI regions, that are the positions where the states are energy degenerated. For states with the same spin multiplicity it is labeled as IC and for states where there is a change in the spin multiplicity of it is labeled as ISC.

with the same spin multiplicity. The time range related to IC is from about tens to hundreds of femtoseconds until nanoseconds in biomolecules. However, in the canonical DNA/RNA nucleobases the time scale of this process, which is related to the transition to the ground state ($S_1 \rightarrow S_0$)[8] is about hundreds of femtoseconds [18, 70–72]. The ultrafast relaxation pathway in canonical DNA/RNA nucleobases gives them great photostability, which is a requirement for the permanence and propagation of life on planet Earth, since this is the requirement for genomic integrity [5].

The radiative process probability has already been discussed and it is given by equation 2.26. Now we will discuss the probability of nonradiative transitions, which are the ones represented by dashed lines in the Figure 5. The nonradiative transition between two states $\Psi_i$ and $\Psi_f$ is given by:

$$\left| \int \Psi_f \hat{J}_N \Psi_i d\tau \right|^2, \tag{2.34}$$

where $\hat{J}_N$ is the nuclear kinetic energy operator related to the perturbation [54]. Using the

[8] It has been identified by Transient Absorption Spectroscopy (TAS) or by time-resolved Photoelectron Spectroscopy (PS) [67–69].

equation 2.24, we obtain:

$$\left| \int \Phi_n \hat{J}_N \Phi_m d\tau_e \int \chi_n^{\nu_i} \chi_m^{\nu_f} d\tau_\nu \int S_n S_m d\tau_S \right|^2 , \tag{2.35}$$

$\hat{J}_N$ acts only in the electronic wave function which is the first term in the above expression, equation 2.35. The second term defines the overlap criterion for the vibrational wave functions of the two combining states. And the last term is the spin integral that, is one for the spin states in the same orientation and equals to zero for the spin states in a different orientation in the absence of SOC.

The nonradiative process is strongly influenced by density of vibrational states, the gap between the two involved states (since the larger the gap the less probable is the transition) and the vibrational overlap between the two electronic states. The nonradiative transition also follows the selection rules. They have exactly opposite selection rules as for the radiative transitions since the operator $\hat{J}_N$ is symmetric. For example, in heteroatomic system the $n\pi^* \rightarrow^3 \pi\pi^*$ and $\pi\pi^* \rightarrow^3 n\pi^*$ are allowed transitions and $n\pi^* \rightarrow^3 n\pi^*$ and $\pi\pi^* \rightarrow^3 \pi\pi^*$ are forbidden due to El-Sayed rule[9].

[9] The El-Sayed rule was formulated in 1963 based on SOC matrix elements calculation and this rule states that the rate of ISC is relatively large if the radiationless transition involves a change of molecular orbital type [73].

# 3 Nonlinear Optics

In this chapter we will present a review of the nonlinear optical processes that are used in the setups for the experimental studies of this thesis. This review was done based on references [74–83].

## 3.1 Ultrashort pulses

This section will briefly discuss how the propagation of an ultrashort light pulse occurs in the absence of nonlinear interactions. Initially, it will be shown how important the Fourier Transform (FT) is in describing linear propagation. Within this context, the equation for pulse propagation will be obtained. Finally, there will be a brief discussion about the concepts of dispersion and spectral phase.

The description of an ultrashort light pulse in the frequency or time domain can be interchangeable thanks to the FT properties. Thus a generic electric field, $E(z,t)$, can be written in either the following two ways:

$$\tilde{E}(\omega) = F\{E(t)\} = \frac{1}{\sqrt{2\pi}}\int_{\Re} E(t)e^{-i\omega t}dt, \tag{3.1}$$

$$E(t) = F^{-1}\left\{\tilde{E}(\omega)\right\} = \frac{1}{\sqrt{2\pi}}\int_{\Re} \tilde{E}(\omega)e^{i\omega t}dt. \tag{3.2}$$

For simplicity in notation the dependence on spatial coordinates has been omitted. The equation 3.2 shows that a light pulse can be described as an overlap of harmonic orthogonal functions: $e^{i\omega t}$. These functions can be interpreted by the angular frequency monochromatic waves $\omega$ and amplitude $\tilde{E}(\omega)$.

A monochromatic plane wave propagating in the $z$ direction can be written as:

$$E(z,t) = \frac{1}{2}A(z,t)e^{i(\omega t - kz)} + c.c, \tag{3.3}$$

where:

$$A(z,t) = B(z,t)e^{i\phi}, \tag{3.4}$$

in which $B(z,t)$ is the amplitude of the plane wave, $w$ is the wave frequency, $k$ is the wave vector module and $\phi$ is the phase.The real part is the initially defined electric field. The amplitude of the field is often called the envelope function. Neglecting the explicit dependency of the envelope function with $z$, the field FT is:

$$\begin{aligned}\tilde{E}(\omega) &= F\left\{\frac{1}{2}A(t)e^{i\omega t} + c.c\right\} \\ \tilde{E}(\omega) &= \frac{1}{2}\tilde{A}(\omega-\omega_0) + \frac{1}{2}\tilde{A}^*(-\omega-\omega_0),\end{aligned} \tag{3.5}$$

where $\tilde{A}(\omega)$ is the FT of the envelope function $A(t)$, and $A^*(\omega)$ is its complex conjugate. To obtain this result, the following Fourier Transform property was used: $F(-\omega) = F^*(\omega)$. Therefore, the equation 3.5 demonstrates that the field can be completely described using the envelope function.

To evaluate how the temporal profile of a pulse relates to its spectral profile, we will consider an example of a pulse with angular frequency $\omega_0$ with a Gaussian envelope:

$$E(t) = \frac{1}{2} A_0 e^{-\frac{t^2}{2\tau^2}} e^{i\omega_0 t} + c.c. \tag{3.6}$$

The pulse duration, $\Delta T$, is calculated by the width at half height of the intensity envelope, which in this case it is easy to show that it is given by: $\Delta T = 2\sqrt{ln2}\tau$. The spectral width can be calculated in the same way, just taking care to make the FT of the envelope function. After the calculation the value found is: $\Delta\Omega = \frac{2\sqrt{ln2}}{\tau}$. Therefore, the product of the spectral width and the pulse duration is a constant: $\Delta T \Delta\Omega = 4ln2$, that is, these quantities are inversely proportional. Thus, it shows that ultrashort pulses have a broad spectral bandwidth. This conclusion was drawn from Gaussian profile pulses, but it is also generally true for other FT limited pulse profiles. Examples for other pulse shapes are shown in [79].

Considering this, the equation for linear propagation of a pulse can now be obtained. In this regime, the wave equation has the form:

$$\frac{\partial^2 E(z,t)}{\partial z^2} - \mu_0 \frac{\partial^2 D(z,t)}{\partial t^2} = 0. \tag{3.7}$$

The linear response of the medium $\epsilon_r$ is time dependent, so the electric displacement is represented by the convolution of $\epsilon_r$ with the electric field. Therefore, the equation 3.7 is rewritten as:

$$\frac{\partial^2 E(z,t)}{\partial z^2} - \frac{1}{c^2} \frac{\partial^2}{\partial t^2} \left[\epsilon_r(t) * E(z,t)\right] = 0. \tag{3.8}$$

The solution of this equation is most easily found in the frequency domain. Thus, applying the FT operator to the above equation and using the convolution theorem, it is rewritten as:

$$\frac{\partial^2 \tilde{E}(\omega,t)}{\partial z^2} + \frac{\omega^2}{c^2} n(\omega)^2 \tilde{E}(z,t) = 0. \tag{3.9}$$

Noting that the wave number is given by:

$$k(\omega) = \frac{\omega}{c} n(\omega). \tag{3.10}$$

Therefore, the solution of this differential equation for each frequency is a linear combination of a progressive wave with a regressive wave both with complex amplitudes:

$$\tilde{E}(z,\omega) = \tilde{E}_p(z,\omega) e^{-ik(\omega)z} + \tilde{E}_r(z,\omega) e^{+ik(\omega)z}. \tag{3.11}$$

In the case of a progressive wave $\tilde{E}_{in}(z,\omega)e^{-ik(\omega)z}e^{i\omega t}$ the time domain field is obtained by the inverse FT:

$$\begin{aligned} E_{out}(z,t) &= \frac{1}{\sqrt{2\pi}}\int_{\Re}\tilde{E}_{in}(\omega)e^{-ik(\omega)z}e^{i\omega t}d\omega \\ &= \frac{1}{\sqrt{2\pi}}\int_{\Re}\tilde{E}_{in}(\omega)e^{i(\omega t-k(\omega)z)}d\omega. \end{aligned} \tag{3.12}$$

This equation mathematically expresses an intuitive concept: at each point in the $z$ coordinate, a propagating pulse is a superposition of monochromatic waves traveling at an angular frequency $\omega$ and a wave vector $k(\omega)$. The spectral phase accumulated by each monochrome wave during propagation is:

$$\phi(\omega) = n(\omega)\frac{\omega z}{c}. \tag{3.13}$$

The dependence of $\phi$ with $n(\omega)$ is responsible for the dispersion. The frequency dispersion of the refractive index and other parameters occurs because matter does not reply instantaneously to an external perturbation [84]. Given that the spectral phase depends of $\omega$, during propagation each monochromatic component of the equation 3.12) accumulates its own phase delay:

$$\tau_p = \frac{\phi(\omega)}{\omega}. \tag{3.14}$$

The phase-dependent delay strongly influences pulse propagation. To support this statement, Taylor's series expansion will be made for $\phi(\omega)$ centered at $\omega_0$ and then the first order approximation will be replaced in the equation 3.12, disregarding for simplicity the coordinates:

$$\phi(\omega) \approx \phi(\omega_0) + \left[\frac{\partial\phi}{\partial\omega}\right]_{\omega_0}(\omega-\omega_0) = \phi_0 + \phi_0'(\omega-\omega_0);$$

$$\begin{aligned} E_{out}(z,t) &= \frac{1}{\sqrt{2\pi}}\int_{\Re}\tilde{E}_{in}(\omega)e^{-i\left[\phi_0+\phi_0'.(\omega-\omega_0)\right]}e^{i\omega t}dt \\ &= \frac{1}{\sqrt{2\pi}}e^{-i\phi_0}e^{i\phi_0'\omega_0}\int_{\Re}\tilde{E}_{in}(\omega)e^{i\left[t-\phi_0'\right]\omega}dt \\ &\propto E_{in}(t-\phi_0'). \end{aligned} \tag{3.15}$$

The result shows that $|E_{out}| = |E_{in}(t-\phi_0')|$, in other words, $|E_{out}(t)|$ is a delayed replica of the input pulse $|E_{in}(t)|$. This delay is known as group delay (GD) and it happens after a wave packet, centered on $\omega_0$, passes through a dispersive medium. The mathematical expression for the GD is the first factor of the second term of the expansion of $\phi(\omega)$:

$$GD = \left[\frac{\partial\phi}{\partial\omega}\right]_{\omega_0} = \tau_p\left\{1+\frac{\omega_0}{n}\left[\frac{\partial n}{\partial\omega}\right]_{\omega_0}\right\}. \tag{3.16}$$

Higher-order terms in the expansion 3.15 conveys important information about the pulse. The first nonconstant factor of the second and third-order term is the Group Delay Dispersion (GDD) and Third Order Dispersion (TOD), respectively:

$$\phi(\omega) \approx \phi(\omega_0) + \underbrace{\left[\frac{\partial\phi}{\partial\omega}\right]_{\omega_0}}_{GD}(\omega-\omega_0) + \frac{1}{2}\underbrace{\left[\frac{\partial^2\phi_{\omega_0}}{\partial\omega^2}\right]_{\omega_0}}_{GDD}(\omega-\omega_0)^2 + \frac{1}{3}\underbrace{\left[\frac{\partial^3\phi}{\partial\omega^3}\right]_{\omega_0}}_{TOD}(\omega-\omega_0)^3 + \dots \quad (3.17)$$

The GDD is responsible for the pulse broadening and TOD is responsible for the pulse distorting its profile and multiple delayed replicas.

### 3.1.1 Pulse compression

The spectral phase accumulated during the pulse propagation through to optical elements is experimentally compensated by the GDD and the TOD controlling. The GDD is known as the pulse chirp. In the setups presented in Chapter 4 and Appendix A.3 we used two types of systems that present a negative dispersion: Chirped Mirrors, CMs, (Figures 10, 11, 49, and 50) and Brewster-cut prism pairs(Figures 49 and 50). The Figure 6 show a schematic representation for both of them.

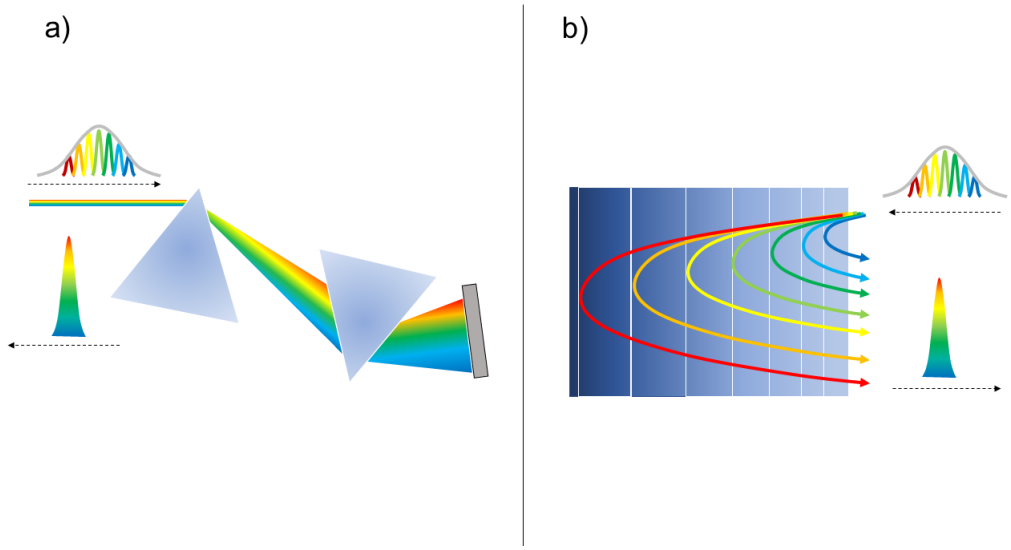



Figure 6 – Pulse compression approach: A) prism pairs, and B) Chirped Mirrors (CMs).

For the Brewster-cut prism pairs, the negative GDD is introduced by controlling the distance between the prisms. The distance control enables the prisms thickness control that the pulse will pass through and thus, control the pulse dispersion. Usually, low dispersion prism material (such as fused silica and $CaF_2$) enables the sensitive control of the GDD and TOD. The Brewster-cut prism pairs disadvantage is that it is very sensitive to the alignment.

A CM is a dielectric dispersive mirror with a spatial variation of the layer thickness values. Different wavelengths pass through different coating layers leading to different speeds which allow the pulse time compression. The CMs are less sensitive to the alignment when compared to the prism pairs. Their alignment is subject only to the number of bounces. Therefore, the CMs introduce a discrete negative dispersion variation (in the visible it is about -50 $fs^2$). The disadvantage is that they can be very expensive since they require a delicate design. Moreover, it is not always available in all wavelength ranges, especially in IR.

## 3.2 Ultrafast parametric amplifiers and the basics of nonlinear optics

Currently most femtosecond pulse sources originate from gain media such as Ti:Sapphire, which operate in a tunable wavelength range close to 800 nm. However, the operation of lasers in a small spectral range contrasts with the need, for example, of time-resolved optical spectroscopy that requires tunable pulses over a wide frequency range.

Lasers, based on population inversion, can not have a wide frequency tuning range. However, continuous frequency variation can be performed by the nonlinear Parametric Optical Amplification (OPA) process. In this process, the tuning frequency can be varied from the infrared (IR) to the visible [74].

To understand this phenomenon, in the context of nonlinear optics, a short summary will be made about this subject.

### 3.2.1 Second-order nonlinear optical effects for monochromatic waves

The electric field is commonly written as shown in equation 3.3. The flat wave described by the electric field induces a polarization $P(z,t)$ when passing through a material medium. Such polarization is given by:

$$P(z,t) = P_L(z,t) + P_{NL}(z,t), \tag{3.18}$$

where $P_L(z,t)$ is the linear term of polarization and $P_{NL}(z,t)$ is the nonlinear term that appears due to strong electric fields (larger than $10^{12}$ V/m) and it depends of $E^2$, $E^3$...

From Maxwell's equations, the D'Alembert equation is obtained:

$$\frac{\partial^2 E(z,t)}{\partial z^2} - \frac{n^2}{c^2}\frac{\partial^2 E(z,t)}{\partial t^2} = \mu_0 \frac{\partial^2 P_{NL}}{\partial t^2}. \tag{3.19}$$

Note that the term dependent on $P_{NL}$ acts as a source in the above equation. It is responsible for a variety of nonlinear optical effects. When only second order nonlinear

optical effects occur[1], the nonlinear polarization term is given by:

$$\begin{aligned} P_{NL}(z,t) &= \epsilon_0 \chi^2 E^2(z,t) \\ P_{NL}(z,t) &= 2\epsilon_0 d_{eff} E^2(z,t), \end{aligned} \tag{3.20}$$

where $d_{eff}$ is the effective nonlinear optical coefficient and $\chi^2$ is the susceptibility tensor of the second order.

An important parameter that together with the nonlinearity of the crystal $d_{eff}$ determines the efficiency of a second order nonlinear process is phase matching: $\Delta k = k_3 - k_2 - k_1 = 0$, when considering three waves with wavevectors $k_1$, $k_2$ and $k_3$. From a wave point of view, during the nonlinear process, fields with new frequencies are generated locally within the material and propagate at their own phase velocities. This process happens in all longitudinal direction. If there is destructive interference between the fields, the macroscopic effects of the nonlinear processes are neglected, even for very strong pumping fields. However, if there is some constructive interference it means that the phase velocity of the fields are the same, and therefore there is phase matching. From the corpuscular point of view, the interpretation of phase matching is given by the conservation of the linear momentum of the photon:

$$\hbar\vec{k_3} = \hbar\vec{k_2} + \hbar\vec{k_1}, \tag{3.21}$$

$$\vec{k_3} = \vec{k_2} + \vec{k_1}. \tag{3.22}$$

In second order processes the electric field is described as a superposition of three fields that carry different frequencies $\omega_1$, $\omega_2$ and $\omega_3$:

$$E(z,t) = \frac{1}{2}\left[A_1(z)e^{i(\omega_1 t - k_1 z)} + A_2(z)e^{i(\omega_2 t - k_2 z)} + A_3(z)e^{i(\omega_3 t - k_3 z)}\right] + c.c. \tag{3.23}$$

For simplicity let's consider that the amplitude of the field is not time dependent (as happens with continuous wave lasers). Taking into account the slow variation of the envelope approximation [85] and the necessary condition for propagation, it is possible to arrive at the following equations:

$$\frac{\partial A_1}{\partial z} = -i\frac{\omega_1}{cn_1} d_{eff} A_2^* A_3 e^{-i\Delta k z}; \tag{3.24}$$

$$\frac{\partial A_2}{\partial z} = -i\frac{\omega_2}{cn_2} d_{eff} A_1^* A_3 e^{-i\Delta k z}; \tag{3.25}$$

$$\frac{\partial A_3}{\partial z} = -i\frac{\omega_3}{cn_3} d_{eff} A_1 A_2 e^{i\Delta k z}. \tag{3.26}$$

[1] Usually, non-center-symmetrical materials have a non-zero susceptibility tensor and have second-order non-linear effects.

From the equations 3.24, 3.25 and 3.26 one can see that the fields from $\omega_1$ and $\omega_2$ play the same role. These equations correspond to a set of three coupled equations. According to the boundary conditions employed, two processes can be described by them: the Sum Frequency Generation (SFG) and the Difference Frequency Generation (DFG) [77].

In SFG the incoming fields have frequencies corresponding to $\omega_1$ and $\omega_2$ and the interaction between them produces the field whose frequency is $\omega_3 = \omega_1 + \omega_2$. See the Figure 7. This corresponds to the general case that includes the special case of Second Harmonic Generation (SHG) that occurs when $\omega_1 = \omega_2$.

At DFG, the incoming fields have frequencies $\omega_1$ and $\omega_3$. In this process the field with frequency $\omega_3$ loses energy in favor of field with frequency $\omega_1$. The interaction between these fields produces a field with frequency $\omega_2 = \omega_3 - \omega_1$. Optical rectification is the limit case where $\omega_3 = \omega_1$.

The OPA mechanism (Figure 8) is similar to DFG except for the difference in interactions between the fields: DFG happens when fields with frequencies $\omega_1$ and $\omega_3$ have comparable intensities. OPA occurs when the intensity of the $\omega_3$ frequency field is much higher than the $\omega_1$ frequency field. In this process the intense beam 3 (pump beam, $\omega_3$) transfers energy to beam 1 (signal, $\omega_1$) that is amplified. Considering energy conservation it generates the beam with frequency $\omega_2$ (idler, $\omega_2$) as shown in the Figure 8.

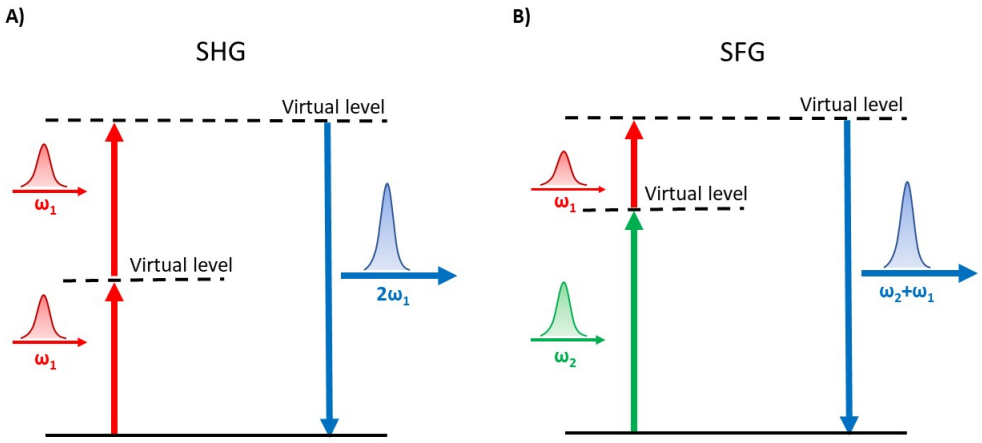



Figure 7 – A) Second Harmonic Generation and B) Sum Frequency Generation

In the OPA process, the exponential dependence on gain with propagation distance is distinct from the quadratic growth that is observed in other second-order processes such as SFG and SHG. In addition, the OPA process has a few different characteristics when compared to population inversion amplifiers. For example, it does not have the ability to store energy. Therefore, there is gain only when there is an overlap between the interaction time of the three pulses. Moreover, the central frequency of the gain is not fixed, it can be adjusted according to the phase matching condition. The gain is strongly influenced by

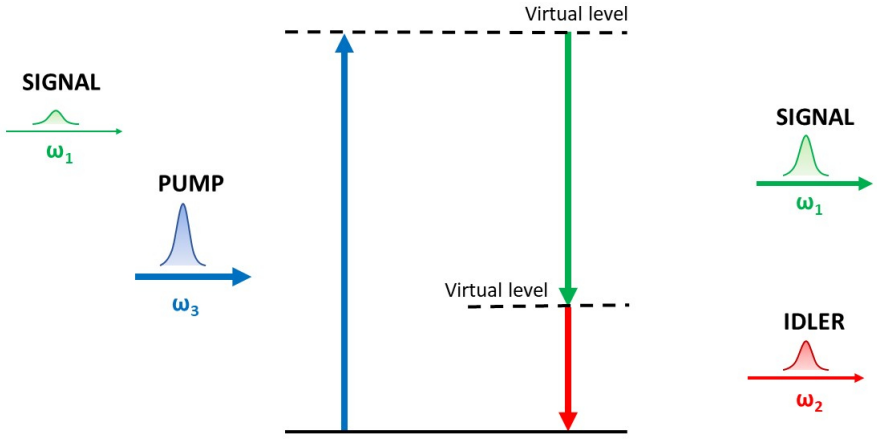



Figure 8 – Optical Parametric Amplification process. For each photon of frequency $w_1$ and $w_3$ that come in, two photons of frequency $w_1$ and one of frequency $w_2$ come out.

some factors such as pumping beam intensity, crystal length, crystal susceptibility tensor and signal and idler frequencies.

Setting the intensity as: $I = \langle E(t)^2 \rangle = \frac{1}{2} |A(t)|^2$ and manipulating the equations 3.24, 3.25 and 3.26, it is possible to obtain:

$$\frac{1}{\omega_1}\frac{\partial I_1}{\partial z} = \frac{1}{\omega_2}\frac{\partial I_2}{\partial z} = -\frac{1}{\omega_3}\frac{\partial I_3}{\partial z}. \tag{3.27}$$

Such an equation is known as the Manley-Rowe equation. It expresses the conservation of energy in nonlinear second order processes. This statement becomes clearer if it is rewritten in the form:

$$\frac{\partial I_1}{\partial z} + \frac{\partial I_2}{\partial z} + \frac{\partial I_3}{\partial z} = 0. \tag{3.28}$$

Furthermore, it can be rewritten as a function of the photon flux $N_i(z)$ that is perpendicular to the surface $S$ for a time interval $\Delta t$:

$$\frac{\partial N_1(z)}{\partial z} = \frac{\partial N_2(z)}{\partial z} = -\frac{\partial N_3}{\partial z}. \tag{3.29}$$

This equation 3.29 shows that second-order parametric interactions involve three photons one of each frequency. Depending on the initial conditions of the process to be addressed, each photon may be absorbed or emitted. Figures 7 and 8 show parametric effects based on absorption and emission from virtual levels.

In the case of SFG, when two photons are absorbed ($\omega_1$ and $\omega_2$) they instantly excite the material to a higher virtual energy level. The decay from this level produces the emission of a frequency photon $\omega_3 = \omega_2 + \omega_1$. Similarly in OPA, the absorption of the pump (with frequency $\omega_3$) excites a higher energy virtual level and a photon signal (with frequency $\omega_1$) stimulates the decay to a virtual intermediate energy level, generating the emission of an identical photon, thus amplifying the signal. To complete the decay to the fundamental level a photon of weakness $\omega_2 = \omega_3 - \omega_1$ is generated.

Parametric interaction only occurs when the photons involved are simultaneously at the same volume of the medium. It is like a photon collision, so the process depends on the number of photons. Therefore, parametric processes are only efficient for intense beams.

The equations in this section were developed considering no polarization and no different propagation directions of the beams involved. For a more general approach, such factors should be considered [82].

### 3.2.2 Parametric amplification over a broadband frequency range

This section will extend the description of parametric amplification for the case of short pulses. A pulse can be described as a superposition of monochromatic waves thanks to the FT properties as shown before. This important tool allows to adapt the results found for monochromatic waves to the case of short pulses.

In parametric amplification, the pump, signal and idler pulses have different wavelengths and different group velocities. For this reason they accumulate distinct group delays after propagating through a crystal length $z$. When the group delay between the pulses is large they no longer have a temporal overlap, so the interaction between them disappears. So to choose the best crystal width (which optimizes the gain), it is necessary to take into account the interaction of the group velocity between the pulses.

For efficient energy exchange between beams, the phase matching must still be maintained for short pulses. It will be evaluated how the phase matching will be modified. If the pump frequency is kept fixed at $\omega_3$ and the signal frequencies change to $\omega_1 + \Delta\omega_1$ by energy conservation the idler frequency will change to $\omega_2 - \Delta\omega_2$, thus the vectors in the first order become:

$$\begin{aligned} k(\bar{\omega_1} - \Delta\omega) &\approx \bar{\omega_1} + \left[\frac{\partial k_1}{\partial \omega}\right]_{\omega_1} \Delta\omega \\ &= k(\bar{\omega_1}) + \frac{1}{v_{g1}}\Delta\omega \\ k(\bar{\omega_2} - \Delta\omega) &\approx \bar{\omega_2} - \left[\frac{\partial k_2}{\partial \omega}\right]_{\omega_2} \Delta\omega \\ &= k(\bar{\omega_2}) - \frac{1}{v_{g2}}\Delta\omega, \end{aligned} \tag{3.30}$$

where $v_{g1}$ and $v_{g2}$ are the velocity of signal and idler respectively. The result of the phase matching wave vector is:

$$\Delta k \approx \left(\frac{1}{v_{g1}} - \frac{1}{v_{g2}}\right)\Delta\omega. \tag{3.31}$$

This equation shows that the lower the relative group velocity between idler and signal, the better the phase matching. Since the gain depends on phase matching, in the case

of short pulse parametric amplification, the gain will be influenced by the relative group velocity of the idler and signal.

## 3.3 White light generation

The process of white light generation occurs when an almost monochromatic laser pulse is converted to a pulse with a large spectral width [86]. This means that if a pulse with a small line width and a high peak intensity is focused on a nonlinear transparent material, the pulse that comes out of it will be like a flash of white light. Spectral widening is mainly driven by the nonlinear optical effects of self phase modulation, which leads to the generation of new frequencies, and self focusing, which is responsible for the high peak intensity. To generate white light, as shown by the setup of the Figures 10, 11, 49, 50 in the Chapter 4 and in the Appendix A.3, a sapphire crystal is used that is centrosymmetric, so when applying a sufficiently strong field, only the odd order terms in the polarization expansion are relevant for nonlinear effects. In this context, the refractive index is given by:

$$n = n_0 + n_2 I(r,t), \tag{3.32}$$

which $n_0$ and $n_2$ are constants.

Therefore, the refractive index will depend on the intensity $I(r,t)$ of the beam. Knowing that the Gaussian is more intense in the middle than at its ends, then, from the above equation, it is clear that the center of the beam will be subjected to a higher refractive index than the edges, therefore it will travel more slowly in this region. This effect causes the beam to begin to focus. This phenomenon is called Self Focusing (SF). For it to occur the laser peak intensity must be high enough. This means that the laser power used must exceed a certain critical threshold characteristic of each material that will depend on the wavelength of the laser.

Another important process that contributes to the formation of the supercontinuous is the Self Phase Modulation (SFM). It also happens because of the intensity dependence of the refractive index as shown by equation 3.32 and because the intensity has also a temporal dependence. Therefore the frequency can be written as:

$$\omega = -\frac{\partial \varphi}{\partial t} = \omega_0 - z n_2 \frac{\omega_0}{c} \frac{\partial I(r,t)}{\partial t}. \tag{3.33}$$

in which $\varphi = kz - \omega_0 t$. By equation 3.33 is clear that there may be a shift to red if the intensity increases or to blue otherwise. Because there is a variation in intensity with time, a variety of frequencies and colors are created from an almost monochromatic light source. Therefore it is possible to create a super continuous filament of white light.

# 4 Technical Approaches

To decipher the main thiobases deactivation mechanism, we used the broadband Transient Transmission Spectroscopy (TTS) to evaluate the dynamic features and we used steady-state: Absorption, Photoluminescence and Raman experiments to evaluate the time independent characteristics.

## 4.1 Ultrafast Transient Transmission Spectroscopy

Understanding how biological systems work requires not only knowing their structures but also their dynamics. The structure provides information about the arrangement, and the function of the elements that make up the system. The dynamics of biological processes can explain how the system evolves after an external stimulus. However, many biological processes involving macromolecules are relatively complex processes, so they can be understood as combinations of many elementary processes [76]. The elementary processes, such as translation and rotation of part of a molecule, breakage or formation of chemical bonds, energy transport, are processes that occur on a very small time scale, in the order of $10^{-12}$ s to $10^{-14}$ s.

Ultrafast optical spectroscopy is the only tool that enables the study of the dynamics of elementary processes. Pump-probe technique enables temporal resolution of various biological systems [76,87–90], semiconductors [91–94] among others [95–97]. This technique consists in optically excite the system and probe it with two laser beams coming from different optical paths. The first beam to arrive in the sample is the pump beam. It has the function of modifying the optical properties of the material and it is resonant with some of the system transitions. Then after a certain amount of time $\tau$, the probe beam arrives to interact with the material and probe the modifications caused by the pump pulse. By performing various measurements by varying the delay time between the pulses, it is possible to monitor the evolution of the system by detecting only the probe beam (see the Figure 9).

The pump-probe technique can be classified as degenerate or non-degenerate. In the degenerate case the pump beam and the probe beam come from the same laser and are superimposed on spectrum. In the non-degenerate case, although the two beams are usually generated from the same laser, one (or both) goes along optical paths that are capable of modifying the pulse frequency. The nonlinear processes required to obtain pulses in various spectral regions that are pertinent to this project are described in the Chapter 3.

There are three types of signals that can be detected from a pump-probe experiment. One is when the pump pulse excites a large number of electrons in the ground state to higher energy levels, so the probe beam can be almost entirely transmitted. This phenomenon is known as Photobleaching (PB). Another phenomenon that can happen is Stimulated Emission (SE) which also increases the transmission. It happens when the probe beam stimulates the electrons that are at higher energy levels to decay to lower energy levels. There is also the case called Photoinduced Absorption (PA). In this case, the electrons excited by the pump beam can be excited again by the probe beam for even higher energy levels. The Figure 9 shows schematically the energy levels of a molecule and the possible transitions that can be probed after the excitation by the pump beam (blue box inset).

In the next sections, we will describe the experimental setup and approaches used to characterize the thiobases dynamics and stationary features which are fundamental to understand the deactivation pathways.

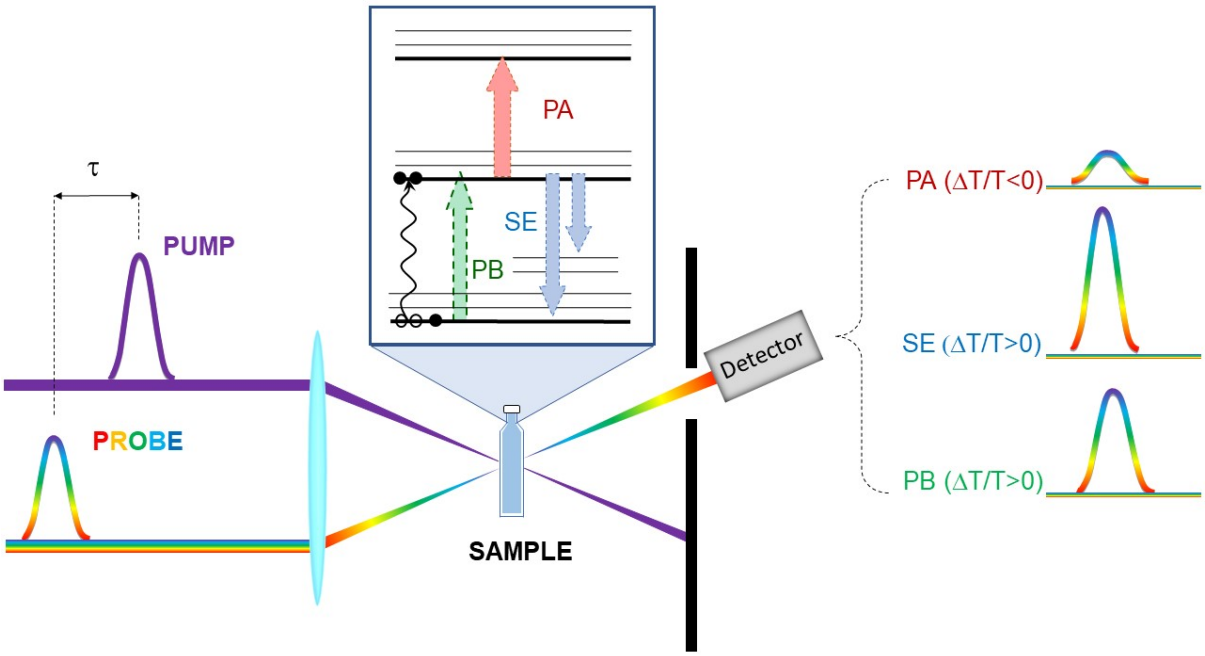



Figure 9 – Schematic representation of the processes observed by pump and probe transient transmission spectroscopy ($\Delta T/T$) of a molecular system.

## 4.2 TTS experimental setup with SFG: broadband pulses centered at 330 nm with sub-20 fs time duration

This section describes the experimental setup used for pump-probe technique with ultrashort pulse in the UV range. In this setup, in the pump beam line, there is a Non-collinear Parametric Amplifier (NOPA) in the visible region that is tunable in the range of 500 nm to 700 nm and produces 10 fs pulses due to the use of a pair of Chirped Mirrors for dispersion compensation (as describe in the section 3.1) with at least 5 bounces at each mirror (see Figure 10). The pump pulses in the UV region can be generated in two ways. One of them is the setup described in this section, that consists on the SFG of the IR and visible pulses from the NOPA, producing broadband pulses centered at 330 nm. The other one is a setup that uses the SHG from the NOPA, which generated broadband pulses centered at 270 nm, that is schematically represent in the Appendix (A.3). The mathematical description of parametric amplification and second-order nonlinear optical processes was presented in the Chapter 3. The descriptions in this section refer to the Figures 10 and 11 that represent the setup used.

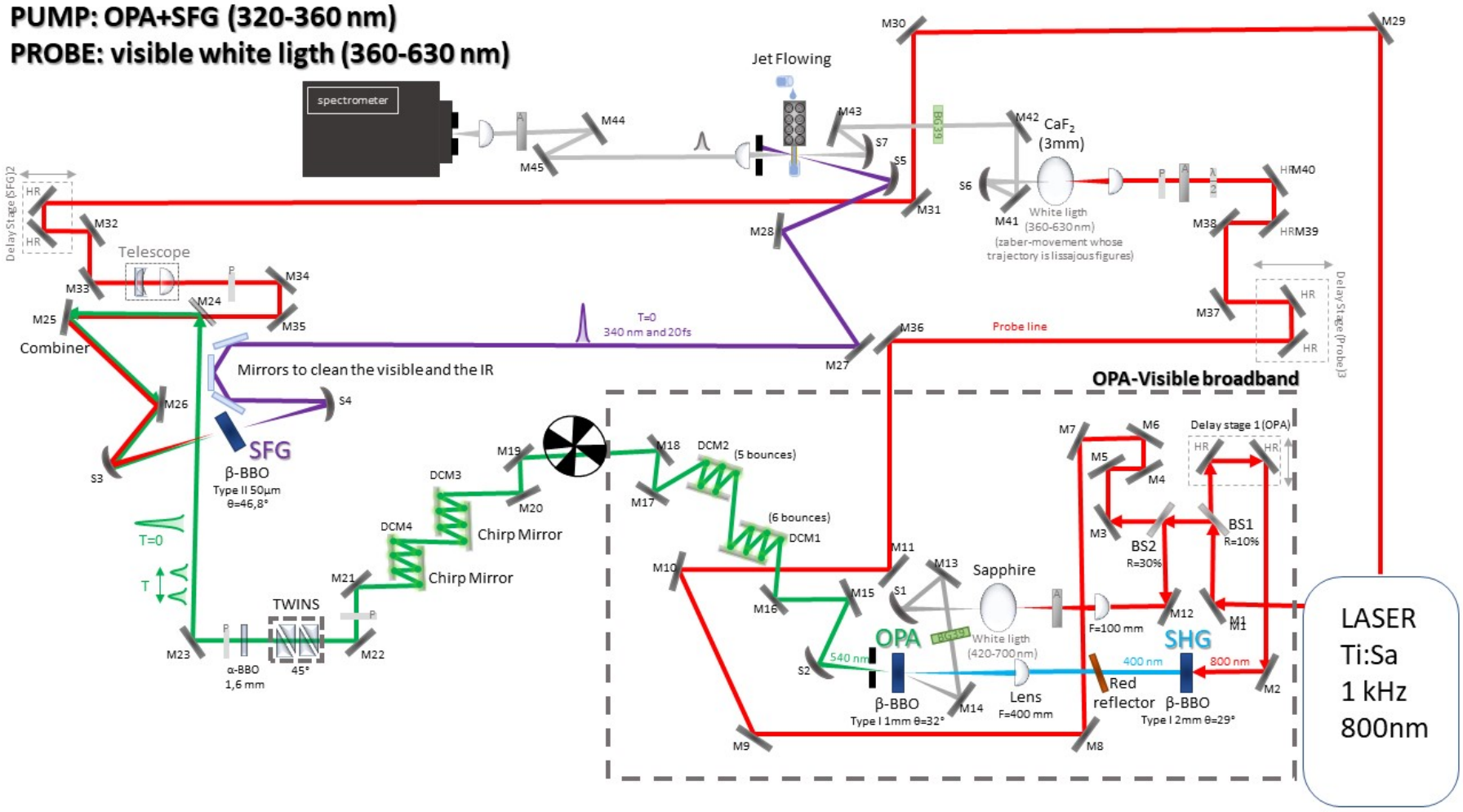



Figure 10 – Experimental setup: pump at 330 nm and probe in the visible.

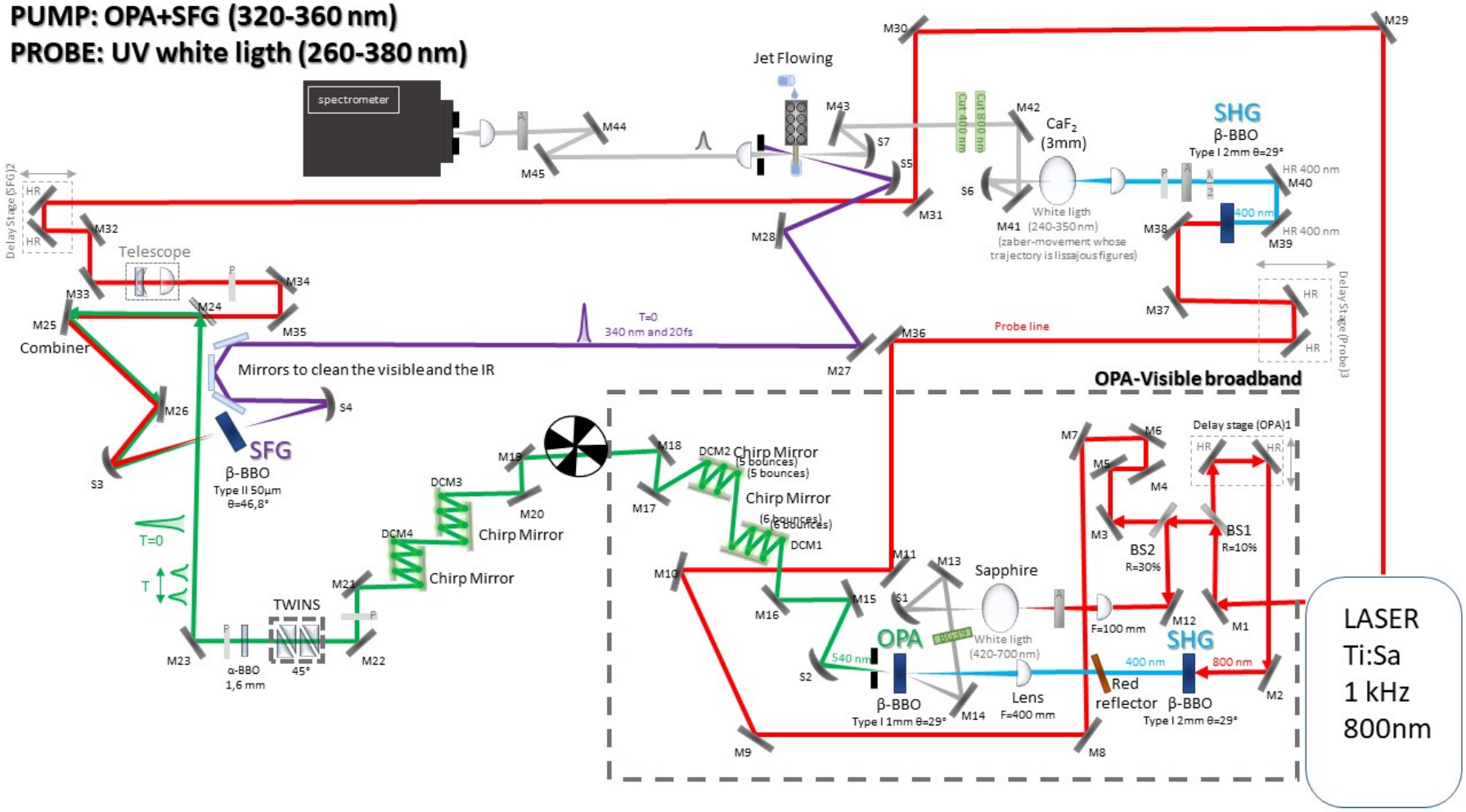



Figure 11 – Experimental setup: pump at 330 nm and probe in the UV.

### 4.2.1 Pump Line

The experimental setup begins with a Ti:Sapphire amplifier laser (Libra, Coherent) with pulses centered at 800 nm with 100 fs time duration (bandwidth of approximately 20 nm) in a repetition rate of 1 kHz and an average power around 3.8 mJ. Before starting the optical path to the NOPA the beam size is reduced by a telescope made of spherical mirrors with focuses of $f = 250$ nm and $f = -600$ nm.

#### 4.2.1.1 NOPA

In the figures 10 and 11 the NOPA is indicated by the region delimited by the gray dashed lines. Realistically these lines represent a box constructed of black cardboard for the purpose of optically isolating the system. The NOPA input power is 1.2 mJ. In the NOPA the optical path begins at mirror M1 which directs the beam to the Beam-splitter (BS1) which transmits 90% and reflects 10% of the incident light. The reflected light will form the NOPA seed and the transmitted light will form the NOPA pump.

The transmitted beam goes to the manually controlled delay stage where there are high reflectivity infrared (IR) mirrors. Then the M2 mirror directs the beam to a type-I $\beta$-BBO cut at 29° where the SHG of the fundamental beam is generated (see 3.2.1). Since the SHG process is not 100% efficient, the beam passes through a filter that is able to reflect the 800 nm wavelength beam and transmit the 400 nm wavelength beam. Then the pump is focused by a silica lens into the OPA beta-BBO crystal. However, to avoid the effect of self-focusing of the pump, the crystal used for amplification is positioned at 50 mm after the lens focus.

The reflected beam of BS1, used to form the NOPA seed, passes through another Beam-Splitter (BS2) that transmits 70% and reflects 30% of the incident light. The transmitted light goes out of the NOPA box, delimited by dashed lines, guided by the mirror array M3 through M11. This beam will be used for the probe beam. While the reflected light from BS2 is directed to the M12 mirror which directs it to a BK7 lens (f=100 mm) that focuses it on a 2 mm thick sapphire crystal. To control the power that reaches the crystal a metal film attenuator with variable thickness is used. The generated white light covers the range 450-700 nm, and it is collected by the spherical mirror S1 with $f = 50$ mm. During alignment, the angle between the incident beam and the reflected beam was as small as possible to avoid aberrations. A bandpass glass BG39 filter from Newport is used to eliminate residual fundamental laser in the white light. The pair of mirrors M13 and M14 are responsible for directing the seed to the NOPA crystal.

The NOPA crystal is a 1 mm type I $\beta$-BBO with 29° phase-matching angle. To have the amplification process the pump beam as well as the seed beam must be in temporal and spatial overlap. The temporal overlap can be controlled with the delay stage. The

spatial overlap is obtained during alignment using a pinhole with diameter of 1 $\mu$m. When the signal is amplified there is a super-flowering ring that is generated by amplification of the background noise. To generate broadband pulses the red color of the super-flowering ring is out, this is possible by rotating the crystal to adjust phase-matching. When it is well aligned, this ring is practically overshadowed due to intense seed amplification. The idler is angularly dispersed due to the non-collinear configuration of NOPA. The control of the laser amplification range is done by simply changing the delay between the pump beam and the seed in the delay stage. To select only the applied beam an iris is placed in front of the crystal. When passing through the iris the beam is collimated by the spherical mirror S2. The M15 and M16 mirror pair is responsible for bringing the beam to two the pairs of double-chirp mirrors (DCM): DCM1 where the pulse is reflected 6 times and DCM2 where the pulse is reflected 5 times (as shown in the section 3.2). M17 and M18 mirrors direct the applied beam out of the NOPA box. The NOPA output pulse covers the range 520-600 nm and has a peak at 540 nm with a power of 7 $\mu$J and a duration of sub-10 fs (see the Figure 12).

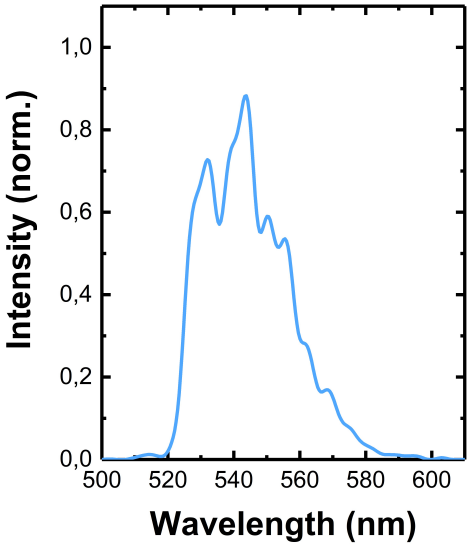



Figure 12 – NOPA spectrum.

#### 4.2.1.2 SFG

As shown in the Figures 10 and 11, before generating the pulse in the UV region the visible region beam passes through the chopper that is responsible for modulating the frequency of the pump beam. The beam then passes through two pairs of CM to compensate for the dispersion that the pulse will experience when it passes through the $\beta$-BBO crystal and the optical instruments before generating pulses in the UV range. Then, the beam reflects in the DCM mirrors pairs. The M21 mirror directs the pulse to a polarizer to ensure beam polarization upon entering in the Translating-Wedge-Based

Identical Pulses eNcoding System (TWINS) device [98] which is positioned at 45° from the optical table. This device is made up of two pairs of wedges of birefringent material ($\alpha$-BBO) that, by moving one relative to other, allows to generate two identical pulses with a controlled time delay between them. The TWINS is used in the Two-dimensional electronic spectroscopy (2DES) experiments (see some results in the appendix B). In the case of the pump-probe experiments they were used to obtain the results described in the Chapter 6 the delay of the two pulses generated by the TWINS is set to zero, so that when passing through this apparatus the pulse characteristics are preserved. The mirror M23 guides the pulses to mirror M24. The M24 mirror reflects light from the visible region and transmits light of the IR region. The beam of the IR region from the fundamental passes through the manually controlled delay stage 2 and a telescope capable of decreasing the beam diameter. The delay stage 2 is responsible for the temporal overlapping of the visible beam and the beam in the IR region in the crystal. Both the visible region beam and the IR beam are combined in mirror M25 which direct them to mirror M26 that in turn guide them to the spherical mirror S3 (f=250 mm) which is responsible for focusing them into the $\beta$-BBO Type II crystal, the 50 $\mu$m thick with cut angle of 46.8°. It is important to note that both the thickness and the cutting angle of the crystal are extremely important parameters. The thickness is important because the higher the crystal thickness the higher the process efficiency, but the increased thickness leads to a thinning of the output pulse bandwidth, so a compromise between these two factors must be established. And the cutting angle of the crystal is closely linked to the condition of phase-matching, for more information check the reference [99]. After the crystal, the pulses are directed to three dielectric mirrors capable of removing light that has not been converted to the UV region. These mirrors have a high reflectivity at the range that is between 310-390 nm when the incidence beam is 56° from the normal reflection surface. They are positioned vertically and decrease the beam height on the optical table by about half.

Therefore the pulse, when optimized for all alignment parameters, has a power of approximately 30 nJ and a duration of 16 fs (value measured by the 2DSI technique described in the section 4.4 ) and covers the range 320-360 nm. See Figure 13 for the pulse spectrum. We also use an experimental setup (see Figure 49) generating pulses of sub-20-fs centered at 270 nm. Its spectrum is shown in Figure 13 b. These are the pump beams used for the pump and probe technique.

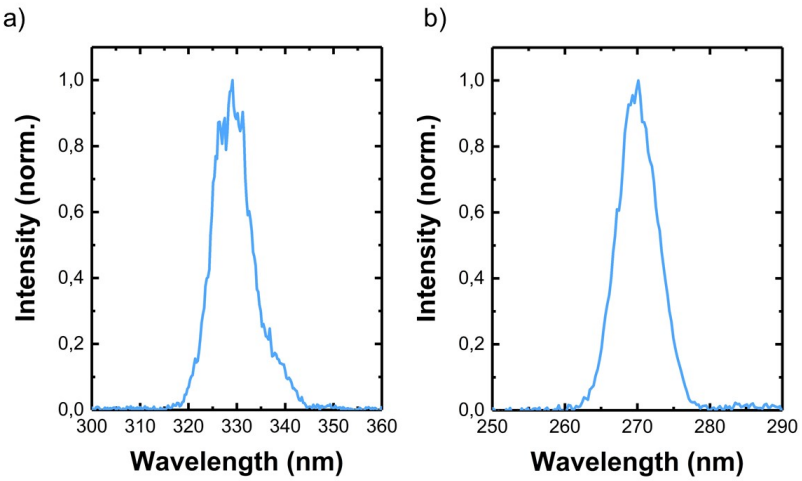



Figure 13 – Pump pulses obtained by: (a) SFG (b) SHG.

## 4.2.2 Probe line

### 4.2.2.1 Probe beam in the visible range

As shown in the Figure 10, the probe beam line starts at mirror M36 that takes the fundamental beam to the stepper motor controlled delay stage, that is responsible for setting the delay between the pump and probe beams (delay stage 3). The beam then passes through the mirror array M37 to the M40 that directs it to a half-wave plate, an attenuator, and a polarizer that controls the polarization and power of the beam. It focuses on a 3 mm $CaF_2$ plate that moves with a horizontal and vertical motion controller (Zaber) following a script that makes the plate move so that its center of mass draw Lissajous figures[1]. This is important since the $CaF_2$ crystal can be seriously damaged due to the high laser power if it remains stationary. The white light generated by this crystal, due to high order nonlinear processes, covers the range of 360-630 nm. It is collimated by the spherical mirror S6 and passes through the BG39 filter which is responsible for eliminating the remaining part of the pulse from the fundamental laser. This elimination is extremely important for two reasons: (I) the beam coming from the fundamental laser is very intense. We want to ensure that the probe beam is less intense than the pump beam (the power of the probe beam is only 10% of the power of the pump laser in this experiment) since the role of the probe beam is only to probe the sample and not pump electrons. (II) If there is sufficient energy from the fundamental beam arriving in the sample, vibrational levels of the system under analysis may be excited by the probe beam and it loses the role of just probing the sample and becomes a second pump beam, thus compromising the interpretation of the obtained results. The spectra of the probe beam in the visible region can be seen in the Figure 14(a).

[1] The range of motion is small. The plate moves perpendicular to the beam and do not disturb the beam direction.

#### 4.2.2.2 Probe beam in the UV range

In some measurements it was necessary for the probe beam to cover the range 240-350 nm. For this, a 1 mm $\beta$-BBO crystal was inserted between the M35 and M39 mirrors and by setting the phase-matching conditions it generates the second harmonic of the fundamental beam (see Figure 11). The M39 and M40 mirrors that were previously high reflectivity for the 800 nm wavelength were now replaced by high reflectivity mirrors for the 400 nm wavelength. Also the half-wave plate and the polarizer were replaced by the proper equivalents for this wavelength range. In addition, the BG39 filter has been replaced by two filters: one capable of eliminating the remains of the fundamental laser and one capable of eliminating the remains of its second harmonic. The spectra of the UV beam can be seen in the Figure 14 (b).

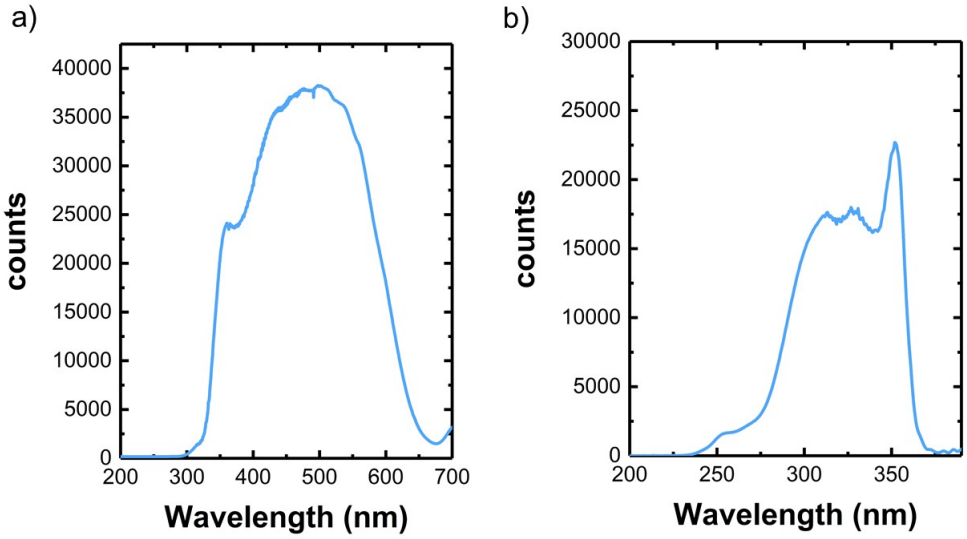



Figure 14 – Spectra of the probe pulses: (a) probe centered in the visible range; (b) probe centered in the UV range.

### 4.2.3 Using liquid sample in a jet flow configuration

After passing through the paths described in the experimental setups the pump and probe beams are focused at the sample by the spherical mirrors S5 and S7, respectively (see Figures 10 and 11). To obtain the overlap of the pump and probe beam we use a 5 $\mu$m diameter pinhole for alignment. Then, the jet (details shown in Figure 15) is fixed at this position. The jet configuration in which the liquid sample flows was chosen for the following reason: In preliminary measurements with a 200 $\mu$m optical path quartz cuvette it was found that the coherent artifact [100–102] produced at zero delay between the pump and probe pulses was enormous and covered the first 100 femtoseconds of sample dynamics. This is because the walls of the cuvette disperse the previously compressed

pump pulse adding too much chirp on it. In other words: the temporal resolution becomes compromised in the cuvette configuration. Since the purpose of this study is to follow the initial relaxation pathways of the thiobases, it is of utmost importance to preserve the high resolution of the setup. We have found empirically that this would not be possible using this 200 $\mu$m optical cuvette (due to its walls). For best results it is necessary that once generated the pulses pass through the smallest possible volume of material during their propagation, as UV beams are easily dispersed by any material. Therefore, to meet this requirement we use the liquid sample flowing in a jet configuration.

The metal part of the jet, machined in stainless steel, is divided into two: (I) the upper part which has 8 holes of diameter 3.4 mm and a cylindrical shoulder of the same diameter and height of approximately 1 cm used to connect the jet to the upper sample container by means of a plastic tube. (II) The bottom wall has 8 threaded holes with M3 thread. Both surfaces that will have contact with the sample have been cleaned and polished. When assembling it, a ductile metal wire of biomolecular inert material is inserted between the two metal parts (see Figure 15). The two metal parts are then connected by M3 threaded screws. The liquid sample is placed in a glass container and the jet is hold by a support such that the height is controlled for the metal wires to lightly touch the liquid. Plastic pipes are connected to a peristaltic pump as shown in the Figure 15. A rotation of 40 rpm is selected to maintain the jet with a stable flow. The thickness of the water film is approximately 200 $\mu$m.

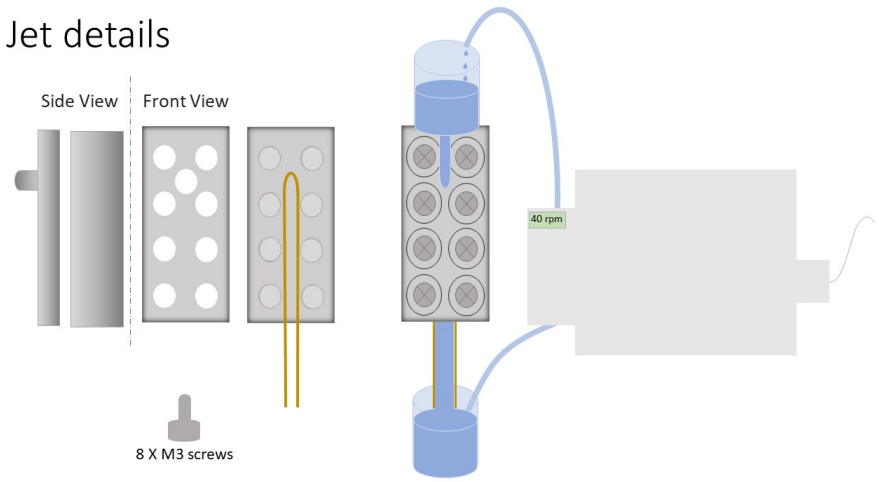



Figure 15 – Details of the metal plates and wire used to obtain the sample in a jet configuration.

## 4.3 Detection scheme

Part of the pump and probe beams are transmitted by the sample flowing in the jet. The transmitted pump beam is blocked by the iris. The transmitted probe beam passes

through a fused silica converging lens, is guided by the M43 and M44 mirrors to a $CaF_2$ lens that focuses the probe beam into the spectrometer (SP2150 Acton, Princeton Instruments). It is detected using a linear image sensor triggered and read by a custom electronic board (Stresing Entwicklungsburo GmbH). The trigger signal from the chopper at 500 Hz allows to detect the transmission of the probe when the pump is on (represent by $T_{ON}(\lambda_{probe}, \tau)$) and when the pump is off (represent by $T_{OFF}(\lambda_{probe}, \tau)$) at the sample. With this information, it is possible to do the measurements of the differential transmission ($\Delta T/T$). A metal film attenuator of varying thickness was used to avoid signal saturation observed during the experiment. For each wavelength of the probe, the differential transmission ($\Delta T/T$) is measured as a function of the time delay between the probe beam and the pump beam:

$$\frac{\Delta T}{T} = \frac{T_{ON}(\lambda_{probe}, \tau) - T_{OFF}(\lambda_{probe}, \tau)}{T_{OFF}(\lambda_{probe}, \tau)} \tag{4.1}$$

## 4.4 Sub-20-fs pulse characterization 2DSI

To be able to measure phenomena that happen in an ultra short time scale is very important to make sure that the pulse duration is well characterized and to have information both about the pulse phase and the amplitude.

Many methods could be used to characterize a pulse. One example is Frequency-resolved Optical Gating (FROG) [103] and Spectral Phase Interferometry for Direct Electric-field Reconstruction (SPIDER) [104].

For broadband pulses, the interferometric techniques are more suitable than spectrograph ones due to the phase-matching issues.

In the UV range, the use of the traditional pulse characterization techniques is a challenge. The difficulty lies in the fact that there is no transparent material in this range and it is hard to obtain phase-matching configuration. Due to UV particularities, the Two-Dimensional spectral Shearing Interferometry (2DSI), which is a robust interferometric technique, becomes a good option [105, 106]

In the 2DSI, two frequency-sheared synchronized collinear ancillae replicas from the fundamental beam are downconverted with the UV test pulse. Scanning the delay ($\tau$) of one ancillae, their interference is directly collected by a detector that generates a 2D-map, encoding for each frequency $\omega$ the phase information. In this way, it is possible to obtain the electric field information.

Considering that the both ancillae are shift by a frequency $\Omega$, the spectra result by the ancillae $A(\omega)$ and the ancillae $A(\omega - \Omega)$ interference and pulse test mix is:

$$I(\omega, \tau_{cw}) = |A(\omega)|^2 - |A(\omega-\Omega)|^2 + 2|A(\omega)||A(\omega-\Omega)|cos(\phi(\omega) - \phi(\omega-\Omega) + \omega_{cw}\tau_{cw}), \tag{4.2}$$

if one of them at the delay $\tau_{cw}$ has the angular frequency $\omega_{cw}$. By scanning $\tau_{cw}$, the $I(\omega, \tau_{cw})$ spectra is recorded as a function of the $\tau_{cw}$ and a 2D-map is obtained with the interference fringes along the $\tau_{cw}$ axis (see the inset map in the Figure 16), in this way the Group Delay (GD) frequency is given by:

$$GD(\omega) = \frac{d\phi(\omega)}{d\omega} \approx \frac{\theta(\omega)}{\Omega}, \tag{4.3}$$

where:

$$\theta(\omega) = \phi(\omega) - \phi(\omega - \Omega) \tag{4.4}$$

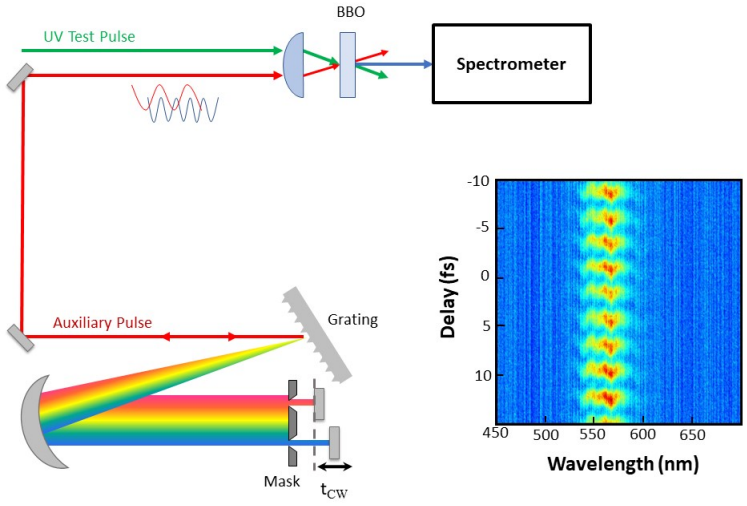



Figure 16 – 2DSI setup and 2D-map. Figure inspired by the reference [105].

The experimental setup is shown in Figure 17, the fundamental beam is sent to a a diffraction grating (2000 lines/mm) where it is spatially dispersed and sent to a V-shape double-slit mask that is able to generate the two almost monochromatic ancillae. Each one of them is sent to independent mirrors and one of them is connect to a piezo translational stage responsible to introduce the delay $\tau_{wc}$. After that, the two ancillae and the test pulse are combined in a Type I 10-$\mu$m thick BBO crystal cut at $\theta = 29°$ and the two downconverted replicas is coupled into the spectrometer and the $\tau_{cw}$ delay is scanned to originate the 2DSI map (Figure 16).

In the UV, the air dispersion effects should be considered. In order to that, the UV beam optical path until the sample place is as short as possible.

The 2DSI measurements was always performed before the data set collection. From it we should obtained the pulses characteristics: flat phase and sub-20-fs time duration (see Figure 17).

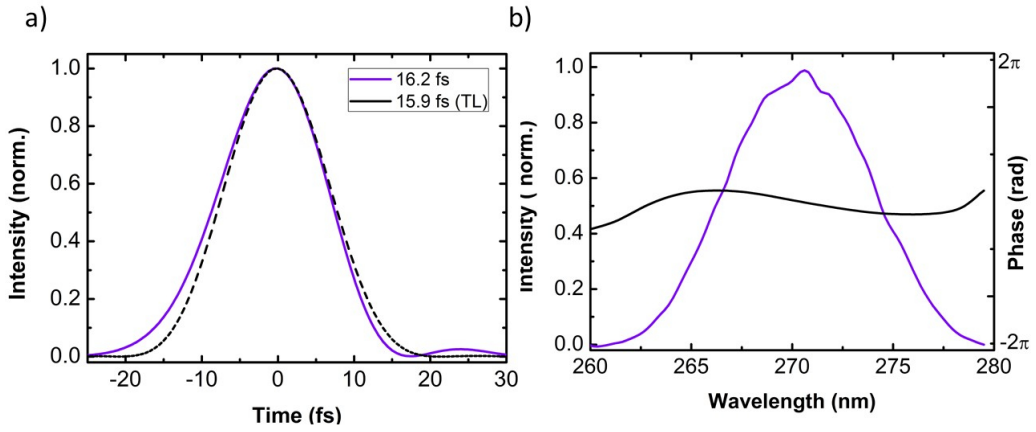



Figure 17 – UV pulse (a) at time domain; (b) at frequency domain.

## 4.5 Global Analysis and data processing

The vast amount of information in a dynamic data set requires a model-based analysis to be understood. In this sense, the TTS data pump with sub-20 fs pulses shown in this thesis were subjected to a global analysis using the software Glotaran [107]. A global analysis of the data [108] allows to obtain the time constants governing the dynamics over the entire dataset. For this, the entire map obtained by the TTS is simultaneously adjusted with specific time constants.That is, a nonlinear least square fit is performed simultaneously on these transients with exponential functions $A_i e^{-\frac{t}{\tau_i}}$. It takes into account the spectral contributions of the exponential decay associated with each time constant and for each probe wavelength. A preliminary step in global analysis is to the perform a singular value decomposition in order to find the number of linearly independent vectors (decay constants) significantly different from the noise. Depending on the sample, in the present work we found three or four dominant components and some others associated to the coherent artefact.

The spectrum resolved in time is represented by the $\Psi(\lambda, t)$ and depends on the wavelengths of the probe and the delay between the pump and the probe. It is a superposition of the contributions of the $n$ different components. The decay rate for each component is given by $k_l$. The exponential decay is coupled with the instrumental response function (IRF) that will depend on time, see equation 4.5.

$$\Psi(\lambda, t) \propto \sum_{l=1}^{n_{comp}} \left(e^{k_l t} \otimes IRF(t)\right) EAS_l(\lambda) \tag{4.5}$$

The amplitudes of the exponential decay are the Evolution Associated Spectra (EAS). The EAS gives information of the relaxation decay path. A molecule in the excited state corresponds to a molecule species different from the one in the ground state. Each curve in the EAS correspond to one species in the excited state. For a given time constant $\tau_i$ the EAS gives the wavelength dependent amplitude associated with it. The analysis

takes into account also the coherent artefact, whose oscillatory time profile was modeled by a sequence of exponentials, and the dispersion due to the chirp of the probe (modelled by a third-order polynomial). The signal of the EAS indicates a rise or a decay depending on whether it refers to negative (PA) or positive (GSB/SE) bands. For positive $\Delta$A (PA bands): a negative EAS is associated to a rise of the signal and a positive EAS to a decay. For negative $\Delta$A (SE bands): a positive EAS is related to a rise of the signal, whereas a negative EAS to a decay.

At least three independent datasets (i.e., recorded on three different days) were used in the analysis and all uncertainties[2] are reported as twice the standard deviation of the average lifetime.

## 4.6 Linear Absorption

The Linear Absorption (LA) of each sample in phosphate-buffered saline (PBS) solution was measured using the JASCO Corp. V-570 spectrometer at room temperature. The samples were placed in a 1 mm internal optical pathway quartz cuvette. It was background corrected by subtracting the solvent spectrum measured under the same experimental conditions. The absorption spectra obtained can be seen in the Figures 18 and 19 at the Chapter 6. The LA was collected before and after each TTS experiments to check if the sample was degraded during the experiments.

## 4.7 Steady-state Photoluminescence

We acquired the steady state emission spectra at room temperature using a Cary Eclipse spectrophotometer[3], with a white lamp excitation. The spectra were measured at 1000 V PMT voltage with excitation and emission slit-widths of 5 nm and averaging times of 0.9 s. The sample concentrations used were about 0.02 mM. We pump $N_2$ after preparing the sample to avoid $0_2$ dissolved in the solution during the measurements and, posteriorly, the formation of singlet oxygen. The photoluminescence (PL) was fundamental to help to understand the TTS data.

## 4.8 Raman

When a beam of light strikes matter, it can be absorbed, transmitted, reflected or even scattered. The electromagnetic interaction of light with the vibrational movement of

[2] The sources of errors are related to the inherent uncertainties of the instruments used and the possible slight misalignment during the execution of the experiment that may occur due to the lab climatic fluctuations (humidity and temperature).

[3] The measurements was done in the UV lab in the Chemistry Department from UFMG.

the nuclei that constitute the studied matter can give rise to Raman scattering. Raman is the inelastic scattering of electromagnetic radiation due to the vibration modes of the molecules that make up the studied sample. In the Raman scattering, monochromatic radiation in the visible, near-infrared or UV interacts with the molecule and is scattered with slightly modified frequencies. This variation of slightly modified frequencies corresponds to the variation of energy between two different vibrational levels. In order to have active Raman modes, there must be variation in the polarizability of the molecule during vibration. To identify the number of active Raman modes in a molecule, the properties of symmetry and group theory must be considered [109].

A oscillatory modulation in the 4TU and 4TT 2D pump-probe maps was identified, as it will be shown in the Chapter 6. Then, to verify that these oscillatory patterns came from molecular vibrational modes, Raman scattering measurements were performed. To perform the measurements, a Horiba T64000 spectrometer was used, which was configured to use a simple diffraction grid of 1800 grooves/mm and excitations were made with incident wavelengths: 488 nm, 514 nm, 568 nm, and 647 nm. The Ar-Kr laser (Coherent Innova 70C) was used to obtain these laser lines. Some results are shown in the sections 6.3 and 5.4.[4]

[4] The Raman measurements were performed using the Raman facilities of the Laboratório de Espectroscopia Raman, UFMG.

# 5 Samples characterization

In this chapter, we will present the steady-state measurements results that we used to characterize the samples that are the subject of this thesis. The techniques used here were: Linear absorption, Photoluminescence, and Raman, these results also support the transient transmission findings that will be present at the Chapter 6.

## 5.1 Samples details

The samples studies in this thesis are: thiouracils (TU), thiothymidines (TT), 2-thiocytosine (2TC) and the thiopurine 6-thioguanine (6TG). The thionucleobases from the thiouracil family, the 6TG and the 2TC were purchased from Sigma-Aldrich. The thiothymidines were purchased from Carbosynth. The purity of the purchased material and the details of the sample solutions used in the experiments can be found in the table 5.1. The sample concentrations were obtained from the measured linear absorption and the Lambert-Beer law.

| Sample | Purity | Hill Notation | Concentration (mM) | $\epsilon_{max}$ ($mM^{-1}cm^{-1}$) | $\lambda_{max}$ (nm) |
|---|---|---|---|---|---|
| 4TU | 97% | $C_4H_4N_2OS$ | 1.2 | 21.3 | 330 |
| 2TU | >99% | $C_4H_4N_2OS$ | 1.7 | 14.7 | 270 |
| 2,4dTU | 98% | $C_4H_4N_2S_2$ | 2.2 | 11.4 | 361 |
| 4TT | >98% | $C_10H_14N_2O_4S$ | 1.8 | 14.0 | 335 |
| 2TT | >95% | $C_10H_14N_2O_4S$ | 1.2 | 20.5 | 277 |
| 2TC | 97% | $C_4H_5N_3S$ | 1.4 | 17.9 | 270 |
| 6TG | 98% | $C_5H_5N_5S$ | 1.4 | 18.0 | 341 |

Table 1 – The concentrations used are the ones to obtain the absorbance as 0.5 OD for all the samples. The molar absorption ($\epsilon_{max}$) is for the maximum of the lowest energy band. And $\lambda_{max}$ is the wavelength of the maximum O.D. at the lowest energy band.

The solvent used was phosphate-buffered saline (PBS) solution. The PBS solution was prepared by dissolving 0.15 g of monosodium phosphate and 0.27 g of sodium disodium phosphate in 200 ml of ultrapure water thus obtaining a PBS solution at the 7.4 pH and 16 mM of concentration. Once the solvent was prepared, the samples were dissolved in the solution to obtain a maximum absorbance around 1 OD at the central wavelength of the pump beam when the probe beam was on the visible (350-630 nm) range. However, when the probe beam cover the UV range (240-340 nm) an absorbance of 0.5 OD was used since the probe beam was all absorbed by the solution for higher absorbance values.

## 5.2 Linear Absorption: results and discussion

The LA experimental results showing the absorbance for the 2TU, 4TU 24TU, 2TC, 2TT, 4TT and 6TG are shown in Figures 18 and 19.

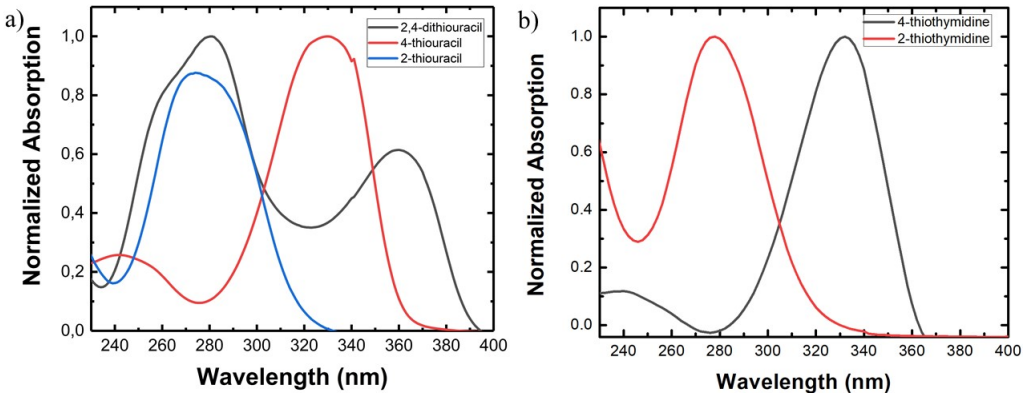



Figure 18 – (a) The thiouracils LA. (b) The thiothymidines LA.

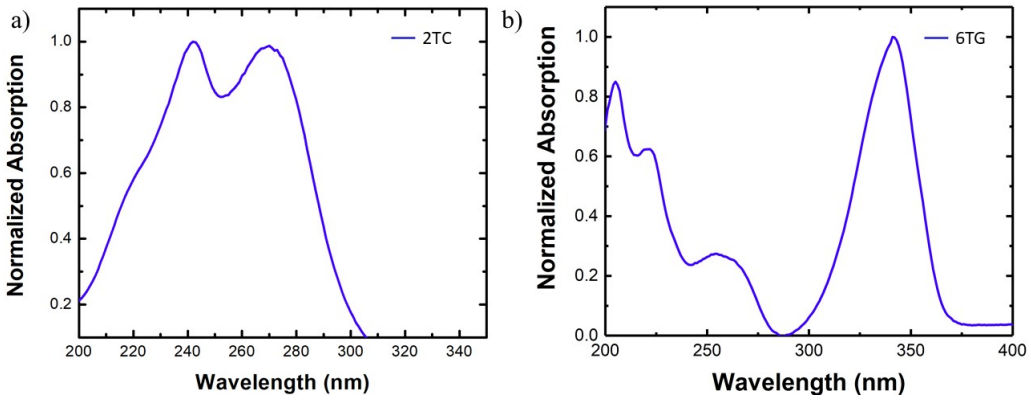



Figure 19 – (a) The 2TC LA. (b) The 6TG LA.

The replacement of the oxygen atom with the sulfur atom leads to important changes in the absorption spectrum of thiobases. There is a redshift of the absorption bands and the substitution also increases the thiobase molar absorption coefficient in a pH 7.4 solution [15].

The lowest energy absorption band of 6TG has a maximum at 341 nm (see Figure 19 b). Several studies [50, 110, 111] have pointed out that this band refers to the $S_0(\pi\pi^*) \rightarrow S_2(\pi\pi^*)$ transition. The comparison between the guanine canonical base with 6TG shows that the substitution of sulfur at the C6 position shifts the peak of the absorption band relative to the lowest energy state to the red by 92 nm [50]. There are others maxima around 256 nm and 203 nm with a shoulder about 220 nm. Semi-empirical [110, 112, 113], single reference [12, 46, 114] and multiconfigurational [111] calculations show that the lower transition absorption tail at the near-visible is related to a transition from $S_1(n\pi*)$ to the ground state.

For the thiopyrimidines the redshift is more pronounced when the oxygen atom is replaced by the sulfur atom at position C4 compared to position C2. Uracil, for example, has the lowest energy band absorption peak at 258 nm [71], but when oxygen is replaced by sulfur at the C2 position this peak shifts to 270 nm. Moreover while replacing oxygen with sulfur at position C4, the same peak shifts to 330 nm. Simultaneous sulfur substitution at positions C2 and C4 leads to even greater shift to 360 nm (see Figure 18 a). Similar behavior occurs for the thymidine-derived bases [71]: the derived bases 2TT and 4TT absorb respectively at 277 nm and 335 nm (see Figure 18 b). And finally, the cytosine canonical base thionation shifts the maximum of the lowest energy state from 266 nm to 270 nm [12].

The effect of the sulfur presence is related with the changes caused in the molecular bonds. The reason why thionation of purine as well as pyrimidine derivatives causes spectral absorption red shift is that the sulfur and carbon atoms bond is weaker than the oxygen and carbon atoms bound [115, 116]. This is justified by the fact that the atomic radius of sulfur (0.104 nm) is greater than the atomic radius of oxygen (0.066 nm). Therefore, due to Coulomb interaction, it is more difficult for the sulfur atom to be close to the carbon atom in a double bond compared to the oxygen atom, which leads to a lower binding energy between the sulfur atom and the atom of carbon.

However, it is not so clear why the lower energy level stabilization in the C2-substituted thiopyrimidine bases is so different from the lower energy level stabilization of the C4-substituted thiopyrimidine bases [12]. Bai and Barbatti [24] have suggested some possible explanations for this in the case of 2TT and 4TT. The lowest level of absorption band corresponds to the $\pi \rightarrow \pi^*$ transition. The $\pi \rightarrow \pi^*$ electronic transition occurs in LUMOs that have different electron density distribution for 2TT and 4TT. While the electronic density of the LUMO extends over the oxygen atom of the carbonyl group in 2TT, it extends over the sulfur atom for 4TT. Manae and Hazra [117] added the important information: the reason why the location of LUMO changes depend on where the replacement is made and of the types of electronic cloud relocation. One factor contributing to the electronic relocation is the conjugation of C4 = X (where X can be O or S) with C5 = C6. Another factor that influences is the size of the X atom: larger atoms (such as sulfur) contribute to the decrease in energy because the C = S bond is weaker than C = O. According to Manae and Hazra, in 2TT these two factors compete with each other, and is dominated by the former. In 4TT both relocations contribute to the significant redshift of the lower energy absorption band. Similar arguments are adopted for the thiouracil family [27].

## 5.3 PL results

In order to better understand the dynamics data, we performed steady-state photoluminescence in the samples prepared with the PBS solution at room temperature for the thiobases following the protocol described in section 4.7. We subtract the contribution from the solvent solution and fit the curve with the Extreme functions[1].

The 4TU PL spectrum (Figure 20 panel a), exciting the sample at 330 nm, shows two bands: one band peaking at 400 nm and another band peaking at 520 nm. This result is in agreement with the literature results, reported by Taras-Goslinska et al. [118] which assigned the first peak as due to photoluminescence from the bright singlet state. The second peak is associated by Taras-Goslinska et al. [118] as the phosphorescence. However, we did not observe any difference in the nitrogen presence or absence dissolved in the sample, as describe in the protocol in the Section 4.7. To clarify the second peak nature undoubtedly, the phosphorescence solved in time should be done. The result is also in good agreement with the pump-probe experiments, that will be shown in Chapter 6, since we observed a SE peaking at 400 nm (Figure 24 to be presented in the Chapter 6). It is also in agreement with the calculations.

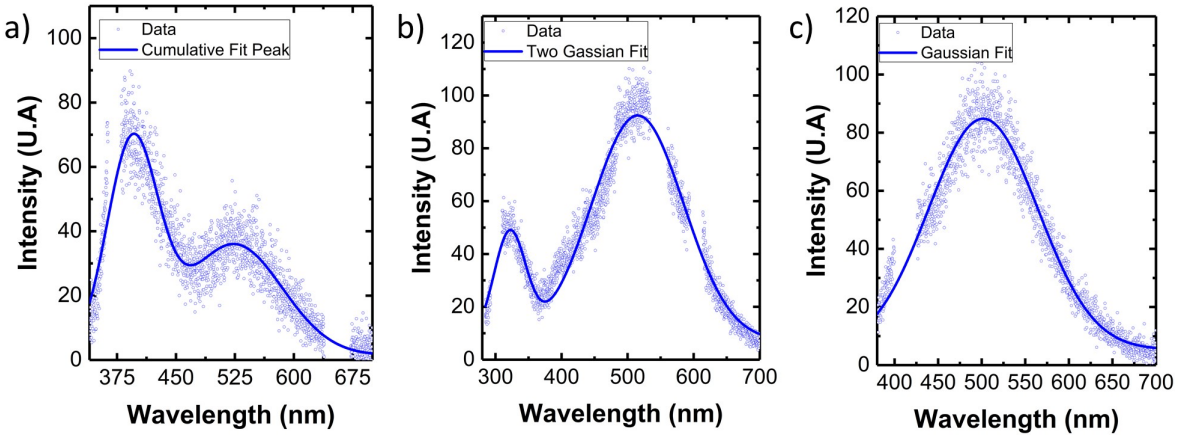



Figure 20 – Steady state PL: a) 4TU with pump at 330 nm; b) 24TU with pump at 275 nm; c) 24TU with pump at 330 nm;

The Figure 20 (panel b) shows the 24TU PL. By an excitation at 275 nm we observe a band from 300 nm to 360 nm (peaking at 320 nm) and another broadband that extends from 360 nm to 700 nm (peaking at 515 nm). They are in good agreement with the SE calculated values and the broad SE band obtained by the pump-probe experiments (Figure 24 to be presented in the Chapter 6). From the calculations, it was predicted emissions: at 370 nm and 385 nm from the Min $^1\pi\pi^{*'}(S4)$ and $^1\pi\pi^{*'}(S2)$, respectively (Figure 32 to be presented in the Chapter 6), which agree with the first PL band. Moreover,

[1] The Extreme function as function of $x$ has the following formula: $f(x) = c + Ae^{\left(-e^{(-z)}-z+1\right)}$, where $z = (x - x_c)/w$.

the calculations also predict SE at 449 nm (from $^1\pi\pi^*(S4)$) and at 538 nm (from $^1\pi\pi^*(S2)$) which agree with the second broad PL band. In the pump-probe experiments, we observed a broad SE in the short time scale at about 400-550 nm (Figure 24 to be presented in the Chapter 6). These results match the second broad PL band.

In the 24TU PL excited at 330 nm (Figure 20, panel c) we observe only one broadband peak that extends from 360 nm to 700 nm (peaking at 500 nm). That is also in agreement with the calculations (Figure 31 to be presented in the Chapter 6) and as well as the pump-probe experiments (Figure 24 to be presented in the Chapter 6) for the second broad PL band in the panel b. We have also tried to measured the 2TU PL. However, in the experimental spectral window we did not observe PL from 2TU. This is consistent with the fact that we also did not observe SE signal for 2TU (it will be shown in Chapter 6).

2TT PL measurements were also performed (Figure 21 a). We observe a weak signal with two bands: one at 350 nm and another at 450 nm. For the 4TT we obtained a peak at 420 nm in agreement also with the literature [40] (Figure 21 b). The 4TT result is qualitatively similar to the 4TU results.

In the 6TG measurements pumping at 340 nm we observe broadband that extends from 350 until 550 nm peaking around 410 nm (Figure 21 c). Some works also analyzed the steady-state emission. Reichardt et al. did not identify emission from 6TG within their spectrometer sensibility, but they mention about a photoproduct emission which the data was not present in the paper [46]. Zou et al. showed that at room temperature the photoluminescence is dominated by the photoproduct guanine-6-sulfonate [119]. Ashwood et al., in an emission measurement at 77 K in a tris buffer 7.4 pH matrix, observe two bands: one weak from 350 nm to 420 nm and another intense one from 430 nm to 550 nm. The intense one is assigned as the phosphorescence from the lowest-energy triplet state since it is quenched by the molecular oxygen at room temperature, it has a long lifetime and a significant redshift from the lowest energy absorption band. However, the weaker one is identified as the fluorescence emission [50]. As our data is at room temperature, we would expect a fill contribution from the phosphorescence emission. We interpreted our data (Figure 21 c) as the superposition from the photoproduct guanine-6-sulfonate luminescence mixed with the 6TG luminescence as predicted in the literature due the nicely agreements between the shape and the range of our curves and the ones reported by Zou et al. [119].

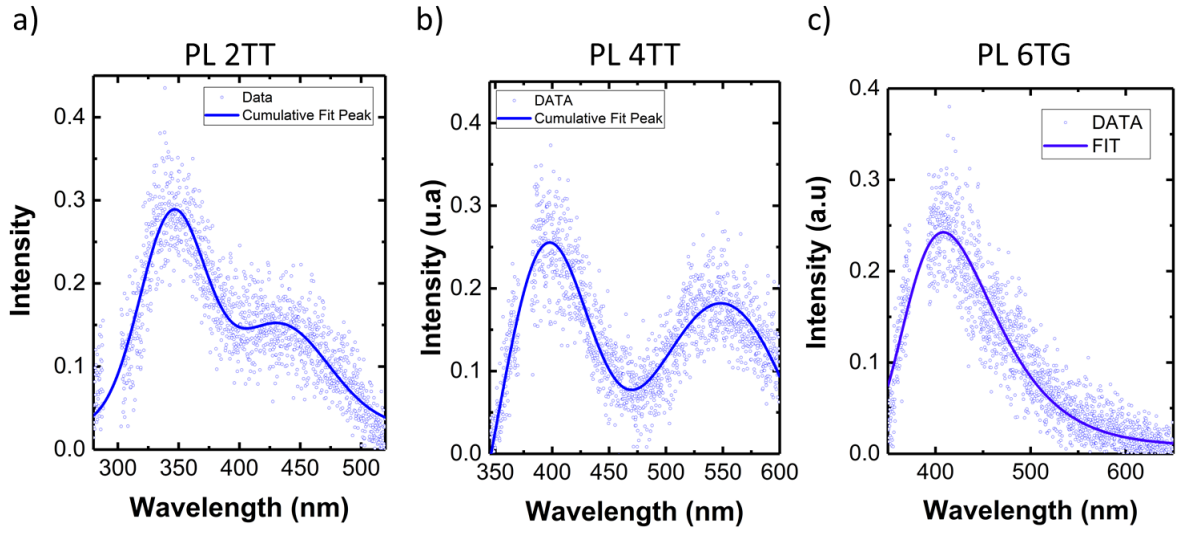



Figure 21 – (a) 2TT PL for excitation at 275 nm, (b) 4TT PL curve obtained for excitation at 330 nm. The first peak is the PL and the second one a phosphorescence, (c) 6TG photoluminescence spectrum pumping at 340 nm.

## 5.4 Raman results

We measured using the Raman technique the samples in different concentrations in quartz cuvettes of different sizes (5 mm and 1 mm) and with different incidence powers without success since there was a lot of noise due to the scattered light coming from the liquid and the low signal intensity. Therefore, for Raman measurements, a powder sample deposited on a glass slide and sealed by another slide identical to the first was used. We also use a 10x lens to focus the laser on the sample. The incidence of power was 1 mW. The integration time of 5 s during 10 accumulations was configured for each thiobase sample. Figure 22 shows some examples of measurements we obtained for some samples studied by pumping at 488 nm.

Measurements were made for all thiobase species studied in this thesis. We observed a pattern common to all of them, which is to present a mode close to 440 $cm^{-1}$ and another close to 700 $cm^{-1}$. In the case of 4TU, these modes are related to the breathing mode of the aromatic ring (440 $cm^{-1}$) and the mode of folding hydrogen atoms outside the molecular plane (700 $cm^{-1}$) [53, 120–127]. For the others, we imagine that there is a similar behavior. The modes could be the same for all states (fundamental or excited). The change is the coupling of the electronic cloud with each vibrational mode leaving the peak more or less intense. The discussion of the results from the perspective of the pump-probe data for the samples that we observed the oscillatory pattern was made in section 6.3.

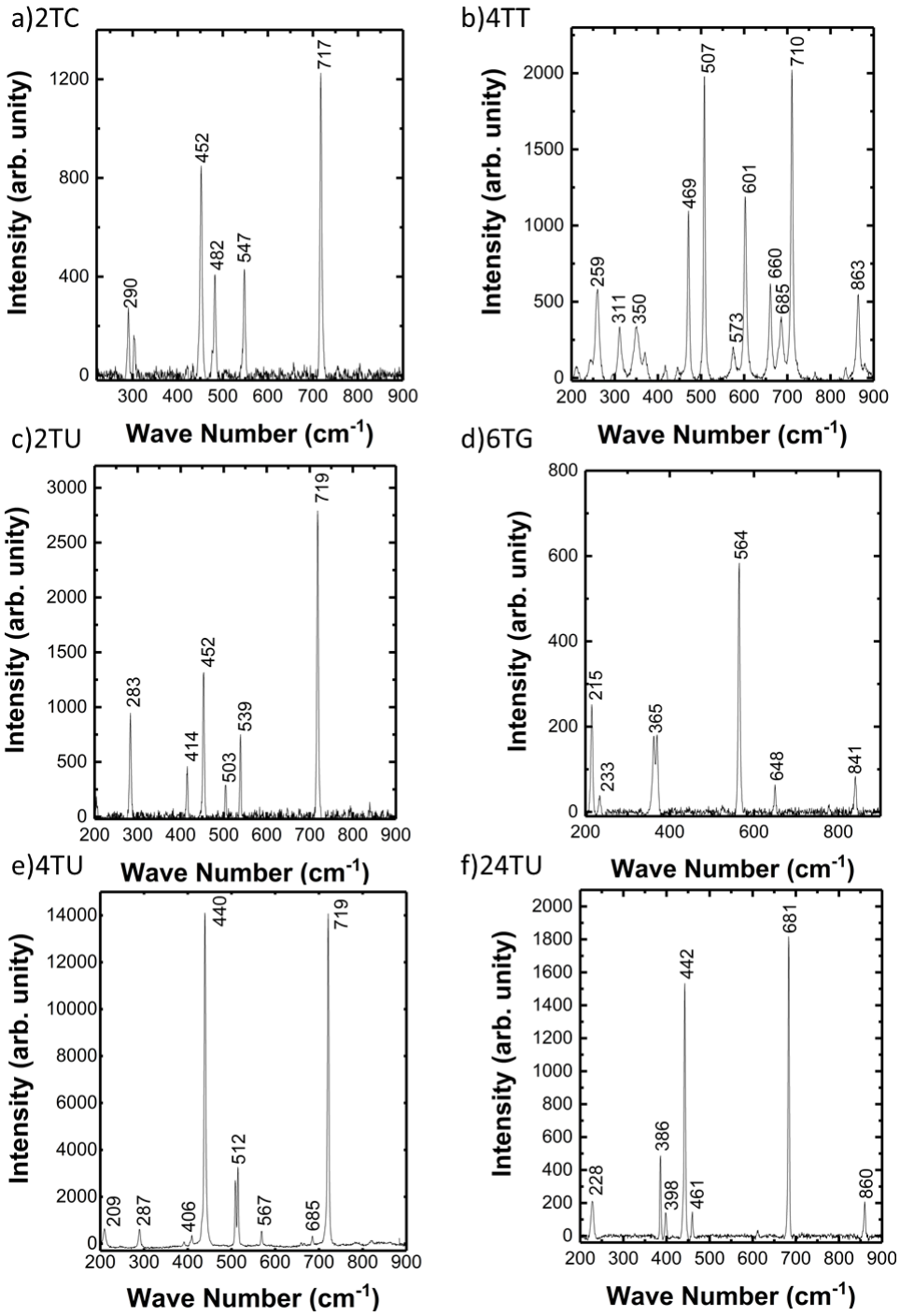



Figure 22 – Raman measurements for: (a) 2TC, (b) 4TT, (c) 2TU, (d) 6TG, (e) 4TU, (f) 24TU.

# 6 Sub-20 fs Transient Transmission Spectroscopy: results and discussions

For the TTS measurements, the pump energy was limited to 27 nJ (leading to about 340 $\mu$Jcm$^{-2}$ of fluency) to avoid sample photodamage (see appendix A) and solvated electrons generated by two-photon absorption from the solvent. A flowing jet configuration was employed (as shown the Figure 15). The sample was flown at a typical rate of 40 rpm. Experiments were performed for the following polarization configurations between the pump and probe beams: parallel, crossed and magic angle (for more information about the magic angle see the A.2). The polarization between the beams did not show any significant change in the short time scale dynamics.

## 6.1 Thiouracils

### 6.1.1 Overview

The thiouracils relaxation pathways and the time constants associated with the involved processes have been a matter of discussion recently [11, 20, 21, 23, 42, 128–130]. In those works, the authors use dynamic and static state of the art computation tool and experimental techniques, such as transient absorption spectroscopy, time-resolved photon-electron spectroscopy, Raman, and others, to characterize the TU dynamics from the excited state until the triplet manifold. Although the computations insights about the relaxation decay processes presented by the authors from the experimental results they could not extract the fastest time constants due to the limited 200-fs time resolution employed.

### 6.1.2 TU Results

The combination between the ultrafast sub-20 fs TTS; PL and Raman experiments with QM/MM calculations, enabled us to unravel for the first time the dynamics and decay relaxation mechanism of the 4TU, 2TU and 24TU [51–53, 131] that will be present in this section. The computational methods and simulations results that will be shown at this section were a kindly contribution of Irene Couti, Artur Nenov and Marco Garavelli from Marco Garavelli group (Dipartimento di Chimica Industriale, Università degli Studi di Bologna, Bologna in Italy), the theory collaborators in this work. On dynamics and statics studies they used hybrid quantum mechanics/molecular mechanics (QM/MM) state-of-the-art computational tools. For the 4TU sample, two-dimensional electronic

spectroscopy in the UV range (2DUV) measurements were also performed, the technique of which is described in the Appendix B. The 2DUV obtained results agree with the pump and probe data, but do not provide additional relevant information, thus they are not described in the main text.

For the TTS experiments, the samples were prepared following the protocol aforementioned (section 5.1). The 4TU was pumped with pulses centered around 330 nm, the 2TU was pumped with pulses centered around 275 nm and for the 24TU the experiments were done with the pump at both wavelengths.

The LA experimental spectrum for 2TU (Figure 23, panel c) features a single intense band peaking at 275 nm with a shoulder about 280 nm, the 4TU LA (panel b) is characterized by one peak at 330 nm and other at 240 nm and the 24TU LA (panel a) is composed of one peak around 280 nm and another around 360 nm as described in section 5.2. Spectral decomposition reveals a complex electronic structure consisting of two ( $^1\pi\pi^*(S_2)$ and $^1\pi\pi^{*'}(S_2)$), four ($^1\pi\pi^*(S_4)$, $^1\pi\pi^*(S_2)$ and $^1\pi\pi^{*'}(S_4)$, $^1\pi\pi^{*'}(S_2)$) and two ($^1\pi\pi^*(S_4)$ and $^1\pi\pi^{*'}(S_4)$) LA bright components for 2TU, 24TU and 4TU respectively, which contribute to the near- and mid-UV bands [51]. In a merely illustrative way, we plotted the experimental LA curves fitted by two (in the case of 2TU and 4TU) or four (in the case of 24TU) Gaussian peaks to represent the bright states. The pump pulse central wavelengths are represented by the dashed lines. Concerning 2TU it means that simultaneously the 2 bright states are excited due to their overlapping bands. Regarding the 4TU, only one state($^1\pi\pi^*(S_4)$) is populated by the sub-20 fs broadband pump pulse centered at 330 nm. And for the 24TU, two bright states are photoexcited by sub-20 fs broadband pulse centered at 275 nm ($^1\pi\pi^*(S_4)$, $^1\pi\pi^*(S_2)$) as well as two bright stated is photoexcited by sub-20 fs broadband pulse centered at 330 nm ($^1\pi\pi^{*'}(S_4)$, $^1\pi\pi^{*'}(S_2)$). And for 2TU two bright states are excited ($^1\pi\pi^*(S_2)$ and $^1\pi\pi^{*'}(S_2)$).

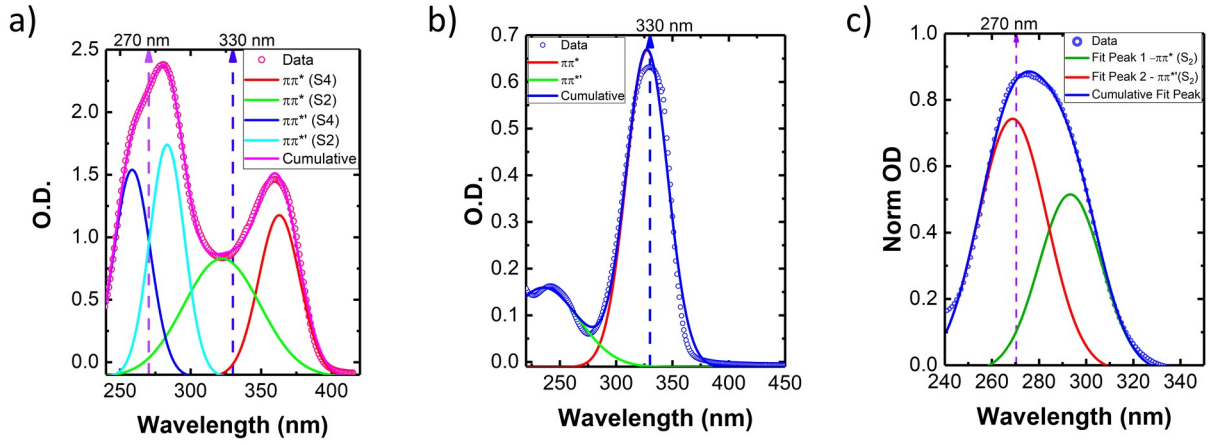



Figure 23 – Linear absorption data fitted with Gaussian curves for: a) 24TU; b) 4TU and c) 2TU.

The 2D TTS maps and the dynamics at selected time delays acquired employing sub-20 fs UV-pulses (details described at Chapter 4) are shown in Figure 24 and 25, respectively.

As it can be seen from the TTS experimental maps, the dynamics and the spectra at selected time delays (Figures: 24, 25 and 26, respectively) the sulfur-substituted uracils keep similar spectroscopy features. For the 4TU and the 24TU, just after the short pump pulses arrives, there is a positive signal assigned to the GSB (this peak at the 360 nm for the 24TU data and its tail appears at the same wavelength at the 4TU data) simultaneously with a SE band decay. The 24TU SE is broad (in the range from 400 nm until 550 nm) and the 4TU SE peaks at 400 nm. The GSB is associated with the depletion of the ground state after excitation to the bright singlet states. The SE is assigned to the emission from the minimum of the bright state photoexcited by the pump pulse as will be discussed in details later on. Afterward, the SE signal disappears and it gives place to a PA band formation. The PA bands are assigned to the negative signals in the range of 400-700 nm

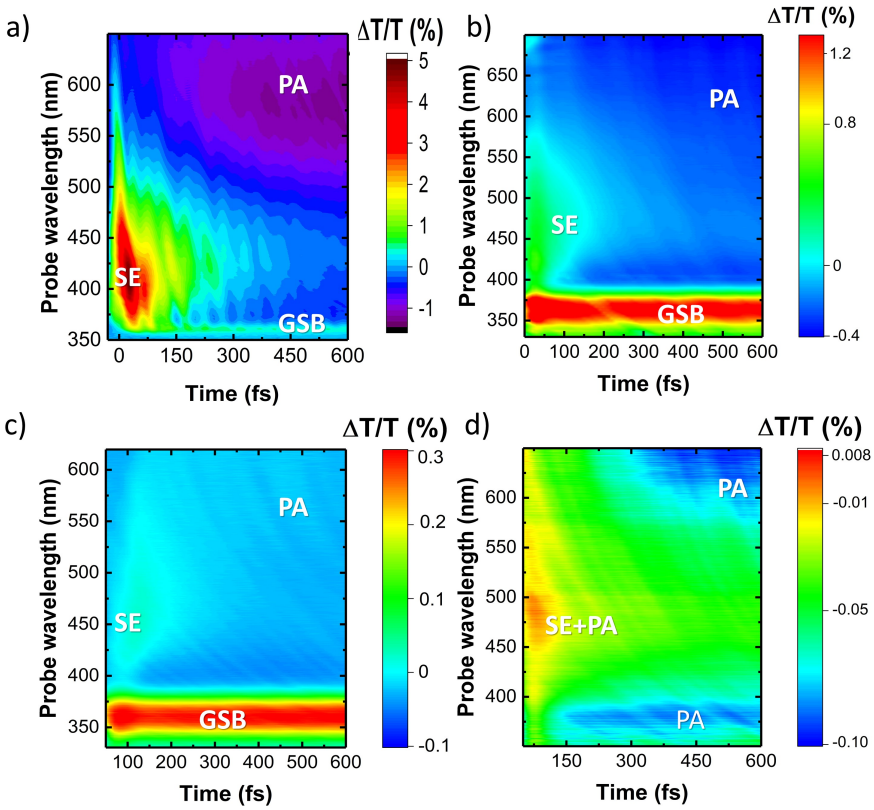



Figure 24 – 2D TTS results maps for: a) 4TU excited at 330 nm; b) 24TU excited at 330 nm; c) 24TU excited at 275 nm; d) 2TU excited at 275 nm. The maps display the probe wavelength as a function of the time delay between the pump and the probe pulses. The transient transmission intensities are represented by the colors in the scale bars. Colors close to red, means a positive signal that could be GSB and SE and colors close to the violet, means a negative signal that is PA.

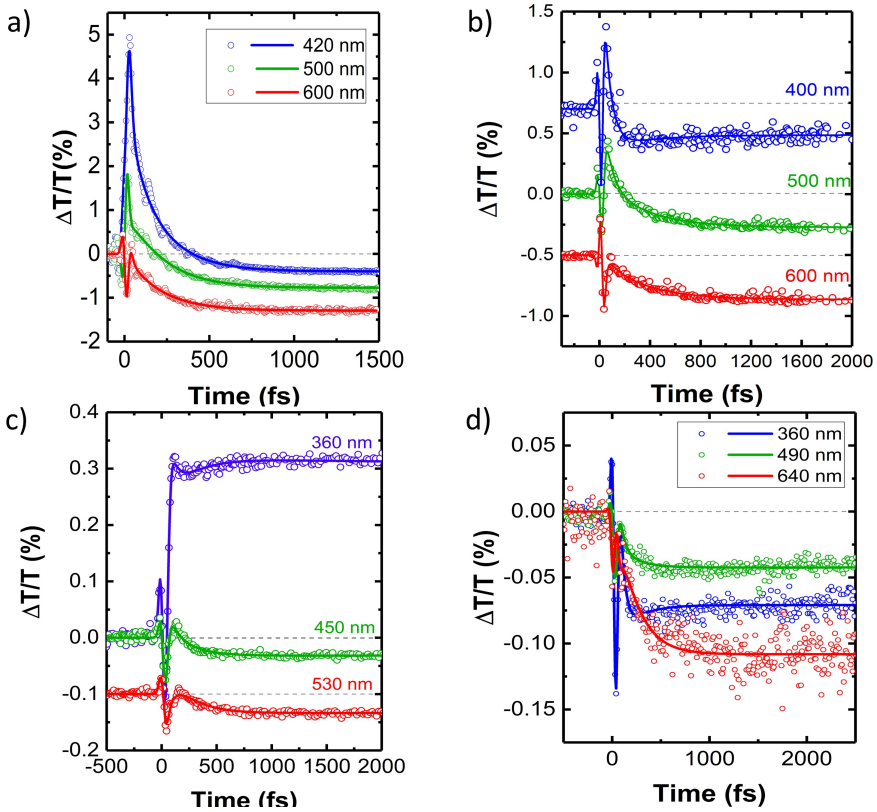



Figure 25 – TTS dynamics at selected wavelengths from: a) 4TU excited at 330 nm; b) 24TU excited at 330 nm (400 nm and 600 nm wavelengths are shifted by 0.75 and -0.5 respectively); c) 24TU excited at 275 nm (530 nm wavelength are shifted by -0.1); d) 2TU excited at 275 nm.

and 380-700 nm for the 24TU and the 4TU, respectively. According to previous thiouracils studies [11], with 200 fs time resolution, the increasing of PA about 600 nm comes from the triplet manifold and is a fingerprint of the ISC process.

For the 2TU, the GSB signal was not identified when probing in the visible range, but it could be seen for the probe in the UV range (Figure 27, panel d). For the probe in the visible, the PA signal was identified (Figure 24, panel b), particularly it is possible to see the formation of two PA bands: one in the UV (350-450 nm) and another in the visible (400-650 nm) range. In between these two bands, about 450 to 550 nm there is a dip in the signal which could be due to a superposition of the PA and a SE, as it is pointed out by the global analysis (positive signal in the black curve, Figure 28) and the calculation results that will be discussed later on.

To extract the decay times, we perform the data global analysis following the procedures describe in section 4.5. Figure 28 shows the obtained EAS results.

For the 4TU, the EAS presents two time constants: 76±16 fs (black curve) and 225±30 fs (red curve) and an offset (blue curve) that account for any phenomena happening out of the observable temporal window (Figure 28, panel a). The time constant of 76±16 fs

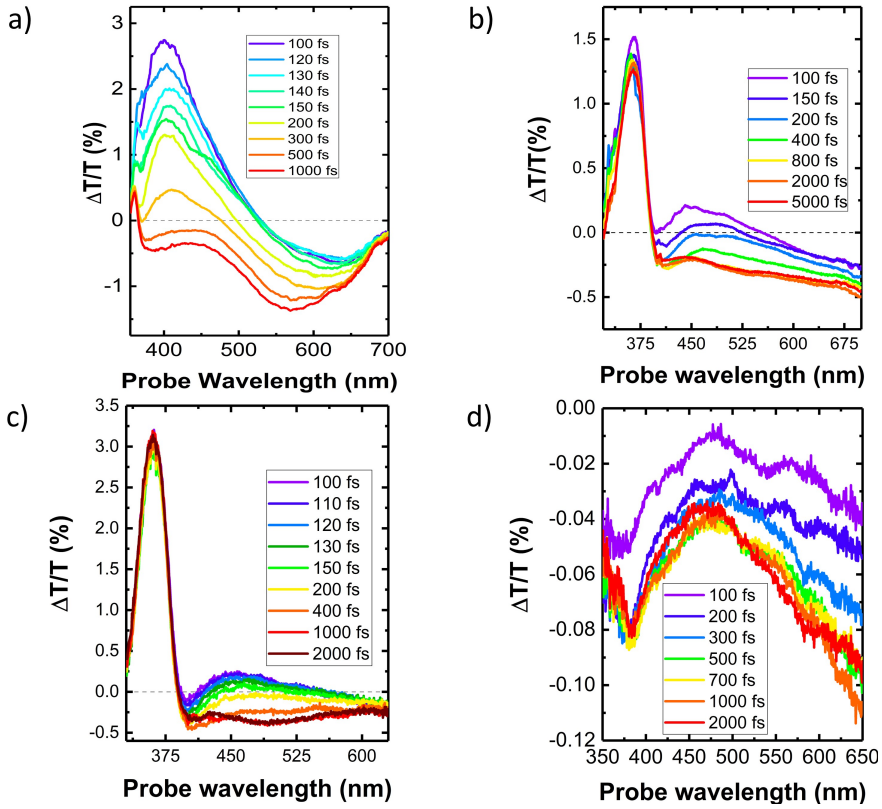



Figure 26 – TTS spectra at selected wavelengths, probing in the visible range, for: a) 4TU excited at 330 nm; b) 24TU excited at 330 nm; c) 24TU excited at 270 nm; d) 2TU excited at 270 nm.

is the SE band decay from the only one accessible bright state (23). The time constant of 225 fs at the ESA shows a negative band around 600 nm which is related to the triplet state PA band formation. The positive signal at the remaining spectral range would be due to a small part of the population unable to reach the CI seam, that remains in $^1\pi\pi^*(S_4)$ for a longer time, giving rise to a residual SE signal [53]. The offset is related to the long lifetime triplet state. This data shows clearly that the mismatch between the time constants related to the triplet PA band formation and the SE band decay from the photoexcited state is an evidence that the triplet state population is mediated by a dark intermediate state that works as a doorway to the triplet manifold as it was predicted by many theoretical studies for other thiobases [25, 41, 44, 45, 47, 128, 129, 132]. The 76±16 fs time constant shows a really good agreement with the 67.5 fs theoretical value found by *ab initio* calculation [53] as well as the 225±30 fs time constant that is in conformity with the 240 fs value obtained by Pollum et. al [11].

The proposed mechanism for 4TU is the following: the $^1\pi\pi^*(S_4)$ state is pumped at FC region, afterward, the populations are ballistically driven to the dark singlet state ($^1n\pi^*(S_4)$) by a CI. At an equilibrium situation, the energy gap that separates the states $^1\pi\pi^*(S_4)$ and $^1n\pi^*(S_4)$ is 1 eV. Due to vibrational modes (that are going to be discussed later on) the IC process is facilitated. The transition to the dark singlet

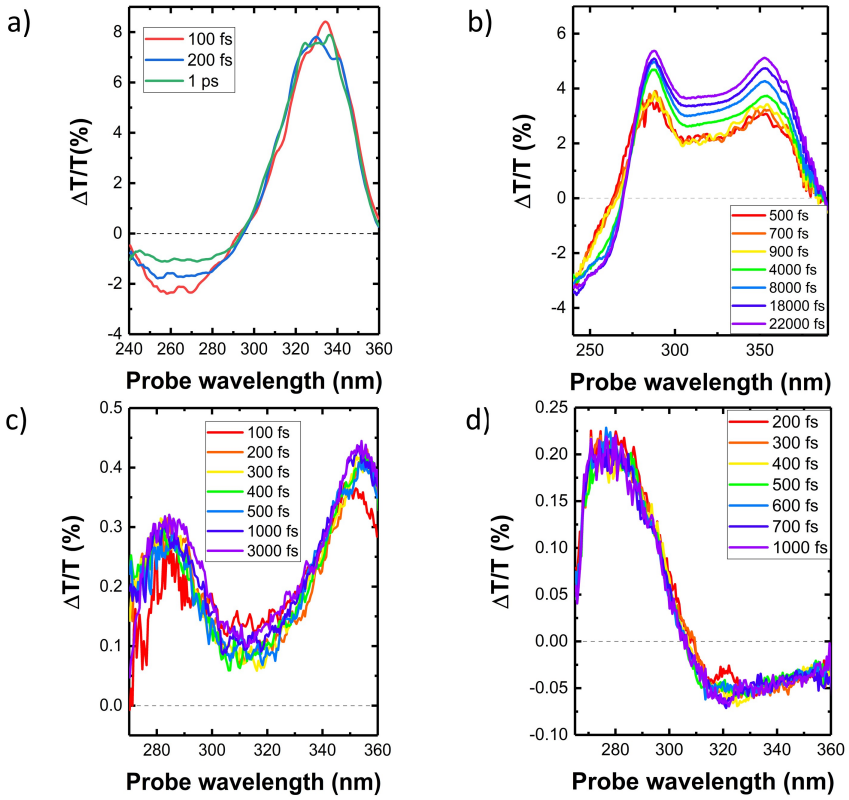



Figure 27 – TTS spectra at selected wavelengths, probing in the UV range, for: a) 4TU pump at 330 nm; b) 24TU pump 330 nm; c) 24TU pump at 270 nm; d) 2TU pump at 270 nm.

state is also facilitated due to the fact that $^1\pi\pi^*(S_4)$, $^3n\pi^*(S_4)$ and $^3\pi\pi^*(S_4)$ minima are almost isoenergetic. The main relaxation process is $^1\pi\pi^*(S_4) \longrightarrow^1 n\pi^*(S_4) \longrightarrow^3 \pi\pi^*(S_4)$. However, we do not discard a second decay: $^1\pi\pi^*(S_4) \longrightarrow^3 n\pi^*(S_4) \longrightarrow^3 \pi\pi^*(S_4)$, path with a minority population involved (13-25%). This decay path is indicated by the dashed arrow in Figure 29.

For 2TU, from the global analysis, we extracted the time constants of 187±16 fs (black curve, Figure 28 panel d) and an offset (red curve). The Figure 30 shows the 2TU system relaxation paths. From the ground state, the $^1\pi\pi^{*'}(S_2)$ (panel a) and S2 $^1\pi\pi^*(S_2)$ (panel b) states can be populated and hence two different deactivation courses can be followed.

The spectra assignments to the $^1\pi\pi^*(S_2)$ route are the PA (negative) between 300 and 380 nm (Figures 24 and 28) matching with the probe absorption calculated values, documented by the blue arrows (Figure 30). At long lifetimes, EAS red line, the negative PA signal could be addressed to the lowest $^3\pi\pi^*(S_2)$ triplet minima population, (calculated PA energy values at the blue arrows at the Figure 30).

In summary, the system relaxes to the $^1\pi\pi^*(S_2)$ minimum, Min $^1\pi\pi^*(S_2)$, then due to the fact that Min $^1\pi\pi^*(S_2)$, and Min $^1n\pi^*(S_2)$ and Min $^3n\pi^*(S_2)$ have similar

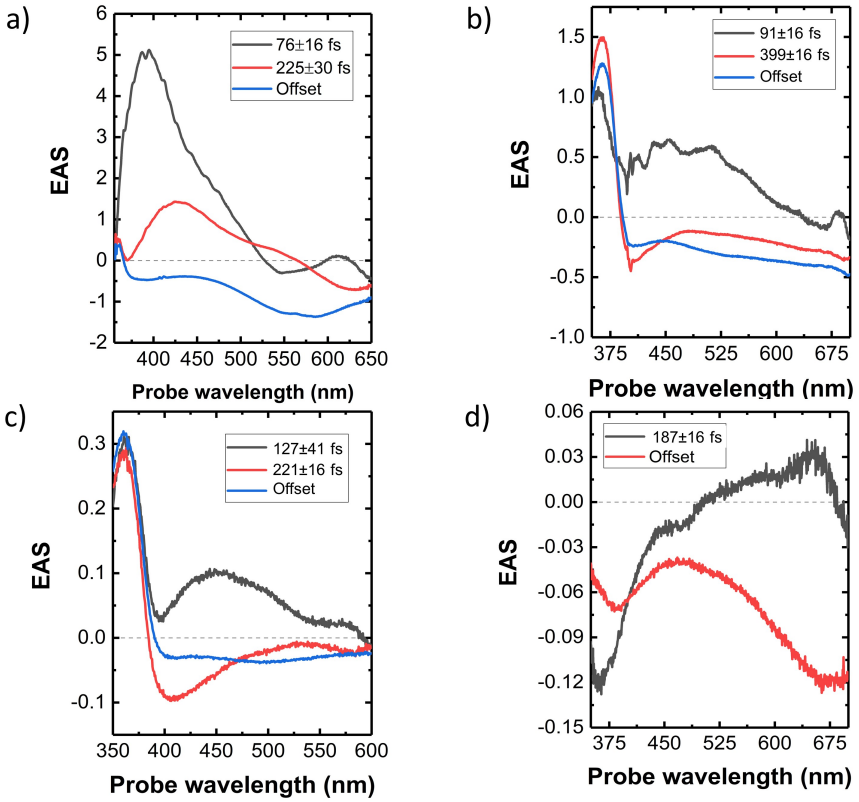



Figure 28 – EAS obtained by global analysis for: a) 4TU excited at 330 nm; b) 24TU excited at 330 nm; c) 24TU excited at 270 nm; d) 2TU excited at 270 nm.

energies [51] there is an exchange of the population between these three different minima that leads to a simultaneous population of the three states at time scale of 187±16 fs.

The $^1\pi\pi^{*'}(S_2)$ decay path (Figure 30 panel a) starts at energy higher than $^1\pi\pi^*(S_2)$. It has a small barrier to reach the $^1\pi\pi^{*'}(S_2)/^1n\pi^{*'}(S_2)$ CI, which involves also a molecular distortion that could, in part, enlarge the $^1\pi\pi^{*'}(S_2)$ depopulation lifetime, to the order of the reported 187±16 fs lifetime. From the Min $^1\pi\pi^{*'}(S_2)$ the system could directly populate the $^3n\pi^{*'}(S_2)$ or the $^1n\pi^{*'}(S_2)$ states. The prove of the $^1\pi\pi^{*'}(S_2)$ decay path depopulation came from the positive PA signal at around 350 nm matching with the $^3\pi\pi^{*'}(S_2)$ triplet minimum. So, our results give evidence of the population of both the decay paths, starting from the $^1\pi\pi^{*'}(S_2)$ or $^1\pi\pi^*(S_2)$ states, respectively. Even though the $^1\pi\pi^{*'}(S_2)$ and the $^1\pi\pi^*(S_2)$ decay paths present processes with different rates and molecular distortions, they both could relax to the triplet manifold directly or mediated by a dark singlet state.

For the 24TU, after the broadband 330 nm centered sub-20-fs pump pulse excitation there are mainly two populated decay paths as shown in Figure 31: the $^1\pi\pi^*(S_2)$ state at panel b and the $^1\pi\pi^*(S_4)$ at the panel a. The $^1\pi\pi^*(S_2)$ decays to the $^1\pi\pi^*(S_2)$ minimum (Min $^1\pi\pi^*(S_2)$) from where the calculated emission is at the 538 nm which matches well with the SE positive signal of EAS at 91±23 fs lifetime (Figure 28). Part of the SE from

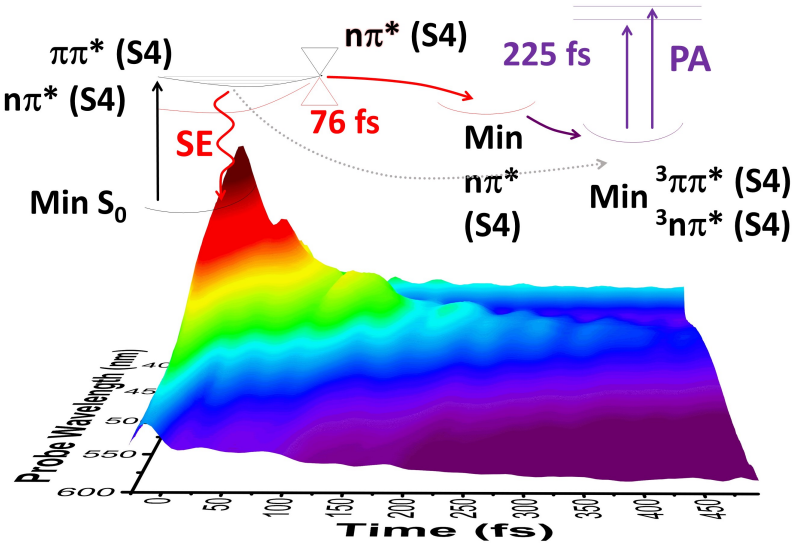



Figure 29 – Proposed relaxation mechanism for 4TU and the transient transmission spectra plotted as a 3D map.

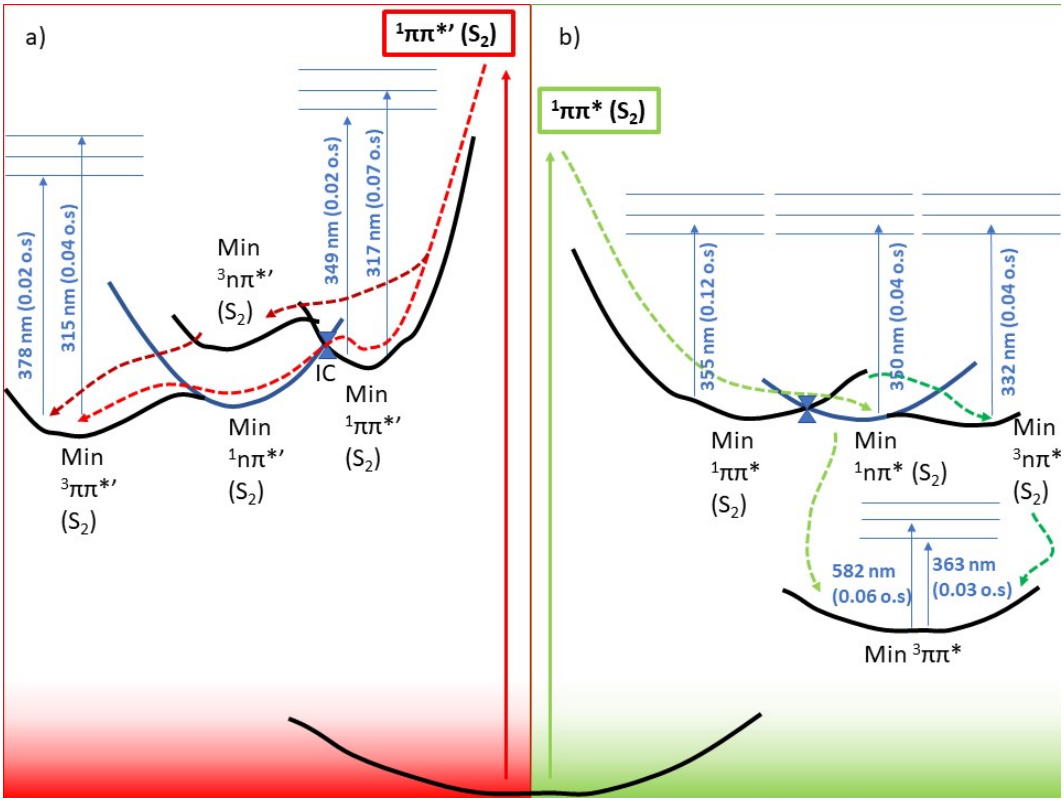



Figure 30 – Sketch illustrating the 2TU relaxation mechanisms.

the Min $^1\pi\pi^*(S_2)$ survives also at the 399±45 fs lifetime (24), indicating that the excited population stays in this minimum. This is confirmed by the red PA negative dip at the 399 fs lifetime curve, at around 330-450 nm, matching with the calculated PA from the Min $^1\pi\pi^*(S_2)$ (blue arrows in figure 30 panel b). Strikingly, at longer wavelengths (above 550 nm), the EAS red line profile is roughly resembling the blue line at the offset. It means that there are the partial population of the lowest triplet state $^3\pi\pi^*(S_2)$ at a few hundred fs timescale. The Min $^1\pi\pi^*(S_2)$, Min $^1n\pi^*(S_2)$, $^3n\pi^*(S_2)$ and $^3\pi\pi^*(S_2)$ have a pronounced structural and energetic likeness suggesting the continuous exchange of population between all four states, in a similar way we documented for the 2TU $^1\pi\pi^*(S_2)$ state profile. This means that populating the Min $^1\pi\pi^*(S_2)$, simultaneously are populated also the other three minima, of singlet and triplet nature. This leads to an exchanging population between them, and then a longer lifetime of the involved states, which altogether contributes to the PA negative signals observed at 435 fs lifetime (Figure 28). Their PA calculated values justify these PA positive signals (between 400-450 nm and over 550 nm, Figure 31 panel b). The blue curve of the EAS is mainly composed of the PA coming from the long-living lowest triplet states ($^3\pi\pi^*(S_2)$ and $^3\pi\pi^*(S_4)$). Concerning the simultaneous decay path of the $^1\pi\pi^*(S_4)$ state (Figure 31 panel a) the SE signal in the EAS (positive part of the black curve), is addressed to the $^1\pi\pi^*(S_4)$, peaking at around 450 nm. It means that 91±23 fs is exactly the lifetime of the Min $^1\pi\pi^*(S_4)$ population, which suddenly crosses the $^1n\pi^*(S_4)$ and $^3n\pi^*(S_4)$ along a barrierless path and without any molecular distortion. We note the evident similarities for the decay mechanism of the $^1\pi\pi^*(S_4)$ state in 4TU, for the lifetime of 76 fs associated with a barrierless decay in a planar ring geometry: $^1\pi\pi^*(S_4) \longrightarrow^1 n\pi^*(S_4) \longrightarrow^3 \pi\pi^*(S_4)$.

When exciting the 24TU at 270 nm, two more simultaneous brights $^1\pi\pi^*$ states could be populated: $^1\pi\pi^{*'}(S2)$ (Figure 32 panel b) and $^1\pi\pi^{*'}(S4)$ (Figure 32 panel a). Global analysis reveals again two time constants: 127±41 fs (black) and 221±16 fs (red) plus also a long-lived product (blue curve) in the Figure 28 panel c. Overall, the EASs resemble their counterparts obtained from the global analysis of the 330 nm pump data. The resemblance between the 221±16 fs and 399±45 fs EAS curves suggests that after departure from the initially populated $^1\pi\pi^{*'}(S2)$ and $^1\pi\pi^{*'}(S4)$ states the system follows a dynamic similar to the one observed after pumping at 330 nm, in agreement with the Kasha's rule [133].

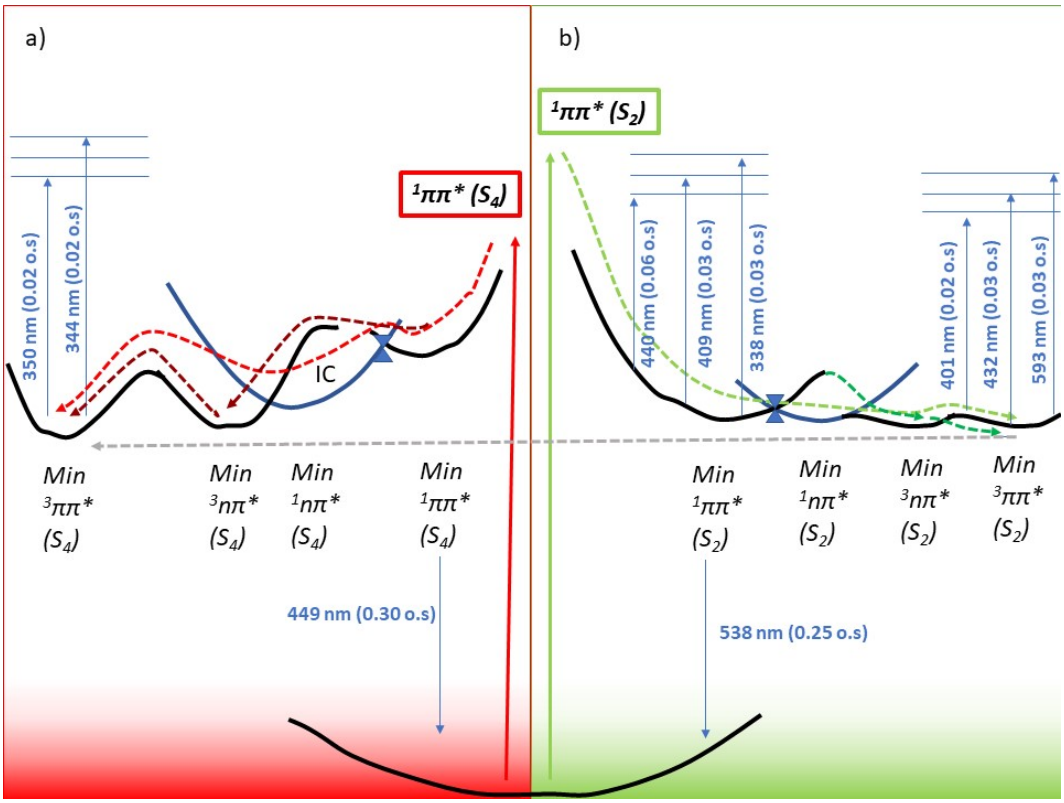



Figure 31 – Proposed relaxation mechanism for the 24TU after excitation with 20 fs pulses centered at 330 nm.

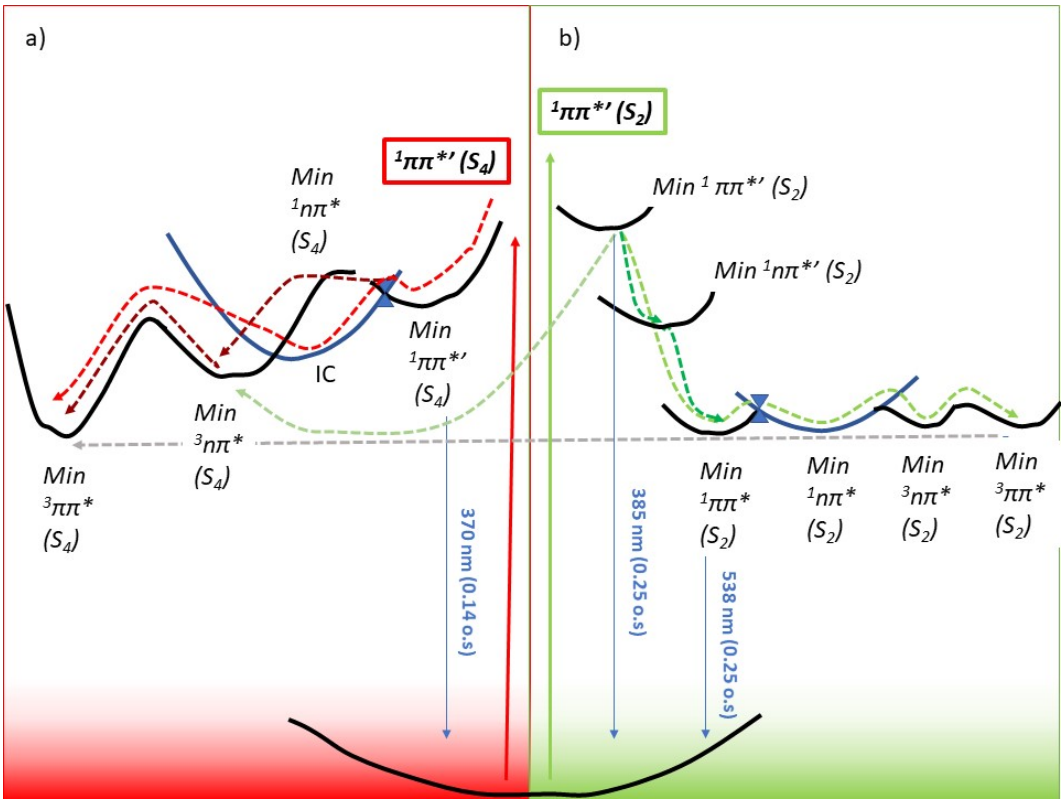



Figure 32 – Proposed relaxation mechanism for the 24TU after excitation with 20 fs pulses centered at 270 nm.

## 6.2 Thiothymidines

### 6.2.1 Overview

The 4TT relaxation pathway to the triplet manifold have been extensively studied, especially after Harada *et al.* TAS [134] experiments presented triplet state formation in less than 10 ps. They also proposed that the deactivation mechanism is by $S_1(^1n\pi^*) \rightarrow T_1(^3\pi\pi^*)$ transition for 4TT in acetonitrile solution [135]. Reichardt and Crespo-Hernandez [47], combining quantum chemical calculation and femtosecond broadband TAS have shown that the triplet state started to be populated in 240 fs. Moreover, they identified a PL at 430 nm and a phosphorescence at 542 nm which are in complete agreement with our result (see Figure 21 b presented in the Chapter 5). In 2014, Cui and Thiel [136] using QM/MM calculations identified three equally possible pathways: (i) $S_2(\pi\pi^*) \longrightarrow S_1(n\pi^*) \longrightarrow T_1(\pi\pi^*)$ (ii) $S_2(\pi\pi^*) \longrightarrow T_2(n\pi^*) \longrightarrow T_1(\pi\pi^*)$ (iii) $S_2(\pi\pi^*) \longrightarrow T_1(\pi\pi^*)$. Only the first path decay comprises with the Kasha's rule [133] and the last one involves vibronic coupling and a large SOC enabling a direct transition to the triplet manifold. Later, Martínez-Fernández and co-workers [40] identified, using molecular simulations, that the $S_2(\pi\pi^*)$ exhibit markedly two different geometries: one twist and other planar conformation. They also identified that all trajectories show oscillatory motion which allows the molecule to explore both $S_2(\pi\pi^*)$ geometries.

For 2TT, the timescale for the triplet state formation was identified to happens at 410±60 fs [31]. From static calculations, Cui and Fang [44] proposed three pathways to the population relaxation: (i) $S_2(\pi\pi^*) \longrightarrow S_1(n\pi^*) \longrightarrow T_1(\pi\pi^*)$; (ii) $S_2(\pi\pi^*) \longrightarrow T_2(n\pi^*) \longrightarrow T_1(\pi\pi^*)$; (iii)$S_2(\pi\pi^*) \longrightarrow T_3(n\pi^*) \longrightarrow T_2(n\pi^*) \longrightarrow T_1(\pi\pi^*)$. Later, the evidence of the singlet state as a doorway to the triplet state population has been also found with TAS 200-fs time resolution experiments [130].

### 6.2.2 TT Results

The 4TT and 2TT relaxation pathways to the triplet manifold have never been studied before with sub-20 fs broadband pulses in the UV. Thus, our experimental data with high temporal resolution would be a key to understand more details about TT mechanisms. In this section, we will show the 4TT and 2TT results.

We characterize the 2TT dynamics pumping at 270 nm and probing in the visible (Figure 33) and in the UV (Figure 34) range with sub-20-fs pump pulses. We observe negative signals that are assigned as PAs, as is shown at the TT 2D map (Figure 33, panel a), the spectra (Figure 33, panel b) and the dynamics for at selected wavelengths (Figure 35, panel b).

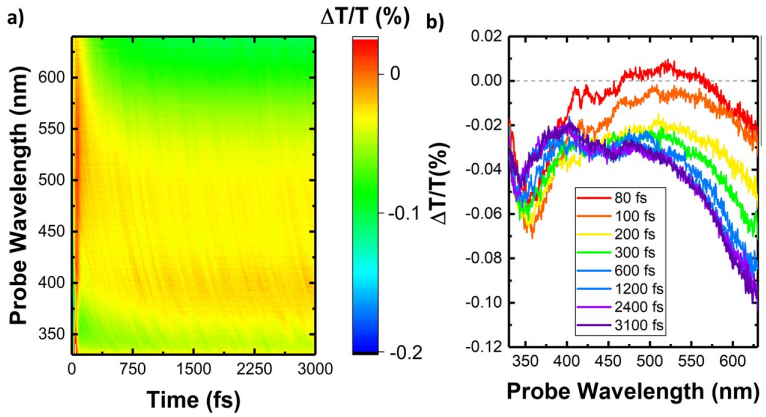



Figure 33 – (a) 2TT 2D map: probe wavelength as function of the delay time between pump and probe, (b) The 2TT spectra at selected time delay.

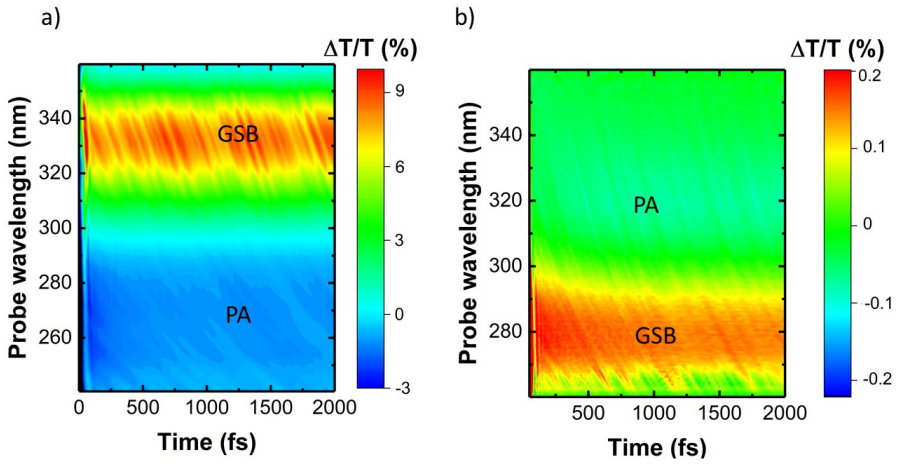



Figure 34 – TTS 2D map for the probe in the UV 2D map. Probe wavelengths as function of the delay time between pump and probe. a) 4TT and b) 2TT.

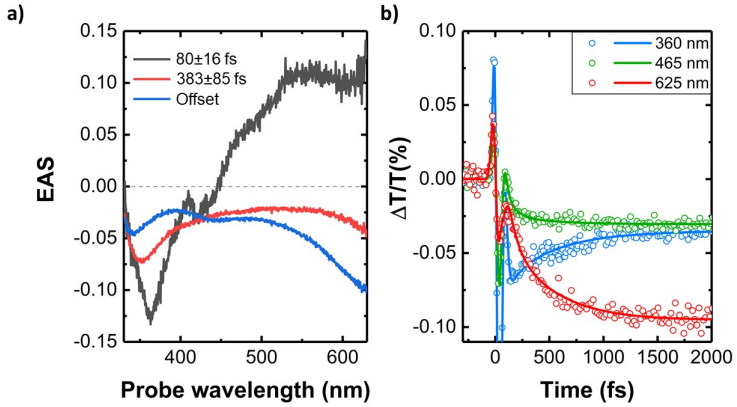



Figure 35 – TTS for 2TT: (a) EAS (b) Dynamics at selected probe wavelengths.

A global analysis of the 2TT data (Figure 35 a) provides us with two time constants: 80±16 fs and 383±85 fs, and a terminal decay. The 383±85 fs time constant is the same value, within the uncertain range, that Pollum et al. [31] obtained from TAS but with 200 fs time resolution measurements. It was associated with the ISC process to the triplet manifold. Therefore, the time constant of 80±16 fs is due to a process that comes before the triplet state population. It could be the transition to the dark singlet state and then to the triplet manifold, as it was previously predicted by Pollum and Crespo-Hernández [130]. Therefore, this experiment provides us for the first time the observation of the 2TT bright singlet state lifetime (Figure 38b).

From the 2D map (Figure 36 a) obtained by the TTS experiments after 330 nm excitation for the 4TT PBS solution, we can clearly identify three signals: the positive long time decay one at 370 nm is the GSB, the positive broader signal around 430 nm is the SE and a negative signal at about 600 nm that is related to the PA from the triplet state. The GSB is related to the depletion of the ground state after excitation of $S_2(\pi\pi^*)$ and it agrees with the linear absorption spectrum which shows the main absorption peak at 330 nm (also seen in figure 34 a). The Figure 36 panel b shows the TTS for selected delays between the pump and probe, where is also possible to identify those signals.

The Figure 37 presents the dynamics at selected probe wavelengths (panel a) and the EAS extracted from the global analysis (panel b). The EAS shows that the data are globally fitted with two time constants: 85±16 fs (black curve) and 243±16 fs (red curve), a terminal decay (blue curve) and one offset. The shortest time constant is also very close to the value obtained for 4TU [53]. The calculations from Martinez-Fernandez et al. [40] showed that the $S_2(\pi\pi^*)$ min has a significant absorption signal between 450-570 nm which matches with the negative signal at this range in the EAS curve. It indicates that the black curve represents the $S_2(\pi\pi^*)$ species. Therefore, the peak at 430 nm in the black curve is the SE from the $S_2(\pi\pi^*)$ state minimum. This is confirmed by the PL experiments, which obtained a peak at 420 nm in agreement also with the literature [40] (Figure 21 presented at the Chapter 5 b). The red curve in the EAS (244 fs time constant) is the time for the triplet state formation [31]. The time constant about 240 fs was also obtained by Pollum and co-workers at experiments with 200-fs pulses [31]. The blue line is the triplet product absorption.

From our experiments, we could determine that the fastest time constant is related to the $S_2(\pi\pi^*)$ depopulation. Due to the mismatch between the triplet formation and the $S_2(\pi\pi^*)$ depopulation we can say that a dark state works as a doorway to the triplet manifold as Martinez et al. and Cui et al. predicted (see the Figure 38).

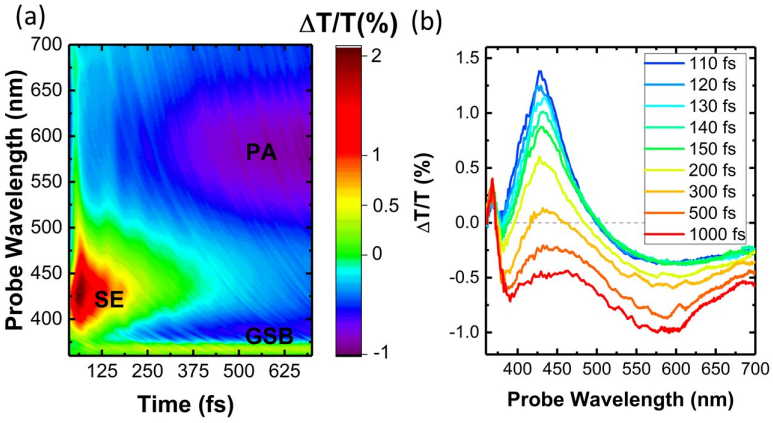



Figure 36 – (a) 2D map for 4TT: probe wavelength as function of the delay time between pump and probe, (b) Spectrum at selected time delay.

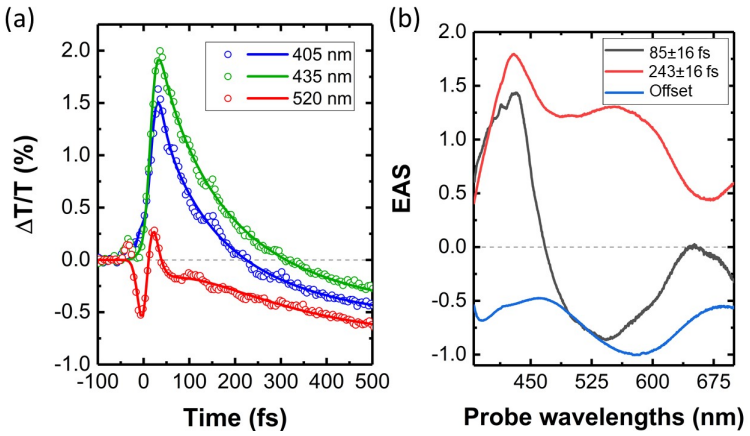



Figure 37 – (a) Dynamics at selected probe wavelengths (b) EAS.

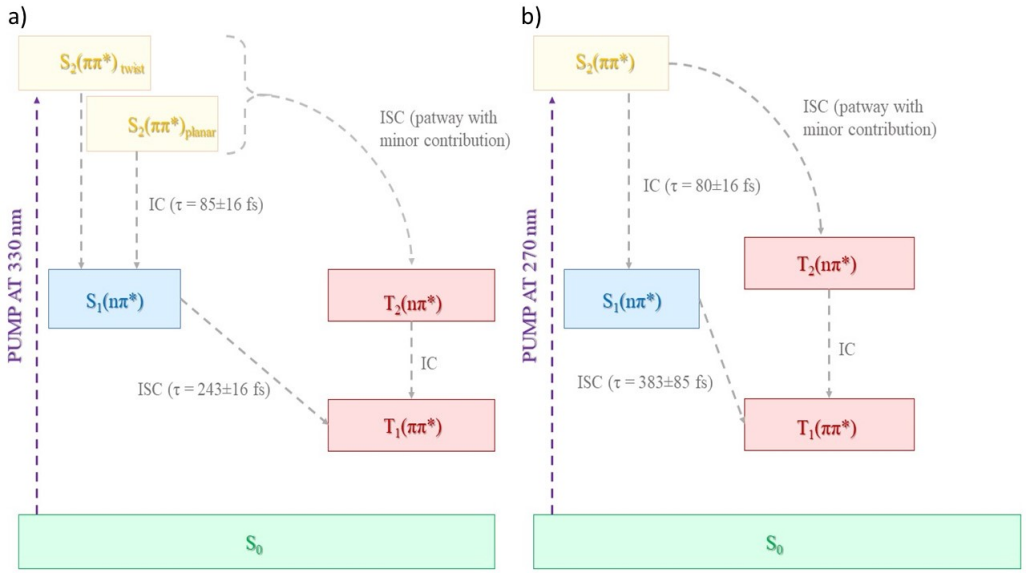



Figure 38 – The main energy relaxation pathway to the triplet states inferred from the literature with the time constants obtained from our TTS data: a) 4TT; b) 2TT.

## 6.3 Coherent Oscillation

The 4TU and 4TT dynamics are modulated by an oscillatory pattern as it can be clearly seen in the Figure 25 (panel a) and Figure 37 (panel a), respectively. This modulation had not yet been reported in the literature. It is a fingerprint of vibrational coherence that is impulsively excited by sub-20-fs pulses, which have been used to study this system. We observe a fast decay of the over-damp oscillation amplitude which is associated with low-frequency modes responsible for the homogeneous broadening of the signal. From the TTS 2D map, after the chirp correction (it was presented at the Chapter 3) and the subtracted exponential signal decay, we perform a Fourier Transform (FT) to obtain the oscillations modes.

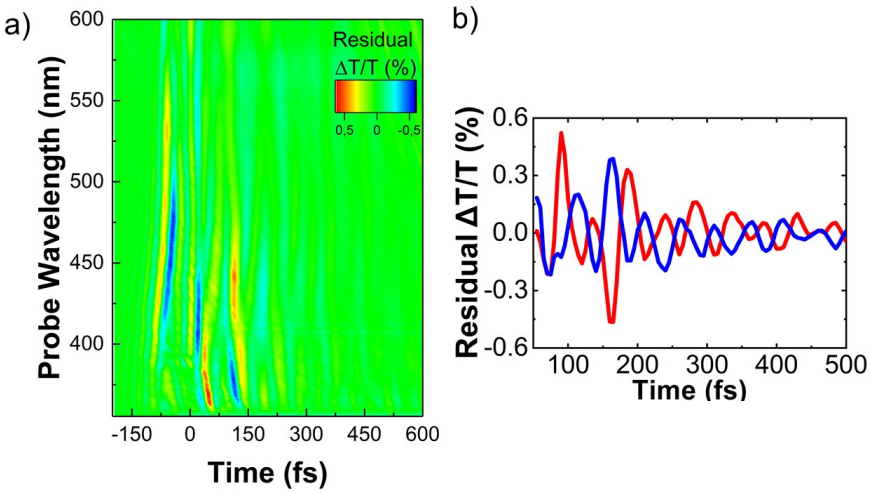



Figure 39 – a) 4TU residue matrix map. b) spectra at the wavelength 380 nm (red) and at the wavelength 450 nm (blue) in the residue matrix map.

The Figure 39 shows the 4TU results after the chirp correction and the subtraction of the exponential decay signal decay for all probe wavelengths while the Figure 40 presents the FT results. By performing a FT on the 2D map, Figure 40 (panel a), it is possible to identify at least two main oscillation frequencies: 400 $cm^{-1}$ and 680 $cm^{-1}$. However, by simulations [53] three vibrational modes were found: 457 $cm^{-1}$, 697 $cm^{-1}$, and 784 $cm^{-1}$. The first one (457 $cm^{-1}$) is due to the ring breathing mode which is in agreement with the experimental value found, while the last two (697 $cm^{-1}$ and 784 $cm^{-1}$) are due to two folds of hydrogen atoms out of the plane and are related to the 680 $cm^{-1}$ frequency obtained from the experiments. The highest intensity of the vibrational modes happens during the SE signal, Figure 40, and its central wavelength (400 nm) coincides exactly with the $S_2(\pi\pi^*)$ minimum. At the 400 nm wavelength the 680 $cm^{-1}$ mode has a minimum (Figure 40 a) while for the 400 $cm^{-1}$ mode there is a maximum. This behavior is associated with the wave packet motion around the $S_2(\pi\pi^*)$ state minimum, which results in the phase flip of the oscillations.

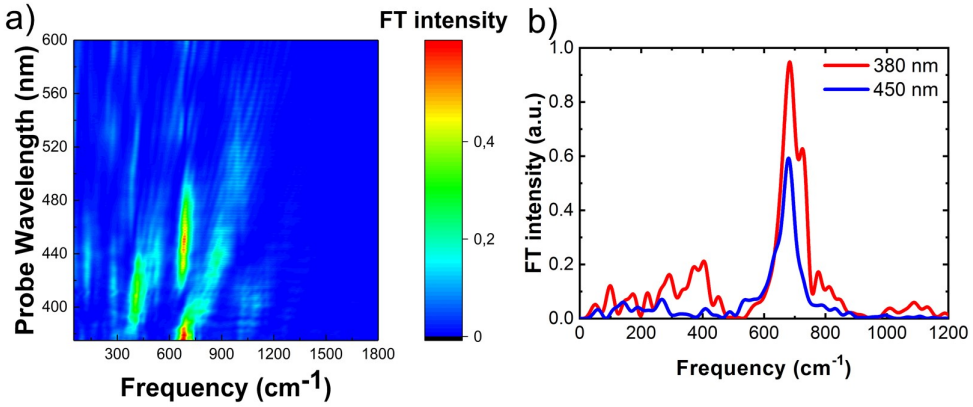



Figure 40 – (a) FT of the 4TU 2D residue map. (b) FT for select wavelengths.

For the 4TT results, we find at least 5 frequency modes, which are: 70 $cm^{-1}$,150 $cm^{-1}$, 258 $cm^{-1}$, 453 $cm^{-1}$ and 736 $cm^{-1}$ (Figure 41, panel a). From Raman experiments (Figure 41, panel c) we found the values 257 $cm^{-1}$, 470 $cm^{-1}$ and 708 $cm^{-1}$. The deviations between the Raman modes and the modes extracted from the pump-probe is about 20%. This may be due to the vibration modes in the pump-probe experiment coming from the excited state and in the Raman experiments from the ground state. The coherent oscillations can enable an easier ISC transition due to the vibronic coupling as predicted by Cui and Thiel [136]. It can also enable to explore all $S_2(\pi\pi^*)$ possible geometries as Martínez-Fernández and co-workers [40] had suggested.

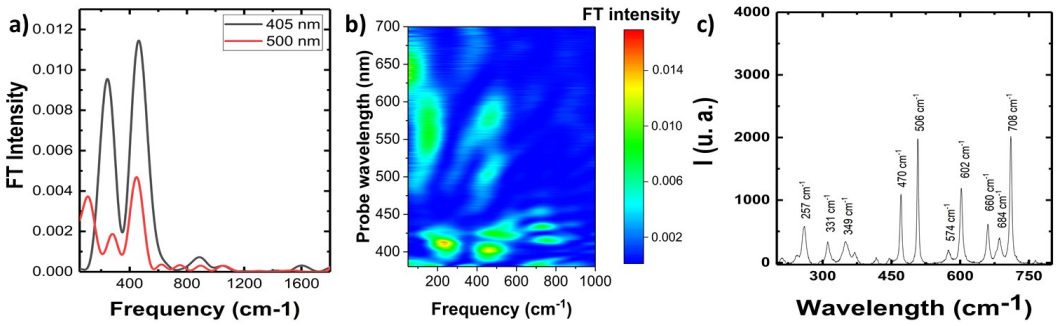



Figure 41 – 4TT oscillations: a) FT at probe wavelength of 405 nm and 500 nm. b) FT of the 2D residue map. c) Raman spectra.

## 6.4 2-Thiocytosine

### 6.4.1 Overview

The 2TC relaxation pathways and the time constants associated with those processes have been a matter of discussion recently. Mai et al. [41] performed TAS measurements (with the time resolution about 200 fs) pumping at 308 nm and in 321 nm. They observe the growing of two distinct absorption band: one in the UV region (350-400 nm) and another in the visible range (400-700 nm). They showed, supported by MS-CASPT2 simulations, that the state $S_1(^1\pi\pi^*)$ strongly absorbs in UV band and the visible band is dominated by the $T_1(^3\pi\pi^*)$ state with two transitions: at 441 nm and 456 nm. Due to these two transitions, the visible band is broad. They found two time constants from their simulations: 160 fs and 250 fs. The first one is related to the IC at the CI between the $S_2(^1\pi\pi^*)$ and $S_1(^1n\pi^*)$ and the second one is related to the ISC between the singlet state and the triplet manifold. From their simulation and measurements, they suggest a relaxation pathway to the bright triplet state $T_1(^3\pi\pi^*)$ in three steps: first an IC, $S_2 \longrightarrow S_1$ (with a time constant associated with the 160 fs ); following by an ISC, $S_1 \longrightarrow T_2$ (with a time constant associated of the 250 fs); and then the IC, $T_2 \longrightarrow T_1$ (with a time constant about 480 fs, obtained from the experiment). Other mentioned pathway to populate $T_1$, with a minor contribution, is the sequence $S_2 \longrightarrow S_1 \longrightarrow T_1$.

### 6.4.2 2TC Results

From our sub-20-fs transient transmission experiments probing in the visible, we acquire the 2D map Figure 42 a. The Figure 42 b shows the TTS spectra at selected delay times at the 2D map, in which we also saw two distinct bands: one negative in the UV (with the maximum at 355 nm) and another in the visible (with the maximum about 500 nm) with a small positive part. After 80 fs, the UV band grows to its maximum amplitude, at around 200 fs, and then the intensity decreases again. The visible band shows only a decay. Although the Mai et al. experimental result had been obtained using pump pulses ten times broader in time them ours, qualitatively our transient transmission spectra endorse their ones. Due to that we also attribute the absorptive UV band as a signature of the transition to $S_1(^1n\pi^*)$ and the visible absorption broadband to the triplet state formation.

The Figure 44 shows the data obtained by probing on at the UV range. There, it is possible to identify the GSB signal. The dynamics at the selected probe wavelengths are showed on Figure 43 a. We perform the global analysis considering the kinetic model and a sequential decay. The EAS curves are displayed in Figure 43 b. We found three time constants and a terminal decay (offset). The time constants obtained are 178 fs (black curve), 273 fs (red curve) and 400 fs (blue curve). Comparing our time constants with Mai

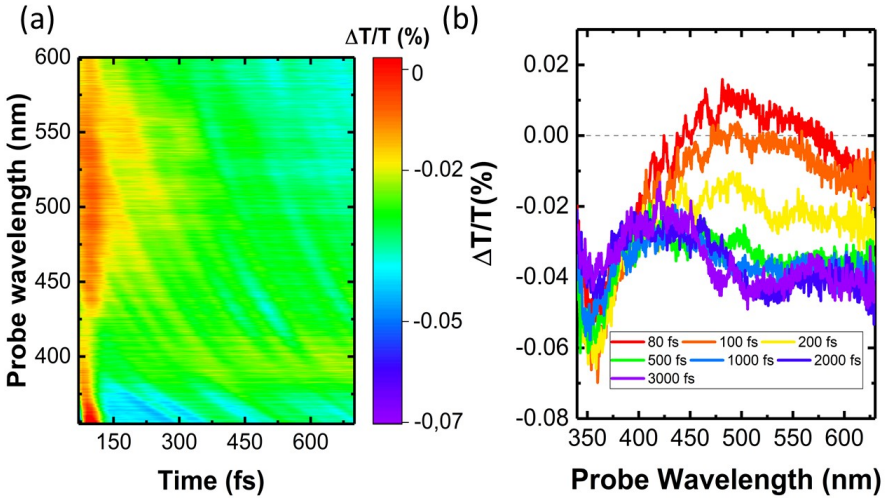



Figure 42 – (a) TTS 2D map for the 2TC: probe wavelengths as function of the delay time between pump and probe, (b) spectra at selected time delay.

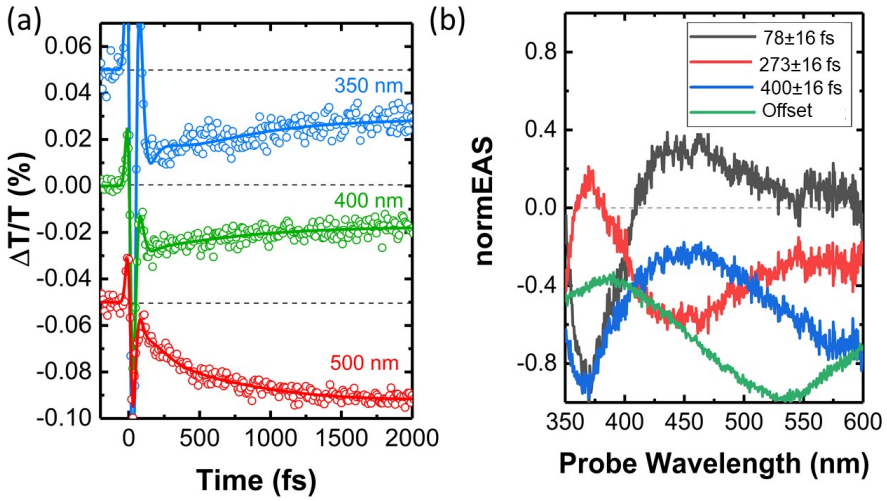



Figure 43 – (a) The 2TC dynamics at selected probe wavelengths, (b) EAS.

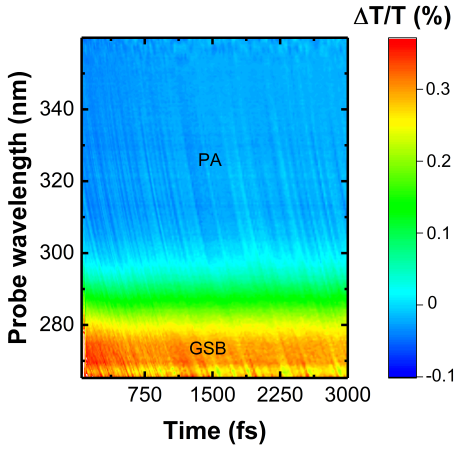



Figure 44 – TTS 2D map for the 2TC probing on the UV range.

et al. ones, there is a divergence of less than 20% between them (see Figure 45). Therefore, our time constants agree with the model proposed by Mai et al. described previously. Thus, the 178 fs is $S_2(^1\pi\pi^*)$ lifetime, the 273 fs is the dark singlet state lifetime, $S_1(^1n\pi^*)$, and the 400 fs is the dark triplet state lifetime $T_2(^3n\pi^*)$. However differently from Mai et al. experiments, at short times (visible range in the black curve, Figure 43 b), we observe a positive signal attributed to a SE which is a fingerprint of the $S_2(^1\pi\pi^*)$ state.

The comparison between the general relaxation mechanism scheme in the literature with our experimental result is presenting in Figure 45. The excited state by the pump pulse is the $S_2(^1\pi\pi^*)$. Then the most part of the population decays to $S_1(^1n\pi^*) \longrightarrow T_2(^3n\pi^*) \longrightarrow T_1(^3\pi\pi^*)$, however a minor part of the population can skip $T_2(^3n\pi^*$ and goes direct to $T_1(^3\pi\pi^*)$ from $S_1(^1n\pi^*)$ [41].

In summary, our experimental results support the model proposed by Mai et al. and as far we know, we show for the first time the experimental lifetime for the bright singlet state $S_2(^1\pi\pi^*)$, thanks to the ultrashort pulse used in our pump-probe experiments.

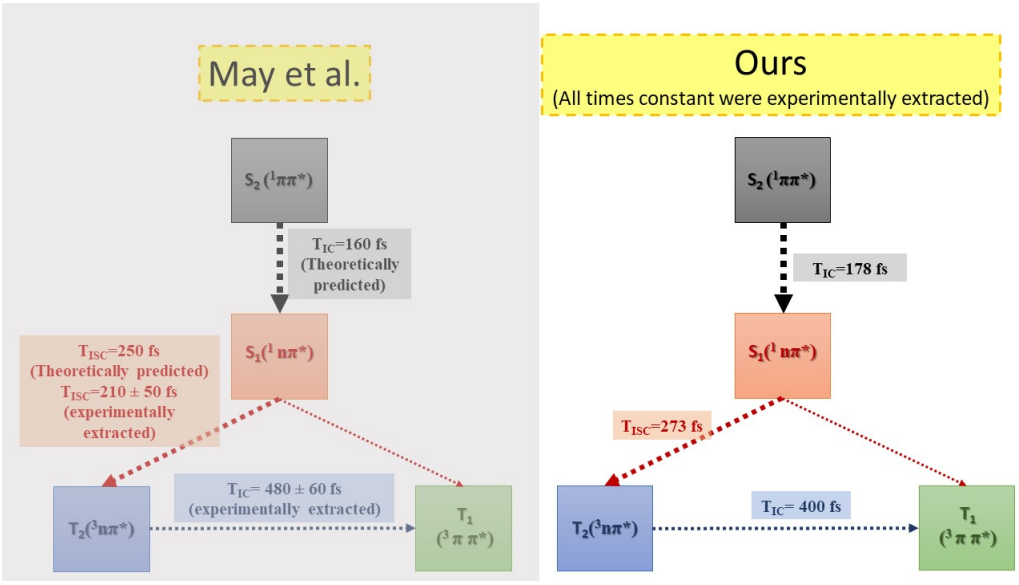



Figure 45 – Schematic diagrams showing a comparison of general relaxation mechanisms for 2TC. Each box is related to the curve of the species in the EAS with the same color.

## 6.5 6-Thioguanine

### 6.5.1 Overview

The thiopurines dynamic properties have been extensively studied in the literature. In particular, currently the most studied topics about the 6TG dynamics have been the glycosylation role in the triplet population [50], the environment influence [46, 50, 137], the excited state relaxation mechanism [43, 46, 111, 138], the depopulation rate of the triplet induced by others heavy-atom substitution [114, 139], and the characterization of the triplet state and also the singlet yield oxygen rate [140].

### 6.5.2 6TG Results

We performed the broadband transition absorption spectroscopy experiments pumping at 340 nm with sub-20 fs pulses for the 6TG in PSB solution. The spectra at selected delay times and the acquired TTS map can be seen in Figure 46. We observed three bands centered about 350 nm, 380 nm, and 520 nm. The intense band centered at 360 nm is partially superimposed with the lowest-energy band observed in the linear absorption spectra (Figure 19 b). Due to that, we assigned it to the ground state depopulation. It is followed by the rise of the bands centered about 380 nm and 450 nm. Previous works, which develop similar TAS experiments but with 200-fs pulse duration, have observed this band and identified them as the triplet state formation based on calculations [46, 50].

The TTS data were globally fitted using a sequential model with two times constants: $90 \pm 30$ fs and $463 \pm 48$ fs and an offset (Figure 47). The results match nicely with the experimental transient absorption spectra (Figure 46). Our results corroborate, in some way, also with the Ashwood et al. global analysis, obtained from TAS data with less than 200 fs time resolution [50].

The offset in the global analysis refers to time constants that are out from our time window observation as the long-lived triplet state (830 ns) [50]. The $463 \pm 48$ time constant is in the order of magnitude to the value obtained by Ashwood et al. [50] ($0.56 \pm 60$ ps) which is assigned to the triplet manifold population. Therefore, the $90 \pm 30$ fs time constant is the ultrafast population of an intermediate state $S_1$ which, according to the literature [46, 50, 137], have both natures: $n\pi$ and $\pi\pi$.

Some authors have proposed a deactivation decay pathway [43, 46, 111, 138]. The proposed mechanism in the literature converges to the following: the 6TG molecules excited by the UVA pulse initially populate the bright state, $S_2(\pi\pi^*)$, that barrierless decay to the $S_1(n\pi^*)$ from the FC region of the potential excited surface in tens of femtoseconds. The $S_1$ have two minima: one of a $n\pi^*$ nature and another of a $\pi\pi^*$ character, which enable a CI to the ground state of , estimated to be about 25% of the $S_1$ population. From the $S_1(n\pi^*)$

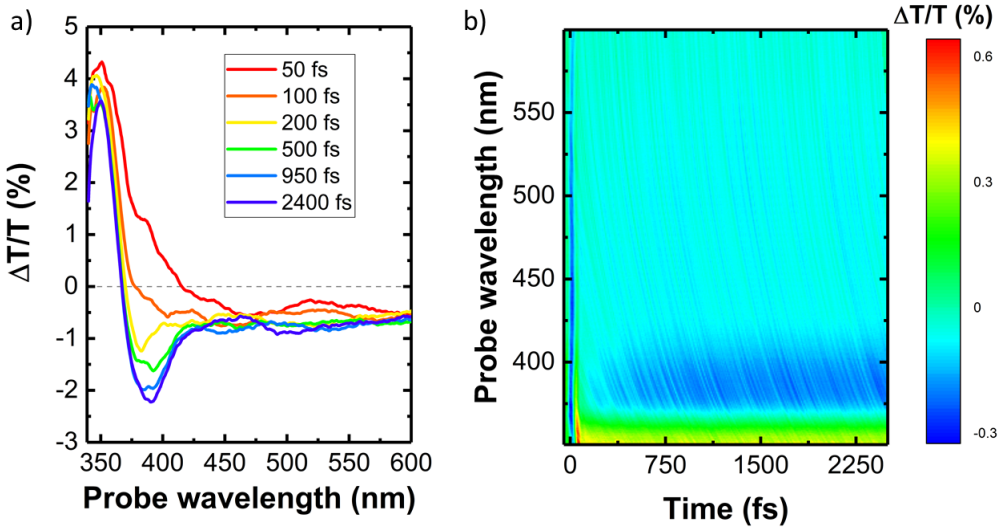



Figure 46 – (a) 6TG spectra at selected times. (b) 2D map obtained by the TTS.

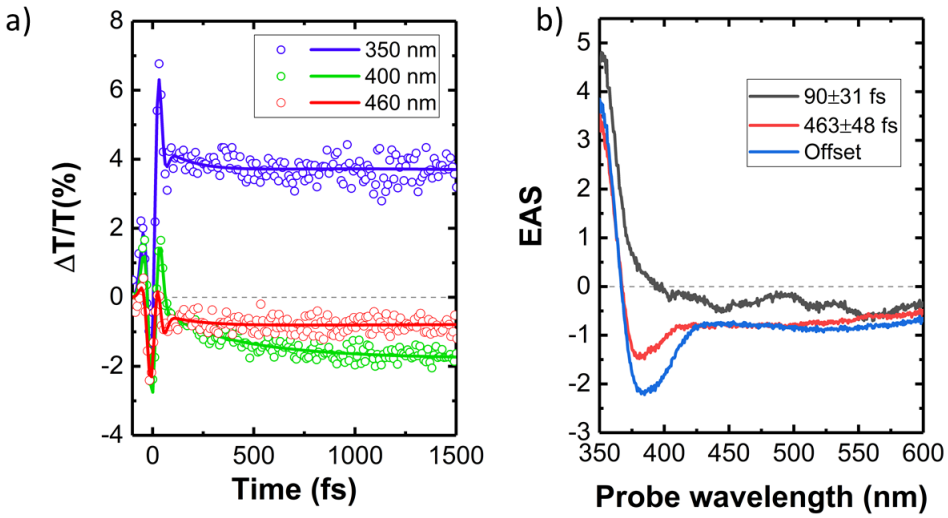



Figure 47 – (a) 6TG dynamics at selected probe wavelengths. (b) EAS obtained by the global analysis.

minimum, there is an efficient population of the bright $T_1(\pi\pi^*)$ and the dark $T_1(n\pi^*)$ triplet states because they are is isoenergetic, enabling an exchange population. The population is trapped in the bright triplet state for hundreds of femtoseconds. The $S_2(\pi\pi^*) \rightarrow S_1(n\pi^*) \rightarrow T_1(\pi\pi^*)/T_2(n\pi^*) \rightarrow T_1(\pi\pi^*)$ is assigned as the main relaxation pathway, but there is a minor contribution from the $S_2(\pi\pi^*) \rightarrow S_1(\pi\pi^*) \rightarrow S_0$ or $S_2(\pi\pi^*) \rightarrow T_2(n\pi^*) \rightarrow T_1(\pi\pi^*)$ pathway. Figure 48 summarize these predictions.

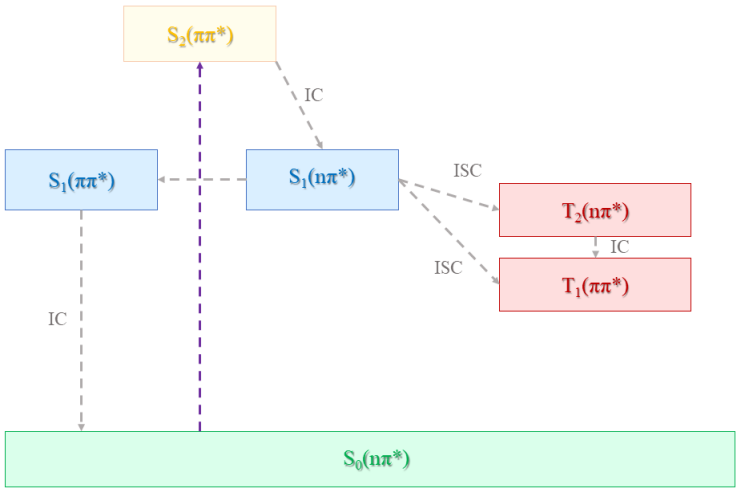



Figure 48 – Scheme for the 6TG decay path mechanism.

# 7 Conclusions and Outlook

All the information and discussions presented previously in the Result Chapter do not exhaust the experiments performed during this PhD. Besides the studies of the ultrafast manifold triplet state population mentioned before and our results published in references [51–53, 131], a significant amount of data has not yet been fully analyzed and published. With the content presented so far, it is possible to draw some conclusions and outlooks that will be discussed below.

## 7.1 Concluding remarks

The details of the dynamics of photoexcitation and energy relaxation processes in nucleic acids make it possible to understand the energy structure of such molecules. And this information allows the understanding of how with a simple exchange of oxygen for sulfur in a DNA/RNA bases the efficiently energy dissipation on an ultrafast time scale is lost, that throws away the photoprotection.

In this thesis, we have presented a study of the energy relaxation pathways for thiobases in PBS solution guided by the open questions in the literature. For this, we used the TTS technique to obtain the molecule dynamics and also the steady-state techniques (LA, PL, Ramam) to complement the discussions.

The LA was very useful to identify the singlet bright states that were exited with the sub-20 fs pulses in the TTS. Analyzing those results and comparing the data with the ones published in the literature [5, 64, 141] we observed a redshift that depends on the position and the number of substitutions. It is small in the case of the 2-thiopyrimidines but it is quite large for the 4 and 2,4-dithioderivatives [11].

The PL and the Raman experiments were also very useful to help to interpret the TTS data. In the TTS the positive signal could be a SE or a GSB, with the PL data we could discriminate without doubts that the signal was a SE. Moreover, with the Raman spectroscopy we could compare the vibrational coherent modes in the ground state with the excited states modes obtain by the TTS.

The TTS with broadband ultrashort pulses enabled us to track the first steps of the excited electron decay paths until it arrives in the triplet manifold. Many predictions about the decay paths have been done in recently literature, and the results presented and here are the first experimental studies that used tools with enough time resolution to see the initial relaxation and also to experimentally detected the vibrational mode in the 4-thiopirimidines. To analyse the data, we used global analysis tools with a sequential

model and with this we extracted the decay time constants. The Table 7.1 summarizes the time constants obtained for each thiobase studied here.

| Thiobase | Time Constants |
|---|---|
| 2TU pump at 270 nm | 187 fs |
| 4TU pump at 330 nm | 76 fs and 225 fs |
| 24TU pump at 270 nm | 127 fs and 221 fs |
| 24TU pump at 330 nm | 91 fs and 399 fs |
| 2TT pump at 270 nm | 80 fs and 383 fs |
| 4TT pump at 330 nm | 85 fs and 243 fs |
| 2TC pump at 270 nm | 178 fs, 273 fs and 400 fs |
| 6TG pump at 330 nm | 90 fs and 463 fs |

Table 2 – Thiobases time constants extracted from the pump and probe results with the sub-20 fs broadband pulses.

In the thiouracils, the bright states shows overlapping $\pi\pi^*$ linear absorption bands in the near-UV window. By considering all these states we were able to disentangle the components of the different paths in the time-resolved spectra. Comparing the three different thionated uracils (2TU, 24TU, and 4TU), we extrapolate two general ways for the their overall relaxation behavior. The first one is along all the $\pi\pi^*$ analyzed decay paths, the final long-living population of the triplet manifold, happens or directly through an ISC process between the bright and the triplet states, or through an intermediate $n\pi^*$ state. The former process could lead to triplet states population at unprecedently short timescales: 167 fs, 109/136 fs and 76 fs for 2TU, 24TU (pumping at 330/270 nm) and 4TU, respectively. The second one presents decay route topologies that depend on which sulfur atom the $\pi$ bonding orbitals (involved electronic transition) localize along a specific relaxation path, S2 or S4. This means that the 24TU decay processes are qualitatively reproducing the 2TU and 4TU processes, depending on the $\pi\pi^*$ electronic transition localization on S2 or S4 side, respectively.

For the 2TT and 4TT transient transmission data, differently from the 2TU and 4TU, we observed similar excited singlet bright state lifetimes (85±16 fs and 80±16 fs for 4TT and 2TT, respectively). The time scale of the ISC processes is in agreement with the values published in the literature (243±16 fs and 383±16 fs for 4TT an 2TT, respectively). The 4TT 2D map is modulated by an oscillatory pattern from which we extracted the oscillations modes. And we speculate that it could be the coupling modes that help the ISC process, making the 4TT ISC process faster than the 2TT ISC process, since we do not observe this behavior in the 2-thiopirimidines. This explanation would also apply to the 4TU and 2TU. We are still working on the analysis to validate this hypothesis.

The 2TC TTS data were globally fitted with three time constants: 178±16 fs, 273±16 fs, and 400±16 fs. This time constants are in agreement with the theoretical

predictions by Mai *et al.*, thus agreeing with the model proposed by them.

The 6TG is the only thiopurine that we evaluated in this thesis. From the transient transmission data and global analysis, we find two time constants: 90±31 fs and 463±48 fs. According to the previous model proposed in the literature the first time constant is related to the IC to a dark intermediate state and the second one is related to the ISC to the triplet manifold process. To complete discuss the spectroscopy results for the 2TC, 6TG and the thiothymidines transient transmission spectra, we would need the theoretical results from the high level calculations as have been done for the thiouracils.

The theoretical results points out that the preferred routes towards the population of triplet states upon UVA excitation in thionated nucleobases involves $^1\pi\pi^*$, $^1n\pi^*$, $^3\pi\pi^*$, and the $^3n\pi^*$ in the deactivation decay path to the triplet state. Following the Kasha's rule [133] and the El-Sayed's rule [73], the most common behavior for decay path is the $^1\pi\pi^* \rightarrow^1 n\pi^* \rightarrow^3 \pi\pi^*$ and a secondary decay path pass to $^1\pi\pi^* \rightarrow^3 n\pi^* \rightarrow^3 \pi\pi^*$, although some of thiobases show an exchange population in isoenergetic states (2TU and 24TU) or an IC to the ground state (6TG).

The high SOC (that improves the efficient ISC process) and also the ultrafast IC from the bright excited state to the triplet state, enables the ultrafast population to the triplet state. So, the dark singlet state act as a doorway to the triplet manifold. The novelty of this work was to follow by spectroscopic techniques these decay pathways and to obtain the time scale of each decay process [51–53, 131]. Thus, this work represents a breakthrough in the understanding of the thiobases photophysics that is the basis for important pharmacological and biotechnological purposes.

## 7.2 Open questions and outlook

Below, some remaining open questions are briefly discussed.

A more complete analysis of the observed coherent oscillations is still lacking. The simple analysis presented in this work have some limitations, since it used the FT of the TTS data residue matrix after the exponetial decay subtraction. The residue matrix extracted from the global analyses [108] contains the oscillatory pattern, but also the experimental noisy. The noise is a problem for the FT analysis, the noise widens the frequency peaks thereby adding larger uncertainty to the frequency value. Moreover, this approach does not consider the Instrument Response Function. One possibility to solve this issue and better analyze the data is to apply the damped oscillation associated spectra methodology [142]. It is a potentially more robust method, and with these analysis, we can obtain the role of the vibrational modes in the decay path. We already started to work on these analysis.

To better explore the nature of the vibrational modes identified in the TTS, it would be interesting to perform time-resolved broadband Raman spectroscopy. That could be a key to obtain the vibrational modes in the excited states and allow a directly comparison with the ones obtained by the TTS and by the steady-state Raman experiments [143]. It would possibly help to decipher if the oscillations are coming only from the excited state or also from the ground state.

One question that these investigations opens about the 24TU is: what would be the channel to access the most efficiently quantum yield for singlet oxygen production, by the S2 or by the S4 routes? The 24TU is the thiobase that has been showed to be the best one for applications in photodynamic therapy [11, 35], so this question is very relevant. It is important to understand the most efficient pathway to populate the triple: if it is by pumping at 270 nm or at 330 nm. It would give us some hints about the better way to have higher singlet oxygen quantum yield. One way to study this would be by measuring singlet oxygen photoluminescence from the solution with the different pump configurations. Another way to indirectly analyze the rate of singlet oxygen production is to prepare the sample in a potassium iodide solution and measure the LA spectra by pumping the sample at 270 nm and 330 nm with the same power [144]. These are experiments that I would like to try in the future.

Time-dependent photoluminescence experiments [66] could also shed light on the triplet state lifetime and its relationship with the singlet oxygen quantum yield. Thiobases are anti-inflammatory, anticancer, and immunosuppressive drugs used for over 50 years [145]. However, the thioanalogs can be incorporated in the DNA after the drug metabolization replacing the canonical nucleobases in the patients DNA due they biosimilarity [146, 147]. It makes the skin of the patients very sensitive to UV light, since when the thioanalogs interacts with UV light the triplet state is ultrafast populated by an ISC with high quantum yields [11, 31, 46] and then oxygen singlet reactive species are efficiently generated and can lead the DNA damage and cell death. Thus, the probability of developing skin cancer is significantly increased if the patients are exposed to long treatments with thiobases drugs. Therefore, to control the singlet oxygen toxicity in the cell an issue for the use of thioderivatives drugs. One way to do this could be through the functionalization of the thiobase with gold nanorods [148]. This field remains unexplored and this is one of the prospects of continuing this work.

# Bibliography

[1] Barbatti, Mario, Antonio Carlos Borin e Susanne Ullrich: *Photoinduced phenomena in nucleic acids*. Springer, 2015. Cited in page 21.

[2] Pattison, David I, Aldwin Suryo Rahmanto e Michael J Davies: *Photo-oxidation of proteins*. Photochemical & Photobiological Sciences, 11(1):38–53, 2012. Cited in page 21.

[3] González, Salvador, Manuel Fernández-Lorente e Yolanda Gilaberte-Calzada: *The latest on skin photoprotection*. Clinics in dermatology, 26(6):614–626, 2008. Cited in page 21.

[4] Prokhorenko, Valentyn I, Alessandra Picchiotti, Martina Pola, Arend G Dijkstra e RJ Dwayne Miller: *New insights into the photophysics of DNA nucleobases*. The journal of physical chemistry letters, 7(22):4445–4450, 2016. Cited 3 times in page 21, 35, and 37.

[5] Nenov, Artur, Javier Segarra-Martí, Angelo Giussani, Irene Conti, Ivan Rivalta, Elise Dumont, Vishal K Jaiswal, Salvatore Flavio Altavilla, Shaul Mukamel e Marco Garavelli: *Probing deactivation pathways of DNA nucleobases by two-dimensional electronic spectroscopy: first principles simulations*. Faraday Discussions, 177:345–362, 2015. Cited 4 times in page 21, 38, 97, and 125.

[6] Tan, Chuang, Zheyun Liu, Jiang Li, Xunmin Guo, Lijuan Wang, Aziz Sancar e Dongping Zhong: *The molecular origin of high DNA-repair efficiency by photolyase*. Nature Communications, 6, 2015. Cited in page 21.

[7] Nelson, David L, Albert L Lehninger e Michael M Cox: *Lehninger principles of biochemistry*. Macmillan, 2008. Cited 2 times in page 21 and 25.

[8] Jordheim, Lars Petter, David Durantel, Fabien Zoulim e Charles Dumontet: *Advances in the development of nucleoside and nucleotide analogues for cancer and viral diseases*. Nature Reviews Drug Discovery, 12(6):447, 2013. Cited in page 21.

[9] Attard, Natalie R e Peter Karran: *UVA photosensitization of thiopurines and skin cancer in organ transplant recipients*. Photochemical & Photobiological Sciences, 11(1):62–68, 2012. Cited in page 21.

[10] Pridgeon, SW, R Heer, GA Taylor, DR Newell, K O'toole, M Robinson, YZ Xu, P Karran e AV Boddy: *Thiothymidine combined with UVA as a potential novel therapy*

*for bladder cancer*. British journal of cancer, 104(12):1869, 2011. Cited 2 times in page 21 and 35.

[11] Pollum, Marvin, Steffen Jockusch e Carlos E Crespo-Hernández: *Increase in the photoreactivity of uracil derivatives by doubling thionation*. Physical Chemistry Chemical Physics, 17(41):27851–27861, 2015. Cited 8 times in page 21, 22, 35, 75, 78, 79, 97, and 100.

[12] Ashwood, Brennan, Marvin Pollum e Carlos E Crespo-Hernández: *Photochemical and Photodynamical Properties of Sulfur-Substituted Nucleic Acid Bases*. Photochemistry and Photobiology, 2018. Cited 4 times in page 21, 35, 68, and 69.

[13] Arslancan, Serra, Lara Martínez-Fernández e Inés Corral: *Photophysics and photochemistry of canonical nucleobases' thioanalogs: From quantum mechanical studies to time resolved experiments*. Molecules, 22(6):998, 2017. Cited in page 21.

[14] Elion, Gertrude B, Walter S Ide e George H Hitchings: *The Ultraviolet Absorption Spectra of Thiouracils1*. Journal of the American Chemical Society, 68(11):2137–2140, 1946. Cited in page 21.

[15] Nenov, Artur, Irene Conti, Rocio Borrego-Varillas, Giulio Cerullo e Marco Garavelli: *Linear absorption spectra of solvated thiouracils resolved at the hybrid RASPT2/MM level*. Chemical Physics, 515:643–653, 2018. Cited 2 times in page 21 and 68.

[16] Middleton, Chris T, Kimberly de La Harpe, Charlene Su, Yu Kay Law, Carlos E Crespo-Hernández e Bern Kohler: *DNA excited-state dynamics: from single bases to the double helix*. Physical Chemistry, 60, 2009. Cited in page 21.

[17] Crespo-Hernández, Carlos E, Boiko Cohen, Patrick M Hare e Bern Kohler: *Ultrafast excited-state dynamics in nucleic acids*. Chemical Reviews, 104(4):1977–2020, 2004. Cited in page 21.

[18] Pecourt, Jean Marc L, Jorge Peon e Bern Kohler: *Ultrafast internal conversion of electronically excited RNA and DNA nucleosides in water*. Journal of the American Chemical Society, 122(38):9348–9349, 2000. Cited 2 times in page 21 and 38.

[19] Harada, Yosuke, Chie Okabe, Takashi Kobayashi, Tadashi Suzuki, Teijiro Ichimura, Nobuyuki Nishi e Yao Zhong Xu: *Ultrafast intersystem crossing of 4-thiothymidine in aqueous solution*. The Journal of Physical Chemistry Letters, 1(2):480–484, 2010. Cited in page 21.

[20] Sánchez-Rodríguez, José A, Abed Mohamadzade, Sebastian Mai, Brennan Ashwood, Marvin Pollum, Philipp Marquetand, Leticia González, Carlos E Crespo-Hernández e Susanne Ullrich: *2-Thiouracil intersystem crossing photodynamics studied by*

*wavelength-dependent photoelectron and transient absorption spectroscopies*. Physical Chemistry Chemical Physics, 19(30):19756–19766, 2017. Cited 3 times in page 21, 22, and 75.

[21] Yu, Hui, Jose A Sanchez-Rodriguez, Marvin Pollum, Carlos E Crespo-Hernández, Sebastian Mai, Philipp Marquetand, Leticia González e Susanne Ullrich: *Internal conversion and intersystem crossing pathways in UV excited, isolated uracils and their implications in prebiotic chemistry*. Physical Chemistry Chemical Physics, 18(30):20168–20176, 2016. Cited 2 times in page 21 and 75.

[22] Jiang, Jie, Teng shuo Zhang, Jia dan Xue, Xuming Zheng, Ganglong Cui e Wei hai Fang: *Short-time dynamics of 2-thiouracil in the light absorbing S2 ($\pi\pi^*$) state*. The Journal of Chemical Physics, 143(17):11B605_1, 2015. Cited in page 21.

[23] Koyama, Daisuke, Matthew J Milner e Andrew J Orr-Ewing: *Evidence for a Double Well in the First Triplet Excited State of 2-Thiouracil*. The Journal of Physical Chemistry B, 121(39):9274–9280, 2017. Cited 2 times in page 21 and 75.

[24] Bai, Shuming e Mario Barbatti: *Why replacing different oxygens of thymine with sulfur causes distinct absorption and intersystem crossing*. The Journal of Physical Chemistry A, 120(32):6342–6350, 2016. Cited 2 times in page 21 and 69.

[25] Zou, Xiaoran, Xiaojuan Dai, Kunhui Liu, Hongmei Zhao, Di Song e Hongmei Su: *Photophysical and photochemical properties of 4-thiouracil: Time-resolved IR spectroscopy and DFT studies*. The Journal of Physical Chemistry B, 118(22):5864–5872, 2014. Cited 2 times in page 21 and 79.

[26] Gobbo, João Paulo e Antonio Carlos Borin: *2-Thiouracil deactivation pathways and triplet states population*. Computational and Theoretical Chemistry, 1040:195–201, 2014. Cited in page 21.

[27] Martinez-Fernandez, L, Tobias Fahleson, Patrick Norman, Fabrizio Santoro, Sonia Coriani e Roberto Improta: *Optical absorption and magnetic circular dichroism spectra of thiouracils: a quantum mechanical study in solution*. Photochemical & Photobiological Sciences, 16(9):1415–1423, 2017. Cited 2 times in page 21 and 69.

[28] Ruckenbauer, Matthias, Sebastian Mai, Philipp Marquetand e Leticia González: *Photoelectron spectra of 2-thiouracil, 4-thiouracil, and 2, 4-dithiouracil*. The Journal of Chemical Physics, 144(7):074303, 2016. Cited in page 21.

[29] Valeur, Bernard: *Molecular fluorescence*. Digital Encyclopedia of Applied Physics, páginas 477–531, 2003. Cited in page 21.

[30] Pollum, Marvin, Steffen Jockusch e Carlos E Crespo-Hernández: *Increase in the photoreactivity of uracil derivatives by doubling thionation.* Physical Chemistry Chemical Physics, 17(41):27851–27861, 2015. Cited in page 21.

[31] Pollum, Marvin, Steffen Jockusch e Carlos E Crespo-Hernandez: *2, 4-Dithiothymine as a potent UVA chemotherapeutic agent.* Journal of the American Chemical Society, 136(52):17930–17933, 2014. Cited 4 times in page 21, 85, 87, and 100.

[32] Sismour, A Michael e Steven A Benner: *The use of thymidine analogs to improve the replication of an extra DNA base pair: a synthetic biological system.* Nucleic acids research, 33(17):5640–5646, 2005. Cited in page 21.

[33] Heuberger, Benjamin D, Ayan Pal, Francesca Del Frate, Ved V Topkar e Jack W Szostak: *Replacing uridine with 2-thiouridine enhances the rate and fidelity of nonenzymatic RNA primer extension.* Journal of the American Chemical Society, 137(7):2769–2775, 2015. Cited in page 21.

[34] Favre, A, G Moreno, MO Blondel, J Kliber, F Vinzens e C Salet: *4-Thiouridine photosensitized RNA-protein crosslinking in mammalian cells.* Biochemical and Biophysical Research Communications, 141(2):847–854, 1986. Cited in page 21.

[35] Pollum, Marvin, Minh Lam, Steffen Jockusch e Carlos E Crespo-Hernández: *Dithionated Nucleobases as Effective Photodynamic Agents against Human Epidermoid Carcinoma Cells.* ChemMedChem, 13(10):1044–1050, 2018. Cited 2 times in page 21 and 100.

[36] Harris, Michael E e Eric L Christian: *RNA crosslinking methods*, volume 468. Elsevier, 2009. Cited in page 21.

[37] Meisenheimer, Kristen M e Tad H Koch: *Photocross-linking of nucleic acids to associated proteins.* Critical reviews in biochemistry and molecular biology, 32(2):101–140, 1997. Cited in page 21.

[38] Reelfs, Olivier, Peter Karran e Antony R Young: *4-thiothymidine sensitization of DNA to UVA offers potential for a novel photochemotherapy.* Photochemical & Photobiological Sciences, 11(1):148–154, 2012. Cited in page 21.

[39] Massey, Andrew, Yao Zhong Xu e Peter Karran: *Photoactivation of DNA thiobases as a potential novel therapeutic option.* Current Biology, 11(14):1142–1146, 2001. Cited in page 21.

[40] Martínez-Fernández, Lara, Giovanni Granucci, Marvin Pollum, Carlos E Crespo-Hernández, Maurizio Persico e Inés Corral: *Decoding the Molecular Basis for the Population Mechanism of the Triplet Phototoxic Precursors in UVA Light-Activated*

*Pyrimidine Anticancer Drugs*. Chemistry–A European Journal, 23(11):2619–2627, 2017. Cited 5 times in page 22, 71, 85, 87, and 90.

[41] Mai, Sebastian, Marvin Pollum, Lara Martínez-Fernández, Nicholas Dunn, Philipp Marquetand, Inés Corral, Carlos E Crespo-Hernández e Leticia González: *The origin of efficient triplet state population in sulfur-substituted nucleobases*. Nature Communications, 7:13077, 2016. Cited 4 times in page 22, 79, 91, and 93.

[42] Mai, Sebastian, Philipp Marquetand e Leticia Gonzalez: *A static picture of the relaxation and intersystem crossing mechanisms of photoexcited 2-thiouracil*. The Journal of Physical Chemistry A, 119(36):9524–9533, 2015. Cited 2 times in page 22 and 75.

[43] Martínez-Fernández, Lara, Inés Corral, Giovanni Granucci e Maurizio Persico: *Competing ultrafast intersystem crossing and internal conversion: a time resolved picture for the deactivation of 6-thioguanine*. Chemical Science, 5(4):1336–1347, 2014. Cited 2 times in page 22 and 94.

[44] Cui, Ganglong e Wei hai Fang: *State-specific heavy-atom effect on intersystem crossing processes in 2-thiothymine: A potential photodynamic therapy photosensitizer*. The Journal of Chemical Physics, 138(4):044315, 2013. Cited 3 times in page 22, 79, and 85.

[45] Xie, Bin Bin, Qian Wang, Wei Wei Guo e Ganglong Cui: *The excited-state decay mechanism of 2, 4-dithiothymine in the gas phase, microsolvated surroundings, and aqueous solution*. Physical Chemistry Chemical Physics, 19(11):7689–7698, 2017. Cited 2 times in page 22 and 79.

[46] Reichardt, Christian, Cao Guo e Carlos E Crespo-Hernandez: *Excited-state dynamics in 6-thioguanosine from the femtosecond to microsecond time scale*. The Journal of Physical Chemistry B, 115(12):3263–3270, 2011. Cited 5 times in page 22, 68, 71, 94, and 100.

[47] Reichardt, Christian e Carlos E Crespo-Hernández: *Room-temperature phosphorescence of the DNA monomer analogue 4-thiothymidine in aqueous solutions after UVA excitation*. The Journal of Physical Chemistry Letters, 1(15):2239–2243, 2010. Cited 3 times in page 22, 79, and 85.

[48] Reichardt, Christian e Carlos E Crespo-Hernández: *Ultrafast spin crossover in 4-thiothymidine in an ionic liquid*. Chemical Communications, 46(32):5963–5965, 2010. Cited in page 22.

[49] Pollum, Marvin, Lara Martínez-Fernández e Carlos E Crespo-Hernández: *Photochemistry of nucleic acid bases and their thio-and aza-analogues in solution*. Em

*Photoinduced Phenomena in Nucleic Acids I*, páginas 245–327. Springer, 2014. Cited in page 22.

[50] Ashwood, Brennan, Steffen Jockusch e Carlos E Crespo-Hernández: *Excited-State Dynamics of the Thiopurine Prodrug 6-Thioguanine: Can N9-Glycosylation Affect Its Phototoxic Activity?* Molecules, 22(3):379, 2017. Cited 4 times in page 22, 68, 71, and 94.

[51] Teles-Ferreira, Danielle Cristina, Irene Conti, Rocío Borrego-Varillas, Artur Nenov, Ivo HM Van Stokkum, Lucia Ganzer, Cristian Manzoni, Ana Maria de Paula, Giulio Cerullo e Marco Garavelli: *A Unified Experimental/Theoretical Description of the Ultrafast Photophysics of Single and Double Thionated Uracils*. Chemistry–A European Journal, 2019. Cited 6 times in page 23, 75, 76, 81, 97, and 99.

[52] Teles-Ferreira, Danielle Cristina, Rocio Borrego-Varillas, Lucia Ganzer, Barbara Elza Nogueira Faria, Cristian Manzoni, Sandro De Silvestri, Artur Nenov, Irene Conti, Marco Garavelli, Giulio Cerullo *et al.*: *Intersystem crossing in thiobases proceeds by a dark intermediate state*. Em *EPJ Web of Conferences*, volume 205, página 10005. EDP Sciences, 2019. Cited 4 times in page 23, 75, 97, and 99.

[53] Borrego-Varillas, Rocío, Danielle C Teles-Ferreira, Artur Nenov, Irene Conti, Lucia Ganzer, Cristian Manzoni, Marco Garavelli, Ana Maria de Paula e Giulio Cerullo: *Observation of the Sub-100 Femtosecond Population of a Dark State in a Thiobase Mediating Intersystem Crossing*. Journal of the American Chemical Society, 140(47):16087–16093, 2018. Cited 8 times in page 23, 72, 75, 79, 87, 89, 97, and 99.

[54] Luther, K. K. Rohatgi Mukherjee: *Fundamentals of Photochemistry*. Berichte der Bunsengesellschaft für physikalische Chemie, 83(8):873–873, 1979. Cited 6 times in page 26, 27, 28, 29, 32, and 38.

[55] Klessinger, Martin e Josef Michl: *Excited states and photochemistry of organic molecules*. Wiley-VCH, 1995. Cited in page 26.

[56] Bunker, Philip R e Per Jensen: *Molecular symmetry and spectroscopy*. NRC Research Press, 2006. Cited in page 26.

[57] Szabo, A e NS Ostlund: *Introduction to advanced electronic structure theory*. Modern Quantum Chemistry, 1996. Cited 2 times in page 26 and 28.

[58] Ballentine, Leslie E: *Quantum Mechanics: a Modern Development*. World scientific, 1998. Cited 2 times in page 26 and 27.

[59] Yamanouchi, Kaoru: *Quantum mechanics of molecular structures*. Springer, 2012. Cited in page 28.

[60] Masters, Barry R: *Molecular fluorescence: Principles and applications*. Journal of Biomedical Optics, 18(3):039901, 2013. Cited 2 times in page 30 and 31.

[61] Blankenship, Robert E: *Molecular mechanisms of photosynthesis*. John Wiley & Sons, 2014. Cited 2 times in page 30 and 31.

[62] Lakowicz, Joseph R: *Principles of fluorescence spectroscopy*. Springer Science & Business Media, 2013. Cited 2 times in page 30 and 31.

[63] wikipedia: *Franck–Condon principle*, 2020. `https://en.wikipedia.org/wiki/Franck-Condon_principle`. Cited in page 31.

[64] Beckstead, Ashley A, Yuyuan Zhang, Mattanjah S de Vries e Bern Kohler: *Life in the light: nucleic acid photoproperties as a legacy of chemical evolution*. Physical Chemistry Chemical Physics, 18(35):24228–24238, 2016. Cited 2 times in page 36 and 97.

[65] Zhang, Yuyuan, Jinquan Chen e Bern Kohler: *Hydrogen bond donors accelerate vibrational cooling of hot purine derivatives in heavy water*. The Journal of Physical Chemistry A, 117(31):6771–6780, 2013. Cited in page 36.

[66] Brister, Matthew M, Thomas Gustavsson e Carlos E Crespo-Hernández: *Excited State Lifetimes of Sulfur-Substituted DNA and RNA Monomers Probed Using the Femtosecond Fluorescence Up-Conversion Technique*. Molecules, 25(3):584, 2020. Cited 2 times in page 37 and 100.

[67] Canuel, Clélia, Michel Mons, François Piuzzi, Benjamin Tardivel, Iliana Dimicoli e Mohamed Elhanine: *Excited states dynamics of DNA and RNA bases: Characterization of a stepwise deactivation pathway in the gas phase*. The Journal of Chemical Physics, 122(7):074316, 2005. Cited in page 38.

[68] Cohen, Boiko, Patrick M Hare e Bern Kohler: *Ultrafast excited-state dynamics of adenine and monomethylated adenines in solution: Implications for the nonradiative decay mechanism*. Journal of the American Chemical Society, 125(44):13594–13601, 2003. Cited in page 38.

[69] Gustavsson, Thomas, Alexei Sharonov, Delphine Onidas e Dimitra Markovitsi: *Adenine, deoxyadenosine and deoxyadenosine 5'-monophosphate studied by femtosecond fluorescence upconversion spectroscopy*. Chemical Physics Letters, 356(1):49–54, 2002. Cited in page 38.

[70] Pecourt, Jean Marc L, Jorge Peon e Bern Kohler: *DNA excited-state dynamics: ultrafast internal conversion and vibrational cooling in a series of nucleosides*. Journal of the American Chemical Society, 123(42):10370–10378, 2001. Cited in page 38.

[71] Buchner, Franziska: *Time-resolved photoelectron spectroscopy of DNA molecules in solution*. Tese de Mestrado, Freie Universität Berlin, 2015. Cited 2 times in page 38 and 69.

[72] Peon, Jorge e Ahmed H Zewail: *DNA/RNA nucleotides and nucleosides: direct measurement of excited-state lifetimes by femtosecond fluorescence up-conversion*. Chemical Physics Letters, 348(3):255–262, 2001. Cited in page 38.

[73] El-Sayed, MA: *Spin-Orbit coupling and the radiationless processes in nitrogen heterocyclics*. The Journal of Chemical Physics, 38(12):2834–2838, 1963. Cited 2 times in page 39 and 99.

[74] Manzoni, C e G Cerullo: *Design criteria for ultrafast optical parametric amplifiers*. Journal of Optics, 18(10):103501, 2016. Cited 2 times in page 41 and 45.

[75] Manzoni, Cristian, Oliver D Mücke, Giovanni Cirmi, Shaobo Fang, Jeffrey Moses, Shu Wei Huang, Kyung Han Hong, Giulio Cerullo e Franz X Kärtner: *Coherent pulse synthesis: towards sub-cycle optical waveforms*. Laser & Photonics Reviews, 9(2):129–171, 2015. Cited in page 41.

[76] Cerullo, Giulio, Cristian Manzoni, Larry Lüer e Dario Polli: *Time-resolved methods in biophysics. 4. Broadband pump–probe spectroscopy system with sub-20 fs temporal resolution for the study of energy transfer processes in photosynthesis*. Photochemical & photobiological sciences, 6(2):135–144, 2007. Cited 2 times in page 41 and 51.

[77] Varillas, Rocio Borrego, Alessia Candeo, Daniele Viola, Marco Garavelli, Sandro De Silvestri, Giulio Cerullo e Cristian Manzoni: *Microjoule-level, tunable sub-10 fs UV pulses by broadband sum-frequency generation*. Optics Letters, 39(13):3849–3852, 2014. Cited 2 times in page 41 and 47.

[78] Diels, Jean Claude e Wolfgang Rudolph: *Ultrashort laser pulse phenomena*. Elsevier, 2006. Cited in page 41.

[79] Weiner, Andrew: *Ultrafast optics*, volume 72. John Wiley & Sons, 2011. Cited 2 times in page 41 and 42.

[80] Svelto, Orazio e David C Hanna: *Principles of lasers*, volume 1. Springer, 2010. Cited in page 41.

[81] Young, Matt: *Óptica e Lasers Vol. 15*. Edusp, 1998. Cited in page 41.

[82] Boyd, Robert W: *Nonlinear optics*. Academic press, 2003. Cited 2 times in page 41 and 49.

[83] Franken, eg PA, Alan E Hill, CW Peters e G Weinreich: *Generation of optical harmonics*. Physical Review Letters, 7(4):118, 1961. Cited in page 41.

[84] Zangwill, Andrew: *Modern Electrodynamics*. Cambridge University Press, 2013. Cited in page 43.

[85] Manzoni, C, G Cirmi, D Brida, S De Silvestri e G Cerullo: *Optical-parametric-generation process driven by femtosecond pulses: Timing and carrier-envelope phase properties*. Physical Review A, 79(3):033818, 2009. Cited in page 46.

[86] Dubietis, Audrius, Gintaras Tamošauskas, Rosvaldas Šuminas, Vytautas Jukna e Arnaud Couairon: *Ultrafast supercontinuum generation in bulk condensed media (Invited Review)*. arXiv preprint arXiv:1706.04356, 2017. Cited in page 50.

[87] Polli, Dario, Piero Altoè, Oliver Weingart, Katelyn M Spillane, Cristian Manzoni, Daniele Brida, Gaia Tomasello, Giorgio Orlandi, Philipp Kukura, Richard A Mathies *et al.*: *Conical intersection dynamics of the primary photoisomerization event in vision*. Nature, 467(7314):440–443, 2010. Cited in page 51.

[88] Nenov, Artur, Rocio Borrego-Varillas, Aurelio Oriana, Lucia Ganzer, Francesco Segatta, Irene Conti, Javier Segarra-Marti, Junko Omachi, Maurizio Dapor, Simone Taioli *et al.*: *UV-light-induced vibrational coherences: the key to understand Kasha rule violation in trans-azobenzene*. The Journal of Physical Chemistry Letters, 9(7):1534–1541, 2018. Cited in page 51.

[89] Borrego-Varillas, Rocio, Giulio Cerullo e Dimitra Markovitsi: *Exciton Trapping Dynamics in DNA Multimers*. The Journal of Physical Chemistry Letters, 10(7):1639–1643, 2019. Cited in page 51.

[90] Ganzer, Lucia: *Tracking primary photoinduced processes in biomolecules by ultrafast UV spectroscopy*. Tese de Doutoramento, 2019. Cited in page 51.

[91] Alencar Souza, Thonimar Vieira de: *Espectroscopia de Femtosegundos e Propriedades Ópticas não Lineares em Nanomateriais Bidimensionais*. Tese de Doutoramento, 2014. Cited in page 51.

[92] Alencar Souza, Thonimar Vieira de: *Dinâmica do Pseudo-Spin de Éxciton-Polariton em Microcavidade Semicondutora*. Tese de Mestrado, Universidade Federal de Minas Gerais, Departamento de Fısica, 2010. Cited in page 51.

[93] Comitti, Victor Schmidt: *Splitting Longitudinal-Transversal em uma Microcavidade Semicondutora*. Tese de Mestrado, Universidade Federal de Minas Gerais, Departamento de Fısica, 2013. Cited in page 51.

[94] Silva, Marina Bezerra Eiras da: *Oscilação Paramétrica: Dinâmica Populacional de Polaritons em uma Microcavidade*. Tese de Mestrado, Universidade Federal de Minas Gerais, Departamento de Fısica, 2013. Cited in page 51.

[95] Huang, Yinjuan, Fugui Xu, Lucia Ganzer, Franco VA Camargo, Tetsuhiko Nagahara, Joan Teyssandier, Hans Van Gorp, Kristoffer Basse, Lasse Arnt Straasø, Vaiva Nagyte *et al.*: *Intrinsic properties of single graphene nanoribbons in solution: synthetic and spectroscopic studies.* Journal of the American Chemical Society, 140(33):10416–10420, 2018. Cited in page 51.

[96] Silva, Mychel Gonçalves, Danielle Cristina Teles-Ferreira, Cristian Manzoni, Lucia Ganzer, Livia Siman, Claudilene Ribeiro Chaves, Luiz Orlando Ladeira, Giulio Cerullo, Stefano Longhi, Sandro De Silvestri *et al.*: *Ultrafast optical response of plasmonic structures beyond the perturbative regime: evidence of universal saturation dynamics.* Em *EPJ Web of Conferences*, volume 205. EDP Sciences, 2019. Cited in page 51.

[97] Silva, MG, DC Teles-Ferreira, L Siman, CR Chaves, Luiz O Ladeira, S Longhi, G Cerullo, C Manzoni, AM de Paula e G Della Valle: *Universal saturation behavior in the transient optical response of plasmonic structures.* Physical Review B, 98(11):115407, 2018. Cited in page 51.

[98] Brida, Daniele, Cristian Manzoni e Giulio Cerullo: *Phase-locked pulses for two-dimensional spectroscopy by a birefringent delay line.* Optics Letters, 37(15):3027–3029, 2012. Cited in page 58.

[99] Oriana, Aurelio: *Two-dimensional electronic spectroscopy in the ultraviolet.* Tese de Doutoramento, Politecnico di Milano, 2016. Cited in page 58.

[100] Rooi, Johan J de, Olivier Devos, Michel Sliwa, Cyril Ruckebusch e Paul HC Eilers: *Mixture models for two-dimensional baseline correction, applied to artifact elimination in time-resolved spectroscopy.* Analytica chimica acta, 771:7–13, 2013. Cited in page 60.

[101] Luo, Chih Wei, YT Wang, FW Chen, HC Shih e T Kobayashi: *Eliminate coherence spike in reflection-type pump-probe measurements.* Optics express, 17(14):11321–11327, 2009. Cited in page 60.

[102] Devos, Olivier, Nicolas Mouton, Michel Sliwa e Cyril Ruckebusch: *Baseline correction methods to deal with artifacts in femtosecond transient absorption spectroscopy.* Analytica chimica acta, 705(1-2):64–71, 2011. Cited in page 60.

[103] Trebino, Rick, Kenneth W DeLong, David N Fittinghoff, John N Sweetser, Marco A Krumbügel, Bruce A Richman e Daniel J Kane: *Measuring ultrashort laser pulses in the time-frequency domain using frequency-resolved optical gating.* Review of Scientific Instruments, 68(9):3277–3295, 1997. Cited in page 62.

[104] Iaconis, Chris e Ian A Walmsley: *Self-referencing spectral interferometry for measuring ultrashort optical pulses*. IEEE Journal of Quantum Electronics, 35(4):501–509, 1999. Cited in page 62.

[105] Borrego-Varillas, Rocio, Aurelio Oriana, Federico Branchi, Sandro De Silvestri, Giulio Cerullo e Cristian Manzoni: *Optimized ancillae generation for ultra-broadband two-dimensional spectral-shearing interferometry*. JOSA B, 32(9):1851–1855, 2015. Cited 2 times in page 62 and 63.

[106] Wen, Jin Hui, Hui Zhang, Juan Lu, Zhong Xing Jiao, Liang Lei e Tian Shu Lai: *Spectral shearing interferometer with broad applicability*. JOSA B, 28(6):1391–1395, 2011. Cited in page 62.

[107] Snellenburg, Joris, Sergey Laptenok, Ralf Seger, Katharine Mullen e Ivo Van Stokkum: *Glotaran: A Java-based graphical user interface for the R package TIMP*. 2012. Cited in page 64.

[108] Stokkum, Ivo HM van, Delmar S Larsen e Rienk van Grondelle: *Global and target analysis of time-resolved spectra*. Biochimica et Biophysica Acta (BBA)-Bioenergetics, 1657(2-3):82–104, 2004. Cited 2 times in page 64 and 99.

[109] Sala, Oswaldo: *Fundamentos da espectroscopia raman no infravermelho*. 1996. Cited in page 66.

[110] Santhosh, C e PC Mishra: *Electronic structures and spectra of 6-mercaptopurine and 6-thioguanine*. Spectrochimica Acta Part A: Molecular Spectroscopy, 49(7):985–993, 1993. Cited in page 68.

[111] Martínez-Fernández, Lara, Leticia González e Inés Corral: *An ab initio mechanism for efficient population of triplet states in cytotoxic sulfur substituted DNA bases: the case of 6-thioguanine*. Chemical Communications, 48(15):2134–2136, 2012. Cited 2 times in page 68 and 94.

[112] Rubin, Yu V, Yu P Blagoi e VA Bokovoy: *6-Thioguanine luminescence probe to study DNA and low-molecular-weight systems*. Journal of Fluorescence, 5(3):263–272, 1995. Cited in page 68.

[113] Rubin, Yuri V: *Physical properties of anticancer drug 6-thioguanine*. Em *XVI International Conference on Spectroscopy of Molecules and Crystals*, volume 5507, páginas 346–357. International Society for Optics and Photonics, 2004. Cited in page 68.

[114] Pirillo, Jenny, Gloria Mazzone, Nino Russo e Luca Bertini: *Photophysical properties of S, Se and Te-substituted deoxyguanosines: Insight into their ability to act as*

*chemotherapeutic agents*. Journal of Chemical Information and Modeling, 57(2):234–242, 2017. Cited 2 times in page 68 and 94.

[115] Maciejewski, Andrzej e Ronald P Steer: *The photophysics, physical photochemistry, and related spectroscopy of thiocarbonyls*. Chemical Reviews, 93(1):67–98, 1993. Cited in page 69.

[116] Mautner, Henry G e Goran Bergson: *Some remarks on position-conditioned differences of the ultraviolet spectra and chemical reactivities of disubstituted pyrimidines and purines*. Acta Chem Scand, 17:1694–1704, 1963. Cited in page 69.

[117] Manae, Meghna A e Anirban Hazra: *Interplay between Conjugation and Size-Driven Delocalization Leads to Characteristic Properties of Substituted Thymines*. The Journal of Physical Chemistry A, 121(42):8147–8153, 2017. Cited in page 69.

[118] Taras-Goślińska, Katarzyna, Grażyna Wenska, Bohdan Skalski, Andrzej Maciejewski, Gotard Burdziński e Jerzy Karolczak: *Spectral and photophysical properties of the lowest excited triplet state of 4-thiouridine and its 5-halogeno derivatives*. Journal of Photochemistry and Photobiology A: Chemistry, 168(3):227–233, 2004. Cited in page 70.

[119] Zou, Xiaoran, Hongmei Zhao, Youqing Yu e Hongmei Su: *Formation of guanine-6-sulfonate from 6-thioguanine and singlet oxygen: A combined theoretical and experimental study*. Journal of the American Chemical Society, 135(11):4509–4515, 2013. Cited in page 71.

[120] Ghomi, M, R Letellier, E Taillandier, L Chinsky, A Laigle e PY Turpin: *Interpretation of the vibrational modes of uracil and its 18O-substituted and thio derivatives studied by resonance Raman spectroscopy*. Journal of Raman spectroscopy, 17(3):249–255, 1986. Cited in page 72.

[121] Thorogood, Harry, Timothy R Waters, Anthony W Parker, Christopher W Wharton e Bernard A Connolly: *Resonance Raman Spectroscopy of 4-Thiothymidine and Oligodeoxynucleotides Containing This Base Both Free in Solution and Bound to the Restriction Endonuclease Eco RV*. Biochemistry, 35(26):8723–8733, 1996. Cited in page 72.

[122] Letellier, R, M Ghomi e E Taillandier: *Out-of-plane vibration modes of nucleic acid bases*. European Biophysics Journal, 14(4):227–241, 1987. Cited in page 72.

[123] Peticolas, Warner L e Thomas Rush III: *Ab initio calculations of the ultraviolet resonance Raman spectra of uracil*. Journal of computational chemistry, 16(10):1261–1270, 1995. Cited in page 72.

[124] Singh, R e RA Yadav: *Raman and IR studies and DFT calculations of the vibrational spectra of 2, 4-Dithiouracil and its cation and anion*. Spectrochimica Acta Part A: Molecular and Biomolecular Spectroscopy, 130:188–197, 2014. Cited in page 72.

[125] Yadav, RA, PNS Yadav e JS Yadav: *Vibrational studies of biomolecules—II. 2-thiocytosine*. Spectrochimica Acta Part A: Molecular Spectroscopy, 44(11):1201–1206, 1988. Cited in page 72.

[126] Yarasi, Soujanya, Brant E Billinghurst e Glen R Loppnow: *Vibrational properties of thymine, uracil and their isotopomers*. Journal of Raman Spectroscopy: An International Journal for Original Work in all Aspects of Raman Spectroscopy, Including Higher Order Processes, and also Brillouin and Rayleigh Scattering, 38(9):1117–1126, 2007. Cited in page 72.

[127] Singh, R, S Jaiswal, M Kumar, P Singh, G Srivastav e RA Yadav: *DFT study of molecular geometries and vibrational characteristics of uracil and its thio-derivatives and their radical cations*. Spectrochimica Acta Part A: Molecular and Biomolecular Spectroscopy, 75(1):267–276, 2010. Cited in page 72.

[128] Ruckenbauer, Matthias, Sebastian Mai, Philipp Marquetand e Leticia González: *Revealing Deactivation Pathways Hidden in Time-Resolved Photoelectron Spectra*. Scientific Reports, 6, 2016. Cited 2 times in page 75 and 79.

[129] Mai, Sebastian, Philipp Marquetand e Leticia Gonzalez: *Intersystem crossing pathways in the noncanonical nucleobase 2-thiouracil: a time-dependent picture*. The Journal of Physical Chemistry Letters, 7(11):1978–1983, 2016. Cited 2 times in page 75 and 79.

[130] Pollum, Marvin e Carlos E Crespo-Hernández: *Communication: The dark singlet state as a doorway state in the ultrafast and efficient intersystem crossing dynamics in 2-thiothymine and 2-thiouracil*. The Journal of Chemical Physics, 140(7):071101, 2014. Cited 3 times in page 75, 85, and 87.

[131] Teles-Ferreira, Danielle C, Rocio Borrego-Varillas, Irene Conti, Artur Nenov, Lucia Ganzer, Cristian Manzoni, Marco Garavelli, Giulio Cerullo e Ana Maria de Paula: *Sub-20 fs UV spectroscopy to track primary photoinduced processes in Thiobases*. Em *2019 SBFoton International Optics and Photonics Conference (SBFoton IOPC)*, páginas 1–3. IEEE, 2019. Cited 3 times in page 75, 97, and 99.

[132] Martínez-Fernández, Lara, Giovanni Granucci, Marvin Pollum, Carlos E Crespo-Hernández, Maurizio Persico e Inés Corral: *Decoding the molecular basis for the population mechanism of the triplet phototoxic precursors in UVA light-activated pyrimidine anticancer drugs*. Chemistry–A European Journal, 23(11):2619–2627, 2017. Cited in page 79.

[133] Kasha, Michael: *Characterization of electronic transitions in complex molecules.* Discussions of the Faraday Society, 9:14–19, 1950. Cited 3 times in page 83, 85, and 99.

[134] Harada, Yosuke, Chie Okabe, Takashi Kobayashi, Tadashi Suzuki, Teijiro Ichimura, Nobuyuki Nishi e Yao Zhong Xu: *Ultrafast intersystem crossing of 4-thiothymidine in aqueous solution.* The Journal of Physical Chemistry Letters, 1(2):480–484, 2009. Cited in page 85.

[135] Harada, Yosuke, Tadashi Suzuki, Teijiro Ichimura e Yao Zhong Xu: *Triplet formation of 4-thiothymidine and its photosensitization to oxygen studied by time-resolved thermal lensing technique.* The Journal of Physical Chemistry B, 111(19):5518–5524, 2007. Cited in page 85.

[136] Cui, Ganglong e Walter Thiel: *Intersystem crossing enables 4-thiothymidine to act as a photosensitizer in photodynamic therapy: an ab initio QM/MM study.* The Journal of Physical Chemistry Letters, 5(15):2682–2687, 2014. Cited 2 times in page 85 and 90.

[137] Arslancan, Serra, Lara Martínez-Fernández e Inés Corral: *Photophysics and Photochemistry of Canonical Nucleobases' Thioanalogs: From Quantum Mechanical Studies to Time Resolved Experiments.* Molecules, 22(6):998, 2017. Cited in page 94.

[138] Siouri, Faady M, Samuel Boldissar, Jacob A Berenbeim e Mattanjah S de Vries: *Excited state dynamics of 6-thioguanine.* The Journal of Physical Chemistry A, 121(28):5257–5266, 2017. Cited in page 94.

[139] Farrell, Kieran M, Matthew M Brister, Michael Pittelkow, Theis I Sølling e Carlos E Crespo-Hernández: *Heavy-Atom-Substituted Nucleobases in Photodynamic Applications: Substitution of Sulfur with Selenium in 6-Thioguanine Induces a Remarkable Increase in the Rate of Triplet Decay in 6-Selenoguanine.* Journal of the American Chemical Society, 140(36):11214–11218, 2018. Cited in page 94.

[140] Pollum, Marvin, Luis A Ortiz-Rodríguez, Steffen Jockusch e Carlos E Crespo-Hernández: *The triplet state of 6-thio-2′-deoxyguanosine: Intrinsic properties and reactivity toward molecular oxygen.* Photochemistry and photobiology, 92(2):286–292, 2016. Cited in page 94.

[141] Buchner, Franziska, Berit Heggen, Hans Hermann Ritze, Walter Thiel e Andrea Lübcke: *Excited-state dynamics of guanosine in aqueous solution revealed by time-resolved photoelectron spectroscopy: experiment and theory.* Physical Chemistry Chemical Physics, 17(47):31978–31987, 2015. Cited in page 97.

[142] Van Stokkum, Ivo HM, Chanelle C Jumper, Joris J Snellenburg, Gregory D Scholes, Rienk Van Grondelle e Pavel Malỳ: *Estimation of damped oscillation associated spectra from ultrafast transient absorption spectra*. The Journal of Chemical Physics, 145(17):174201, 2016. Cited in page 99.

[143] Cadena, Alejandro De la, Carlo M Valensise, Marco Marangoni, Giulio Cerullo e Dario Polli: *Broadband stimulated Raman scattering microscopy with wavelength-scanning detection*. Journal of Raman Spectroscopy, 2020. Cited in page 100.

[144] Zhao, Qiang, Yao Wang, Yanshuang Xu, Yun Yan e Jianbin Huang: *Out-of-plane coordinated porphyrin nanotubes with enhanced singlet oxygen generation efficiency*. Scientific Reports, 6:31339, 2016. Cited in page 100.

[145] Karran, Peter e Natalie Attard: *Thiopurines in current medical practice: molecular mechanisms and contributions to therapy-related cancer*. Nature Reviews Cancer, 8(1):24, 2008. Cited in page 100.

[146] Penn, I: *The problem of cancer in organ transplant recipients: an overview*. Transpl Sci, 4:23–29, 1994. Cited in page 100.

[147] Perrett, CM, SL Walker, P O'Donovan, J Warwick, CA Harwood, P Karran e JM McGregor: *Azathioprine treatment photosensitizes human skin to ultraviolet A radiation*. British Journal of Dermatology, 159(1):198–204, 2008. Cited in page 100.

[148] Wang, Rennian, Ling Yue, Youqing Yu, Xiaoran Zou, Di Song, Kunhui Liu, Yajun Liu e Hongmei Su: *Gold nanoparticles modify the photophysical and photochemical properties of 6-thioguanine: preventing DNA oxidative damage*. The Journal of Physical Chemistry C, 120(26):14410–14415, 2016. Cited in page 100.

[149] Schott, Sebastian, Andreas Steinbacher, Johannes Buback, Patrick Nuernberger e Tobias Brixner: *Generalized magic angle for time-resolved spectroscopy with laser pulses of arbitrary ellipticity*. Journal of Physics B: Atomic, Molecular and Optical Physics, 47(12):124014, 2014. Cited in page 121.

[150] Ernst, Richard R, Geoffrey Bodenhausen, Alexander Wokaun *et al.*: *Principles of nuclear magnetic resonance in one and two dimensions*, volume 14. Clarendon Press Oxford, 1987. Cited in page 125.

[151] Grumstrup, Erik M, Sang Hee Shim, Matthew A Montgomery, Niels H Damrauer e Martin T Zanni: *Facile collection of two-dimensional electronic spectra using femtosecond pulse-shaping technology*. Optics express, 15(25):16681–16689, 2007. Cited in page 125.

[152] Hamm, Peter e Martin Zanni: *Concepts and methods of 2D infrared spectroscopy*. Cambridge University Press, 2011. Cited in page 125.

[153] Cundiff, Steven T e Shaul Mukamel: *Optical multidimensional coherent spectroscopy*. Phys. Today, 66(7):44, 2013. Cited in page 125.

[154] Li, Jun, Mingsen Deng, Dmitri V Voronine, Shaul Mukamel e Jun Jiang: *Two-Dimensional Near Ultraviolet (2DNUV Spectroscopic Probe of Structural-Dependent Exciton Dynamics in a Protein*. The Journal of Physical Chemistry B, 119(4):1314–1322, 2015. Cited in page 125.

[155] Jiang, Jun e Shaul Mukamel: *Two-Dimensional Ultraviolet (2DUV) Spectroscopic Tools for Identifying Fibrillation Propensity of Protein Residue Sequences*. Angewandte Chemie International Edition, 49(50):9666–9669, 2010. Cited in page 125.

[156] Brixner, T, IV Stiopkin e GR Fleming: *Tunable two-dimensional femtosecond spectroscopy*. Optics letters, 29(8):884–886, 2004. Cited in page 125.

[157] West, Brantley A e Andrew M Moran: *Two-dimensional electronic spectroscopy in the ultraviolet wavelength range*. The Journal of Physical Chemistry Letters, 3(18):2575–2581, 2012. Cited in page 125.

[158] Zigmantas, Donatas, Elizabeth L Read, Tomáš Mančal, Tobias Brixner, Alastair T Gardiner, Richard J Cogdell e Graham R Fleming: *Two-dimensional electronic spectroscopy of the B800–B820 light-harvesting complex*. Proceedings of the National Academy of Sciences, 103(34):12672–12677, 2006. Cited in page 125.

[159] Manzoni, Cristian, Rocio Borrego-Varillas, Aurelio Oriana, Giulio Cerullo e Lucia Ganzer: *Two-dimensional spectroscopy in the ultraviolet by a birefringent delay line*. Em *CLEO: Science and Innovations*, páginas SF1I–6. Optical Society of America, 2016. Cited in page 125.

[160] Borrego-Varillas, Rocio, Aurelio Oriana, Lucia Ganzer, Anton Trifonov, Ivan Buchvarov, Cristian Manzoni e Giulio Cerullo: *Two-dimensional electronic spectroscopy in the ultraviolet by a birefringent delay line*. Optics express, 24(25):28491–28499, 2016. Cited in page 125.

# Appendix

# APPENDIX A – Technical Details

In this appendix, we present some details of the sample preparation to avoid sample degradation during the experiments.

## A.1 Number of absorbed photons in the jet experiments

As shown in the Section 3, ultrafast pulses are highly energetic as they concentrate a large energy density over a short period of time. This feature can easily degrade biological samples. Therefore, prior to the start of transient transmission experiments, the concentration of absorbed photons in the time interval of 1h (which is the predicted duration of an experiment) was calculated to compare it with the concentration of molecules in the solution and ensure that during the experiment there would always be healthy molecules, that is, not degraded by light, to be excited. In other words, the sample concentration must be greater than the photon concentration in the solution at the end of the experiment.

To do so, we first calculated the excitation volume that given by the area of the laser spot, with radius $r$ multiplied by the optical path in the solution $l$:

$$r = 50\ \mu m \tag{A.1}$$

$$l = 0.2\ mm \tag{A.2}$$

$$V = \pi r^2 l \tag{A.3}$$

$$V = 1.57 \times 10^{-6}\ ml \tag{A.4}$$

The laser spot was measured with the Coherent Laser Beam Profilers camera and used the Beam View-USB-4.3.1 softwer as an interface. The optical path is the estimated thickness of the sample stream that runs from the jet (see the Figure 15).

Then the number of photons per pulse was calculated, $n$. Considering the pulse energy of $E = 30$ nJ and the excitation wavelength of $\lambda = 340$ nm obtain $5.10^{10}$

$$E = \frac{nhc}{\lambda} \tag{A.5}$$

$$n = 5 \times 10^{10} \tag{A.6}$$

The percentage of photons per pulse absorbed by the sample, considering the optical density of $A = 0.5$ OD, is given by:

$$Abs(\%) = 1 - 10^{-A} = 1 - 10^{-0.5} \tag{A.7}$$

$$n_{abs} = 3.5 \times 10^{10} \tag{A.8}$$

Measurements were made using a 1 kHz repetition rate laser, thus within 1 h there will be $3.6 \times 10^6$ pulses. For each pulse there are $3.5 \times 10^{10}$ absorbed photons by the sample. Then in 1 h of measurement there will be a total of $n_{total} = 12.6 \times 10^{16}$ absorbed photons. Therefore the molar concentration of absorbed photons, $C_n$, by the total sample volume ($V_t = 20$ ml) circulating in the jet will be:

$$C_n = \frac{n_{total}}{V_t N_{avg}} = 1.05 \times 10^5, \tag{A.9}$$

where $N_{avg}$ represents the number of Avogrado.

The photon concentration after 1 h of experiment is two orders of magnitude smaller than the average sample concentrations we used for the measurements (see table 5.1). This increases the likelihood that each molecule will be excited only once during the experiment and consequently decreases the likelihood of degraded molecules in the solution after the experiment.

Still, to ensure that there was no contamination or degradation of the sample during the experiment the linear absorption spectrum was measured before and after each transient transmission experiment.

The same calculations were performed for A = 1 OD and for $\lambda = 275$ nm since measurements were also made with these parameters as previously mentioned (see the Section 5.1)[1].

## A.2 Magic angle in the TTS

Stochastic rotation can appear for molecules in solution due to the liquid phase. If the pump and probe pulses are parallel to each other, the pump finds a distribution of dipole moments aligned in all directions, and those aligned with its polarization will be excited preferentially. As time elapses after excitation, some of the molecules originally excited by the pump will rotate and their dipole will misalign with the original probe polarization. As the probe polarization is the same as the pump, the probe will induce signal emission also only on the molecules that have not yet rotated out of alignment with its polarization, and thus a signal decay due to this rotation will be observed. The timescale of this signal reflects the timescale of the molecular rotation in the sample, and for molecules in a solvent it is typically in the the order of tens to hundreds of picoseconds (depending on molecular size and inertia moment, solvent temperature and viscosity).

If the pump and probe are not parallel polarized, then some excited molecules will align and some will misalign with the probe's polarization as rotation takes place,

[1] Even with A = 1 OD and for paum pulse wavelength $\lambda = 270$ nm, the same conclusions were qualitatively preserved.

meaning that this phenomenon can also originate rising components. What makes the magic angle magical (54.7°) is that exactly the same number of molecules are aligning and misalignment, thereby canceling this effect [149].

## A.3 Experimental setup SHG: 270 nm centered broadband pulses with sub-20 fs duration

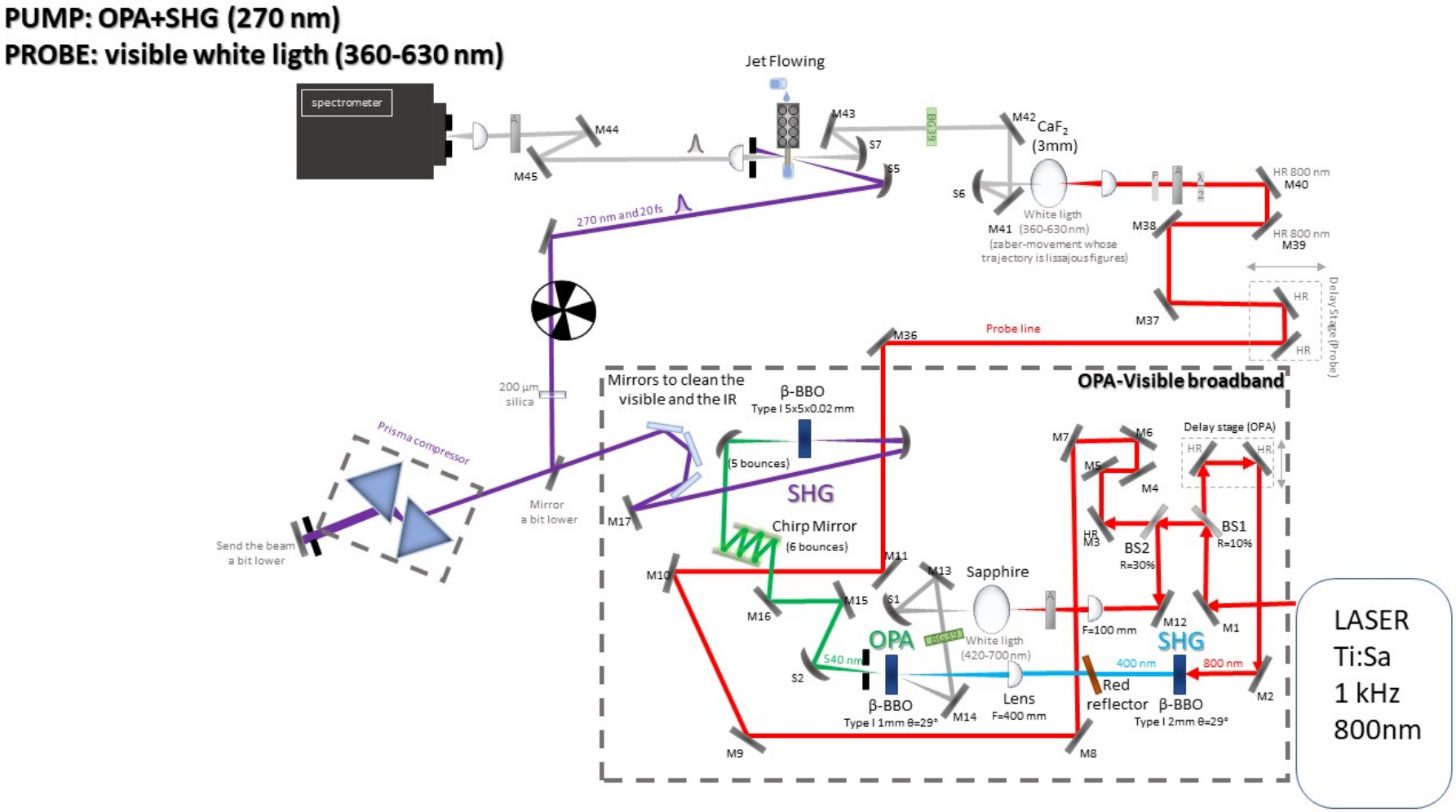



Figure 49 – Experimental setup to generate the 270 nm pump pulses and the visible probe pulses.

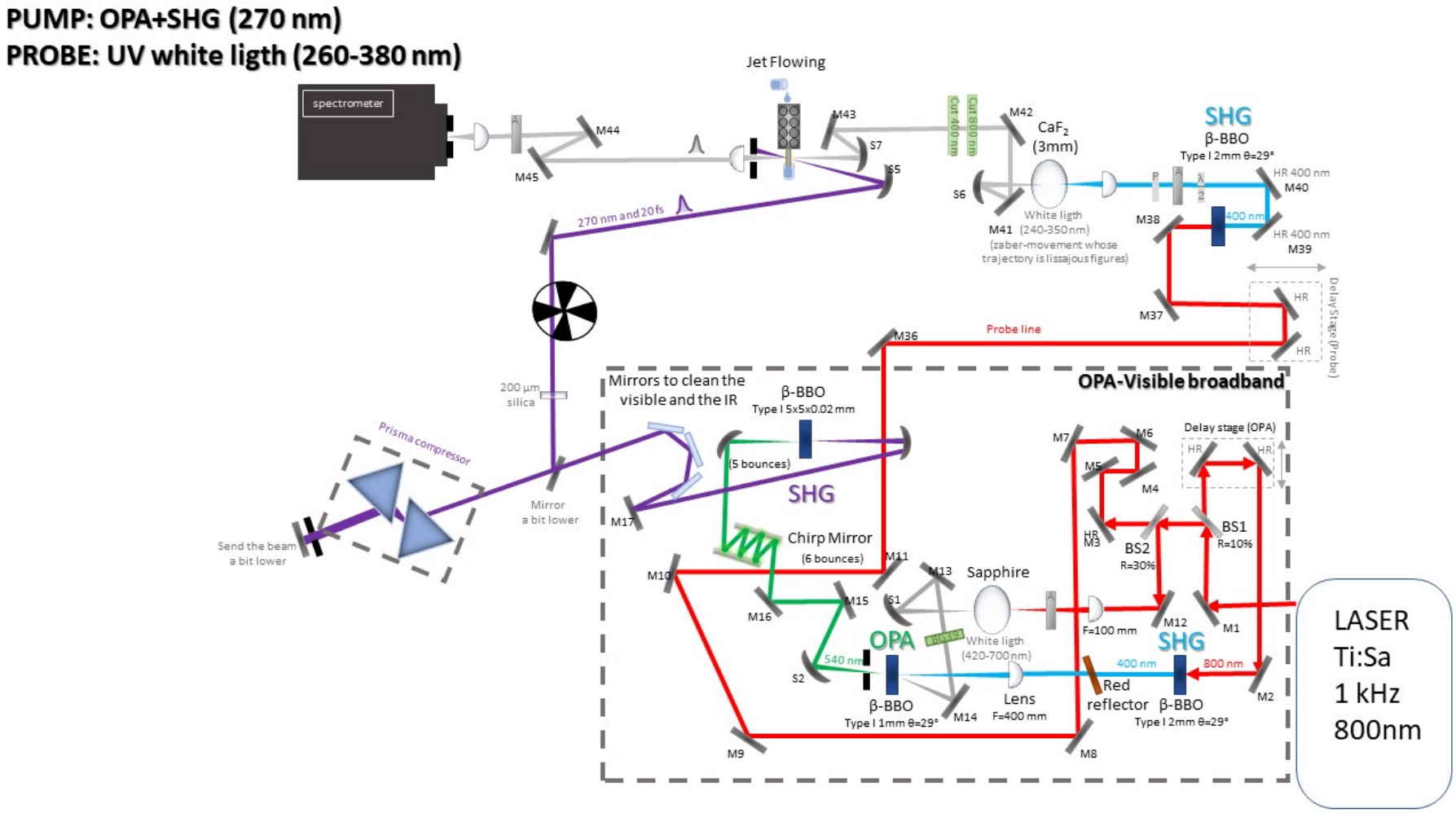



Figure 50 – Experimental setup to generate the 270 nm pump pulses and the UV probe pulses. To generated short pulses centered at 270 nm we used the SHG of the NOPA and to compress the pulses we use prisms in the place of the CM.

# APPENDIX B – Two-dimensional Spectroscopy in the UV Range results

2D spectroscopy was inspired by the Nuclear Magnetic Resonance (NMR) technique. NMR is widely used to determine complex molecular structures [150]. However, the study of system dynamics in NMR is limited due to the duration of radio frequency pulses. But much information can still be gained by extrapolating this same technique to the optical frequency domain and using ultra-short light pulses [151]. The 2D electron spectroscopy technique is based on the initial concepts of pump probe discussed before. However, this technique uses two ultra-short and collinear pumping pulses and one non-collinear test pulse. The measurement consists of detecting the transmission of the test pulse as a function of the delay of the pumping pulses.

The first application of this technique was for infrared range that allows to measure the coupling of vibrational modes of some molecules [152]. This captured transient structures in the femtosecond range. Subsequently, the 2D optical technique was employed for the visible region to study the electronic transitions of materials as semiconductors [153]. Recently, this technique has been extended to the ultraviolet range to study biomolecules such as proteins and nucleic acids [5, 154, 155]. In this context, the 2D spectroscopy technique in the UV wavelength range is called 2DUV. However, there are some challenges encountered during the implementation of this technique in the UV range. These include: adequate laser line width, interferometric phase stability, and spread-induced scattering in the UV range. Therefore, few papers are reported for the UV region. [156]. Overcoming such problems is motivated by the large amount of biological systems they absorb in the UV range such as DNA/RNA and various proteins. [157]. The main advantages of using this technique are: it makes it possible to extract inhomogeneous line widening and to measure the homogeneous line width of the optical transition, thus facilitating the identification of individual levels; distinguish the contribution of spectrally overlapping signals in 1D experiments; obtain high temporal and spectral resolution within Fourier limits; the way the system evolves after photoexcitation; obtain coupling information between different excited states that appear as cross peaks in the 2D spectrum and thereby obtain structural information of the system in question; the way the system evolves after photoexcitation [152, 158].

The experimental setup for the 2DUV system is the same as the setup described in the Chapter 4 [159, 160]. To use the 2DES-UV configuration it is just to scan the delay between the two replicas.

Using this assembly it is possible to measure, with the aid of a spectrometer, the transmission of the probe pulse. Thus, after the Fourier transform of the delay between the two pump pulses, it is possible to obtain a frequency map. In other words, in such technique, the information content of the nonlinear signal is spread along two frequency axes. One of the simplest schemes is the partially pump-probe geometry, where two phase-locked pump pulses with variable delay $\tau$ excite the sample. The transmission (absorption) of the probe beam is detected by a spectrometer as a function of the delay between the two pump pulses, obtaining an interferogram as a function of $\tau$ and the probe wavelength. A Fourier transform along the $\tau$-axis resolves the transmission signal as a function of the pump and probe wavelengths. This two-dimensional map is measured for each delay T between pump and probe (therefore a transient spectra at a delay T in a normal pump-probe measurement, corresponds to the map integrated along the pump frequency axis). We have done a preliminary test on 4-thiouracil using the recently developed 2DES in the UV setup in Milan. Figure 51 shows three representative maps at delays T= 75, 200 and 600 fs.

By plotting the temporal evolution of one the points of the previous maps, we will obtain the kinetics at a given probe wavelength for a certain pump frequency. In the following figures, we have plotted the kinetics for pump wavelengths of 325 nm (blue) and 345 nm (red) for two representative probe wavelengths of the stimulated emission (424 nm, left panel) and the photoinduced absorption (628 nm, right panel) bands. From this preliminary test, we could not find any differences on the timescale of the ISC as already measured by the pump-probe spectroscopy.

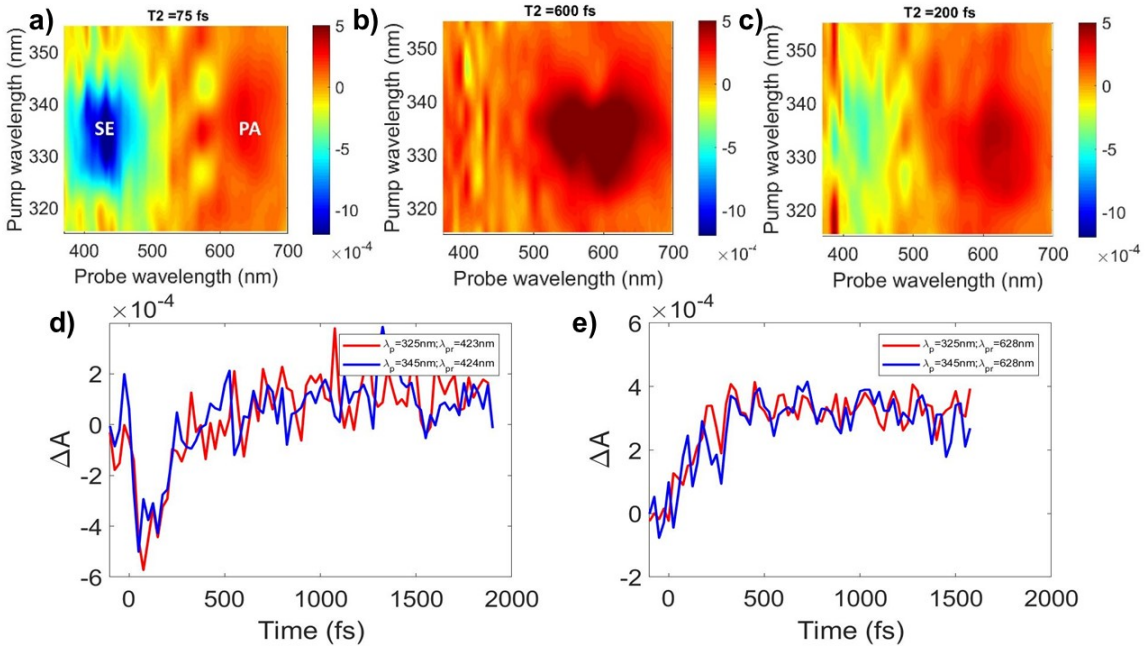



Figure 51 – Results in ΔA. a) b) c) 2DES maps at different probe T delays, d) Kinetics for pump wavelengths of 325 nm (blue) and 345 nm (red) for two representative probe wavelengths of the stimulated emission (424 nm) e) Kinetics for pump wavelengths of 325 nm (blue) and 345 nm (red) for two representative probe wavelengths of the photoinduced absorption (628 nm) bands.

# APPENDIX C – Transient Transmission Spectroscopy with long pulses results

Here we show the results using a setup with 100 fs pulse. In order to obtain pump pulses with narrow bandwidth at 266 nm we assembled a setup to submit the fundamental beam (at 800 nm) to the Third Harmonic Generation (THG) process and to get pump pulses with narrow bandwidth at 330 nm another setup was builded with the SHG of the NOPA centered at 660 nm. To both setups the probe pulses are the UV white light. Our goal with these measurements was to try to obtain the information about the lifetime from the triplet state, that would allow to complete the characterization of the thiobases dynamics. For that we use different setups described at the Chapter 4 where the delay stage enables to get 1 ns of the time delay between the pump and probe. We use the pump pulses in the 330 nm and 270 nm and we probe with pulses in the UV range (280-340 nm). The obtained results are presented in the Figure 52.

However, we had several technical issues that did not allow us to get the information we were looking for. We will discuss some of them here:

- In this setup the fundamental laser has 5 times less power than the one in the sub-20 fs UV setup. Thus, the probe in the UV, that uses the SHG of the fundamental is very weak and the measurements are too noisy.

- For these measurements, it is really important use the magic angle (54.7°) between the pump and probe, because with other polarization configuration the dynamics are completely corrupted by the molecular rotational motion. However, the magic angle could not be exactly implemented due to the polarizer setup that is able to set only integer values. Details about the magic angle are presented in the appendix A.2.

- Although the set up is no collinear, some scattered pump could be observed in the measurements. However, no filter or polarizer could be used to block the pump, since it would also make the probe even more weak and it could not be detected by the spectrometer.

Due to that above reasons, it was not possible to extract more information from the long pulse measurements than we already had with the short-pulse setup.

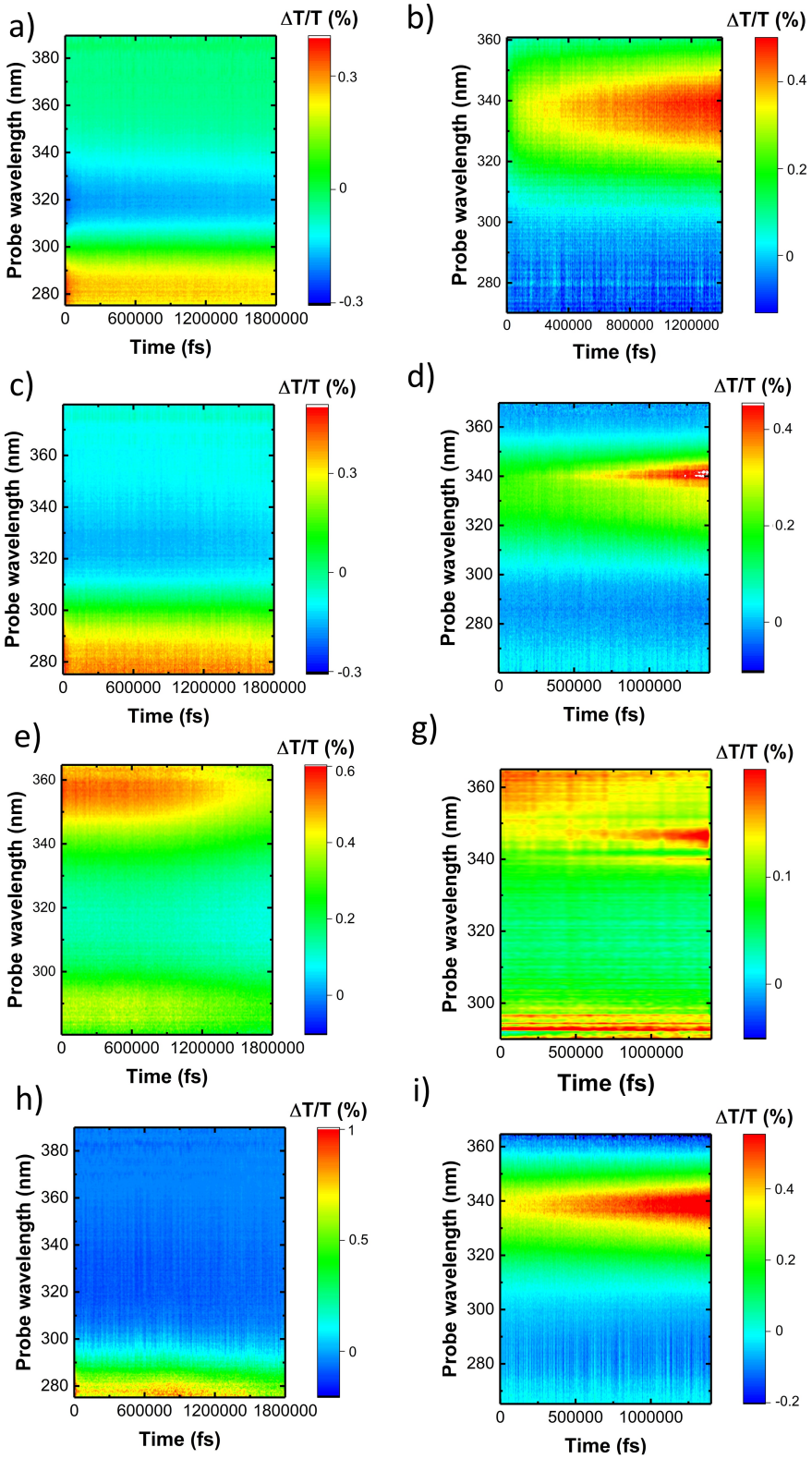



Figure 52 – 2D map obtained with the long pulses set up. the maps in the right side refer to the sample pump at 330 with the SHG of the OPA and in the left side refers to the samples pump at 266 nm with the THG. a) 2TT b) 4TT c) 2TU d) 4TU e) 24TU pump at 267 nm f) 24TU pump at 330 nm g) 2TC and h) 6TG.

# Annex

# ANNEX A – Thesis-related articles published during the Ph.D

JACS
JOURNAL OF THE AMERICAN CHEMICAL SOCIETY
Article
Cite This: J. Am. Chem. Soc. 2018, 140, 16087−16093
pubs.acs.org/JACS

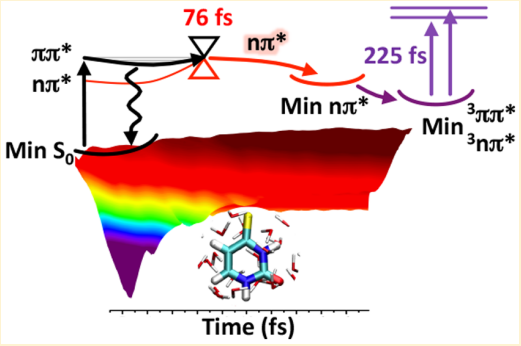
# Observation of the Sub-100 Femtosecond Population of a Dark State in a Thiobase Mediating Intersystem Crossing

Rocío Borrego-Varillas,[†,#] Danielle C. Teles-Ferreira,[‡,#] Artur Nenov,[§,#] Irene Conti,[§,#] Lucia Ganzer,[†] Cristian Manzoni,[†] Marco Garavelli,[*,§] Ana Maria de Paula,[*,‡] and Giulio Cerullo[*,†]

[†]IFN-CNR, Dipartimento di Fisica, Politecnico di Milano, Piazza Leonardo da Vinci 32, I-20133 Milano, Italy
[‡]Departamento de Física, Universidade Federal de Minas Gerais, 31270-901 Belo Horizonte-MG, Brazil
[§]Dipartimento di Chimica Industriale, Università degli Studi di Bologna, Viale del Risorgimento 4, I-40136 Bologna, Italy

Supporting Information

**ABSTRACT:** We combined sub-30 fs broadband transient absorption spectroscopy in the ultraviolet with state-of-the-art quantum mechanics/molecular mechanics simulations to study the ultrafast excited-state dynamics of the sulfur-substituted nucleobase 4-thiouracil. We observed a clear mismatch between the time scales for the decay of the stimulated emission from the bright $\pi\pi^*$ state (76 ± 16 fs, experimentally elusive until now) and the buildup of the photoinduced absorption of the triplet state (225 ± 30 fs). These data provide evidence that the intersystem crossing occurs via a dark state, which is intermediately populated on the sub-100 fs time scale. Nonlinear spectroscopy simulations, extrapolated from a detailed CASPT2/MM decay path topology of the solvated system together with an excited state mixed quantum-classical nonadiabatic dynamics, reproduce the experimental results and explain the experimentally observed vibrational coherences. The theoretical analysis rationalizes the observed different triplet buildup times of 4- and 2-thiouracil.




## INTRODUCTION

Thiobases[1,2] are DNA or RNA nucleobases where an exocyclic carbonyl oxygen is replaced by a sulfur atom. They have attracted much attention in recent years due to their biological relevance and their increasing amount of applications.[3] They have been used to improve polymerase chain reaction for DNA/RNA replication[4,5] and as cross-linking chromophores for investigation of specific interactions between nucleic acids and proteins.[6,7] Thanks to their near-unity triplet yields, they have been also demonstrated as potent chemotherapeutic agents[8−10] for the treatment of some types of nonmalignant hyperproliferative skin conditions and cancers. Besides their practical applications, they provide an excellent model system to understand how a single atom substitution can modify the energy relaxation pathways of the canonical DNA/RNA nucleobases. In comparison to the canonical nucleobases, thiation causes a red-shift in the absorption spectrum to the 280−400 nm range, leading to remarkable changes in the photophysics:[11−18] while in DNA/RNA monomers excited state deactivation occurs on an ultrafast time scale through a high rate of $S_1 \rightarrow S_0$ internal conversion,[19−21] the major relaxation pathway in thiobases is via the population of long-lived triplet states through intersystem crossing (ISC)[14] occurring on the subpicosecond time scale.

Over the past decade, major efforts, both experimental[12−16,22−28] and computational,[12,16,23,24,27,29−39] have been made to gain deeper understanding of the energy relaxation pathways and triplet state formation mechanisms in thiobases. Computational studies have suggested that the bright $\pi\pi^*$ state relaxes on the sub-100 fs time scale by means of a conical intersection (CI) to a dark singlet $n\pi^*$ state, which acts as a doorway to the triplet manifold. Such mechanism has been proposed for a number of thiobases, including 2-thiouracil,[23,24] 4-thiothymine,[16] 2-thiothymine,[31] 2,4-dithiothymine,[32] 2-thiocytosine,[36] and 6-thioguanine.[30] While the femtosecond dynamics of the triplet states formation through ISC have been measured,[14,16,35] so far there has been a lack of ultrafast spectroscopy data with sufficiently high temporal resolution to access the time scale of population of the dark state, proposed theoretically, to mediate ISC. Molecular dynamics simulations suggest time scales for this process ranging from sub-100 fs[39] to several picoseconds.[16]

Here, we combined broadband transient absorption (TA) spectroscopy featuring a sub-30 fs instrumental response function in the ultraviolet (UV) with hybrid quantum mechanics/molecular mechanics (QM/MM) state-of-the-art computational tools to study the ultrafast photoinduced dynamics of 4-thiouracil. We provide experimental evidence, quantitatively supported by the computational results, that ISC

Received: July 9, 2018
Published: October 31, 2018

Downloaded via UNIV FED DE MINAS GERAIS on March 15, 2019 at 12:10:40 (UTC).
See https://pubs.acs.org/sharingguidelines for options on how to legitimately share published articles.


© 2018 American Chemical Society

DOI: 10.1021/jacs.8b07057
J. Am. Chem. Soc. 2018, 140, 16087−16093

occurs predominantly via a dark state of nπ* character that is intermediately populated on the sub-100 fs time scale from the bright photoexcited ππ* state.

## MATERIALS AND METHODS

**Sample Preparation.** 4-Thiouracil (97% purity) was purchased from Sigma-Aldrich and used as received. A phosphate-buffered saline (PBS) solution was prepared by dissolving 0.15 g of sodium dihydrogen phosphate and 0.27 g of sodium hydrogen phosphate in 200 mL of ultrapure water to obtain a pH 7.4 and a concentration of 16 mM. The 4-thiouracil in PBS solution was prepared to obtain a concentration of 6 mM, resulting in an absorbance of 2 OD at the central pump wavelength. The steady-state absorption spectrum is provided in the Supporting Information (SI) section 3.

**Experimental Setup.** TA spectra measurements were carried out on a homemade pump−probe setup based on a regeneratively amplified Ti:sapphire laser (Libra, Coherent) at 800 nm wavelength with 100 fs pulse duration and 1 kHz repetition rate. A detailed description of the system can be found in ref 40. Briefly, a fraction of the laser beam is sent to a noncollinear optical parametric amplifier (NOPA) whose output covers a broad bandwidth in the visible range (520−720 nm). The visible pulse and a fraction of the fundamental pulse are focused and mixed on a 50-μm-thick Type II β-barium-borate crystal to generate UV light by sum frequency.[41] The spectrum of the so-generated UV pulse spans from 320 to 360 nm (Figure S7 of the SI). A two-dimensional spectral-shearing interferometry measurement[42] revealed a duration of 16 fs. To avoid photodamage of the sample and generation of solvated electrons by two-photon absorption from water, the pump energy was limited to 27 nJ (resulting in a fluence of ∼340 $\mu J/cm^2$), and a flowing jet configuration (0.2 mm path length) was employed. The sample was flown at a typical rate of 40 rpm. A broadband probe is obtained through white light continuum generation by focusing either the fundamental beam or its second harmonic in a slowly moving $CaF_2$ plate. The white light spectrum extends respectively in the visible (350−670 nm) or in the ultraviolet range (250−380 nm). After the sample, the transmitted probe is sent to a spectrometer (SP2150 Acton, Princeton Instruments) and detected using a linear image sensor driven and read out by a custom-built electronic board (Stresing Entwicklungsburo GmbH). For each probe wavelength, the differential absorption (Δ$A$) is measured as a function of the pump−probe time delay. For the experiments reported, the measurements were performed with parallel pump and the probe polarizations. Experiments performed for crossed and magic angle (Θ = 54.7°) polarizations did not show any significant change in the dynamics.

**Global Analysis.** The acquisition of transient absorption spectra produces a 2D map of the differential absorption (Δ$A$) as a function of the wavelength and the time delay. A global analysis of the data, performed using the Glotaran software,[43] allows for extracting the time constants governing the dynamics over the entire data set. A two-dimensional (2D) Fourier transform of the residuals of the global fit was performed to study the excited-state coherent oscillations.

## COMPUTATIONAL METHODS

**Classical Molecular Dynamics.** The 4-thiouracil starting geometry was obtained running a classical molecular dynamics simulation, using the AMBER 12 suite[44,45] with the ff10 force field. Periodic boundary conditions were applied to a 40 × 39 × 35 Å periodic box containing 1210 water molecules, described by the TIP3P force field.[46] The hydrogen-containing bonds were restrained by the SHAKE algorithm,[47] while the water geometry was rigidized by the SETTLE scheme.[48] Nonbonding and electrostatic interactions were evaluated with a cutoff of 9 Å, making use of the particle mesh Ewald method for quantification of the long-range electrostatics. The time step was set to 0.5 fs, and integration of the equations of motion was done with the leapfrog algorithm. Thermalization of the systems was reached by heating of the preoptimized system to 300 K in 15 ps steps of 100 K. A production run at 300 K and 1 atm was carried out for 500 ps. The lowest energy structure along the dynamics was selected as a starting point for subsequent QM/MM refinement.

**QM/MM Calculations: Geometry Refinement and Electronic Structure Computations.** QM/MM calculations were executed with the COBRAMM program, developed in our group interfacing various QM codes with AMBER.[49] A High/Medium/Low layers partitioning was applied to a spherical droplet centered at 4-thiouracil with a radius of 12 Å (containing 245 waters), obtained from the cubic box. The QM region comprises the thionucleobase. The water molecules in 3 Å distance were included in the movable Medium (MM) layer. The remaining water molecules were kept fixed in the (MM) Low layer. Ground state geometry minimum was obtained at the Møller−Plesset second order perturbation theory (MP2) level. The geometry optimizations were computed at the MS-CASPT2[50] level using an active space including the sulfur lone pair and the valence π-orbitals to a total of 12 electrons in 9 orbitals (Figure S6 in the SI). The ANO-L basis set was used,[51] adopting contractions 5s4p2d1f on sulfur, 4s3p2d1f on carbon/oxygen/nitrogen, and 3s2p1d on hydrogen atoms. State-average was performed over the lowest five states. The electronic structure at critical points was refined through a larger active space, extended by the lone pair of the oxygen and a pair of bonding and antibonding carbon−sulfur σ orbitals to a total of 16 electrons in 12 orbitals (Figure S6 in the SI), together with an enlarged ANO-RCC basis set,[52] adopting the contractions 6s5p3d2f1g on sulfur, 5s4p3d2f1g on carbon/oxygen/nitrogen, and 4s3p2d1f on hydrogen atom contractions. Thereby, seven states were included in the state-averaging. The CASPT2 computations at critical points were performed both in the single-state and multistate flavor. Thereby, the ionization-potential-electron-affinity (IPEA) shift[53] was set to 0.0, and an imaginary shift[54] of 0.2 au was used throughout. The Cholesky decomposition was adopted to speed the evaluation of two-electron integrals.[56] CI optimizations were performed with the gradient projection algorithm of Bearpark et al.[55] implemented in COBRAMM. All calculations were performed using the Molcas 8 package through its interface with COBRAMM.[56]

**Sampling and Nonadiabatic Mixed Quantum-Classical Dynamics Simulations.** For each system, 500 initial conditions were generated using the Wigner sampling technique through an interface with a stand-alone script, part of the quantum molecular dynamics program JADE,[57] which considers temperature effects and mode-specific excitation. Consequently, sampling was performed at room temperature (300 K). High frequency modes, belonging to C−H and N−H stretchings, were excluded from the sampling. Additionally, one normal mode with a very low frequency (<100 $cm^{-1}$) was excluded from the sampling as it was asserted through preliminary sampling that displacement along this mode breaks the harmonic approximation and distorts excessively the geometry. Each realization was subjected to a 100 ps long MM equilibration run in which the QM region was kept fixed through harmonic constraints. This strategy allows the mobile MM region to adapt to each sampled geometry, thereby removing the bias of the water arrangement of the initial snapshot. The water coordinates of the last snapshot of the MM equilibration run were combined with the sampled thiouracil geometry to form the snapshot used to compute the electronic properties.

We recently documented a detailed study on the dependence of the linear absorption (LA) spectrum of 4-thiouracil on various parameters (active space, protocol (SS-CASPT2 vs MS-CASPT2), basis set).[18] Based on this study, we conclude that the SS-RASPT2/SA-3-RASSCF(12,9|2,4) level of theory, comprising all valence π-orbitals, the lone pair of the sulfur, and four extra-valence virtual orbitals with up to double excitations in the latter is best suited for the dynamics simulations due to the very good agreement between simulated and experimental LA spectra,[18] whereas the full-valence active space red-shifts the absorption band of the lowest bright ππ* state by 20 nm. Thirty geometry realizations for which the $^1\pi\pi^*$ ($S_2$) transition falls under the envelope of the pump pulse (Figure S20 in the SI) were selected, and for each, a 180 fs long nonadiabatic mixed quantum-classical molecular dynamics simulation following Newton's equations


DOI: 10.1021/jacs.8b07057
J. Am. Chem. Soc. 2018, 140, 16087−16093

of motion for the nuclei and utilizing hybrid QM/MM gradients was performed at the SS-RASPT2/SA-3-RASSCF(12,9|2,4) level of theory with a time step of 1.0 fs applying the Tully's fewest switches surface hopping algorithm[58] with the Tully–Hammes–Schiffer scheme[59] using the COBRAMM's parallel environment for computing numerical gradients (details in the SI section 1.2). The state averaging covered the ground, the lowest (dark) $n\pi^*$ ($S_1$) and the lowest (bright) $\pi\pi^*$ states ($S_2$), and the dynamics was always initiated in the $S_2$ state. The movable (MM) water layer was extended to 5 Å to accommodate pronounced distortions of the aromatic ring.

**Spectroscopy Simulations.** The $\Delta A$ signal was computed as the marginal (with respect to the delay time $t_1$) of the two-dimensional Fourier transform (with respect to $t_1$ and $t_3$) of the nonlinear response of the system, which becomes equal to the third-order signal within the limit of temporally well-separated ultrashort laser pulses (impulsive limit). The nonlinear response can be expressed within the framework of the cumulant expansion of Gaussian fluctuations (CGF)[60−62] (the working equations can be found in the SI section 1.3). It allows for calculating the shapes of electronic transition bands coupled to a bath for fluctuations with arbitrary time scales by using the formalism of line shape functions when the fluctuations follow Gaussian statistics. The spectral diffusion is described via composite line shape functions, consisting of a portion describing the vibrational progressions in the spectra due to undamped molecular vibrations represented through the multidimensional uncoupled displaced harmonic oscillator (DHO)[61,63] and a portion describing the homogeneous broadening due to a coupling to a continuum of low-frequency modes, represented by the line shape function of the semiclassical Brownian oscillator (OBO).[61,63,64] DHO parameters necessary to describe the spectral dynamics were obtained from electronic structure calculations within the RASSCF/RASPT2 framework (see SI sections 1.3.4 and 1.3.5). OBO parameters were chosen to reproduce the linear absorption spectrum of the $\pi\pi^*$ state at room temperature (Figure S7 in the SI). Further details are provided in the SI (section 1.3.6). Population relaxation processes are described by the Pauli master equation solved for a sequential model that describes the decay of the dominant part of the population via the path $S_2 \rightarrow S_1 \rightarrow T_1$ (section 1.3.2 in the SI). The secondary path $S_2 \rightarrow T_2 \rightarrow T_1$ was neglected in the simulations as it gives rise only to weak photoinduced absorption contributions. Spectra simulations were performed with a development version of Spectron 2.7.[62]

## RESULTS AND DISCUSSION

Figure 1 shows the experimental (Figures 1A, B) and theoretical (Figures 1 C, D) two-dimensional (2D) maps of the differential absorption ($\Delta A$) signal of 4-thiouracil dissolved in a phosphate saline buffer (PSB) solution at pH 7.4. The upper panel in (A) shows the dynamics at 400 and 600 nm (dotted lines in the map), and the upper panel in (C) shows the calculated $S_2(\pi\pi^*)$ population decay. Immediately after the pump pulse, we observe a negative signal, which is assigned to the superposition of two bands: the tail of the ground state bleaching (GSB) band at 360 nm and a stimulated emission (SE) band peaking around 400 nm. The GSB is associated with depletion of the ground state after excitation of $S_2$. The SE is assigned to the bright $S_2$ state photoexcited by the pump ($\pi\pi^*$ transition). An additional excited state absorption (ESA) signature of $S_2$ at around 275 nm was found by probing in the UV (see SI section 4.5). The pump pulse populates the lowest $\pi\pi^*$ state in the Franck–Condon (FC) region. The vibrational dynamics in this bright state gives rise to intensity beats in the SE signal, whose central wavelength (400 nm) matches also the energy gap at the $\pi\pi^*$ state minimum (Min $\pi\pi^*$).

Both the SE (Figure 1) and the ESA (Figures S24 and S25) bands associated with $S_2$ display a first ultrafast decay on the sub-100 fs time scale, which is followed by the delayed buildup

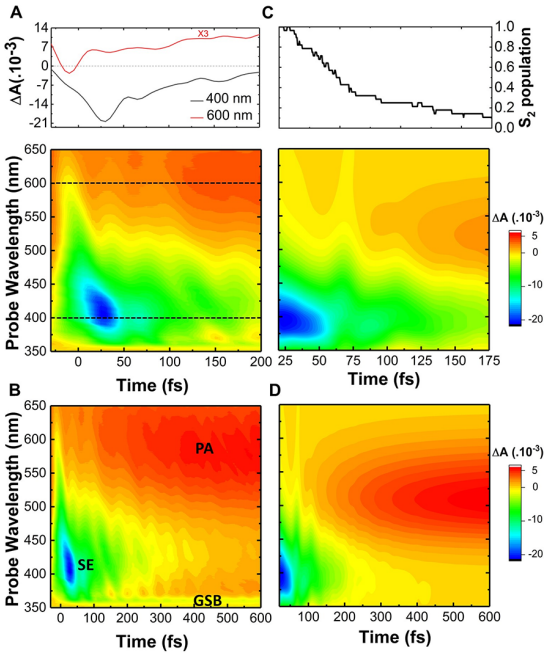



**Figure 1.** ΔA maps of 4-thiouracil in PBS solution. Experimental panels: A (short scale from −30 fs until 200 fs) and B (long scale from 30 fs until 600 fs). Simulated panels: C (short scale) and D (long scale). Upper panel in (A) shows the dynamics at 400 and 600 nm (dotted lines in the map), upper panel in (C) shows the calculated $S_2(\pi\pi^*)$ population decay.

of a photoinduced absorption (PA) band around 600 nm on the ∼500 fs time scale. The dynamics at 400 and 600 nm are shown in Figure 1A. The PA band, whose buildup has been observed in previous studies with a lower 200 fs time resolution,[14] has been assigned to triplet–triplet absorption, thus providing a fingerprint of the ISC. Following its formation, the PA band undergoes a blue-shift on the subpicosecond time scale (Figure 2A), which is assigned to vibrational cooling of the long-lived[65,66] triplet state.

Our experimental data clearly show a mismatch between the decay time of the SE and the buildup time of the PA signal, thus delivering an experimental confirmation that ISC does not occur directly from the photoexcited bright $\pi\pi^*$ state but is predominantly mediated by an intermediate dark state as proposed by previous theoretical works.[16,23,31−33,35,36,39]

Figure 2B shows the decay associated spectra (DAS) obtained by a global fit of the data, revealing time constants of 76 ± 16 and 225 ± 30 fs. The 76 fs time constant (black line) is attributed to the decay of the SE band. The 225 fs DAS band between 500 and 650 nm is associated with the subsequent triplet PA formation. A long living component was fixed as an offset to account for the decay beyond our time observation window. This offset is therefore related to the long-living triplet state.

At all wavelengths, the ΔA signal is modulated by a complex oscillatory pattern that is assigned to vibrational coherences impulsively excited by the sub-20 fs pump pulse (Figure 2 C).To extract the frequencies of the observed coherent oscillations, we performed a 2D Fourier analysis of the oscillatory component of the spectra. To separate this component, we subtracted from the experimental data the exponential decay part obtained from the fit (see more details


DOI: 10.1021/jacs.8b07057
J. Am. Chem. Soc. 2018, 140, 16087−16093

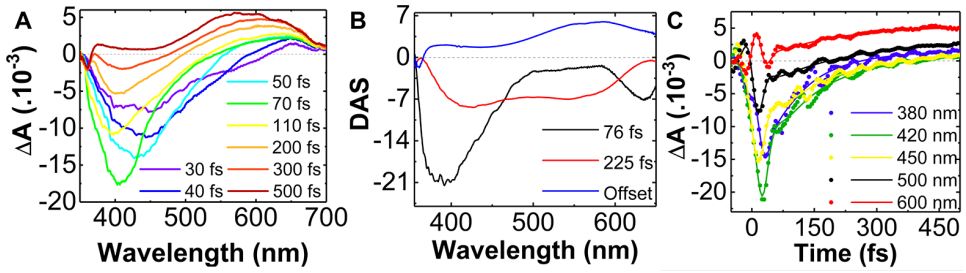



**Figure 2.** (A) ΔA spectra of 4-thiouracil at selected time delays. (B) DAS obtained by global analysis. (C) Dynamics at given wavelengths: experimental data (dots) fitted by a global analysis (solid line).

in the SI). Figure 3 A shows the obtained 2D map showing two modes with frequencies of 680 and 400 $cm^{-1}$, which are in agreement with the Fourier transform of the simulated spectra. To shed light into the underlying molecular deformations, we ran a limited ensemble of 30 room temperature trajectories employing Tully's fewest switches surface hopping algorithm (see SI Figures S9–S12, a representative trajectory depicted in the lower panel of Figure 4). A decomposition of the ground state-$\pi\pi^*$ energy gap dynamics along each trajectory into contributions from the individual normal modes within the framework of the DHO model (SI, section 2.5) allows for identifying the normal modes responsible for the coherent beatings of the SE. In particular, we observed coherent dynamics in the 457 $cm^{-1}$ breathing mode and in two hydrogen-out-of-plane (HOOP) bending modes with frequencies 697 and 784 $cm^{-1}$ (Figure 3B), in good agreement with the experimentally observed frequencies. We associated both HOOP modes with the 680 $cm^{-1}$ frequency in the 2D Fourier transform.

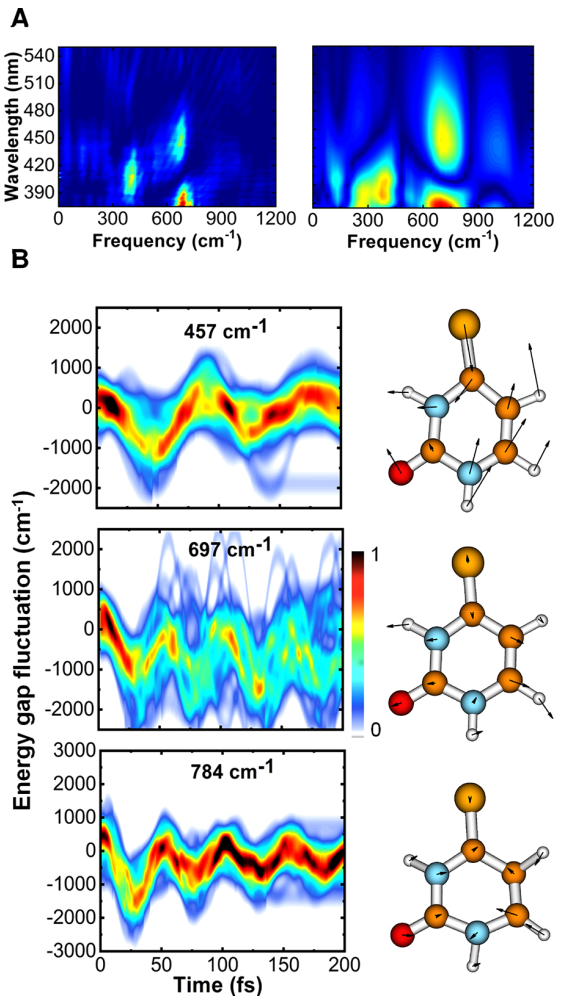



**Figure 3.** (A) 2D Fourier transform of the residuals of the experimental (left) and theoretical (right) Δ*A* dynamics. (B) Coherent energy gap fluctuations along selected vibrational modes at 457 $cm^{-1}$ (ring breathing), 697 $cm^{-1}$ (H7 and H11 HOOP bending), and 784 $cm^{-1}$ (H7, H11, and H12 out-of-plane). The breathing mode gives rise to the 400 $cm^{-1}$ peak in the 2D Fourier transforms, while both HOOP modes are responsible for the 680 $cm^{-1}$ peaks. Intensities associated with trajectory density.

The population of the $\pi\pi^*$ singlet state is ballistically driven toward the $n\pi^*$ singlet state through a sloped CI separated from the minimum by ca. 0.2 eV barrier (Figure 4). The population decay dynamics (Figure 1C) is fitted with a time constant of 67.5 fs in agreement with the 76 fs time constant extracted from the global analysis. This ultrafast decay is remarkable considering the relatively large $S_2/S_1$ energy gap of 1.0 eV at the $S_0$ equilibrium. We note, however, that already the sampling of vibrational degrees of freedom in the 330–360 nm pump window decreases the $S_2/S_1$ gap to about 0.5 eV (see Figure S8). The molecular dynamics simulations show that the access to the CI seam is facilitated through bond stretching deformations (mainly $C_5$–$C_6$ and $C_4$–S elongation) and occurs in half of the trajectories within one to two periods of the oscillation (section 2.3 in the SI). Thereby, the $\pi\pi^*/n\pi^*$ crossings are characterized by significantly elongated $C_5$–$C_6$ and $C_4$–S bond lengths with values well beyond the $\pi\pi^*$ equilibrium (Figure S19 in the SI). Consequently, 4-thiouracil does not have time to redistribute the energy into out-of-plane modes during the ultrashort life span of the $S_2$ state. This scenario is supported by the very good agreement between theory and experiment regarding the vibrational features extracted out of the TA spectra (Figure 3A). The only vibrational modes below 1200 $cm^{-1}$ observed experimentally could be unequivocally assigned to ring breathing and hydrogen out-of-plane vibrations, which preserve the planarity of the ring. The lack of further vibrational signatures in the 2D Fourier transform maps suggests that no ring-distortion modes, which would carry their characteristic frequencies, are involved. The in-plane decay mechanism is in line with the results of CASPT2 dynamics simulations by Mai et al.[39] on 2-thiouracil, who also report a sub-100 fs $\pi\pi^*$ lifetime originating from competing $S_2 \rightarrow S_1 \rightarrow T_1$ and $S_2 \rightarrow T_2 \rightarrow T_1$ pathways, the former being more efficient (ca. 75%). On the contrary, semiempirical simulations on the closely related 5-methyl-4-


DOI: 10.1021/jacs.8b07057
J. Am. Chem. Soc. 2018, 140, 16087–16093

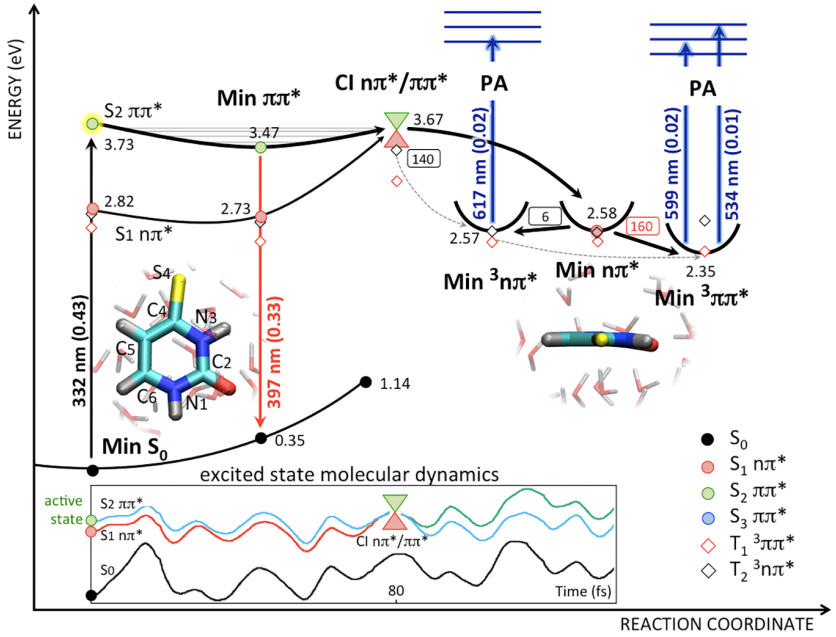



**Figure 4.** CASPT2/MM decay path from the lowest $\pi\pi^*$ bright state ($S_2$ at the FC point) of 4-thiouracil in water. Vertical black arrow indicates the absorption wavelength of the lowest bright state $S_2$ at the FC point. Red arrow indicates the stimulated emission out of the minimum on the lowest $\pi\pi^*$ bright state. Blue arrows indicate the photoinduced absorption from the triplet minima, giving rise to the excited state absorption band between 500 and 650 nm in the transient absorption spectra (see Figures 1 B, D). Dashed gray arrows show the secondary decay path involving $S_2 \rightarrow T_2 \rightarrow T_1$ transitions. Spin−orbit couplings are highlighted in text boxes. Inset: a representative trajectory of nonadiabatic molecular dynamics showing the energies of the electronic states [ground ($S_0$, black), $n\pi^*$ (S1, red), and $\pi\pi^*$ ($S_2$, green)] at the geometries sampled along the dynamics. The "active" state, i.e. the state responsible for the quantum feedback on the nuclei, is shown in light blue. The dynamics is initiated in the $S_2$ state (i.e., the initial vibrational dynamics is driven by the potential energy surface of the $\pi\pi^*$ state); after ca. 80 fs, it reaches the CI through which it decays to $S_1$.

thiouracil see ring-twisting deformations, which occur on a picosecond time scale, essential for reaching the $\pi\pi^* \rightarrow n\pi^*$ crossing seam.[16]

Upon decay to the $n\pi^*$ state, the high frequency stretching modes exhibit partial damping on the 180 fs time scale of the simulation, whereas low frequency ring-puckering modes are activated (see Figure S16 in the SI) and the system can explore regions beyond the planar minimum (Min $n\pi^*$ in Figure 4). Virtually everywhere on the accessible $n\pi^*$ potential energy surface, the $n\pi^*$ is found to be isoenergetic with two triplet states of $^3n\pi^*$ and of $^3\pi\pi^*$ nature, respectively (black and red diamond labels in Figure 4). Hence, the $n\pi^*$ state acts as a doorway for the effective population of the triplet manifold. The $^1n\pi^*/^3\pi\pi^*$ ISC is facilitated by a 160 $cm^{-1}$ spin−orbit coupling. The longer time constant of 225 fs is assigned to the buildup of the PA from the $^3\pi\pi^*$ triplet state around 600 nm (Figure 1B), supported by our static computations revealing higher lying states in the triplet manifold (marked in blue in Figure 4) being the source of a PA around 525 nm in the simulated spectra (Figure 1D). We note that the $^1n\pi^*$ state is completely dark in the probed spectral window as it exhibits only one weak PA signal at 376 nm, which falls under the much more intense GSB/SE band. While we cannot make a conclusive assignment for the 400−425 nm band present in the 225 fs DAS, we propose two possible explanations for this band. One is a small component of $S_2$ population unable to reach the CI seam, which remains in $S_2$ for a longer time, giving rise to a residual SE signal. Another possibility is the population of the $T_2$ triplet state, which is nearly degenerate with $T_1$. As it can be seen in Table 1, $T_2$ presents ESA signal at 397 nm, which could contribute to the 400−425 nm peak in the 225 fs DAS and to the positive component in the offset DAS in the same wavelength region.

In the present work, the presence of the possible secondary decay channel $S_2(^1\pi\pi^*) \rightarrow T_2(^3n\pi^*) \rightarrow T_1(^3\pi\pi^*)$ (involving at least 13−25% of the population[16,31]) is mapped only statically at the QM/MM level (dashed gray arrows in Figure 4). While at the $S_2$ minimum the $S_2/T_2$ and $S_2/T_1$ energy gaps are rather large (0.8−1.0 eV), thus making an ISC rather inefficient in

**Table 1. Energetics (nm) and Oscillator Strength of Electronic States Giving Rise to Stimulated Emission (Bold) and Photoinduced Absorption Out of the Corresponding Electronic State Indicated on Top of Each Column**[a]

| Min $S_0$ ($S_2$) | Min $n\pi^*$ ($S_1$) | Min $S_0$ $\pi\pi^*$ ($S_2$) | Min $^3\pi\pi^*$ ($T_1$) | Min $^3n\pi^*$ ($T_2$) |
|---|---|---|---|---|
| **341 (0.42)** | 376 (0.02) | **415 (0.28)** | 599 (0.02) | 617 (0.02) |
| 469 (0.01) | 279 (0.01) | 765 (0.01) | 534 (0.01) | 397 (0.01) |
| 379 (0.01) | 246 (0.01) | 355 (0.08) | 335 (0.02) | 349 (0.03) |
| 378 (0.04) | | 284 (0.08) | 327 (0.01) | 343 (0.01) |
| 312 (0.01) | | 259 (0.01) | 308 (0.01) | 330 (0.01) |
| 295 (0.11) | | 256 (0.09) | 299 (0.01) | 285 (0.04) |
| 290 (0.01) | | 245 (0.01) | 273 (0.05) | 244 (0.05) |
| 282 (0.03) | | | 250 (0.01) | 241 (0.01) |
| 268 (0.04) | | | 243 (0.03) | |
| 267 (0.02) | | | | |
| 267 (0.04) | | | | |

[a]Computations were performed at the SS-CASPT2/SA-CASSCF-(16,12)/ANO-RCC level averaging over 30 states.

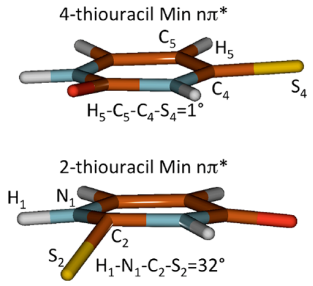


DOI: 10.1021/jacs.8b07057
J. Am. Chem. Soc. 2018, 140, 16087−16093

this region, the $S_2/T_2$ energy gap is significantly reduced in the vicinity of the $S_2/S_1$ CI crossing (0.2 eV). Furthermore, we obtained a large $S_2/T_2$ spin−orbit coupling of 140 $cm^{-1}$ rationalized by the different nature of the two states. The involvement of the $S_2 \rightarrow T_2 \rightarrow T_1$ path is supported by the peak at 600−650 nm observed in the DAS (Figure 2B) with the fast time constant (76 fs). This peak coincides with the PA from the $T_2$ minimum (~620 nm, see Table 1), which builds up concomitantly with the $S_2$ decay, revealing that $S_2 \rightarrow T_2$ intersystem crossing could take place at the same time scale of the nonadiabatic $S_2 \rightarrow S_1$ transition. In a joint experimental/theoretical study on 4-thiothymine,[16] the authors also reported a three-state ($S_2/S_1/T_2$) quasi-degenerate region and suggest, based on dynamics simulations, that 13% of the population undergoes the $S_2 \rightarrow T_2 \rightarrow T_1$ path. Simulations on 2-thiouracil predict 25% of the population to populate this secondary channel. The subsequent $T_1$ ($^3\pi\pi^*$) population (from the Min $^3n\pi^*$) occurs at longer lifetimes (~225 fs), as documented by the peak around 550 nm assigned to the PA of the $T_1$ state (see Table 1).

Notably, we measured an ISC time in 4-thiouracil which is about two times faster compared to that of 2-thiouracil. Pollum et al.[14] measured a triplet buildup time of 360 fs for 2-thiouracil, in agreement with our results on 2-thiouracil of ≈400 fs (see Figure S26 in the SI).[67] According to our calculations, there are two possible explanations for this behavior. On one side, the minimum on the $n\pi^*$ state in 4-thiouracil is planar in contrast to 2-thiouracil (see Scheme 1),

**Scheme 1. Structures of the $^1n\pi^*$ Minima (Min $^1n\pi^*$) in 4- and 2-Thiouracil**




which exhibits an out-of-plane bending of the sulfur,[23,24] also characteristic for nucleobases.[68−70] On the other side, in 4-thiouracil, the $n\pi^*$ minimum coincides with the ISC, whereas in 2-thiouracil, a barrier of ca. 0.1 eV has to be overcome[23,24] (see SI).

## CONCLUSION

In conclusion, high time resolution transient absorption spectroscopy in the UV range allowed us to observe for the first time an ultrafast (sub-100 fs) decay component in the photoinduced dynamics of 4-thiouracil following excitation of its bright $\pi\pi^*$ state, which does not match the buildup time of the fingerprint signals of the triplet states. This is a proof of the involvement of intermediate dark states, mainly the $^1n\pi^*$, acting as doorway to the triplet manifold. This interpretation is supported by high-level *ab initio* static and dynamic numerical modeling, which allows us also to characterize the leading vibrational modes responsible for the experimentally observed coherences. In addition, the modeling is able to rationalize the faster triplet population in 4-thiouracil compared to its isomer 2-thiouracil.

## ASSOCIATED CONTENT

### Supporting Information

The Supporting Information is available free of charge on the ACS Publications website at DOI: 10.1021/jacs.8b07057.

Materials and steady-state spectroscopy, description of the experimental setup, transient spectra, dynamics, global analysis, coherent oscillations, details on the QM/MM protocol, details on the nonadiabatic mixed quantum-classical dynamics simulations, theoretical background of nonlinear spectroscopy, protocols for acquisition of the simulation parameters, electronic structures at representative geometries, active space orbitals, trajectory plots, normal-mode analysis, and Cartesian coordinates (PDF)

## AUTHOR INFORMATION


### Corresponding Authors

*marco.garavelli@unibo.it
*ana@fisica.ufmg.br
*giulio.cerullo@polimi.it

### ORCID

Artur Nenov: 0000-0003-3071-5341
Irene Conti: 0000-0001-7982-4480
Marco Garavelli: 0000-0002-0796-289X
Giulio Cerullo: 0000-0002-9534-2702

### Author Contributions

#R.B.V., D.C.T.F., A.N., and I.C. equally contributed to this work.


### Notes

The authors declare no competing financial interest.

## ACKNOWLEDGMENTS

This work was supported by the European Research Council Advanced Grant STRATUS (ERC-2011-AdG No. 291198), the Marie Curie actions (FP7-PEOPLE-IEF-2012), and the H2020 Grant Agreement number 765266 (LightDyNAmics). D.C.T.F. and A.M.d.P. acknowledge financial support from the funding agencies Fapemig, CNPq, and CAPES. We thank Dr. Stefano Santabarbara for preparing the PBS.

## REFERENCES


(1) Ashwood, B.; Pollum, M.; Crespo-Hernández, C. E. *Photochem. Photobiol.* **2018**, *0*−2. DOI: 10.1111/php.12975
(2) Arslancan, S.; Martínez-Fernández, L.; Corral, I. *Molecules* **2017**, *22* (6), 998.
(3) Pollum, M.; Martínez-Fernández, L.; Crespo-Hernández, C. E. In *Top Curr. Chem.*; Springer, 2014; pp 245−327.
(4) Sismour, A. M. *Nucleic Acids Res.* **2005**, *33* (17), 5640−5646.
(5) Heuberger, B. D.; Pal, A.; Del Frate, F.; Topkar, V. V.; Szostak, J. W. *J. Am. Chem. Soc.* **2015**, *137* (7), 2769−2775.
(6) Meisenheimer, K. M.; Koch, T. H. *Crit. Rev. Biochem. Mol. Biol.* **1997**, *32* (2), 101−140.
(7) Favre, A.; Moreno, G.; Blondel, M. O.; Kliber, J.; Vinzens, F.; Salet, C. *Biochem. Biophys. Res. Commun.* **1986**, *141* (2), 847−854.
(8) Pollum, M.; Jockusch, S.; Crespo-Hernández, C. E. *J. Am. Chem. Soc.* **2014**, *136* (52), 17930−17933.
(9) Reelfs, O.; Karran, P.; Young, A. R. *Photochem. Photobiol. Sci.* **2012**, *11* (1), 148−154.
(10) Pollum, M.; Lam, M.; Jockusch, S.; Crespo-Hernández, C. E. *ChemMedChem* **2018**, *13* (10), 1044−1050.

(11) Reichardt, C.; Crespo-Hernández, C. E. *J. Phys. Chem. Lett.* **2010**, *1* (15), 2239−2243.
(12) Reichardt, C.; Guo, C.; Crespo-Hernández, C. E. *J. Phys. Chem. B* **2011**, *115* (12), 3263−3270.
(13) Pollum, M.; Crespo-Hernández, C. E. *J. Chem. Phys.* **2014**, *140* (7), 071101.
(14) Pollum, M.; Jockusch, S.; Crespo-Hernández, C. E. *Phys. Chem. Chem. Phys.* **2015**, *17* (41), 27851−27861.
(15) Ashwood, B.; Jockusch, S.; Crespo-Hernández, C. E. *Molecules* **2017**, *22* (3), 379.
(16) Martínez-Fernández, L.; Granucci, G.; Pollum, M.; Crespo-Hernández, C. E.; Persico, M.; Corral, I. *Chem. - Eur. J.* **2017**, *23* (11), 2619−2627.
(17) Nenov, A.; Borrego-Varillas, R.; Oriana, A.; Ganzer, L.; Segatta, F.; Conti, I.; Segarra-Marti, J.; Omachi, J.; Dapor, M.; Taioli, S.; et al. *J. Phys. Chem. Lett.* **2018**, *9* (7), 1534−1541.
(18) Nenov, A.; Conti, I.; Borrego-Varillas, R.; Cerullo, G.; Garavelli, M. *Chem. Phys.* **2018**. DOI: 10.1016/j.chemphys.2018.07.025
(19) Middleton, C. T.; de La Harpe, K.; Su, C.; Law, Y. K.; Crespo-Hernández, C. E.; Kohler, B. *Annu. Rev. Phys. Chem.* **2009**, *60* (1), 217−239.
(20) Crespo-Hernández, C. E.; Cohen, B.; Hare, P. M.; Kohler, B. *Chem. Rev.* **2004**, *104* (4), 1977−2019.
(21) Pecourt, J. M. L.; Peon, J.; Kohler, B. *J. Am. Chem. Soc.* **2000**, *122* (38), 9348−9349.
(22) Harada, Y.; Okabe, C.; Kobayashi, T.; Suzuki, T.; Ichimura, T.; Nishi, N.; Xu, Y. Z. *J. Phys. Chem. Lett.* **2010**, *1* (2), 480−484.
(23) Mai, S.; Marquetand, P.; González, L. *J. Phys. Chem. Lett.* **2016**, *7* (11), 1978−1983.
(24) Mai, S.; Marquetand, P.; González, L. *J. Phys. Chem. A* **2015**, *119* (36), 9524−9533.
(25) Sánchez-Rodríguez, J. A.; Mohamadzade, A.; Mai, S.; Ashwood, B.; Pollum, M.; Marquetand, P.; González, L.; Crespo-Hernández, C. E.; Ullrich, S. *Phys. Chem. Chem. Phys.* **2017**, *19* (30), 19756−19766.
(26) Yu, H.; Sanchez-Rodriguez, J. A.; Pollum, M.; Crespo-Hernández, C. E.; Mai, S.; Marquetand, P.; González, L.; Ullrich, S. *Phys. Chem. Chem. Phys.* **2016**, *18* (30), 20168−20176.
(27) Jiang, J.; Zhang, T. S.; Xue, J. D.; Zheng, X.; Cui, G.; Fang, W. H. *J. Chem. Phys.* **2015**, *143* (17), 175103.
(28) Koyama, D.; Milner, M. J.; Orr-Ewing, A. J. *J. Phys. Chem. B* **2017**, *121* (39), 9274−9280.
(29) Bai, S.; Barbatti, M. *J. Phys. Chem. A* **2016**, *120* (32), 6342−6350.
(30) Martínez-Fernández, L.; Corral, I.; Granucci, G.; Persico, M. *Chem. Sci.* **2014**, *5* (4), 1336.
(31) Cui, G.; Fang, W. *J. Chem. Phys.* **2013**, *138* (4), 044315.
(32) Xie, B.-B.; Wang, Q.; Guo, W.-W.; Cui, G. *Phys. Chem. Chem. Phys.* **2017**, *19* (11), 7689−7698.
(33) Zou, X.; Dai, X.; Liu, K.; Zhao, H.; Song, D.; Su, H. *J. Phys. Chem. B* **2014**, *118* (22), 5864−5872.
(34) Gobbo, J. P.; Borin, A. C. *Comput. Theor. Chem.* **2014**, *1040−1041*, 195−201.
(35) Reichardt, C.; Crespo-Hernández, C. E. *Chem. Commun.* **2010**, *46* (32), 5963.
(36) Mai, S.; Pollum, M.; Martínez-Fernández, L.; Dunn, N.; Marquetand, P.; Corral, I.; Crespo-Hernández, C. E.; González, L. *Nat. Commun.* **2016**, *7* (May), 13077.
(37) Mai, S.; Ashwood, B.; Marquetand, P.; Crespo-Hernández, C. E.; González, L. *J. Phys. Chem. B* **2017**, *121* (20), 5187−5196.
(38) Martinez-Fernandez, L.; Fahleson, T.; Norman, P.; Santoro, F.; Coriani, S.; Improta, R. *Photochem. Photobiol. Sci.* **2017**, *16* (9), 1415−1423.
(39) Ruckenbauer, M.; Mai, S.; Marquetand, P.; González, L. *J. Chem. Phys.* **2016**, *144* (7), 074303.
(40) Borrego-Varillas, R.; Ganzer, L.; Cerullo, G.; Manzoni, C. *Appl. Sci.* **2018**, *8* (6), 989.
(41) Varillas, R. B.; Candeo, A.; Viola, D.; Garavelli, M.; De Silvestri, S.; Cerullo, G.; Manzoni, C.; et al. *Opt. Lett.* **2014**, *39* (13), 3849−3852.
(42) Borrego-Varillas, R.; Oriana, A.; Branchi, F.; De Silvestri, S.; Cerullo, G.; Manzoni, C. *J. Opt. Soc. Am. B* **2015**, *32* (9), 1851−1855.
(43) Snellenburg, J. J.; Laptenok, S. P.; Seger, R.; Mullen, K. M.; van Stokkum, I. H. M. *J. Stat. Softw.* **2012**, *49* (3). DOI: 10.18637/jss.v049.i03
(44) Case, D. A.; Darden, T.; Cheatham, T. E.; Simmerling, C.; Wang, J.; Duke, R. E.; Luo, R.; Walker, R. C.; Zhang, W.; Merz, K. M.; et al. University of California: San Francisco, 2012.
(45) Salomon-Ferrer, R.; Case, D. A.; Walker, R. C. *Wiley Interdiscip. Rev. Comput. Mol. Sci.* **2013**, *3* (2), 198−210.
(46) Jorgensen, W. L.; Chandrasekhar, J.; Madura, J. D.; Impey, R. W.; Klein, M. L. *J. Chem. Phys.* **1983**, *79* (2), 926−935.
(47) Ryckaert, J. P.; Ciccotti, G.; Berendsen, H. J. C. *J. Comput. Phys.* **1977**, *23* (3), 327−341.
(48) Miyamoto, S.; Kollman, P. A. *J. Comput. Chem.* **1992**, *13* (8), 952−962.
(49) Weingart, O.; Nenov, A.; Altoè, P.; Rivalta, I.; Segarra-Martí, J.; Dokukina, I.; Garavelli, M. *J. Mol. Model.* **2018**, *24* (9), 271.
(50) Finley, J.; Malmqvist, P.-Å.; Roos, B. O.; Serrano-Andrés, L. *Chem. Phys. Lett.* **1998**, *288* (2−4), 299−306.
(51) Widmark, P.-O.; Malmqvist, P.-A.; Roos, B. O. *Theor. Chim. Acta* **1990**, *77* (5), 291−306.
(52) Roos, B.; Lindh, R.; Malmqvist, P.-Å.; Veryazov, V.; Widmark, P.-O. *J. Phys. Chem. A* **2004**, *108* (15), 2851−2858.
(53) Ghigo, G.; Roos, B. O.; Malmqvist, P.-Å. *Chem. Phys. Lett.* **2004**, *396* (1−3), 142−149.
(54) Forsberg, N.; Malmqvist, P.-Å. *Chem. Phys. Lett.* **1997**, *274* (1−3), 196−204.
(55) Bearpark, M. J.; Robb, M. A.; Bernhard Schlegel, H. *Chem. Phys. Lett.* **1994**, *223* (3), 269−274.
(56) Aquilante, F.; Autschbach, J.; Carlson, R. K.; Chibotaru, L. F.; Delcey, M. G.; De Vico, L.; Fdez. Galván, I.; Ferré, N.; Frutos, L. M.; Gagliardi, L.; et al. *J. Comput. Chem.* **2016**, *37* (5), 506−541.
(57) Du, L.; Lan, Z. *J. Chem. Theory Comput.* **2015**, *11* (4), 1360−1374.
(58) Tully, J. C. *Faraday Discuss.* **1998**, *110*, 407−419.
(59) Hammes-Schiffer, S.; Tully, J. C. *J. Chem. Phys.* **1994**, *101* (6), 4657−4667.
(60) Mukamel, S.; Abramavicius, D. *Chem. Rev.* **2004**, *104* (4), 2073−2098.
(61) Mukamel, S. *Principles of Nonlinear Optical Spectroscopy*; Oxford University Press on Demand, 1999.
(62) Abramavicius, D.; Palmieri, B.; Voronine, D. V.; Šanda, F.; Mukamel, S. *Chem. Rev.* **2009**, *109* (6), 2350−2408.
(63) Li, B.; Johnson, A. E.; Mukamel, S.; Myers, A. B. *J. Am. Chem. Soc.* **1994**, *116* (24), 11039−11047.
(64) Butkus, V.; Valkunas, L.; Abramavicius, D. *J. Chem. Phys.* **2012**, *137* (4), 044513.
(65) Bai, S.; Barbatti, M. *Phys. Chem. Chem. Phys.* **2017**, *19* (20), 12674−12682.
(66) Taras-Goślińska, K.; Wenska, G.; Skalski, B.; Maciejewski, A.; Burdziński, G.; Karolczak, J. *J. Photochem. Photobiol., A* **2004**, *168* (3), 227−233.
(67) A detailed investigation of the 2-thiouracil ultrafast excited-state dynamics will be presented in a forthcoming contribution that is in the process of preparation.
(68) Pepino, A. J.; Segarra-Martí, J.; Nenov, A.; Improta, R.; Garavelli, M. *J. Phys. Chem. Lett.* **2017**, *8* (8), 1777−1783.
(69) Conti, I.; Garavelli, M. *J. Phys. Chem. Lett.* **2018**, *9* (9), 2373−2379.
(70) Conti, I.; Martínez-Fernández, L.; Esposito, L.; Hofinger, S.; Nenov, A.; Garavelli, M.; Improta, R. *Chem. - Eur. J.* **2017**, *23* (60), 15177−15188.


DOI: 10.1021/jacs.8b07057
*J. Am. Chem. Soc.* 2018, 140, 16087−16093

ChemPubSoc Europe

DOI: 10.1002/chem.201904541

CHEMISTRY A European Journal Full Paper

Ultrafast Spectroscopy

# A Unified Experimental/Theoretical Description of the Ultrafast Photophysics of Single and Double Thionated Uracils

Danielle Cristina Teles-Ferreira[+],[a, b] Irene Conti[+],[c] Rocío Borrego-Varillas[+],[d] Artur Nenov[+],[c] Ivo H. M. Van Stokkum,[e] Lucia Ganzer,[d] Cristian Manzoni,[d] Ana Maria de Paula,*[a] Giulio Cerullo,*[d] and Marco Garavelli*[c]

**Abstract:** Photoinduced processes in thiouracil derivatives have lately attracted considerable attention due to their suitability for innovative biological and pharmacological applications. Here, sub-20 fs broadband transient absorption spectroscopy in the near-UV are combined with CASPT2/MM decay path calculations to unravel the excited-state decay channels of water solvated 2-thio and 2,4-dithiouracil. These molecules feature linear absorption spectra with overlapping ππ* bands, leading to parallel decay routes which we systematically track for the first time. The results reveal that different processes lead to the triplet states population, both directly from the ππ* absorbing state and via the intermediate nπ* dark state. Moreover, the 2,4-dithiouracil decay pathways is shown to be strongly correlated either to those of 2- or 4-thiouracil, depending on the sulfur atom on which the electronic transition localizes.

## Introduction

Thiobases are nucleobase derivatives obtained by the replacement of oxygen atoms in the canonical exocyclic carbonyl group with sulfur.[1,2] Thionation redshifts the absorption spectra[3] and radically changes the photophysics[4] of sulfur-substituted bases. In nucleobases, after UV-light absorption, ultrafast nonradiative repopulation of the ground state occurs through conical intersections (CIs),[5] leading to their remarkable photostability.[6] In contrast, in thiobases the main photoexcited state deactivation pathway is intersystem crossing (ISC) to long-lived reactive triplet states. The selective UV absorption and the high triplet quantum yield[7–9] confer to thiobases great potential in the field of photodynamic therapeutic applications[10–14] as well as for their use as photolabels.[15–17] Elucidating the photophysical mechanisms leading to population of the triplet state and their timescales has become increasingly relevant.[8,9,18–20] To date, transient absorption (TA) spectroscopy experiments, with approximately 200-fs time resolution, for 2-thiouracil (2TU), 4-thiouracil (4TU) and 2,4-dithiouracil (24TU) have shown an ultrafast ISC occurring within hundreds of femtoseconds.[7,10,21] For 2TU[21–27] and 4TU,[28,29] high-level calculations have pointed out two possible energy relaxation pathways from the lowest bright excited singlet state: direct ISC to the triplet manifold or a two-step process, whereby the population of the triplet state is mediated by a dark singlet state of nπ* symmetry.[18,20,21,23,24,26,28–33] However, comprehensive experimental data with high enough time resolution and calculations mapping all the simultaneously populated decay paths are still lacking for this class of compounds, preventing a detailed picture of the ultrafast triplet state formation mechanisms.

Here, we combine broadband TA spectroscopy with sub-20 fs pulses in the UV and target analysis thereof with quantum mechanics/molecular mechanics (QM/MM) simulations to decipher the relaxation pathways of thio-substituted uracils in solution and model the TA experimental spectra (see Experimental Section and Supporting Information for details). We measure accurate singlet-state lifetimes leading to the triplet manifold of 2TU and 24TU, originating from simultaneously populated ππ* decay pathways, resolved by a detailed QM/MM computational mapping. This work establishes a unified view of the photophysics of thiouracils.

[a] D. C. Teles-Ferreira,[+] Dr. A. M. de Paula
Departamento de Física, Universidade Federal de Minas Gerais
31270-901 Belo Horizonte, MG (Brazil)
E-mail: ana@fisica.ufmg.br

[b] D. C. Teles-Ferreira[+]
Electrical Engineering Department, Federal Institute of Minas Gerais
Formiga, MG (Brazil)

[c] Dr. I. Conti,[+] Dr. A. Nenov,[+] Prof. M. Garavelli
Dipartimento di Chimica Industriale, Università degli Studi di Bologna
Viale del Risorgimento 4, 40136 Bologna (Italy)
E-mail: marco.garavelli@unibo.it

[d] Dr. R. Borrego-Varillas,[+] Dr. L. Ganzer, Dr. C. Manzoni, Prof. G. Cerullo
IFN-CNR, Department of Physics, Politecnico di Milano
P.za L. da Vinci 32, 20133 Milano (Italy)
E-mail: giulio.cerullo@polimi.it

[e] Dr. I. H. M. Van Stokkum
Department of Physics and Astronomy
Faculty of Sciences, Vrije Universiteit Amsterdam
De Boelelaan 1081, 1081HV Amsterdam (The Netherlands)

[+] These authors contributed equally to this work.

Supporting information and the ORCID identification number(s) for the author(s) of this article can be found under: https://doi.org/10.1002/chem.201904541.


© 2020 Wiley-VCH Verlag GmbH & Co. KGaA, Weinheim

## Results and Discussion

Figure 1 shows the chemical structures of the three investigated thiobases and the corresponding linear absorption (LA) spectra (dashed lines). The calculated spectra (solid lines)[3] are in satisfactory agreement with the experimental ones. Spectral decomposition (grey lines) of the computed LA spectra reveals a complex electronic structure consisting of two [ππ*(S2), ππ*′(S2)] and four [ππ*(S4), ππ*(S2), ππ*′(S4), ππ*′(S2)] bright components for 2TU and 24TU, respectively. Overlapping bands excited simultaneously by a specific pump pulse (red dashed lines) give rise to competing decay channels. Differently from previous studies,[3,23,24,27,34] which considered only the lowest ππ* state, we perform a complete analysis by mapping all decay pathways from the ππ* states populated simultaneously at a specific pump wavelength (ππ* grey overlapping bands in Figure 1) for the first time.

Figure 2 compares the TA spectra of the thiobases for different time delays. For 2TU (panel a) we observe the formation of two photoinduced absorption (PA, $\Delta A > 0$) bands: one in the UV (350–450 nm) and another in the visible (400–650 nm) range. Between these two bands in the 450–550 nm range there is at early delays a dip in the signal that we assign to a superposition of the PA with a stimulated emission (SE, $\Delta A < 0$) signal, as confirmed by the target analysis and calculations discussed later. For 24TU (panels b and c) we observe, for both 330 and 270 nm excitation wavelengths, a negative band at 360 nm assigned to the ground-state bleaching (GSB), because it corresponds to the ππ*(S4) peak in the LA spectrum (Figure 1, central panel). We also observe a broad, redshifted

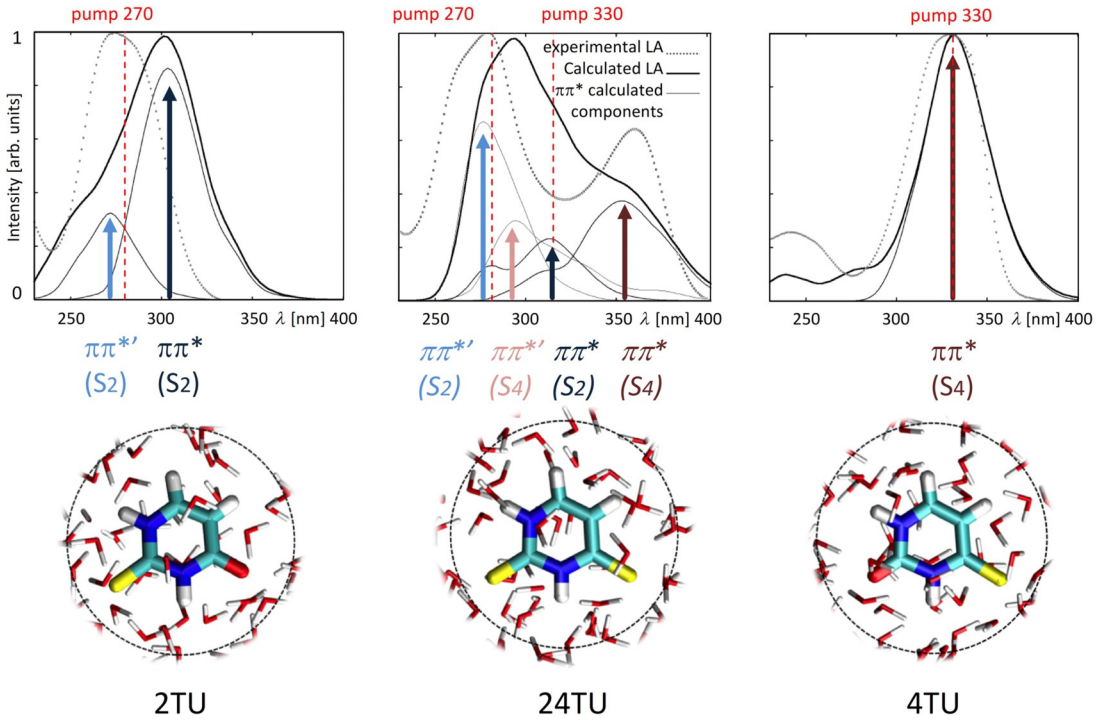



**Figure 1.** Experimental (dashed lines) and computed (black lines) LA spectra for 2TU and 4TU (at the MS-RASPT2/SA-6-RASSCF(12,9|2,4)/ANO-LS level) and for 24TU (at the MS-RASPT2/SA-9-RASSCF(2,2|14,10|2,2)/ANO-LS level), from Ref. [3]. Individual components, associated to specific ππ* electronic transitions, are shown in gray and their band maxima are indicated with arrows. State labels (Sx) are chosen according to the sulfur atom on which the frontier occupied orbitals are localized. The involved orbitals are documented in Figure S2 and Tables S1 and S2 (Supporting Information). Red dashed lines indicate the wavelength at which each system is excited in the TA experiments.

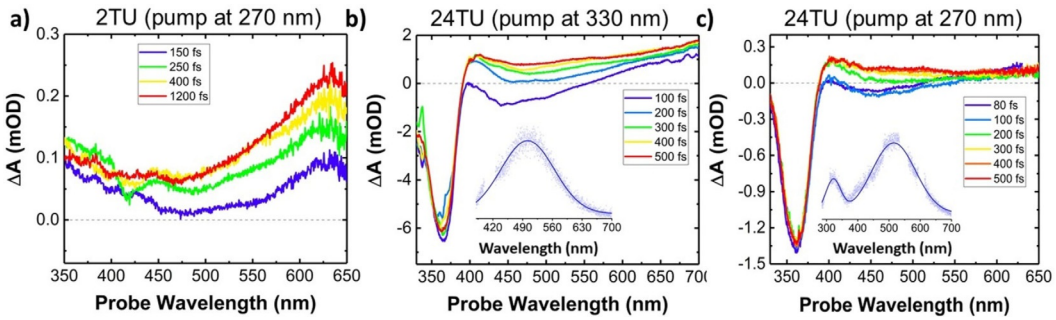



**Figure 2.** TA spectra at selected time delays: a) 2TU pumped at 270 nm. b) 24TU pumped at 330 nm. Inset: PL spectrum under excitation at 330 nm. c) 24TU pumped at 270 nm. Inset: PL spectrum under excitation at 270 nm.


© 2020 Wiley-VCH Verlag GmbH & Co. KGaA, Weinheim

negative band extending from 400 to 550 nm, which is assigned to SE. After about 200 fs the SE band evolves into a PA band which covers the 400–700 nm range. 2TU and 24TU dynamics at selected time delays are shown as insets in Figure 3 and Figure 4, respectively. Our previous studies on 4TU presents similar results, showing a SE band followed by the delayed build-up of a PA band in the visible.[29] The 24TU steady-state photoluminescence (PL) shows a broad peak in the visible (400–700 nm) for both excitation wavelengths (insets Figure 2). For the 270 nm pump there is also a small peak centered at 350 nm.

The TA data were subjected to target analysis, extracting the evolution-associated difference spectra (EADS) which, combined with the QM/MM calculations, allow to obtain an overall picture of the decay pathways. Figure 3 illustrates the decay pathways of 2TU excited at 270 nm. The EADS reveal an excited state that decays with a time constant of 167 fs (red line) into a long-lived product (blue line). There is no decay on the ground state within the time window of 2 ps and the fittings indicate a long-lived state $>1$ ns. The 167 fs EADS is characterized by a broad negative contribution, due to SE, between 400 and 650 nm and a narrow PA band peaking around 350 nm. The product does not show SE bands, but rather two distinct PA bands around 350 and 640 nm. We attribute the 167 fs EADS to the initially excited bright states $\pi\pi^*$(S2) and $\pi\pi^{*\prime}$(S2), whereas the product arises from the triplet manifold. QM/MM calculations allow to assign the observed spectral features and shed light on the underlying non-adiabatic processes. The photoexcitation at 270 nm (Figure 1) populates simultaneously two bright states—$\pi\pi^*$(S2) and $\pi\pi^{*\prime}$(S2)—each of which undergoes a different decay path, illustrated on the right and left hand side of Figure 3 (dark-blue and light-blue circles). The $\pi\pi^*$(S2) state relaxes in a local minimum [Min $\pi\pi^*$(S2)]. The 456 nm wavelength of the calculated vertical emission from Min $\pi\pi^*$(S2) is in good agreement with the peak of the negative contribution to the 167 fs EADS between 400–500 nm (highlighted in a full red box). The minimum is nearly isoenergetic with the minima on the $n\pi^*$ and $^3n\pi^*$ states, denoted Min $n\pi^*$(S2) and Min $^3n\pi^*$(S2). Moreover, the geometries of the three structures are nearly identical (see Figure S3, Supporting Information), suggesting the existence of a three-state near-degeneracy region allowing for the continuous exchange of population between them. Notably, according to our calculations, all three states contribute to an intense PA around 350 nm in the 167 fs EADS (highlighted as a hollow red box). We correlate this continuous population exchange to an increase of the $\pi\pi^*$ lifetime in 2TU, as compared to 4TU (results in Ref. [29]), for which we have recently reported a sub-100 fs lifetime, associated with the ballistic depopulation of the $\pi\pi^*$ state.[29] For the product EADS, the PA bands around 350 nm and between 550–700 nm (highlighted as hollow blue boxes) are in very good agreement with the calculated PAs of the lowest $^3\pi\pi^*$ triplet states [Min $^3\pi\pi^*$(S2) and Min $^3\pi\pi^{*\prime}$(S2)]. Similar bands have also been related to the triplet state in the literature.[21] The non-adiabatic decay pathway following excitation of $\pi\pi^{*\prime}$(S2) (left hand side of Figure 3) evolves through critical

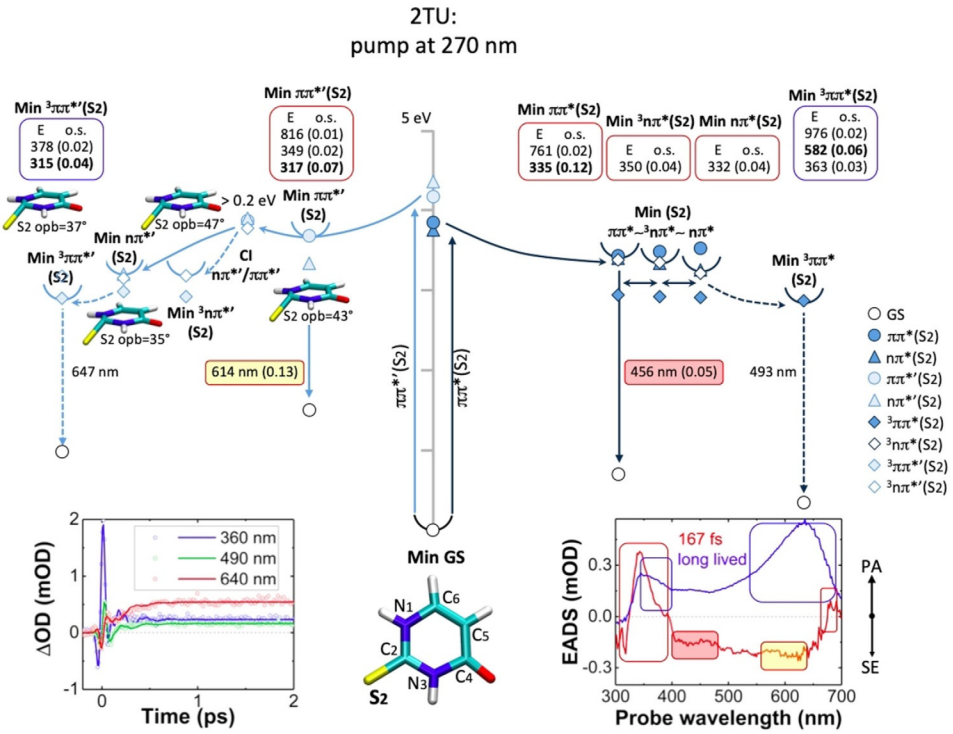



**Figure 3.** $\pi\pi^*$(S2) (on the right) and $\pi\pi^{*\prime}$(S2) (on the left) decay paths of 2TU, starting from the Franck–Condon region. The two bright states are excited with the same pump pulse at 270 nm. The insets shows the dynamics at selected wavelengths and the EADS with the corresponding time constants: 167 fs (red curve) and a long-lived product (blue curve). The calculated SE or PA energies and oscillator strengths (o.s.) are indicated in a red or blue box when they match with 167 fs or the product signals, respectively. For the calculated SE signals, the box background colors refer to different wavelength windows of the experimental ultrafast component (red curve, negative EADS signals).


© 2020 Wiley-VCH Verlag GmbH & Co. KGaA, Weinheim

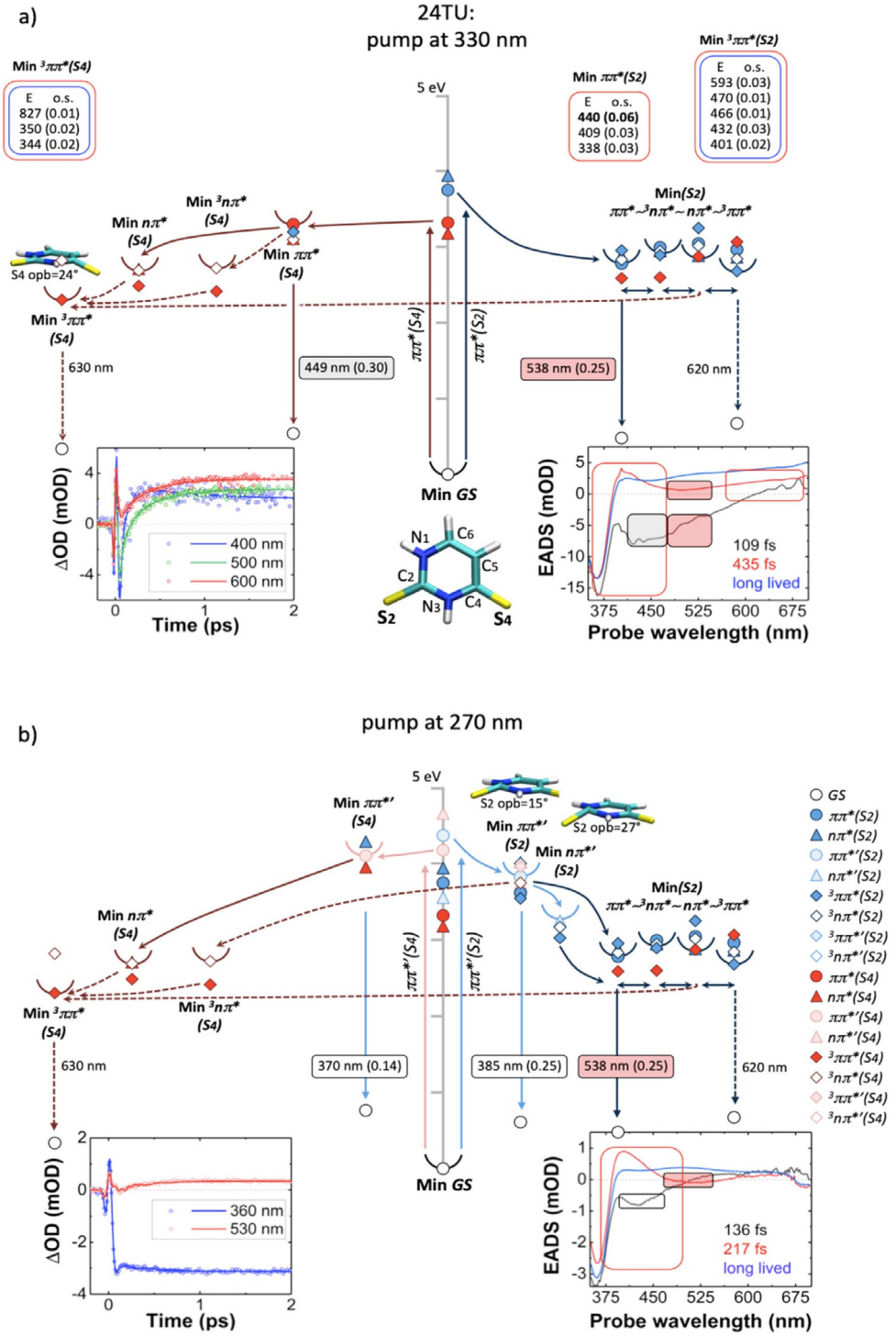



**Figure 4.** a) ππ*(S2) (on the right) and ππ*(S4) (on the left) decay paths, starting from the Franck–Condon region at 330 nm excitation wavelength. Insets: dynamics at selected wavelengths and EADS. b) ππ*′(S2) (on the right) and ππ*′(S4) (on the left) decay paths, starting from the Franck-Condon region at 270 nm excitation wavelength. Insets: dynamics at selected wavelengths and EADS. SE or PA values evaluated on all the minima are indicated with black, red and blue boxes according to the experimental lifetimes that they match. For the calculated SE signals, the box background colors refer to different wavelength windows of the experimental ultrafast component (black curve, negative EADS signals).

points decreasing in energy [Min ππ*′→Min $^3$nπ*′ or Min nπ*′→Min $^3$ππ*′(S2)]. However, a small barrier along the route to reach the ππ*′/nπ*′/$^3$nπ*′ degeneracy region (CI nπ*′/ππ*′) could increase the ππ*′ lifetime to a few hundred fs. Notably, this pathway exhibits a strong sulfur out-of-plane bending (contributing to the longer lifetime) in all involved electronic states, unlike the ππ*(S2) relaxation route described above, for which the system remains planar. This is attributed to the nodal structure of the π*′ orbital (Figure S2 and Table S1, Supporting Information) which leads to an increased


© 2020 Wiley-VCH Verlag GmbH & Co. KGaA, Weinheim

antibonding character. According to our calculations the Min ππ*′(S2) contribute to the intense PA at approximately 350 nm in the 167 fs EADS, as the Min ππ*(S2) region. The SE signal at about 600 nm in the EADS (highlighted in yellow) is typical of the ππ*′(S2) state, considering that it peaks at a similar wavelength to that of the calculated vertical emission from Min ππ*′(S2) (614 nm). Finally, the PA signal at about 350 nm in the product EADS (highlighted in a hollow blue box), corresponds to a transition from the Min $^3$ππ*′.

Summarizing, the observation of a broad 2TU SE band peaking in the range 400–500 nm and around 600 nm [matching with ππ* and ππ*′(S2) SE calculated energies, respectively; see Figure 3] strongly supports the hypothesis that the 167 fs lifetime could be addressed to the simultaneous population of both ππ*(S2) and ππ*′(S2), driving to the final long-lived triplet states.

Figure 4 shows the decay pathways of 24TU excited at 330 nm (upper panel) and 270 nm (lower panel). A target analysis of the 330 nm pump data (EADS in Figure 4a) reveals two time constants −109 fs (black) and 435 fs (red)—plus a long-living signal (blue). The 109 fs EADS shows a broad negative contribution (due to SE) peaking around 450 nm. The 435 fs EADS shows a broad positive signal (PA) covering the whole spectral window, which is superimposed with an SE band peaking around 500 nm, leading to a dip in the positive signal. The product shows a broad positive signal increasing in intensity for longer wavelengths. All EADS exhibit a strong narrowband negative signal around 360 nm, attributed to GSB. We assign the EADS to the initially excited bright states in the Franck–Condon region (109 fs) and after relaxation to the minimum (435 fs), whereas the product EADS arises from the triplet manifold trapping the population on a ns-timescale.

As can be seen in the computed LA spectra (Figure 1), two bright states—ππ*(S2) and ππ*(S4), denoted by dark blue and red circles in Figure 4a—are populated simultaneously by pumping at 330 nm. Each of them undergoes a different decay path, as indicated on the right- and left-hand side of Figure 4a. The ππ*(S2) state (right-hand side of Figure 4a) shows great similarities with the decay mechanism in 2TU. Upon relaxing to the local minimum, Min ππ*(S2), the calculated vertical emission of which (538 nm) matches with the tail of the negative signal above 475 nm in the 109 fs EADS, as well as with dip in the positive signal in the 435 fs EADS (highlighted in full red boxes), the population can undergo a non-adiabatic transfer to any of the states nπ*(S2), $^3$nπ*(S2) or $^3$ππ*(S2). Their corresponding minima show pronounced structural (see Figure S5, Supporting Information) and energetic resemblance, suggesting the continuous exchange of population between all four states, as also hypothesized for 2TU. The presence of a SE signature in the 435-fs EADS is indicative of the long ππ*(S2) lifetime. This is further corroborated by the calculations evidencing that the PA signal around 400–450 nm in the 435 fs EADS can only be attributed to the Min ππ*(S2) (highlighted in hollow red box). Notably, the 435 fs EADS resembles the product EADS at longer wavelengths (>550 nm), in support of the partial population of the lowest triplet state $^3$ππ* on the hundred-fs timescale.

We now turn our attention to the non-adiabatic decay path involving the ππ*(S4) state (left side of Figure 4a). The contribution to the negative signal at lower wavelengths (425–475 nm) in the 109 fs EADS (highlighted in a full grey box) is assigned to the SE from ππ*(S4). The analysis of the critical points reveals a barrierless path [Min ππ*→Min $^3$nπ* or Min nπ*→Min $^3$ππ*(S4)] connecting energetically well-separated minima, which do not exhibit significant out-of-plane distortions. This energy profile suggests the ballistic depopulation of the bright state, in agreement with the obtained 109 fs time constant. The hypothesis of the ultrafast depopulation of the ππ*(S4) state is supported by the absence of negative signal around 450 nm in the 435 fs EADS. Thus, rather than a relaxation process in the bright state, the two time constants 109 and 435 fs describe the parallel decay of the two ππ* states ππ*(S4) and ππ*(S2), respectively. We note the obvious similarities with the decay mechanism of the ππ*(S4) state in 4TU, for which we have recently reported an even shorter lifetime of 76 fs associated with a fast ππ*→nπ* decay in planar ring geometry.[29] Pumping at 270 nm, two other bright ππ* states, ππ*′(S2) and ππ*′(S4), denoted by light-blue and red circles—are populated, the decay paths of which are shown on the right- and left-hand side of Figure 4b. Target analysis reveals again two time constants −136 fs (black) and 217 fs (red)—plus a long-lived product state (blue). Overall, the EADS resemble their counterparts obtained from the 330 nm pump data target analysis, the main difference being the absence of the tail in the negative signal in the 136 fs EADS, now narrowed between 400–475 nm (highlighted in black box). Furthermore, we note the decrease of the intensity of the strong negative band at 360 nm between the 136 fs and 217 fs EADS. The spectral dynamics can be understood as the SE decay on a 136 fs timescale. Calculations show that the SE could be attributed to both ππ*′(S2) and ππ*′(S4), for which the vertical transition energies from their corresponding Min ππ*′(S2) and Min ππ*′(S4) fall at 370 and 385 nm, respectively. The calculated peak positions match the weak band in the PL spectrum (Figure 2c) visible only after 270 nm pump.

The resemblance between the 217 fs and the 435 fs EADS lifetimes, observed upon excitation at 270 or 330 nm, respectively, as well as between the long-lived EADS, suggests that, after departure from the initially populated ππ*′(S2) and ππ*′(S4) states, the system follows dynamics similar to the one observed after 330 nm pump, in agreement with Kasha's rule. This conclusion is reinforced by the PL spectra (Figure 2b,c) showing, for both pump wavelengths, a broadband peak at approximately 500 nm.

The joint analysis of the thio-substituted uracil derivatives 2TU, 24TU and 4TU[29] evidences that, although the decay paths activated through excitation of the bright ππ*/ππ*′ states are characterized by different energetics, lifetimes, and molecular distortions, they exhibit a common pattern. The ππ*/ππ*′ states relax either to their corresponding singlet nπ*/nπ*′ states or directly to the triplet manifold ($^3$nπ*/$^3$nπ*′) through an efficient ISC process. Eventually, the population is trapped in the lowest triplet state in each channel ($^3$ππ*/$^3$ππ*′). Our calculations strongly suggest the involvement of the dark


© 2020 Wiley-VCH Verlag GmbH & Co. KGaA, Weinheim

nπ*/nπ*′ states in the non-adiabatic decay, in agreement with a previous dynamical calculation[24] and time-resolved photoelectron spectroscopy experiments in the gas phase.[26,28,29,32] Nonetheless, the fingerprint PA signals of the nπ*/nπ*′ states are either weak in intensity (e.g., 24TU; for more details see Figures S6 and S7 in the Supporting Information) or coincide with more intense PA signals coming from the ππ*/ππ*′ states and the triplet manifold (e.g., 2TU; Figure S4, Supporting Information).

A deeper analysis of the ππ* decay pathways of the doubly substituted 24TU shows that they resemble the behavior observed for the single substituted 2TU or 4TU systems. This can be rationalized by looking at the shape of π orbitals. The ππ*(S2) transitions in 2TU and 24TU are defined by the same pair of π/π* orbitals, with the bonding orbital localized on $S_2$ (Figure 5a). Accordingly, we predict a similar deactivation mechanism characterized by population exchange between near-degenerate singlet/triplet states resulting in a comparably long ππ* lifetime. The ππ*(S4) transitions in 4TU and 24TU involve the same pair of π/π* orbitals with the bonding orbital localized on S4, leading to a similar ballistic decay route with a 100 fs ππ* time constant (Figure 5b). The ππ*(S4) decay path for 4TU is reported in Ref. [29]. Finally, the ππ*′(S2) transitions on 2TU and 24TU show an evident out-of-plane distortion of the $C_2$═$S_2$ group along the decay path, attributed to the nodal structure of the π*′ orbital, showing a nodal plane along the $C_2$═$S_2$ bond (Figure 5c), which facilitates out-of-plane deformations. The ππ*′(S4) decay path is not reported because at the excitation wavelength employed for 4TU (330 nm), this higher state is not populated due both to its blue shift and to its small intensity [see the 4TU ππ*′(S4) light-blue band in Figure S2, Supporting Information].

## Conclusions

In summary, we have presented a complete study of the simultaneous decay paths for solvated thiouracils, considering all the bright states showing overlapping ππ* linear absorption bands and disentangling the different paths giving rise to the dynamical features in the TA spectra. Comparing the three systems 2TU, 24TU and 4TU, we identify common features. 1) The photoexcited ππ* manifold features an ultrafast decay to the triplet manifold, where it remains trapped on the nanosecond timescale. This non-adiabatic decay happens either directly through an ISC process between the bright ππ* and the $^3$nπ* triplet states, or through an intermediate nπ* state, which remains spectroscopically elusive. 2) The former process leads to triplet formation on an approximately 100 fs timescale [167 fs for 2TU, 109/136 fs for 24TU and 76 fs for 4TU]. 3) Finally, the energetics and molecular deformations along the individual decay routes are correlated to the sulfur atom involved in the frontier π-orbitals, that is, $S_2$ or $S_4$, justifying the similarity of the behavior of 24TU with 2TU/4TU.

## Experimental Section

Femtosecond TA measurements used sub-20 fs pump pulses centered at 330 nm or 270 nm[35–37] and broadband probe pulses obtained by white-light generation in $CaF_2$, covering the 350–630 nm range. The instrumental response function was 25–35 fs FWHM,

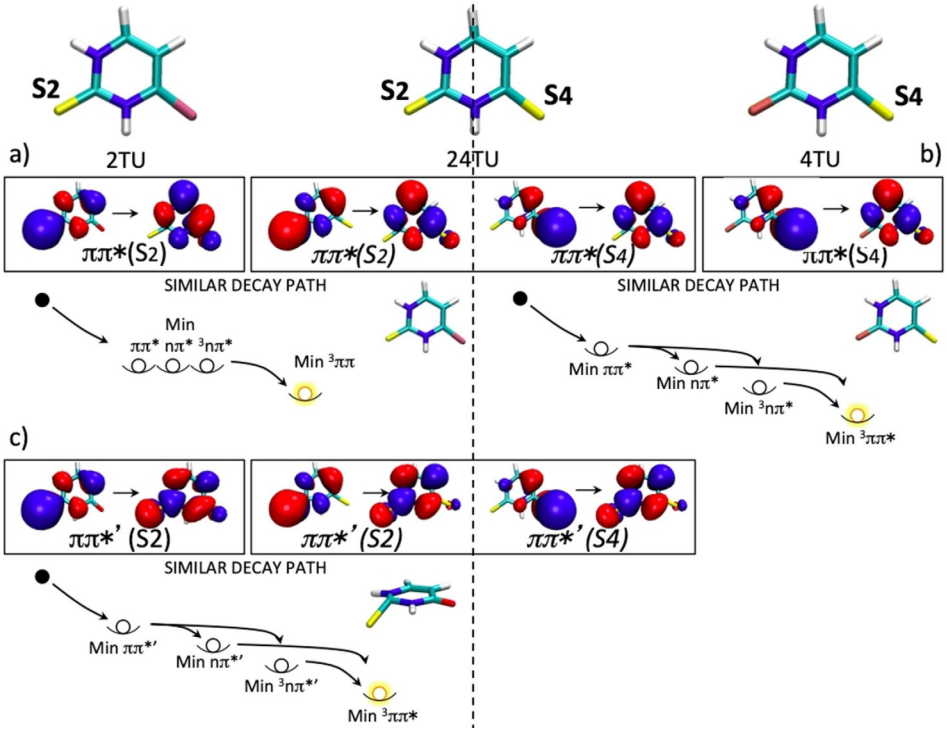



**Figure 5.** Molecular orbitals and schemes of the decay pathways for a) the ππ*(S2) and ππ*(S2) transitions on 2TU and 24TU; b) the ππ*(S4) and the ππ*(S4) transitions on 4TU and 24TU; c) the ππ*′(S2) and the ππ*′(S2) transitions on 2TU and 24TU.


© 2020 Wiley-VCH Verlag GmbH & Co. KGaA, Weinheim

depending on the probe wavelength. Samples were dissolved in phosphate buffer solution. Details on sample preparation and the experimental setup can be found in the Supporting Information. 24TU samples were pumped at 330 and 270 nm, whereas 2TU was pumped at 270 nm (see Figure 1). To describe the spectral evolution, we used global and target analyses with a sequential kinetic model.[38–40] We also measured steady-state photoluminescence (PL) at the same pump wavelengths.

### Computational Methods

The TA spectra and the decay paths were modeled by COBRAMM, our hybrid QM/MM scheme,[29,41–47] that couples high level ab initio multireference dynamically correlated methods (CASPT2//CASSCF)[48] of the photoactive thiouracil system with an explicit classical atomistic model (Amber force field)[49,50] of the solvent (see Supporting Information for more details).

An High/Medium/Low layers partitioning was applied to a spherical droplet centered at 2TU and 24TU with a radius of 12 Å (containing 261 and 265 waters), obtained from the cubic box. The QM region comprises the thionucleobase and the water molecules in 3 Å distance were included in the movable (MM) Medium layer (Figure S1, Supporting Information). The remaining water molecules were kept fixed in the (MM) Low layer. Ground-state geometry minimum was obtained using the optimizer of Gaussian 09[51] at the Møller–Plesset second-order perturbation theory (MP2) level as implemented in the Molcas 8 package[48] through its interface with COBRAMM. The excited-state geometry optimizations were computed at the MS-CASPT2 level (as implemented in Molcas 8 through its interface with COBRAMM), by using an active space including the sulfur lone pairs and the valence $\pi$-orbitals to a total of 12 electrons in 9 orbitals for 2TU and 14 electrons in 10 orbitals for 24TU (Tables S1 and S2, Supporting Information). The ANO-L basis set was used,[52] adopting contractions 5s4p2d1f on sulfur, 4s3p2d1f on carbon/oxygen/nitrogen and 3s2p1d on hydrogen atoms. The optimizing procedure is still done with the G09 optimizer, following the COBRAMM structure.

Critical points and conical intersections vertical energies were refined through a larger active space, extended by two bonding (n on O2 n and $\pi$ on sulfur) and one anti-bonding orbital ($\pi^*$ on sulfur, Table S1 and S2), together with an enlarged ANO-RCC basis set, adopting the contractions 6s5p3d2f1g on sulfur, 5s4p3d2f1g on carbon/oxygen/nitrogen and 4s3p2d1f on hydrogen atoms. So, an active space of (16e,12°) for 2TU and (18e,14°) for 24TU. Eleven states average calculations were employed.

The CASPT2 computations were always performed both in the single-state and multi-state approach. The ionization-potential-electron-affinity (IPEA) shift[53,54] was set to 0.0 and an imaginary shift[55] of 0.2 a.u. was used throughout. Transition dipole moments (TDMs) were calculated both at the SA-CASSCF level and at the MS-CASPT2 level by using the RASSI routine[56] of the Molcas code.

Conical intersections optimizations were performed with the gradient projection algorithm by Bearpark et al.,[57,58] as implemented in COBRAMM.[41]

## *Acknowledgements*

D.C.T.F. and A.M.d.P. acknowledge financial support from the funding agencies Fapemig, CNPq, and CAPES and INCT in Carbon Nanomaterials. We thank Dr. S. Santabarbara for preparing the PBS and T. A. S. Brandão (UFMG, Department of Chemistry) for helping with PL measurements. I.H.M.V.S. and G.C. acknowledge support from Horizon 2020 (Grant No. 654148, Laserlab-Europe). G.C. and M.G. acknowledge support from the H2020 Grant Agreement number 765266 (LightDyNAmics) and the European Research Council Advanced Grant STRATUS (ERC-2011-AdG No. 291198).

## Conflict of interest

The authors declare no conflict of interest.

**Keywords:** CASPT2 · conical intersections · QM/MM · thiobases · transient absorption · ultrafast spectroscopy

[1] B. Ashwood, M. Pollum, C. E. Crespo-Hernández, *Photochem. Photobiol.* **2019**, *95*, 33 – 58.
[2] S. Arslancan, L. Martínez-Fernández, I. Corral, *Molecules* **2017**, *22*, 998.
[3] A. Nenov, I. Conti, R. Borrego-Varillas, G. Cerullo, M. Garavelli, *Chem. Phys.* **2018**, *515*, 643 – 653.
[4] J. M. L. Pecourt, J. Peon, B. Kohler, *J. Am. Chem. Soc.* **2001**, *123*, 10370 – 10378.
[5] A. Nenov, J. Segarra-Martí, A. Giussani, I. Conti, I. Rivalta, E. Dumont, V. K. Jaiswal, S. F. Altavilla, S. Mukamel, M. Garavelli, *Faraday Discuss.* **2015**, *177*, 345 – 362.
[6] C. T. Middleton, K. de La Harpe, C. Su, Y. K. Law, C. E. Crespo-Hernández, B. Kohler, *Annu. Rev. Phys. Chem.* **2009**, *60*, 217 – 239.
[7] M. Pollum, S. Jockusch, C. E. Crespo-Hernández, *Phys. Chem. Chem. Phys.* **2015**, *17*, 27851 – 27861.
[8] B. Ashwood, S. Jockusch, C. E. Crespo-Hernández, *Molecules* **2017**, *22*, 379.
[9] M. Pollum, L. Martínez-Fernández, C. E. Crespo-Hernández, *Top. Curr. Chem.* **2014**, *355*, 245 – 327.
[10] M. Pollum, M. Lam, S. Jockusch, C. E. Crespo-Hernández, *ChemMedChem* **2018**, *13*, 1044 – 1050.
[11] C. Reichardt, C. E. Crespo-Hernaíndez, *J. Phys. Chem. Lett.* **2010**, *1*, 2239 – 2243.
[12] C. Reichardt, C. Guo, C. E. Crespo-Hernández, *J. Phys. Chem. B* **2011**, *115*, 3263 – 3270.
[13] O. Reelfs, P. Karran, A. R. Young, *Photochem. Photobiol. Sci.* **2012**, *11*, 148 – 154.
[14] A. Massey, Y. Z. Xu, P. Karran, *Curr. Biol.* **2001**, *11*, 1142 – 1146.
[15] A. Favre, G. Moreno, M. O. Blondel, J. Kliber, F. Vinzens, C. Salet, *Biochem. Biophys. Res. Commun.* **1986**, *141*, 847 – 854.
[16] M. Harris, H. Cote, C. Ochoa, C. Allavena, E. Negredo, P. Cahn, C. Zala, F. Raffi, *J. Acquired Immune Defic. Syndr.* **2009**, *50*, 339 – 340.
[17] K. M. Meisenheimer, T. H. Koch, *Crit. Rev. Biochem. Mol. Biol.* **1997**, *32*, 101 – 140.
[18] M. Pollum, S. Jockusch, C. E. Crespo-Hernández, *J. Am. Chem. Soc.* **2014**, *136*, 17930 – 17933.
[19] D. Valverde, A. Vasconcelos Sanches de Araujo, A. C. Borin, S. Canuto, *Phys. Chem. Chem. Phys.* **2017**, *19*, 29354 – 29363.
[20] X. Zou, X. Dai, K. Liu, H. Zhao, D. Song, H. Su, *J. Phys. Chem. B* **2014**, *118*, 5864 – 5872.
[21] M. Pollum, C. E. Crespo-Hernández, *J. Chem. Phys.* **2014**, *140*, 071101.
[22] See Ref. [20].
[23] S. Mai, P. Marquetand, L. González, *J. Phys. Chem. A* **2015**, *119*, 9524 – 9533.
[24] S. Mai, P. Marquetand, L. González, *J. Phys. Chem. Lett.* **2016**, *7*, 1978 – 1983.
[25] G. Cui, W. H. Fang, *J. Chem. Phys.* **2013**, *138*, 044315.
[26] S. Mai, A. Mohamadzade, P. Marquetand, L. González, *Molecules* **2018**, *23*, 2836.
[27] J. P. Gobbo, A. C. Borin, *Comput. Theor. Chem.* **2014**, *1040*, 195 – 201.
[28] A. Mohamadzade, S. Bai, M. Barbatti, S. Ullrich, *Chem. Phys.* **2018**, *515*, 572 – 579.


© 2020 Wiley-VCH Verlag GmbH & Co. KGaA, Weinheim

[29] R. Borrego-varillas, D. C. Teles-ferreira, A. Nenov, I. Conti, L. Ganzer, C. Manzoni, M. Garavelli, A. M. De Paula, G. Cerullo, *J. Am. Chem. Soc.* **2018**, *140*, 16087 – 16093.
[30] M. Ruckenbauer, S. Mai, P. Marquetand, L. González, *J. Chem. Phys.* **2016**, *144*, 074303.
[31] D. Koyama, M. J. Milner, A. J. Orr-Ewing, *J. Phys. Chem. B* **2017**, *121*, 9274 – 9280.
[32] J. A. Sánchez-Rodríguez, A. Mohamadzade, S. Mai, B. Ashwood, M. Pollum, P. Marquetand, L. González, C. E. Crespo-Hernández, S. Ullrich, *Phys. Chem. Chem. Phys.* **2017**, *19*, 19756 – 19766.
[33] J. Jiang, T. S. Zhang, J. D. Xue, X. Zheng, G. Cui, W. H. Fang, *J. Chem. Phys.* **2015**, *143*, 175103.
[34] L. Martinez-Fernandez, T. Fahleson, P. Norman, F. Santoro, S. Coriani, R. Improta, *Photochem. Photobiol. Sci.* **2017**, *16*, 1415 – 1423.
[35] A. Nenov, R. Borrego-Varillas, A. Oriana, L. Ganzer, F. Segatta, I. Conti, J. Segarra-Marti, J. Omachi, M. Dapor, S. Taioli, C. Manzoni, S. Mukamel, G. Cerullo, M. Garavelli, *J. Phys. Chem. Lett.* **2018**, *9*, 1534 – 1541.
[36] R. B. Varillas, A. Candeo, D. Viola, M. Garavelli, S. De Silvestri, G. Cerullo, C. Manzoni, S. De Silvestri, G. Cerullo, C. Manzoni, *Opt. Lett.* **2014**, *39*, 3849 – 3852.
[37] R. Borrego-Varillas, A. Oriana, F. Branchi, S. De Silvestri, G. Cerullo, C. Manzoni, *J. Opt. Soc. Am. B* **2015**, *32*, 1851 – 1855.
[38] J. J. Snellenburg, S. P. Laptenok, R. Seger, K. M. Mullen, I. H. M. van Stokkum, *J. Stat. Softw.* **2012**, *49*, 1 – 22.
[39] I. H. M. Van Stokkum, C. C. Jumper, J. J. Snellenburg, G. D. Scholes, R. Van Grondelle, P. Malý, *J. Chem. Phys.* **2016**, *145*, 174201.
[40] I. H. M. Van Stokkum, D. S. Larsen, R. Van Grondelle, *Biochim. Biophys. Acta Bioenerg.* **2004**, *1657*, 82 – 104.
[41] O. Weingart, A. Nenov, P. Altoè, I. Rivalta, J. Segarra-Martí, I. Dokukina, M. Garavelli, *J. Mol. Model.* **2018**, *24*, 271.
[42] I. Conti, L. Martínez-Fernández, L. Esposito, S. Hofinger, A. Nenov, M. Garavelli, R. Improta, *Chem. Eur. J.* **2017**, *23*, 15177 – 15188.
[43] I. Conti, P. Altoe, M. Stenta, M. Garavelli, G. Orlandi, *Phys. Chem. Chem. Phys.* **2010**, *12*, 5016 – 5023.
[44] A. Giussani, I. Conti, A. Nenov, M. Garavelli, *Faraday Discuss.* **2018**, *207*, 375 – 387.
[45] I. Conti, A. Nenov, S. Höfinger, S. F. Altavilla, I. Rivalta, E. Dumont, G. Orlandi, M. Garavelli, *Phys. Chem. Chem. Phys.* **2015**, *17*, 7291 – 7302.
[46] I. Conti, M. Garavelli, *J. Phys. Chem. Lett.* **2018**, *9*, 2373 – 2379.
[47] S. F. Altavilla, J. Segarra-Martí, A. Nenov, I. Conti, I. Rivalta, M. Garavelli, *Front. Chem.* **2015**, *3*, 29.
[48] F. Aquilante, J. Autschbach, R. K. Carlson, L. F. Chibotaru, M. G. Delcey, L. De Vico, I. F. Galván, N. Ferré, L. M. Frutos, L. Gagliardi, M. Garavelli, A. Giussani, C. E. Hoyer, G. L. Manni, H. Lischka, D. Ma, P. Å. Malmquist, T. Müller, A. Nenov, M. Olivucci, *J. Comput. Chem.* **2016**, *37*, 506 – 541.
[49] Amber 12, D. A. Case, T. A. Darden, T. E. Cheatham III, C. L. Simmerling, J. Wang, R. E. Duke, R. Luo, R. C. Walker, W. Zhang, K. M. Merz, B. Roberts, S. Hayik, A. Roitberg, G. Seabra, J. Swails, A. W. Götz, I. Kolossváry, K. F.Wong, F. Paesani, J. Vanicek, R. M.Wolf, J. Liu, X. Wu, S. R. Brozell, T. Steinbrecher, H. Gohlke, Q. Cai, X. Ye, J. Wang, M.-J. Hsieh, G. Cui, D. R. Roe, D. H. Mathews, M. G. Seetin, R. Salomon-Ferrer, C. Sagui, V. Babin, T. Luchko, S. Gusarov, A. Kovalenko, P. A. Kollman, University of California, San Francisco **2012**.
[50] R. Salomon-Ferrer, D. A. Case, R. C. Walker, *WIREs Comput. Mol. Sci.* **2013**, *3*, 198 – 210.
[51] Gaussian 09, Revision B01, M. J. Frisch, G. W. Trucks, H. B. Schlegel, G. E. Scuseria, M. A. Robb, J. R. Cheeseman, G. Scalmani, V. Barone, G. A. Petersson, H. Nakatsuji, X. Li, M. Caricato, A. Marenich, J. Bloino, B. G. Janesko, R. Gomperts, B. Mennucci, H. P. Hratchian, J. V. Ortiz, A. F. Izmaylov, J. L. Sonnenberg, D. Williams-Young, F. Ding, F. Lipparini, F. Egidi, J. Goings, B. Peng, A. Petrone, T. Henderson, D. Ranasinghe, V. G. Zakrzewski, J. Gao, N. Rega, G. Zheng, W. Liang, M. Hada, M. Ehara, K. Toyota, R. Fukuda, J. Hasegawa, M. Ishida, T. Nakajima, Y. Honda, O. Kitao, H. Nakai, T. Vreven, K. Throssell, J. A. Montgomery Jr., J. E. Peralta, F. Ogliaro, M. Bearpark, J. J. Heyd, E. Brothers, K. N. Kudin, V. N. Staroverov, T. Keith, R. Kobayashi, J. Normand, K. Raghavachari, A. Rendell, J. C. Burant, S. S. Iyengar, J. Tomasi, M. Cossi, J. M. Millam, M. Klene, C. Adamo, R. Cammi, J. W. Ochterski, R. L. Martin, K. Morokuma, O. Farkas, J. B. Foresman, D. J. Fox, Gaussian, Inc. Wallingford CT, **2010**..
[52] P.-O. Widmark, P. Å. Malmqvist, B. O. Roos, *Theor. Chem. Acc.* **1990**, *77*, 291 – 306.
[53] G. Ghigo, B. O. Roos, P. Å. Malmqvist, *Chem. Phys. Lett.* **2004**, *396*, 142 – 149.
[54] J. P. Zobel, J. J. Nogueira, L. González, *Chem. Sci.* **2017**, *8*, 1482 – 1499.
[55] N. Forsberg, P. Å. Malmqvist, *Chem. Phys. Lett.* **1997**, *274*, 196 – 204.
[56] P. Å. Malmqvist, *Int. J. Quantum Chem.* **1986**, *30*, 479 – 494.
[57] M. J. Bearpark, M. A. Robb, H. B. Schlegel, *Chem. Phys. Lett.* **1994**, *223*, 269 – 274.
[58] M. J. Bearpark, S. M. Larkin, T. Vreven, *J. Phys. Chem. A* **2008**, *112*, 7286 – 7295.

Manuscript received: October 3, 2019
Accepted manuscript online: November 21, 2019
Version of record online: December 10, 2019


© 2020 Wiley-VCH Verlag GmbH & Co. KGaA, Weinheim

# Intersystem crossing in thiobases proceeds by a dark intermediate state

*Danielle Cristina* Teles-Ferreira[1], *Rocío* Borrego-Varillas[2], *Lucia* Ganzer[2], *Barbara Elza* Nogueira Faria[1], *Cristian* Manzoni[2], *Sandro* De Silvestri[2], *Artur* Nenov[3], *Irene* Conti[3], *Marco* Garavelli[3*], *Giulio* Cerullo[2*], and *Ana Maria* de Paula[1*]

[1]Departamento de Física, Universidade Federal de Minas Gerais, 31270-901 Belo Horizonte-MG, Brazil
[2]IFN-CNR, Dipartimento di Fisica, Politecnico di Milano, Piazza Leonardo da Vinci 32, I-20133 Milano, Italy
[3]Dipartimento di Chimica Industriale, Università degli Studi di Bologna, Viale del Risorgimento 4, I-40136 Bologna, Italy

**Abstract.** 4-thiouracil (4TU) is studied by transient absorption spectroscopy employing sub-20 fs UV-pulses and hybrid QM(CASPT2) / MM(AMBER) computations (static and dynamic), evidencing that, along the photoexcited relaxation pathway, intersystem crossing originates from a dark intermediate state.

Thiobases are DNA or RNA nucleobases where an exocyclic carbonyl oxygen is replaced by a sulfur atom [1]. Thiation induces a red-shift in the absorption spectrum of the thiobases to the 280-400 nm range and causes also a dramatic change in the photophysics with respect to the canonical nucleobases [2,3]: while in DNA/RNA monomers repopulation of the ground state occurs on an ultrafast timescale through a high rate of internal conversion $S_1 \rightarrow S_0$ mediated by a conical intersection (CI), the major relaxation pathway in thiobases is via the population of triplet states via an ultrafast intersystem crossing (ISC) [4]. Thiobases have attracted much interest in the last few years due to their biological relevance and also the many possibilities of photo-therapeutic applications [1]. In spite of that, their ultrafast deactivation mechanisms are not yet fully understood. In this work we combine UV transient absorption spectroscopy featuring sub-20-fs time resolution in the UV with hybrid quantum mechanics/molecular mechanics (QM/MM) state-of-the-art computational tools to analyse the ultrafast photoinduced dynamics in 4TU. We provide the first experimental evidence that ISC occurs from a dark state of $n\pi^*$ character, that is intermediately populated from the bright $\pi\pi^*$ state excited by near-UV light [5].

Pump-probe measurements were carried out starting from a Ti:Sapphire laser producing 100-fs pulses at 800 nm wavelength and 1-kHz repetition rate. Sub-20 fs UV pump pulses (320-360 nm) were generated by frequency up-conversion of a visible NOPA with the fundamental beam (Figure 2b) [6]. The probe pulses (250-700nm) were obtained by white

*Corresponding author: ana@fisica.ufmg.br , giulio.cerullo@polimi.it, marco.garavelli@unibo.it.

© The Authors, published by EDP Sciences. This is an open access article distributed under the terms of the Creative Commons Attribution License 4.0 (http://creativecommons.org/licenses/by/4.0/).

light generation in a $CaF_2$ plate [7]. The 4TU solution was prepared in a PBS solution at pH 7.4 with concentration of 4 mM.

The QM/MM scheme couples a state-of-the-art ab-initio multireference dynamically correlated description (CASPT2) of the 4TU with an explicit classical atomistic model (AMBER force field) of the solvent [8]. A topological analysis of the populated excited states (stationary points, CIs and ISCs) is supplemented by mixed-quantum classical molecular dynamics simulations realized through a limited ensemble of 30 room temperature trajectories employing Tully's fewest switches surface hopping algorithm run for 200 fs with a time step of 1.0 fs at the SS-RASPT2/SA-3-RASSCF(12,9|2,4) level of theory comprising all valence π-orbitals, the lone pair of the sulfur and four extra-valence virtual orbitals with up to double excitations. The state averaging covers the ground, the lowest (dark) nπ* ($S_1$) and the lowest (bright) ππ* states ($S_2$), the dynamics was initiated in $S_2$.

A 2D map of the differential transmission (ΔT/T) is displayed in Figure 1a. Panel 1b shows the dynamics for selected wavelengths. At early times we observe three signatures that we attribute to the bright photoexcited ππ* state: the ground state bleaching (GSB, below 360 nm) a stimulated emission (SE) signal peaking at 400 nm and a photo-induced absorption (PA) band above 500 nm. The SE band displays a first ultrafast decay on the sub-100-fs timescale and subsequently a second PA band peaking at 550 nm grows in on a ≈500-fs timescale. This band has been observed in previous studies with lower, 200-fs time resolution [4] and has been assigned to triplet-triplet absorption, thus providing a fingerprint of the ISC process. Our data clearly show that ISC does not occur directly from the photoexcited bright state but is mediated by an intermediate dark state. A global analysis of the data confirms this scenario and reveals time constants of 78 fs and 201 fs for the ππ* SE decay and triplet PA formation. Furthermore, in the 2D map we can also clearly observe the ultrafast impulsively excited vibrational motions with two frequencies: 400 $cm^{-1}$ and 680 $cm^{-1}$ which are in good agreement with the calculated: a breathing mode with frequency of 457 $cm^{-1}$ and in two hydrogen-out-of-plane bending modes with frequencies 697 $cm^{-1}$ and 784 $cm^{-1}$.

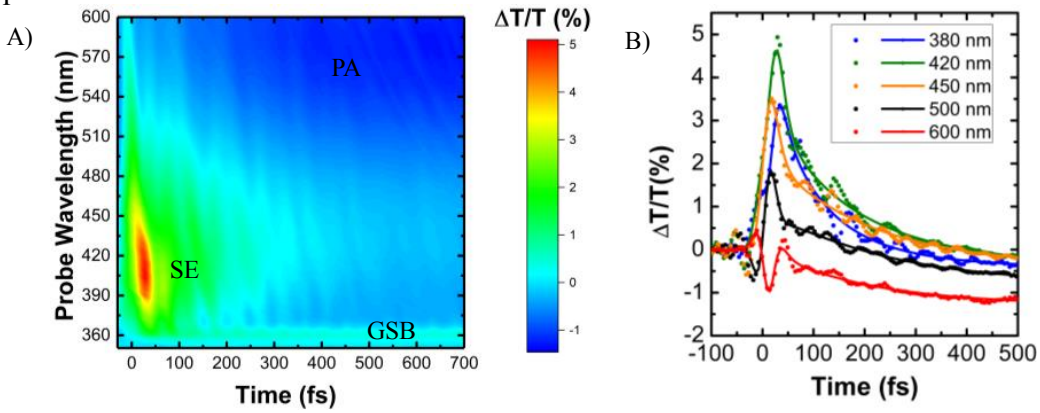



**Fig 1**. Transient absorption measurements: a) 2D map, b) Transient dynamics at selected wavelengths, experimental data in circles and fittings in solid lines.

By supplementing the experiments with topology analysis and molecular dynamics simulations we provide a complete picture of the photo-induced events. Figure 2b shows the experimental (black) and calculated (green, blue and magenta) linear absorption spectra [9] together with the pump pulse spectrum (yellow-dashed area). The good agreement allows to assign the underlying transitions to the lowest bright ππ* states (bands A, B and C in Figures 2a and 2b). The pump pulse populates the lowest ππ* state (S2 in the Franck-

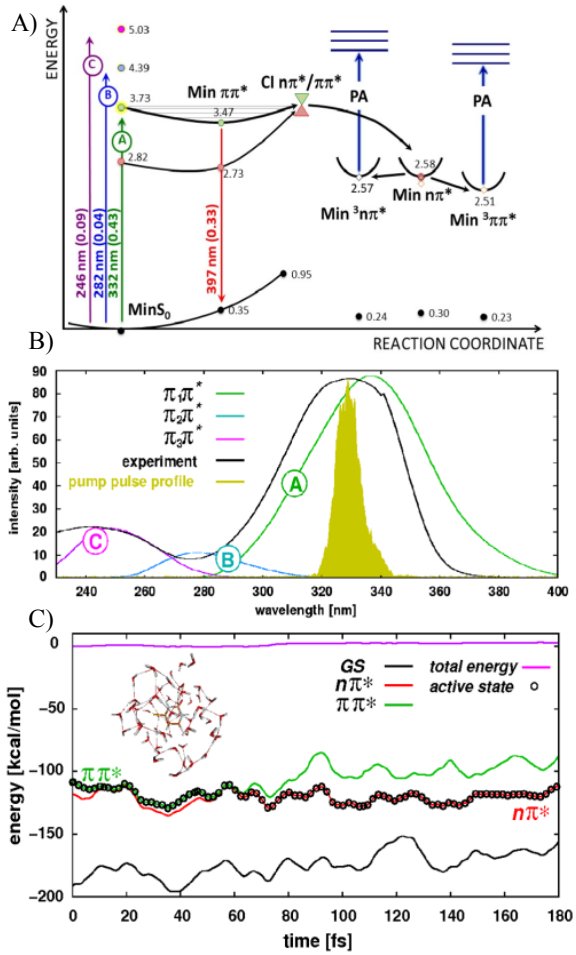



Fig 2. Computational results: a) Schematic picture of the ES deactivation processes; b) linear absorption spectrum of the lowest three bright ππ* transitions (green, blue and magenta), experimental spectrum (black), pump pulse spectrum (yellow dashed); c) a representative molecular dynamics trajectory.

Condon (FC) region, green circles in Figure 2a). From there the decay path leads to a sloped CI seam with the dark nπ* state populated upon thermal fluctuations. We find that the nπ* state minimum (Min nπ*) is isoenergetic with two triplet states, of nπ* and of ππ* nature, respectively, allowing for the effective population of the triplet manifold. The limited ensemble of room temperature trajectories (example trajectory shown in Figure 2c) shows that ultrafast ππ*→nπ* transition is facilitated when thermal energy is inserted in the system despite the pronounced ππ*/nπ* energy gap of 1 eV at equilibrium (Figure 2a). ππ*→nπ* population decay is found to occur with a time constant of 67.5 fs, in agreement with the 78 fs time constant extracted from the global analysis. The longer time constant of 201 fs is assigned to the build up of PA from the $^3$ππ* triplet state, supported by our computations revealing higher lying states in the triplet manifold absorbing around 550 nm (see PA label in Figure 1a and in Figure 2b). We note that the $^1$nπ* state is completely dark in the probed spectral window as it exhibits no SE or PA.

In conclusion, the combination of high time resolution transient spectroscopy in the UV range with ab initio numerical modelling allowed us to capture the dark intermediate state in the relaxation path to the triplet state in the 4TU.

## References

[1] S. Arslancan, L. Martínez-Fernández, and I. Corral, Molecules **22**, 998 (2017).
[2] S. Mai, M. Pollum, L. Martínez-Fernánez, N. Dunn, P. Marquetand, I. Corral, C. E. Crespo-Hernández and L. González, Nat. Commun **7**, 13077 (2016).
[3] S. Mai, P. Marquetand, and L. González, J. Phys. Chem. A **119**, 9524 (2015).
[4] M. Pollum, S. Jockusch, and C. E. Crespo-Hernández, Phys. Chem. Chem. Phys **17**, 27851 (2015).
[5] R. Borrego-Varillas, D. C. Teles-Ferreira, A. Nenov, I. Conti, L. Ganzer, C. Manzoni, M. Garavelli, A. M. De Paula and G. Cerullo, submitted 2018.
[6] R. Borrego-Varillas, et al. Opt. Lett **39**, 3849 (2014).
[7] R. Borrego-Varillas, L. Ganzer, G. Cerullo and C. Manzoni, Appl. Sci. **8**, 2076 (2018).
[8] O. Weingart, A. Nenov, P. Altoé, I. Rivalta, J. Segarra-Martí, I. Dokukina and M. Garavelli, J. Mol. Model., in press (2018) DOI: 10.1007/s00894-018-3769-6.
[9] A. Nenov, I. Conti, R. Borrego-Varillas, G. Cerullo and M. Garavelli, Chem. Phys. in press (2018), DOI: 10.1016/j.chemphys.2018.07.025.
DCTF, BENF and AMdeP acknowledge the CNPq, Fapemig, CAPES for financial support.